

USING COMPLIANCE IN LIEU OF SENSORY FEEDBACK FOR AUTOMATIC ASSEMBLY

by

SAMUEL HUNT DRAKE

S.B., Massachusetts Institute of Technology
(1965)

S.M., Massachusetts Institute of Technology
(1970)

MECH.E., Massachusetts Institute of Technology
(1974)

SUBMITTED IN PARTIAL FULFILLMENT
OF THE REQUIREMENTS FOR THE
DEGREE OF

DOCTOR OF SCIENCE

at the

MASSACHUSETTS INSTITUTE OF TECHNOLOGY

September, 1977

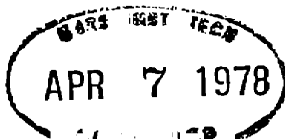
(i.e. February, 1978)

Signature of Author..... *Samuel H. Drake*
Department of Mechanical Engineering, September 26, 1977

Certified by.....
Thesis Supervisor

Accepted by.....
Chairman, Department Committee on Graduate Students

ARCHIVES



USING COMPLIANCE IN LIEU OF SENSORY FEEDBACK FOR AUTOMATIC ASSEMBLY

by

SAMUEL HUNT DRAKE

Submitted to the Department of Mechanical Engineering on September 26, 1977 in partial fulfillment of the requirements for the degree of Doctor of Science.

ABSTRACT

A technique has been developed for performing mechanical assembly without active sensory feedback when using a programmable assembly machine or assembly robot that has positional errors more than an order of magnitude larger than the clearances of the pieces to be assembled. Most of the past research in programmable automatic assembly has been focused on adding either visual or force feedback to overcome the accuracy problem. The technique discussed in this thesis is based on designing a passive compliance structure or mechanism that will essentially mimic an active force feedback system. In response to a lateral positional error, the passive compliance system allows the part being assembled to realign laterally, provided that the parts have chamfered edges and that the parts can be brought together with an initial positional error less than the dimensions of the chamfers. In response to an angular misalignment, the passive compliance allows the part to realign rotationally. A locking mechanism is used to hold the compliance device in a relatively rigid state while the parts to be assembled are being transported and positioned. This allows the compliance system which otherwise has a low natural frequency to be positioned using high velocities and accelerations.

This thesis shows both theoretically and experimentally that the forces that occur during the assembly process are a function of (a) the values of the compliance matrix (a 6 x 6 symmetric matrix of the compliance seen at the assembly interface), (b) the initial positional errors, (c) the relative clearance of the pieces, and (d) the coefficient of friction between the pieces. This thesis also shows that the important parameters for the insertion of a shaft or a peg into a hole are the spatial center of compliance, the lateral stiffness, and the rotational stiffness.

The compliance system was used both in experiments that measured assembly forces and moments and as part of a programmable assembly demonstration project. Seventeen parts of an automobile alternator were assembled in approximately two minutes thirty seconds using the compliance system mounted on an electrically actuated four-degree-of-freedom programmable assembly machine. The nominal clearances between the parts were as small as 0.01mm (0.0004 in).

Using a properly engineered compliance system for automatic assembly instead of force feedback has a number of important advantages. A force sensor is not required nor is any additional computational power required. As the compliant structure or mechanism allows small corrective motions, many assembly operations can be performed using a programmable assembly machine with fewer than six degrees of freedom (generalized force feedback requires a minimum of six active degrees of freedom). The speed at which the assembly can be accomplished is limited only by the impact dynamics and the speed of the assembly machine.

While the compliance system was developed for use in programmable automatic assembly, it could also be used with transfer line or fixed automation machines. The use of compliance should reduce the design, tolerance, alignment, and debugging requirements and make it possible to perform tasks that could not otherwise be performed automatically because of problems with the stack-up of tolerances.

Thesis Supervisor: Richard S. Sidell, Associate Professor, Department of Mechanical Engineering

FOREWORD

This thesis comprises six chapters and seven appendices. Chapters 1 and 2 describe the problem, its relevancy, the proposed solution, and a review of other work in the field. Chapter 3 presents the theory behind the proposed solution and some limitations of the solution. Chapter 4 briefly describes the equipment and procedures used to measure forces during the parts assembly experiments using the compliance system. Chapter 5 contains the results of these experiments. Chapter 6 contains conclusions and recommendations.

Appendix A briefly describes the use of the compliance system in the experimental assembly of an automobile alternator with a four-axis programmable assembly machine or assembly robot. The reader may wish to read this Appendix after reading Chapters 1 and 2. Appendices B and C describe the limitations of the compliance system caused by impact forces and impact dynamics. These appendices should be read only by the reader interested in problems of high-speed insertions. Appendix D discusses in detail the design of the compliance element and Appendix E discusses the experimental technique used to determine the 6 x 6 compliance matrix of this element. Appendix F discusses the design of the six axis force sensors used to measure the assembly forces and Appendix G discusses the calibration procedures for these sensors. The last four appendices should be read only by the reader specifically interested in the details of the hardware.

ACKNOWLEDGEMENTS

I sincerely thank the members of my thesis committee, Professors Adam Bell, Nathan Cook, Woodie Flowers and, especially, my thesis supervisor Professor Richard Sidell for the advice, help, and encouragement they have given me.

I thank my wife, Alice for her patience, understanding, and encouragement. I appreciate the many hours of effort she spent editing this document and the contribution she has made toward improving my writing skills.

The results of the Programmable Assembly Demonstration Project represent the efforts of many people. Dr. Daniel Whitney was the program manager for the contract under which this work was done. Don Seltzer designed the electronics hardware and wrote many of the computer programs for both running the assembly machine and taking data. Tony Kondoleon designed the parts feeders, laid out the location of the feeders and fixtures, and developed the assembly program. Dr. Daniel Killoran was the systems programmer. The assembly machine control program was originally developed by Mark Spencer as part of his masters thesis (M.I.T., E.E., 1975). Paul Watson demonstrated a mechanism approach to designing the compliance. Manny Consales prepared most of the drawings for the hardware and contributed many design ideas. Ray Roderick helped make and keep the hardware functional and contributed many ideas.

I especially acknowledge the many ideas and much valuable discussion contributed by Al Woodin and fellow student Sergio Simunovic.

I thank Linda Martinez for her cheerful attitude in typing this document and the numerous drafts that preceeded it.

I also acknowledge the support of the Ford Motor Company and the Bendix Corporation. The work was funded primarily by the National Science Foundation contract number APR 74-18173 A03.

TABLE OF CONTENTS

TITLE PAGE	1
ABSTRACT	2
FOREWORD	3
ACKNOWLEDGEMENTS	4
TABLE OF CONTENTS	5
LIST OF FIGURES	7
LIST OF TABLES	13
1. INTRODUCTION	14
2. BACKGROUND	16
2.1. Basic Concepts and Problems	16
2.2. Work Leading to the Use of Compliance	19
2.3. Brief Description of the Compliance System	23
2.4. Review of Other Work in the Field	27
3. THEORY	33
3.1. Quasi-Static Theory	33
3.1.1. Spatial Transformation of the Compliance Matrix	34
3.1.2. Two-Dimensional Analysis	36
3.1.3. Jamming	40
3.1.4. Position Information	47
3.2. Limitations Caused by an Impact Forces and Dynamics	49
3.2.1. Contact Forces Caused by an Impact	49
3.2.2. Impact Dynamics	50
4. EXPERIMENTAL APPARATUS AND PROCEDURES	53
5. EXPERIMENTAL RESULTS	57
5.1. Results Using the Cantilever Beam Compliance	57
5.2. Results Using the Deformable Structure Compliance	60
6. CONCLUSIONS AND RECOMMENDATIONS	80
6.1. Conclusions from Experiments Using the Cantilever Beam Compliance	80

6.2.	Conclusions from Experiments Using the Deformable	
	Structure Compliance	81
6.3.	Recommendations for Further Work	83
REFERENCES	85
APPENDIX A:	PROGRAMMABLE ASSEMBLY DEMONSTRATION PROJECT	90
APPENDIX B:	IMPACT FORCES	100
APPENDIX C:	IMPACT DYNAMICS	105
	C.1. Dynamics of a Single-Point Impact on a Chamfer	105
	C.2. Dynamics of Two-Point Contact	116
APPENDIX D:	COMPLIANCE DESIGN	121
APPENDIX E:	DETERMINATION OF THE COMPLIANCE MATRIX	138
APPENDIX F:	FORCE SESNSOR DESIGN	143
APPENDIX G:	FORCE SENSOR CALIBRATION	148
BIOGRAPHY	154

LIST OF FIGURES

Figure	Page
2.1. Forces that cause a tipping moment during a chamferless insertion.....	18
2.2. Maximum lateral error with a single-point contact.....	20
2.3. Schematic drawing of the first compliance system.....	21
2.4. Desired response of compliance system to applied forces and moments.....	22
2.5. Cross-sectional drawing of complete compliance system.....	24
2.6. Schematic drawing of the deformable structure used to provide the desired compliance.....	25
2.7. Photograph of the second compliance system mounted on the programmable assembly machine.....	26
3.1. Transformation of displacement coordinates.....	35
3.2. Transformation of force coordinates.....	35
3.3. Contact Forces.....	39
3.4. Jamming caused by residual reaction forces.....	43
3.5. Reaction forces with the parts sliding.....	44
3.6. Conditions for sliding at the onset of 2-point contact for the insertion of a ball bearing into the automobile alternator housing.....	45
3.7. Conditions for sliding with the ball bearing fully inserted into the automobile alternator housing.....	45
3.8. Moment caused by the insertion force when the center of compliance is displaced from the assembly interface.....	46
4.1. Overall view of the milling machine setup with the second compliance system mounted in the milling machine spindle.....	54
4.2. Close-up view of the insertion of the automobile alternator rotor into a ball bearing using the second compliance system.....	55
4.3. Close-up view of the insertion of the steel test plug into a drill bushing using simplified apparatus and the more sensitive aluminum six-axis force sensor.....	56
5.1. Force and moment data; 0.6 mm x-axis offset, 0.002 clearance ratio.....	58
5.2. Force and moment data; 0.6 mm x-axis offset, 0.001 clearance ratio.....	58

Figure	Page
5.3. Force and moment data: zero lateral offset, +3.0 mrad angular offset, 0.002 clearance ratio.....	59
5.4. Force and moment data; -0.4 mm lateral offset, +3.0 mrad angular offset, 0.002 clearance ratio.....	59
5.5. Force and moment data; insertion of a 35.00 mm diameter hardened steel plug into a 35.02 mm diameter drill bushing, center of compliance at the assembly interface, 0.25 mm x-axis offset.....	65
5.6. Force and moment data; insertion of a 35.00 mm diameter hardened steel plug into a 35.02 mm diameter drill bushing, center of compliance at the assembly interface, 0.50 mm x-axis offset.....	65
5.7. Force and moment data; insertion of a 35.00 mm diameter hardened steel plug into a 35.02 mm diameter drill bushing, center of compliance at the assembly interface, 0.75 mm x-axis offset.....	66
5.8. Force and moment data; insertion of a 35.00 mm diameter hardened steel plug into a 35.02 mm diameter drill bushing, center of compliance at the assembly interface, 5.0 mrad θ_y offset.....	66
5.9. Force and moment data; insertion of a 35.00 mm diameter hardened steel plug into a 35.02 mm diameter drill bushing, center of compliance at the assembly interface, 0.50 mm x-axis and 5.0 mrad θ_y offset.....	67
5.10. Force and moment data; insertion of a 35.00 mm diameter hardened steel plug into a 35.02 mm diameter drill bushing, center of compliance +50 mm from the assembly interface, 0.75 mm x-axis offset....	67
5.11. Force and moment data; insertion of a 35.00 mm diameter hardened steel plug into a 35.02 mm diameter drill bushing, center of compliance +50 mm from the assembly interface, 5.0 mrad θ_y offset.....	68
5.12. Force and moment data; insertion of a 35.00 mm diameter hardened steel plug into a 35.02 mm diameter drill bushing, center of compliance +50 mm from the assembly interface, 0.5 mm x-axis and 5.0 mrad θ_y offsets...	68
5.13. Force and moment data; insertion of a 35.00 mm diameter hardened steel plug into a 35.02 mm diameter drill bushing, center of compliance -50 mm from the assembly interface, 0.75 mm x-axis offset.....	69
5.14. Force and moment data; insertion of a 35.00 mm diameter hardened steel plug into a 35.02 mm diameter drill bushing, center of compliance -50 mm from the assembly interface, 5.0 mrad θ_y offset.....	69

Figure	Page
5.15. Force and moment data; insertion of a 35.00 mm diameter hardened steel plug into a 35.02 mm diameter drill bushing, center of compliance -50 mm from the assembly interface, 0.50 mm x-axis and 5.0 mrad θ_y offsets...	70
5.16. Force and moment data; insertion of a ball bearing with a 35.00 mm diameter into a 35.02 mm diameter drill bushing, center of compliance -50 mm from the assembly interface, 0.75 mm x-axis offset.....	70
5.17. Force and moment data; insertion of a ball bearing with a 35.00 mm diameter into a 35.02 mm diameter drill bushing, center of compliance -50 mm from the assembly interface, 5.0 mrad θ_y offset.....	71
5.18. Force and moment; insertion of a 35.00 mm diameter hardened steel plug into a 35.02 mm diameter drill bushing, center of compliance -100 mm from the assembly interface, 0.75 mm x-axis offset.....	71
5.19. Force and moment data; insertion of a 35.00 mm diameter hardened steel plug into a 35.02 mm diameter drill bushing, center of compliance -100 mm from the assembly interface, 5.0 mrad θ_y offset.....	72
5.20. Force and moment data; insertion of a 35.00 mm diameter hardened steel plug into a 35.02 mm diameter drill bushing, center of compliance -150 mm from the assembly interface, 0.75 mm x-axis offset.....	72
5.21. Force and moment data; insertion of a 35.00 mm diameter hardened steel plug into a 35.02 mm diameter drill bushing, center of compliance -150 mm from the assembly interface, 5.0 mrad θ_y offset.....	73
5.22. Force and moment data; insertion of a 35.00 mm diameter hardened steel plug into a 35.02 mm diameter drill bushing, center of compliance -150 mm from the assembly interface, 0.75 mm x-axis and 5.0 mrad θ_y offsets.....	73
5.23. Force and moment data; insertion of a ball bearing with a 40 mm outer diameter into an alternator housing with a burnished hole, 0.5 mm x-axis offset.....	74
5.24. Force and moment data; insertion of a ball bearing with a 40 mm outer diameter into an alternator housing with a burnished hole, 0.75 mm x-axis offset.....	74
5.25. Force and moment data; first insertion of a ball bearing with a 40 mm outer diameter into a new alternator housing, 0.75 mm x-axis offset.....	75

Figure	Page
5.26. Force and moment data; second insertion of a ball bearing with a 40 mm outer diameter into a new alternator housing, 0.75 mm x-axis offset.....	75
5.27. Force and moment data; third insertion of a ball bearing with a 40 mm outer diameter into a new alternator housing 0.75 mm x-axis offset.....	76
5.28. Force and moment data; first insertion of a ball bearing with a 40 mm outer diameter into a new alternator housing, 0.75 mm x-axis offset.....	76
5.29. Force and moment data; second insertion of a ball bearing with a 40 mm outer diameter into a new alternator housing, 0.75 mm x-axis offset.....	77
5.30. Insertion forces for the first three insertions of a ball bearing with a 40 mm outer diameter into a new alternator front housing.....	77
5.31. Force and moment data; insertion of a well-polished alternator rotor shaft into a 17 mm ball bearing, 0.75 mm x-axis offset.....	78
5.32. Force and moment data; first insertion of a new alternator rotor shaft into a 17 mm ball bearing, 0.75 mm x-axis offset.....	78
5.33. Force and moment data; second insertion of a new alternator rotor shaft into a 17 mm ball bearing, 0.75 mm x-axis offset.....	79
A.1. Photograph of the complete programmable assembly machine setup.....	91
A.2. Photograph of the programmable assembly machine work area.....	92
A.3. Cross-sectional drawing of the complete compliance system (shown with a six-axis force sensor).....	93
A.4. Photograph illustrating a tool-change operation.....	94
A.5. Parts of the automobile alternator.....	96
A.6. Tools used in the assembly of the automobile alternator.....	97
A.7. Front housing subassembly being inserted on the main nest. Note the plunger holding the fan and fan spacer in place.....	98
A.8. Modification to the alternator rotor. Note the chamfer to the right of the threads on the top rotor. Bottom rotor is not modified.....	99
B.1. Definition of parameters for Hertzian stress between two generalized bodies.....	102
C.1. Part impacting chamfer at finite velocity with resulting impulse not thru the center of mass.....	106

Figure	Page
C.2. Free body oscillation of the compliance system resulting from a single impulse at the center of compliance.....	111
C.3. Digital simulation of bearing bounce during insertion. Impact velocity, 120 mm/sec; coefficient of restitution, 0.95.....	113
C.4. Digital simulation of bearing bounce during insertion. Impact velocity, 120 mm/sec; coefficient of restitution, 0.3.....	113
C.5. Digital simulation of bearing bounce during insertion. Impact velocity, 50 mm/sec; coefficient of restitution, 0.95.....	114
C.6. Enlarged section of figure C.5 showing detail of interaction between bearing and housing during insertion.....	114
C.7. Digital simulation of bearing bounce during insertion. Impact velocity, 50 mm/sec; coefficient of restitution, 0.3.....	115
C.8. Enlarged section of figure C.7 showing detail of interaction between bearing and housing during insertion.....	115
C.9. Part undergoing two-point impact at finite velocity.....	116
D.1. Original compliance device with the center of compliance at the assembly interface.....	122
D.2. Schematic representation of the compliance device shown in Figure D.1...	122
D.3. Deflection of the lateral compliance mechanism part of Figure D.2.....	123
D.4. Deflection of the rotational compliance mechanism part of Figure D.2....	123
D.5. Schematic representation of a compliance mechanism with all of the links in tension.....	125
D.6. Photograph of one of the deformable structure compliance devices used in the experimental verification of the theory and in the programmable assembly demonstration project.....	125
D.7. Schematic drawing of the deformable structure compliance shown in Figure D.6 illustrating the deflections due to a lateral force applied to the center of compliance.....	127
D.8. Idealized deflection of the top structure caused by an applied moment.....	130

Figure	Page
D.9. Idealized deflection of the side structure caused by an applied lateral force.....	132
D.10. Distributed compliant mechanism using elastomeric joints.....	135
D.11. Compliance device using two elastomeric elements that deform only in shear.....	136
D.12. Compliance device using an elastomeric element that deforms in both shear and compression/extension.....	137
E.1. Apparatus used to experimentally determine the 6 X 6 compliance matrix.....	141
F.1. Original aluminum six-axis wrist force sensor.....	144
F.2. Steel six-axis force sensor with integrated instrumentation amplifier package.....	144
F.3. High-sensitivity aluminum six-axis force sensor.....	145
G.1. Drawing of original calibration fixture illustrating f_y force loading.....	150
G.2. Drawing of original calibration fixture illustrating m_x moment loading.....	150
G.3. Photograph of the force sensor calibration procedure with a -z-axis force being applied to the force sensor.....	151
G.4. Photograph of the force sensor calibration procedure with a force vector containing + x-axis force, + y-axis moment, and + z-axis moment components being applied to the force sensor.....	152

LIST OF TABLES

Table	Page
3.1. Two-dimensional analysis of the insertion forces for the insertion of a ball bearing into the alternator housing.....	41
3.2. Two-dimensional analysis of the insertion forces for the insertion of a ball bearing into the alternator housing. Center of compliance -75 mm from the assembly interface.....	42
3.3. Jamming conditions resulting from a moment caused by the insertion force.....	48
A.1. Sequence of operations for the automobile alternator assembly using the programmable assembly machine.....	96
B.1. Calculated maximum contact force and Hertzian stress for the insertion of a ball bearing into an automobile alternator housing.....	104
C.1. Maximum values of v_i that will not result in a secondary impact.....	110
C.2. Maximum value of v_i that will not result in a secondary two-point contact.....	120
E.1. Matrices of the input displacement vectors and the resulting compliance calibration matrix for one of the deformable structure compliance devices.....	142
G.1. Matrices of the input force vectors and the measured voltage vectors and the resulting force sensor calibration matrix for the high sensitivity aluminum force sensor.....	153

1. INTRODUCTION

The concepts presented in this thesis were developed in support of research work on programmable automatic assembly. However, these same concepts should prove equally useful for the design of conventional or fixed automatic assembly equipment to assemble close-fitting parts and may also be useful as an aid in manual assembly.

The assembly of discrete parts is one area of the manufacturing sector where the increase in productivity has lagged. It is possible to build special purpose fixed automatic assembly equipment for some products. However, the relatively high capital cost, the costs associated with the long setup and tuning or debugging times, and the limited adaptability of this equipment requires that the given product be assembled in large volume over a long period of time [21]. If the assembly is to be fully automated, the parts must be of a limited size and weight such that they can be oriented and fed automatically. As faulty or even out-of-tolerance but otherwise functional parts will cause this equipment to jam and malfunction, high quality parts are required for the assembly machine to have sufficient uptime. Once a fixed automatic assembly machine is in operation, there is a great reluctance to make any product change that might affect the performance of the assembly machine.

Because the bulk of discrete products are assembled in low to moderate volume batches, most assembly is presently performed manually. Also a large number of products that are assembled in sufficient volume to warrant fixed automation are otherwise unsuited for automation and are now being assembled manually. The concept of programmable or flexible automatic assembly is being developed primarily to economically automate the assembly of these products.

Programmable automatic assembly is sometimes referred to as robot assembly as most of the machines built to date bear a strong resemblance to the so-called industrial robots. However, the term robot must be used with some caution as it has been used to describe a wide range of devices that perform some automatic or pre-programmed function. The machines used in the programmable automatic assembly research that has been done to date are primarily mechanical manipulators or arms that have between two and six separate motions or degrees-of-freedom. Conceptually,

programmable automatic assembly is analogous to numerically controlled (NC) machining. In NC machining, a machine tool equipped with servo actuators is programmed to perform a sequence of operations that a human operator would normally perform. In programmable assembly, a servo actuated machine is programmed to follow a sequence of assembly tasks. A major difference between the economics of NC machining and programmable assembly is that in the machining operation, a machine tool is required even when the machining is performed by a machinist while manual assembly is performed by a person using simple hand tools. In NC machining, the machine tool is automated in a programmable manner while, in programmable assembly, a machine must be constructed that can compete with a person.

2. BACKGROUND

The basic concepts and problems in programmable automatic assembly are discussed in the first section of this chapter. The second section is a brief history of the initial work that led to the use of the present compliance system. This system is described in the third section. The final section is a review of past and concurrent work in the field of programmable automatic assembly.

2.1. Basic Concepts and Problems

A major problem in programmable automatic assembly is designing a fast low-cost machine capable of assembling close-fitting parts that can compete economically with manual labor. The traditional approach to the design of transfer line or fixed automatic assembly machines is to build a machine that has positional accuracy equal to or greater than the clearances of the parts to be assembled. This is achieved by making the machine structurally stiff and by using precision bearings and slides.

The stiff accurate type of programmable assembly machine is used successfully to insert electronic components in printed circuit boards. To assemble larger parts, the requirements for stiffness and accuracy imply a fairly massive machine. Both the cost of the machine and the power needed to accelerate and decelerate the large inertial loads have made it impractical to design a multi-axis manipulator or robot arm for assembly that can compete economically with manual assembly. Even with a highly accurate machine, it is still not possible to assemble parts where the stack-up of tolerances between the machine and the parts exceeds the assembly clearances. Because of this problem, the current transfer line technology is not entirely successful in the assembly of close-fitting parts.

One potential solution to the accuracy problems of high-speed manipulator arms is using sensory feedback. Two basic types of sensory feedback have been tried to a limited extent: visual feedback and force feedback. A person normally uses both these types in manual assembly, using vision to acquire the parts and to make gross positional moves while sensing forces to actually fit the parts together.

Experiments in using vision to aid assembly have ranged from locating parts on a conveyor using silhouette techniques to analyzing complex scenes under ambient light and then using this information to guide a manipulator arm in stacking up parts. It is relatively difficult, however, to make use of visual feedback in making the final small corrective motions to assemble parts because the tools and fixtures and the parts that are being assembled tend to block the view of the assembly interface. In the near future, the use of visual feedback in assembly probably will be limited to identifying parts and their location and orientation under controlled lighting conditions.

Conceptually, force feedback is more applicable to the problem of sensing and removing small positional errors between the parts that are being assembled. Most force feedback assembly research has involved using forces and torques resolved at the assembly interface to generate feedback signals to null the positional errors of the assembly machine. For the common example of inserting a shaft or peg into a close-fitting hole, the problem, once the insertion has been started, is to null the lateral forces and moments while continuing the insertion. If either or both of the parts are chamfered and the initial positional errors are not larger than the chamfers, starting the insertion is simply a matter of nulling the lateral forces after the parts come into contact. Until the shaft is actually into the hole, there should be only a single-point contact and therefore no moments. If the positional errors are larger than the chamfers or if there are no chamfers, the problem is considerably more complex but feasible. If the magnitude of the positional error and the geometry of the shaft and hole is such that the centerline of the shaft lies between the centerline of the hole and the line of contact between the two parts, a moment will exist that will tend to tip the shaft into the hole (Figure 2.1). By measuring this moment, it is possible to generate a corrective motion to center the shaft over the hole [35],[26].

Although possible to use, force feedback suffers from several practical problems. If the direction of the applied force vector is outside certain bounds, it is possible that the parts being assembled may become jammed [34]. When this

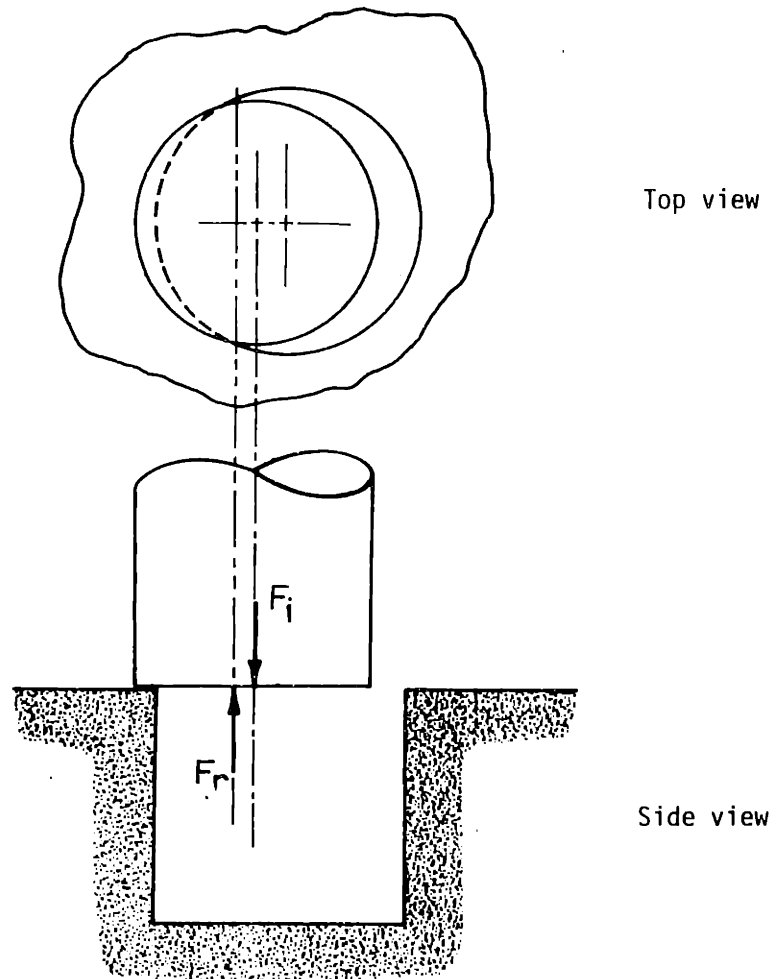


Figure 2.1. Forces that cause a tipping moment during a chamferless insertion.

occurs, the component of force in the insertion direction no longer causes the insertion to proceed. At the same time, the friction forces become ambiguous and the reaction forces cannot be properly resolved. An analogy exists in manually assembling close-fitting parts. Once the parts become jammed, it is not possible to ascertain from the reaction forces in which direction the force vector should be applied to free the parts. If sufficient force is applied to parts that are jammed, it is possible to cause deformations such that no force vector applied in the insertion direction will cause the insertion to continue.

The speed at which a force feedback assembly operation can be accomplished is limited by the permissible assembly forces. The lateral forces and the moments

that occur during the assembly operation or insertion are proportional to both the stiffness of the assembly machine at the assembly interface and the instantaneous positional error at the assembly interface. For a given machine with a certain stiffness and inertia, the positional error during an assembly operation is proportional to the speed at which the machine is driven.

2.2. Work Leading to the Use of Compliance

An auxiliary device attached to the end of the manipulator arm or assembly machine capable of making small, high-speed, high-resolution motions could be used to increase the speed of a force feedback system. While this device would need six degrees of freedom to correct general positional errors, it might not be necessary for the assembly machine proper to have six degrees of freedom. Although this system would be faster, the additional cost would make the economics questionable.

Prior to the start of this work, the effect of compliance had been noticed when parts had been assembled without force feedback even though positional errors existed that were considerably larger than the available clearance. The part-gripping tools used for these experiments had sufficient play so that gripping point could be modeled as a compliance. If the parts being assembled have a clearance of c and an insertion depth of d , the assembly has a permissible wobble angle of:

$$\theta = \frac{c}{d} \quad 2.1$$

(Figure 2.2). Assuming that the part is gripped compliantly at a distance ℓ from the assembly interface, the assembly machine can have a maximum lateral error of:

$$\epsilon_{\ell} = \theta \ell \quad 2.2$$

and still fully insert the part into the hole without the possibility of jamming. If the parts are chamfered and the lateral error is less than the dimensions of the chamfers, it is possible to assemble the parts by simply pushing them together.

The initial assembly system using compliance was designed to utilize this wobble angle effect. A cantilever beam spring was used to provide the necessary compliance while the part-gripping tools were designed to hold the parts rigidly (Figure 2.3). A locking mechanism was designed and constructed that allowed the

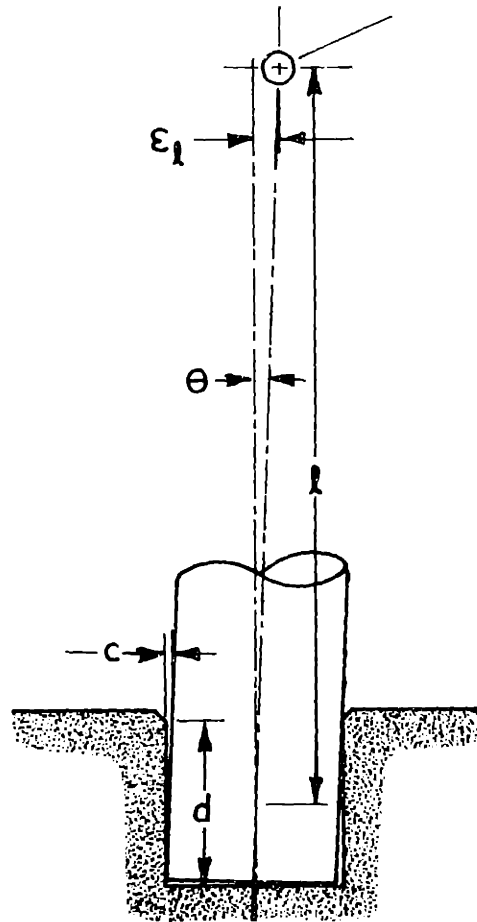


Figure 2.2. Maximum lateral error with a single-point contact.

system to be locked in a relatively rigid state to retain the stiffness of the basic assembly machine while the parts to be assembled are being transported and positioned.

In addition to being potentially very fast, a compliance-based assembly system is relatively simple. If certain conditions are met, the system can operate in a totally passive manner. The parts must be chamfered and the lateral position errors must be less than the dimensions of the chamfers to initiate the assembly operation. To use the wobble angle effect, the required angle must be less than the angle defined in equation 2.1 for a given clearance and insertion depth. The combined lateral and angular error that can exist and not exceed the maximum wobble angle is

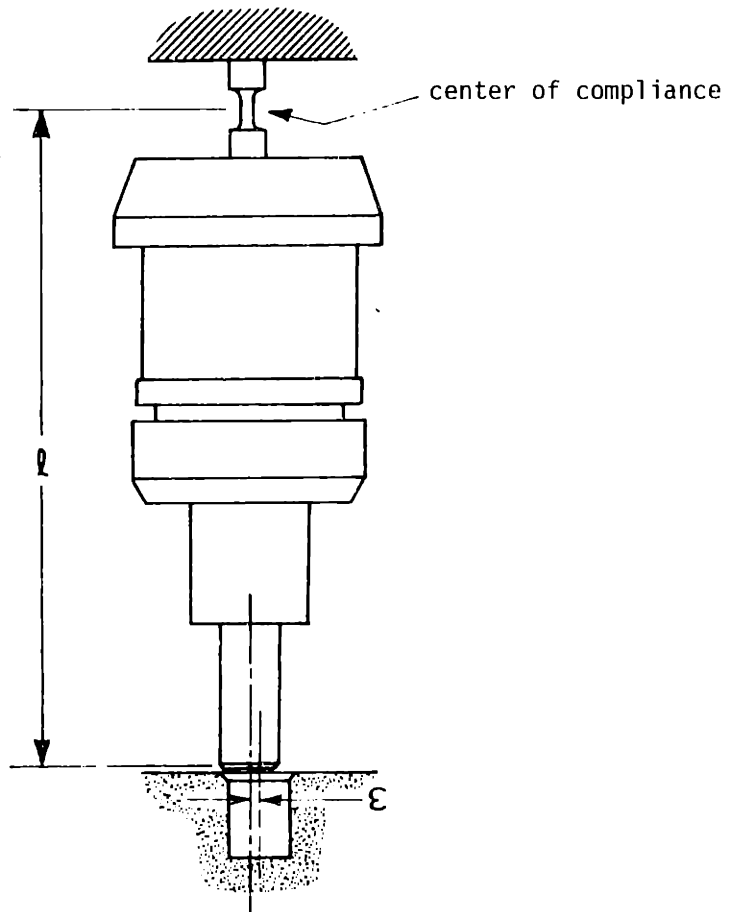


Figure 2.3. Schematic drawing of the first compliance system.

given by:

$$\frac{\epsilon_l}{l} + \epsilon_\theta \leq \theta \quad 2.3$$

where ϵ_l is the lateral error and ϵ_θ is the angular error.

The original intent was to use a simplified form of force feedback when the combined error was greater than the maximum permissible wobble angle. Two-point contact will cause a moment at the assembly interface. Resolving and measuring this moment would yield a feedback signal with which to servo the assembly machine. Consideration was also given to designing an auxiliary small-motion, high-speed device with two lateral degrees of freedom. This device could be servoed directly to null any moments measured at the assembly interface. Although there was no difficulty in resolving the moment after two-point contact occurred, this simplified

form of force feedback was not tried.

When the insertion of the shaft into the hole was continued after the initial two-point contact, the moment, the lateral force, and the insertion force became large but remained finite. Jamming did not occur, largely because of the inherent compliance of the tooling, the test fixtures, and the parts. From these initial experiments it was clear that by designing a compliance that would yield lateral displacements in response to lateral forces at the assembly interface and would yield rotational displacements in response to moments at the assembly interface, force feedback or active accommodation would not be needed for these tasks (See Figure 2.4). As making lateral displacements in response to lateral forces and rotational displacements in response to moments is exactly what was originally desired from force feedback, this type of compliance can be considered a mechanical analog of force feedback. Or, force feedback can be considered simply synthesized compliance.

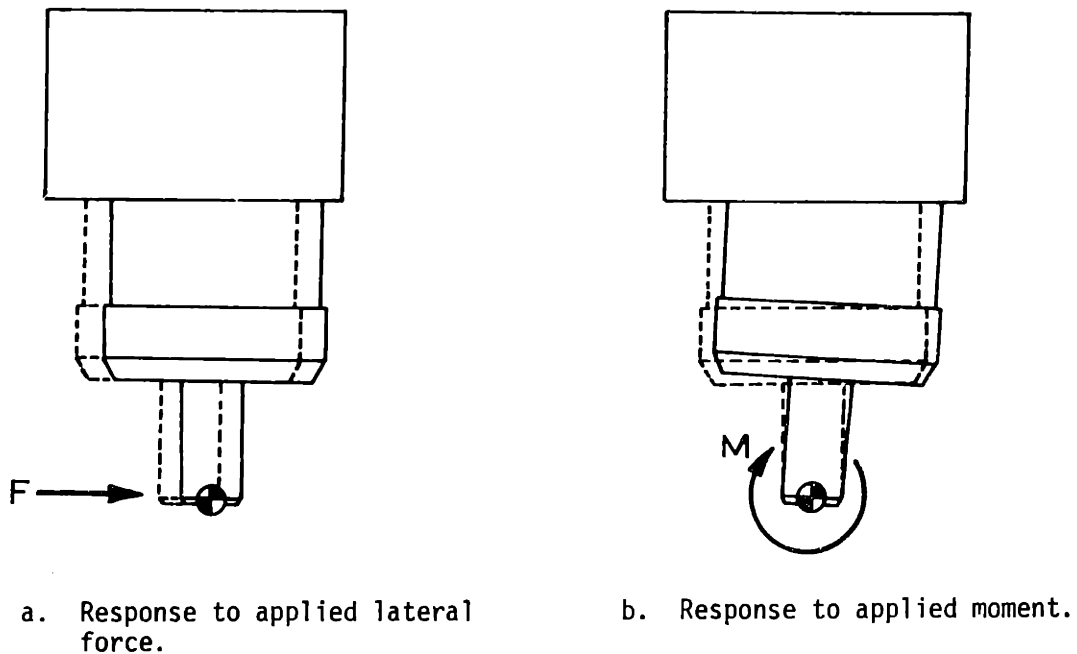


Figure 2.4. Desired response of compliance system to applied forces and moments.

2.3. Brief Description of the Compliance System

The second compliance system comprised a deformable structure to provide the necessary compliance, a compliance-locking mechanism, and an automatic tool-change mechanism (see Figures 2.5 through 2.7). This system was used both for experiments that measured assembly forces and moments and for assembly experiments that used a programmable assembly machine. The experimental assembly of an automobile alternator using this system mounted on a programmable assembly machine is discussed in detail in Appendix A. A six-axis force sensor was used during experiments that measured assembly forces and moments but was not used during assembly experiments with the programmable assembly machine. The deformable or compliant structure used to provide the desired compliance properties was designed to have a center of compliance approximately 200mm (7.9 in) from the top of the structure, a lateral stiffness of 10 N/mm (5.7 lb_f/in), and a rotational stiffness at the center of compliance of 0.40 Nm/mrad (3.5 in-lb_f/mrad). See Appendix D for detailed discussion on compliance design.

The compliance is locked with a pneumatically actuated single-taper collet with a large expansion/contraction range. The collet also acts as a limit stop for the compliance in the unlocked state. In the locked state, the compliance is essentially set to zero to allow the system to be positioned using high velocities and accelerations.

The automatic tool-changing mechanism is incorporated to facilitate the use of different tools needed for the programmable assembly demonstration. Functionally, this mechanism is similar to the tool changers used on many numerically controlled machine tools.

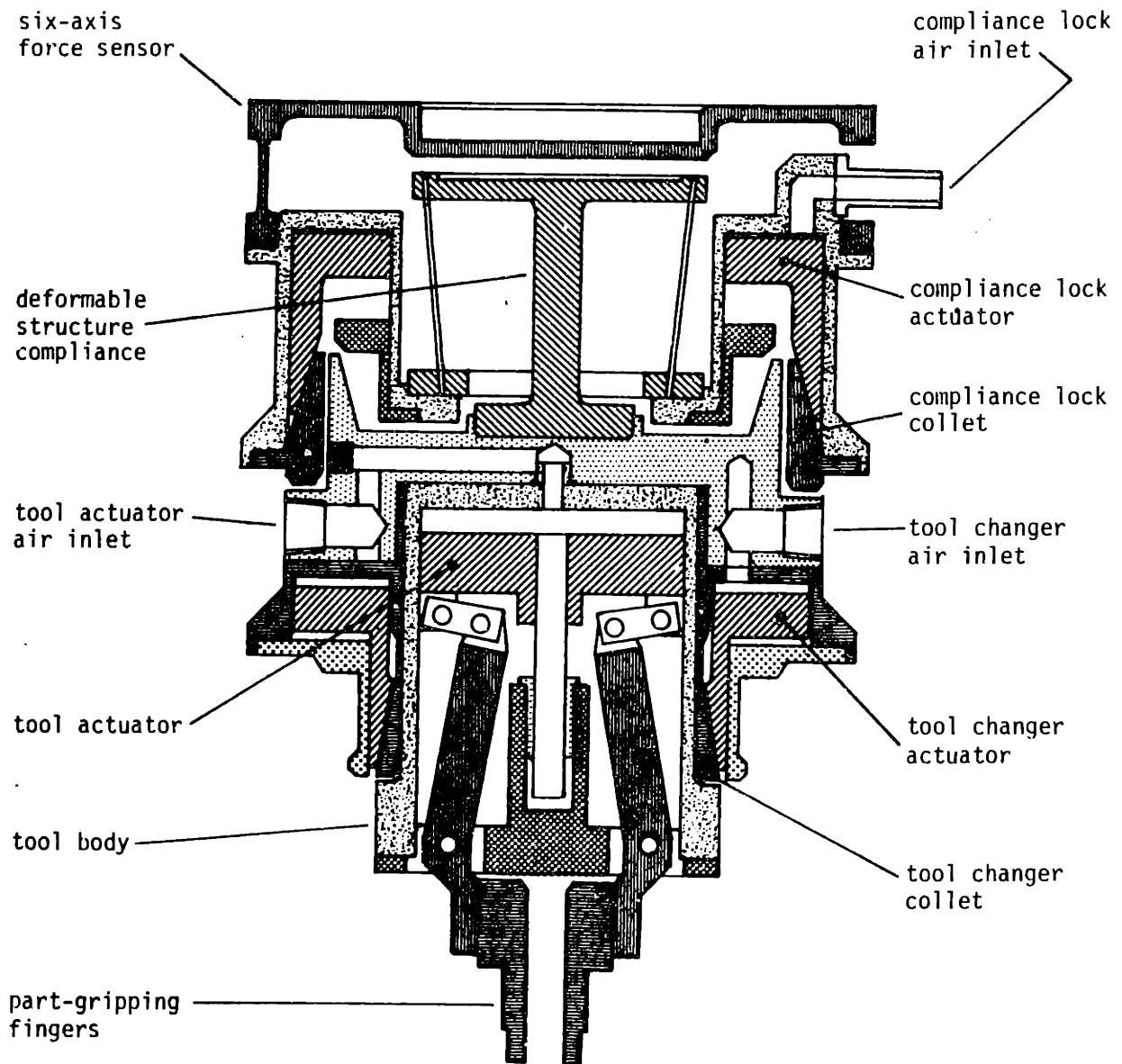


Figure 2.5. Cross-sectional drawing of complete compliance system.

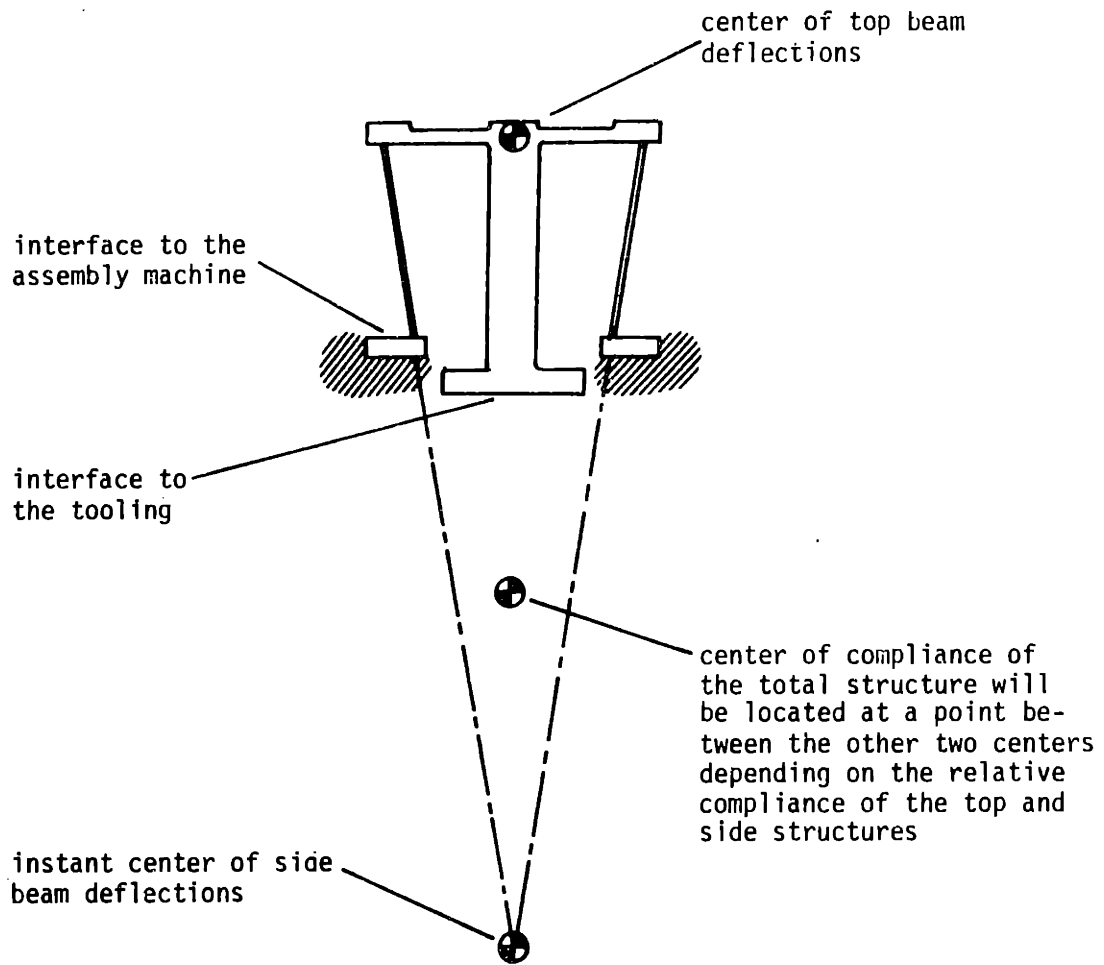


Figure 2.6. Schematic drawing of the deformable structure used to provide the desired compliance.

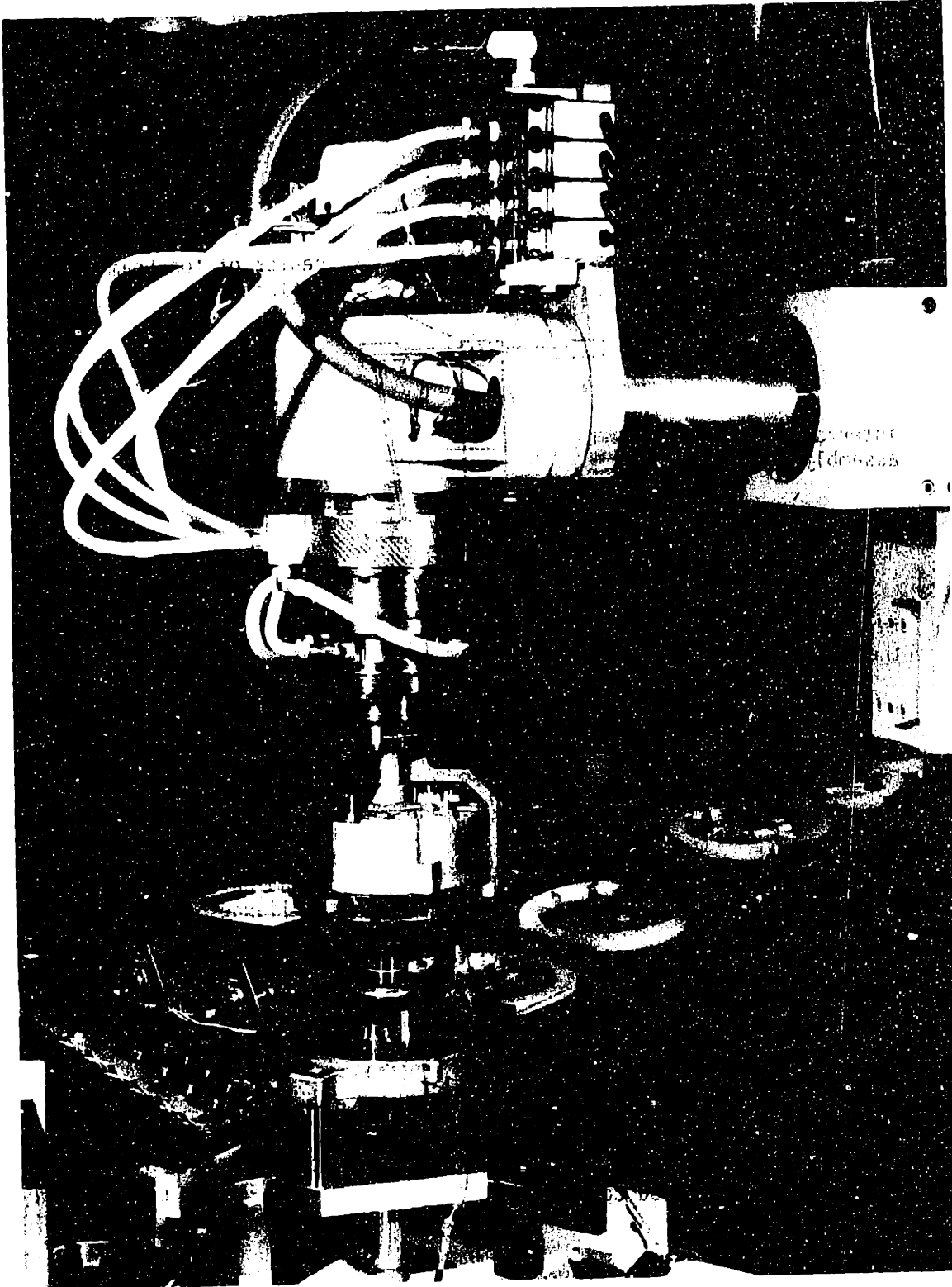


Figure 2.7. Photograph of the second compliance system mounted on the programmable assembly machine. The system is shown with a tool holding an alternator rear housing/stator subassembly.

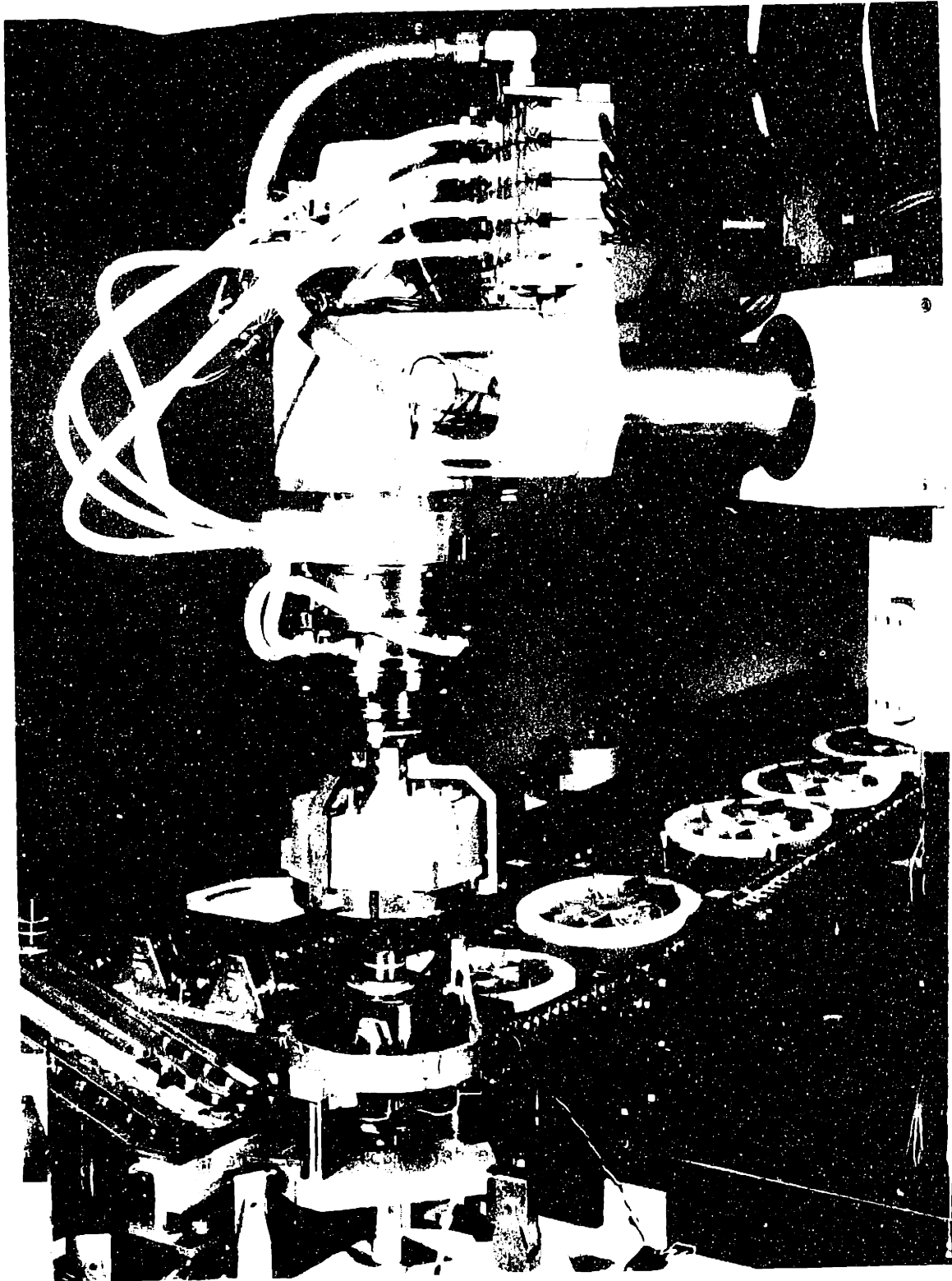


Figure 2.7. Photograph of the second compliance system mounted on the programmable assembly machine. The system is shown with a tool holding an alternator rear housing/stator subassembly.

2.4. Review of Other Work in the Field

Most of the earlier work at M.I.T. and the Charles Stark Draper Laboratory (previously the M.I.T. Instrumentation Laboratory) was concerned with the control of remote manipulators [42], [43]. Some significant developments in this work were resolved motion rate control (a technique for obtaining straight-line controlled rate motion with a multi-jointed manipulator arm) [38], the design and construction of a series of six-axis hand controllers and a six-axis force sensor, the design and construction of a laser ranging and pointing system for determining the location of parts, and some of the original work on the use of force feedback steering or accommodation for part insertion or assembly [18], [39].

The first work at Draper Laboratory specifically directed toward programmable automatic assembly was the design of a high-performance six-axis manipulator arm with a maximum reach of approximately 1 meter (40 in) [22]. All the axes were to be directly actuated with specially designed hydraulic vane actuators. The primary design goals were to make a typical point-to-point move within one-half second and have a positional accuracy to within 0.25mm (0.010 in). Although some components were built and tested, the arm was not constructed due to termination of funding.

The more recent work on programmable automatic assembly at the Draper Laboratory has been part of a larger study on this subject funded by the National Science Foundation. Several different research groups were given different parts of the overall problem to investigate. The Draper Laboratory was funded to investigate the interaction of the parts during the assembly process (sometimes referred to as parts mating) and to investigate the use of force feedback accommodation in assembly. Stanford Research Institute received funding for investigating the use of vision and pattern recognition in assembly while the Stanford University Artificial Intelligence Laboratory was funded to develop a general purpose computer language for programmable assembly. The use of vision and pattern recognition in acquiring and orienting parts is being investigated at the University of Rhode Island while more conventional parts feeding and orienting techniques are being investigated

for use in programmable assembly at the University of Massachusetts. In addition, a feasibility study for a programmable assembly demonstration system is underway at Westinghouse Research and Development Center. This project, jointly funded by NSF and Westinghouse, is designed to use some of the technology being developed by the other NSF grantees.

This thesis represents only one part of the work done at the Draper Laboratory under the NSF funding. A series of reports covering the overall work have been issued under the title "Exploratory Research in Industrial Modular Assembly"[23],[24],[25],[26]. These reports cover the development of force sensor technology, the description of assembly tasks and an analysis of task geometry, the development of the assembly demonstration equipment, the development of control algorithms, the development of the computer software systems, an analysis of the economics of programmable assembly systems, an analysis of the causes of parts jamming, and some of the preliminary work on the use of compliance that led to this thesis.

A more complete analysis of assembly system design criteria based on economic and technological modeling can be found in the doctoral thesis "Economic-Technological Modeling and Design Criteria for Programmable Assembly Machines" by Lynch [21]. One of the conclusions is that the measure of value of a programmable assembly machine is the price-time product, i.e., the cost of the machine multiplied by the time it takes to complete an operation. The smaller this number, the greater the value of the machine. Lynch uses this criterion to compare projected programmable assembly machines to manual assembly and fixed automation.

An analysis of the causes of parts jamming and criteria for the avoidance of jamming are presented in the paper "Force Information in Assembly Processes" by Simunovic [34]. Further work on parts interaction and jamming along with work on the use of estimation theory to assemble parts with large positional errors is presented in the doctoral thesis "An Information Approach to Parts Mating" by Simunovic [35].

Ongoing work at the Stanford Research Institute is presented in a series of reports entitled "Exploratory Research in Advanced Automation" [28], and "Machine

Intelligence Applied to Industrial Automation" [30]. The work includes the use of vision to locate and identify parts in a random orientation on a moving conveyor line, to palletize parts in a moving box, and to spray-paint parts on a moving conveyor. Two manipulator arms, a conveyor line, and various sensors have been interfaced to a minicomputer. Software and hardware have been developed to teach and control the manipulators with the aid of joysticks and voice control. In addition to the above work, an overview of the general field of programmable automation is presented in the paper "Programmable Industrial Automation" by Nitzan and Rosen [29].

Earlier work at the Stanford University Artificial Intelligence Laboratory included programming a manipulator arm to assemble a waterpump using both visual and force feedback [10]. The waterpump parts included a base casting, a gasket, a number of screws, and a cover plate with the impeller and pulley. Force feedback was used to locate holes in conjunction with a search pattern. The forces were sensed indirectly by monitoring currents in the drive motors. Present work includes the development of a high level language for programmable automatic assembly that has been named AL. This work is documented in a series of progress reports titled "Exploratory Study of Computer Integrated Assembly Systems" [6], [7].

Current work at the University of Rhode Island is presented in a series of progress reports titled "Robot Computation for Orienting Workpieces" [8], [9]. Digitized television images are being used to identify individual parts in a bin filled with randomly oriented parts. An algorithm based on identifying key features in two views is used to determine the exact orientation once an individual part has been acquired by the robot. Earlier work on using a device with an array of lights in conjunction with a television camera to aid in programming a manipulator arm is presented in a paper titled "Visual Robot Instruction" by Seres, Kelly, and Birk [33].

A major part of the NSF funded work at the University of Massachusetts is the development of a unified code to classify small parts for conventional parts-feeding techniques. Techniques for feeding and orienting the parts are provided for the different code numbers. Information is also provided on the efficiency in feed-

ing the parts. In addition, work is being done on developing feeders that can be easily modified to feed families of similar parts. The work is being published as a loose-leaf handbook titled "Handbook on Feeding and Orientating Parts" [11], [12].

While considerable work has been done by researchers at the MIT Artificial Intelligence Laboratory in the general field of machine intelligence and robotics, only a relatively small amount pertains to industrial assembly. In the paper "Force Feedback in Precise Assembly Tasks" by Inoue [20], an experimental assembly system is described. A number of parts including two ball bearings, several spacers and washers, a threaded shaft, and a nut are assembled using a combination of strategies. The initial positioning is done with a landfall navigation search (an initial offset larger than any expected positional error is made in one direction so that the search need be made in only one direction). Force feedback was used for the assembly or parts mating. The parts with close fits were chamfered.

There has been considerable industrial interest and experimentation in programmable automatic assembly. However, to a great extent the work is considered proprietary and therefore most but not all, of this work is unpublished. At the IBM T.J. Watson Research Center, a computer controlled system has been developed for mechanical assembly experimentation. A multiple-degree-of-freedom manipulator with linear hydraulic motors is used in conjunction with touch and force sensors and a sonic proximity sensor. This work is documented in the paper "Computer Controlled Mechanical Assembly" by Will [40] and "An Experimental System for Computer Controlled Mechanical Assembly" by Will and Grossman [41].

A four-axis programmable manipulator has been developed at Westinghouse Electric Corporation to perform arc welding. This work is presented in a paper titled "Robot-Arc Welder with Contouring Teach Mode" by Abraham and Shum [1]. As previously mentioned, Westinghouse is currently involved in a programmable assembly demonstration project which is funded jointly by NSF and Westinghouse. This work is documented in a series of progress reports titled "Programmable Assembly Technology Transfer to Industry" [2]. Also a review of the past and current work titled "State-of-the-Art in Adaptable-Programmable Assembly Systems" has been written by Abraham,

Stewart, and Shum[3]. It is largely an evaluation of the applicability of the available technology to their project. It does, however, contain a very complete list of references.

Kawasaki Heavy Industries, a Japanese licensee of Unimation, has demonstrated one of the more impressive programmable assembly experiments. Small gasoline engines are assembled on a pilot line with five work stations. Each work station has two minicomputer-controlled small Kawasaki Unimate robots with special tools and fixtures. The assembly is performed without sensory feedback. However, at least some of the work pallets are floated on air-bearing pads to provide some compliance. While this experimental system was technically successful, it is too slow and expensive to be cost effective. The work has been documented in a paper titled "Development and Application Report in the Arc Welding and Assembly Operation by a High Performance Robot" by Siko and Toda [32].

Hitachi of Japan has developed a series of experimental systems for performing precision insertion operations. The present "HI-TI-HAND" or tactile controlled robot system makes use of an engineered compliance in an attempt to mimic the rocking or orbital motion often employed by people attempting to assemble a close-fitting piston in a cylinder. After the insertion has been initiated, the device is driven downward inserting the piston into the cylinder until a present axial force limit is exceeded. The search pattern is then re-entered. As presently implemented, the "HI-TI-HAND" will successfully assemble close-fitting parts while exerting only small forces on the parts. It does, however, require that the parts be chamfered. Earlier experiments involved tipping the piston at a slight angle and dragging it across the mouth of the cylinder to determine the exact location of the hole. The present device requires five to ten seconds to complete a typical insertion. The work has been documented in several papers by Goto, Inoyama, and Takeyasu [16], [17]. Also a United States patent has been issued for the device[36].

A device that is very similar to the present "HI-TI-HAND" has been designed and constructed at the University of Stuttgart. The work is documented in a thesis titled "Design and Construction of a Self-Steering Robot Hand" by Schneider [51].

Olivetti of Italy is presently marketing a programmable assembly system or robot for the assembly of small parts. The assembly robot is part of a family of similar machines that also includes a numerically controlled drilling machine, hot riveting machine and plasma torch cutter. The mini-computer controlled assembly machine is equipped with a wrist that allows small relative motions in the x,y, and z directions. Transducers are used to detect this motion and provide signals for servo correction. A paper titled "Sigma - An Integrated General Purpose System for Automatic Manipulator" by d'Auria and Salmon documents some of the features of this machine [13].

Considerable work has been done at the University of Nottingham in both the fields of programmable assembly and fixed automation. A manipulator-mounted television camera has been used to identify and determine the position and orientation of objects. The television camera is mounted on a turret with the part-gripping tools. The camera is rotated out of the way after the arm has been centered over the object. A paper on this work titled "Robot Research at the University of Nottingham" has been published by Heginbotham, Page, and Pugh [19].

The above work pertains mostly to programmable automatic assembly or robot assembly. Additional published work exists in the more general field of industrial robotics and also in the field of artificial or machine intelligence. A review of robotics titled "Robots Systems" has been published by Albus and Evans [4]. They have also been involved in the development of a hierarchical control system for a manipulator at the National Bureau of Standards. This work has been published in a paper titled "A Hierarchical Structure for Robot Control" [5].

3. THEORY

This section is divided into two parts. A quasi-static analysis of the forces resulting from the assembly of two parts using compliance is presented in the first part. A simplifying assumption made throughout is that the assembly is the insertion of a round shaft or peg into a round hole. This is one of the most common operations during the assembly of mechanical parts that have close fits. The analysis is equally valid for the placement of a part with a hole over a round shaft. The limitations caused by impact forces and dynamics are discussed in the second part.

The general quasi-static theory with the 6 x 6 compliance matrix is valid for any compliant structure, mechanism, or other body assuming that the deflections are sufficiently small that effects due to the distortion of the reference frame can be ignored. Assuming certain symmetries and assuming that the compliance in the insertion direction is much less than the compliance in the lateral direction, the 6 x 6 matrix can be replaced with a 2 x 2 matrix for engineering design purposes. The examples given assume that the compliance has the properties of the deformable structure designed for the second compliance system.

3.1. Quasi-Static Theory

The forces considered in this analysis are the forces that are a result of deflections being imposed on the compliance device and frictional forces. The deflections of the compliance are caused by the positional errors of the pieces that are being assembled. The compliance is represented mathematically by a 6 x 6 matrix C that relates the six-dimensional deflection vector D of a given structure to a six-dimensional force and moment vector F applied to the structure. Thus for a given point in space the compliance matrix can be defined by the relationship:

$$D = CF \tag{3.1}$$

The compliance matrix can also be thought of as the inverse of the general 6 x 6 stiffness matrix S which relates the force vector that must be applied to the structure to generate a particular displacement or deflection vector:

$$K = C^{-1} \quad 3.2$$

or:

$$F = KD \quad 3.3$$

3.1.1. Spatial Transformation of the Compliance Matrix

If the compliance matrix is known for a point in space it can be found for any other point in space by using transformation matrices. At the new point in space, the relationship between the deflection vector and the applied force vector can be written as:

$$D' = C'F' \quad 3.4$$

where D' is the deflection vector at this new point, F' is the force vector at this new point, and C' is the new compliance matrix. Figure 3.1 shows the relationship between the deflection vector at the new point in space and the original point. Written in matrix form this relationship is:

$$\begin{bmatrix} d'_x \\ d'_y \\ d'_z \\ d'_{\theta_x} \\ d'_{\theta_y} \\ d'_{\theta_z} \end{bmatrix} = \begin{bmatrix} 1 & 0 & 0 & 0 & +a_z & -a_y \\ 0 & 1 & 0 & -a_z & 0 & +a_x \\ 0 & 0 & 1 & +a_y & -a_x & 0 \\ 0 & 0 & 0 & 1 & 0 & 0 \\ 0 & 0 & 0 & 0 & 1 & 0 \\ 0 & 0 & 0 & 0 & 0 & 1 \end{bmatrix} \begin{bmatrix} d_x \\ d_y \\ d_z \\ d_{\theta_x} \\ d_{\theta_y} \\ d_{\theta_z} \end{bmatrix} \quad 3.5$$

or:

$$D' = GD \quad 3.6$$

Figure 3.2 shows the relationship between the force and moment vector at the original point in space and the new point in space. Written in matrix form this relationship is:

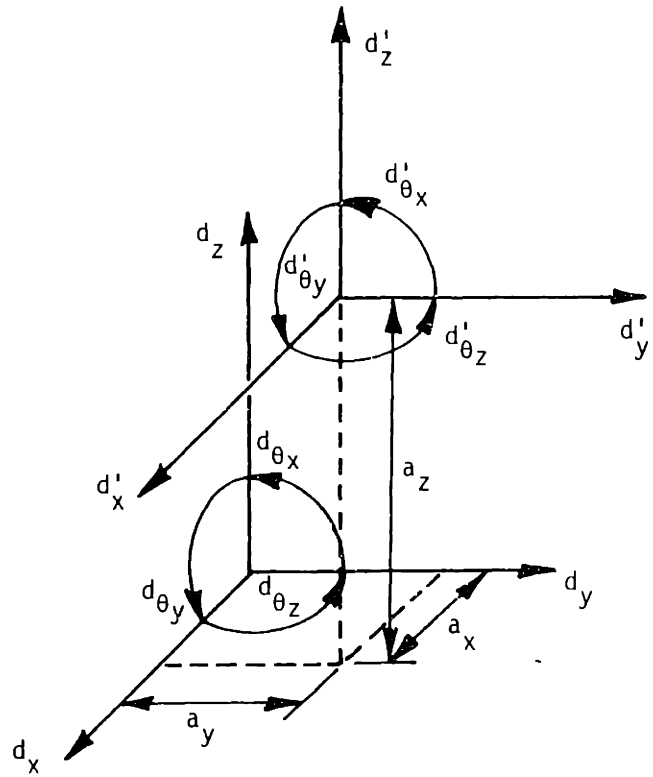


Figure 3.1. Transformation of displacement coordinates.

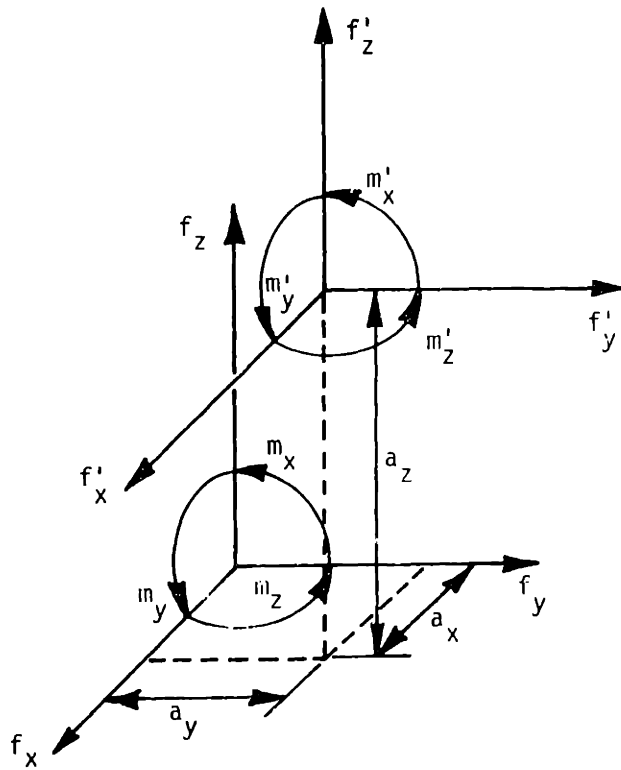


Figure 3.2. Transformation of force coordinates.

$$\begin{bmatrix} f_x \\ f_y \\ f_z \\ m_x \\ m_y \\ m_z \end{bmatrix} = \begin{bmatrix} 1 & 0 & 0 & 0 & 0 & 0 \\ 0 & 1 & 0 & 0 & 0 & 0 \\ 0 & 0 & 1 & 0 & 0 & 0 \\ 0 & -a_z & +a_y & 1 & 0 & 0 \\ +a_z & 0 & -a_x & 0 & 1 & 0 \\ -a_y & +a_x & 0 & 0 & 0 & 1 \end{bmatrix} \begin{bmatrix} f'_x \\ f'_y \\ f'_z \\ m'_x \\ m'_y \\ m'_z \end{bmatrix} \quad 3.7$$

As this transformation matrix is the transpose of the transformation matrix of equation 3.5, equation 3.7 can be expressed as:

$$F = G^T F' \quad 3.8$$

Using equations 3.6 and 3.8, equation 3.4 can be written in the form:

$$D' = GCG^T F' \quad 3.9$$

Therefore:

$$C' = GCG^T \quad 3.10$$

3.1.2. Two-Dimensional Analysis

For engineering design purposes, the 6 x 6 compliance matrix can be replaced with a simplified 2 x 2 planar compliance matrix provided that a number of conditions are met. Both the compliance and the parts being assembled must be rotationally symmetric about the insertion axis. The compliance in the insertion direction must be several orders of magnitude less than the compliance in the lateral direction. The 2 x 2 matrix is formed from a lateral compliance term along an axis orthogonal to the insertion direction, a rotational compliance term about an axis orthogonal to both the insertion and the lateral compliance axes, and the two off-diagonal terms. Equation 3.1 becomes:

$$\begin{bmatrix} d_\ell \\ d_\theta \end{bmatrix} = \begin{bmatrix} c_{11} & c_{12} \\ c_{21} & c_{22} \end{bmatrix} \begin{bmatrix} f_\ell \\ m_\theta \end{bmatrix} \quad 3.11$$

where d_ℓ is the lateral displacement, d_θ is the angular displacement, f_ℓ is the lateral force, and m_θ is the moment or torque all at the point where the compliance is defined. This matrix along with the full 6 x 6 compliance matrix of equation 3.1 is constrained to be symmetric due to reciprocity.

The transformation matrix G for the 2 x 2 compliance matrix becomes:

$$G = \begin{bmatrix} 1 & +a \\ 0 & 1 \end{bmatrix} \quad 3.12$$

where a is the distance along the insertion axis from the point where the compliance matrix was originally defined or measured to the point where the forces and moments are being applied or where the displacements are being imposed. This new point will normally be what is referred to as the assembly interface. Using this transformation matrix in equation 3.10, the compliance matrix at a new point in space becomes:

$$\begin{bmatrix} c'_{11} & c'_{12} \\ c'_{21} & c'_{22} \end{bmatrix} = \begin{bmatrix} c_{11} + 2ac_{12} + a^2c_{22} & c_{12} + ac_{22} \\ c_{12} + ac_{22} & c_{22} \end{bmatrix} \quad 3.13$$

The center of compliance is defined as the point in space where a lateral force will cause only a lateral deflection and a torque or moment will cause only a rotation. Mathematically stated, the compliance matrix is a diagonal matrix at the center of compliance. The point in space where this occurs for the 2 x 2 compliance matrix can be determined by setting the c'_{12} term of equation 3.13 to zero. Therefore, the center of compliance is located at:

$$a = \frac{-c_{12}}{c_{22}} \quad 3.14$$

A true center of compliance will exist for the full 6 x 6 compliance matrix only if the compliance has an axis of symmetry.

The quasi-static forces that occur during the insertion of a shaft into a hole are determined by the compliance at the assembly interface, the displacements that must be accommodated and the coefficient of friction. The displacements are a function of the positional errors between the centerline of the shaft and the centerline of the hole and the clearance ζ between the shaft and the hole. The

lateral displacement d_ℓ that must be accommodated is:

$$\begin{aligned}
 d_\ell &= \epsilon_\ell - \frac{\zeta}{2} & \text{if } \epsilon_\ell > \frac{\zeta}{2} \\
 d_\ell &= 0 & \text{if } \epsilon_\ell \leq \frac{\zeta}{2} \\
 d_\ell &= \epsilon_\ell + \frac{\zeta}{2} & \text{if } \epsilon_\ell < -\frac{\zeta}{2}
 \end{aligned}
 \tag{3.15}$$

where ϵ_ℓ is the lateral error between the centerline of the insertion axis and the centerline of the hole at the mouth of the hole and ϵ_θ is the angular error between the centerline of the insertion axis and the centerline of the hole. The angular displacement d_θ that must be accommodated is:

$$\begin{aligned}
 d &= \epsilon_\theta - \frac{\zeta}{z} & \text{if } \epsilon_\theta > \frac{\zeta}{z} \\
 d &= 0 & \text{if } \epsilon_\theta < \frac{\zeta}{z} \\
 d &= \epsilon_\theta + \frac{\zeta}{z} & \text{if } \epsilon_\theta \leq -\frac{\zeta}{z}
 \end{aligned}
 \tag{3.16}$$

where z is the depth that the shaft is inserted into the hole. The shaft that is being inserted could also have a lateral and angular error relative to the insertion axis. To simplify this analysis, these errors were assumed to be small.

The lateral force on the shaft during the insertion of the shaft into the hole is simply the inverse of the compliance matrix at the assembly interface multiplied by the lateral displacement that must be accommodated. The moment on the shaft is the inverse of the compliance matrix multiplied by the angular error that must be accommodated. There is also a moment caused by the friction component of the lateral force acting on the radius of shaft. This term is generally small and is ignored in the following analysis.

Inverting equation 3.11, the lateral force and the moment caused by the lateral and angular displacements are:

$$\begin{bmatrix} f_\ell \\ m_\theta \end{bmatrix} = \begin{bmatrix} k_{11} & k_{12} \\ k_{21} & k_{22} \end{bmatrix} \begin{bmatrix} d_\ell \\ d_\theta \end{bmatrix}
 \tag{3.17}$$

where $K = C^{-1}$. The vertical or insertion force is a function of both the coefficient of friction and the geometry of the chamfer while the shaft is sliding down the chamfer on the hole. Once the shaft is in the hole, the insertion force is the coefficient of friction multiplied by the total contact force. For a single-point contact between the shaft and the hole, the contact force is simply the lateral force. When there is two-point contact, the contact forces must equal the lateral force plus twice the moment divided by the insertion depth (see Figure 3.3).

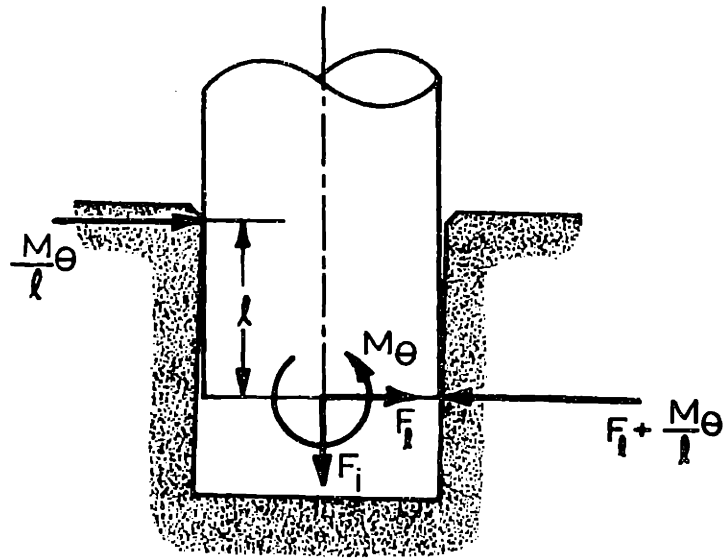


Figure 3.3. Contact Forces.

If it is assumed that the compliance matrix is defined at the center of compliance or where the compliance matrix is diagonal, the inverse of the compliance matrix or the stiffness matrix is simply:

$$\begin{bmatrix} c_{11} & 0 \\ 0 & c_{22} \end{bmatrix}^{-1} = \begin{bmatrix} \frac{1}{c_{11}} & 0 \\ 0 & \frac{1}{c_{22}} \end{bmatrix} = \begin{bmatrix} k_{11} & 0 \\ 0 & k_{22} \end{bmatrix} \quad 3.18$$

Using these values for k_{11} and k_{22} , the forces and moments at a point removed a distance a from the center of compliance become:

$$\begin{bmatrix} f_{\ell} \\ m_{\theta} \end{bmatrix} = \begin{bmatrix} k_{11} & -ak_{11} \\ -ak_{11} & k_{22} + a^2 k_{11} \end{bmatrix} \begin{bmatrix} d_{\ell} \\ d_{\theta} \end{bmatrix} \quad 3.19$$

For given values of compliance, the forces are clearly minimized when the center of compliance is at the assembly interface.

As an example, the expected forces for the insertion of a ball bearing into a housing are shown in Tables 3.1 and 3.2. The forces are calculated assuming certain positional errors. The compliance coefficients and the data on the bearing and the clearance are taken from values measured and used for the programmable assembly demonstration. Initially the center of compliance is assumed to be at the center of the bearing. Then the center of compliance is moved away from the assembly interface. Using the compliance values of the device as implemented, the calculated contact forces resulting from a typical angular error are much larger than the calculated contact force resulting from a typical lateral error. This implies that the ratio of the angular stiffness to the lateral stiffness of the compliance device as constructed is higher than would be desired. In the actual insertions of these bearings, the high contact forces are not observed. A common radial ball bearing exhibits considerable angular compliance. The existence of this additional compliance tends to make the location of the designed center of compliance relatively unimportant for this particular task. To obtain experimental data with moments, a solid piece with the external dimensions of the bearing was made.

3.1.3. Jamming

It can be seen from Tables 3.1 and 3.2 that it is possible to generate very high contact forces, particularly for shallow insertions, when either the angular stiffness is high or the center of compliance is not close to the assembly interface. These high-contact forces can, under certain conditions, lead to jamming of the parts. The phenomena of parts jamming was studied previously at the Draper Laboratory by Simunovic [33]. Two major conclusions were obtained:

Assumed two-dimensional compliance matrix (c_{11} is in mm/N, c_{22} is in mrad/Nm):

$$C = \begin{bmatrix} 0.1 & 0 \\ 0 & 2.5 \end{bmatrix}$$

as:

$$F = C^{-1}D$$

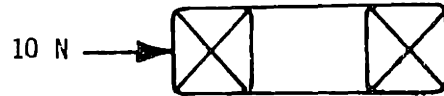
$$\begin{bmatrix} f_{\ell} \\ m_{\theta} \end{bmatrix} = \begin{bmatrix} 10 & 0 \\ 0 & 0.4 \end{bmatrix} \begin{bmatrix} d_{\ell} \\ d_{\theta} \end{bmatrix}$$

For a lateral offset of 1 mm:

$$\begin{bmatrix} f_{\ell} \\ m_{\theta} \end{bmatrix} = \begin{bmatrix} 10 & 0 \\ 0 & 0.4 \end{bmatrix} \begin{bmatrix} 1 \\ 0 \end{bmatrix}$$

$$f_{\ell} = 10 \text{ N}$$

$$m_{\theta} = 0$$



For a lateral offset of 1 mm and an angular offset of 10 mrad:

$$\begin{bmatrix} f_{\ell} \\ m_{\theta} \end{bmatrix} = \begin{bmatrix} 10 & 0 \\ 0 & 0.4 \end{bmatrix} \begin{bmatrix} 1 \\ 10 \end{bmatrix}$$

$$f_{\ell} = 10 \text{ N}$$

$$m_{\theta} = 4 \text{ Nm}$$

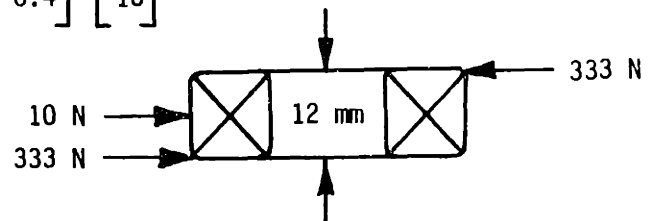


Table 3.1. Two-dimensional analysis of the insertion forces for the insertion of a ball bearing into the alternator housing.

Compliance matrix for a point - 75 mm from the designed center of compliance:

$$C' = GCG^T$$

$$C' = \begin{bmatrix} 1 & -0.075 \\ 0 & 1 \end{bmatrix} \begin{bmatrix} 0.1 & 0 \\ 0 & 2.5 \end{bmatrix} \begin{bmatrix} 1 & 0 \\ -0.075 & 1 \end{bmatrix}$$

$$C' = \begin{bmatrix} 0.114 & -0.187 \\ -0.187 & 2.5 \end{bmatrix}$$

as:

$$F = C^{-1}D$$

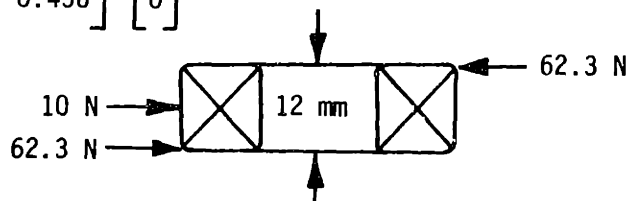
$$\begin{bmatrix} f_l \\ m_\theta \end{bmatrix} = \begin{bmatrix} 10 & 0.748 \\ 0.748 & 0.456 \end{bmatrix} \begin{bmatrix} d_l \\ d_\theta \end{bmatrix}$$

For a lateral offset of 1 mm:

$$\begin{bmatrix} f_l \\ m_\theta \end{bmatrix} = \begin{bmatrix} 10 & 0.748 \\ 0.748 & 0.456 \end{bmatrix} \begin{bmatrix} 1 \\ 0 \end{bmatrix}$$

$$f_l = 10 \text{ N}$$

$$m_\theta = 0.748 \text{ Nm}$$



For a lateral offset of 1 mm and a angular offset of 10 mrad:

$$\begin{bmatrix} f_l \\ m_\theta \end{bmatrix} = \begin{bmatrix} 10 & 0.748 \\ 0.748 & 0.456 \end{bmatrix} \begin{bmatrix} 1 \\ 10 \end{bmatrix}$$

$$f_l = 17.5 \text{ N}$$

$$m_\theta = 5.31 \text{ N}$$

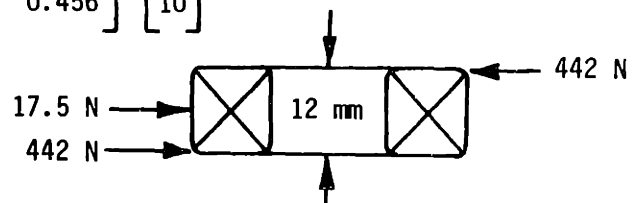


Table 3.2. Two-dimensional analysis of the insertion forces for the insertion of a ball bearing into the alternator housing. Center of compliance -75 mm from the assembly interface.

First, it is desirable to avoid two-point contact before the ratio of penetration of the shaft into the hole to the diameter of the hole satisfies the relationship:

$$\frac{\delta}{D} \geq \mu + C \frac{1}{\mu} + \mu^2 \quad 3.20$$

where C is the clearance to diameter ratio. When the shaft is not actually sliding, the friction force is only defined by the relationship:

$$\frac{F_f}{F_n} \leq \mu = \tan \phi \quad 3.21$$

where F_f is the friction force and F_n is the normal or contact force. The resultant force can be anywhere within a cone of angle 2ϕ . It is possible to have the condition shown in Figure 3.4, if the minimum penetration ratio condition of equation 3.20 is not met. The two reaction forces balance each other and have an undetermined magnitude.

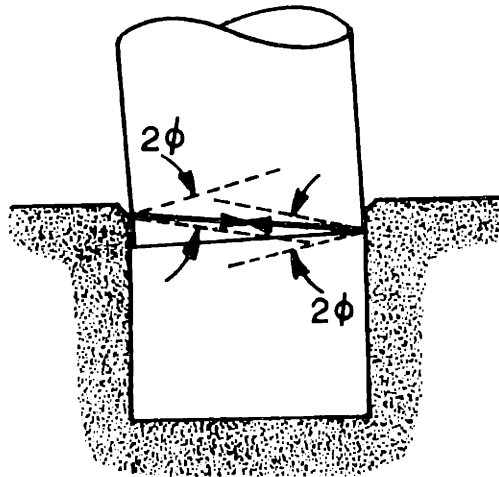


Figure 3.4. Jamming caused by residual reaction forces.

Secondly, if the condition of equation 3.20 is met, it is possible to avoid jamming by requiring that the applied moment around point I of Figure 3.5 have the opposite sign of the angular misalignment angle ϵ_0 . Assuming that the misalignment angle is small compared to the friction angle ϕ and that both coefficients of friction are equal, this condition can be expressed in non-dimensional parameters as:

$$-1 < \frac{M_o/rF_z}{\lambda} + \frac{F_y/F_z}{\lambda/(\lambda+1)\mu} < 1 \quad 3.22$$

where:

$$\lambda = \frac{\ell}{2r\mu} \quad 3.23$$

The relationship is plotted in Figures 3.6 and 3.7 for two values of λ taken from the ball bearing insertion data. The first value is just prior to two-point contact assuming an angular error of 10 mrad. The second value is with the bearing fully inserted into the housing.

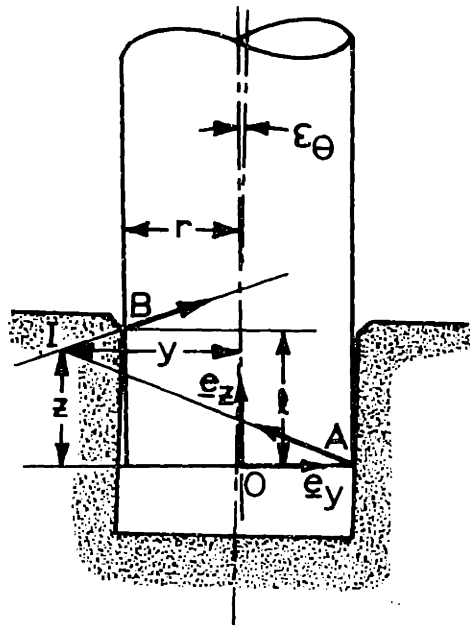


Figure 3.5. Reaction forces with the parts sliding.

From the form of equation 3.22, it can be seen that if neither the moment nor the lateral force is proportional to the insertion force, the inequality can always be satisfied by increasing the insertion force. Jamming will not be predicted using the forces and moments calculated with equation 3.17 or 3.19 because the lateral force and the moment are determined only by the inverse of the compliance matrix seen at the end of the shaft and lateral and angular displacement errors. However, there is an implicit assumption in equations 3.17 and 3.19 that there is no distort-

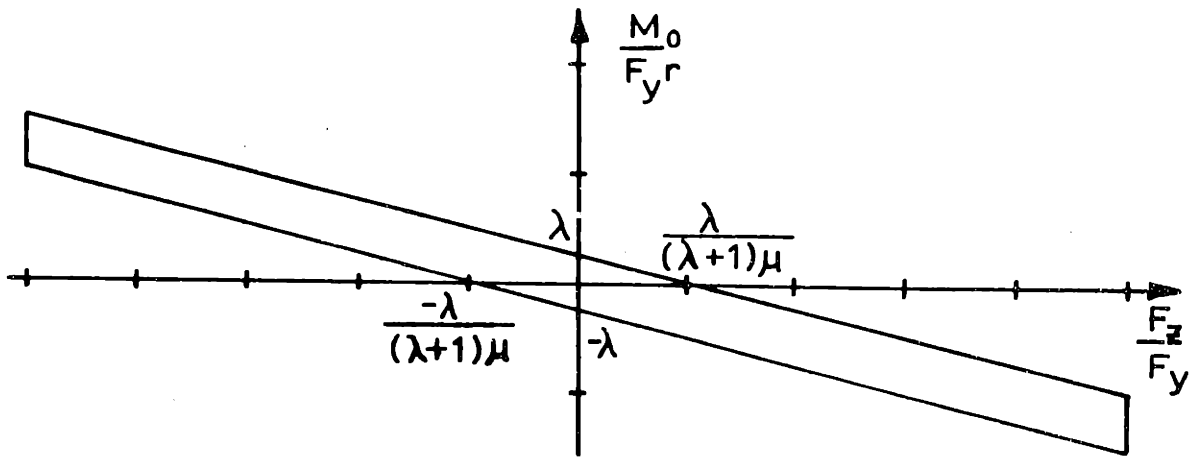


Figure 3.6. Conditions for sliding at the onset of 2-point contact for the insertion of a ball bearing into the automobile alternator housing.

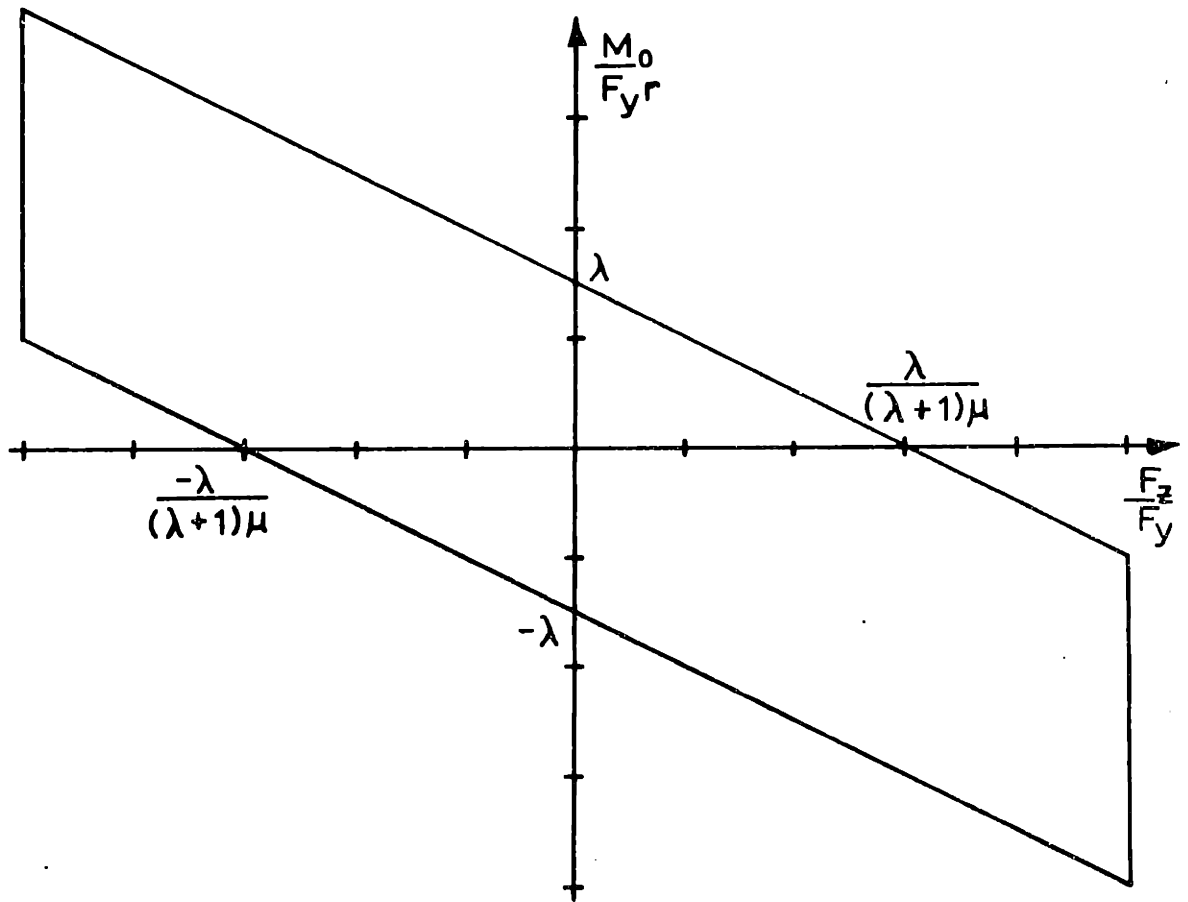


Figure 3.7. Conditions for sliding with the ball bearing fully inserted into the automobile alternator housing.

tion of the reference frame. Figure 3.8 shows that the vertical or insertion force can cause a moment about the end of the shaft if the center of compliance does not lie at this point. This moment is proportional to the insertion force, the angular deflection, and the distance from the center of the compliance to the end of the shaft or:

$$M = F_z a d_\theta \quad 3.24$$

For a given compliance and set of initial lateral and angular errors, this relationship can be used to set a bound on the maximum distance that the center of compliance can be displaced from the assembly interface. If, for example, with an initial angular error of 10 milliradians, zero lateral error, and the values for the clearance and the coefficient of friction as given in Table 3.3, the maximum value for a is found to be ± 250 mm. At this value of a , the insertion force goes to infinity.

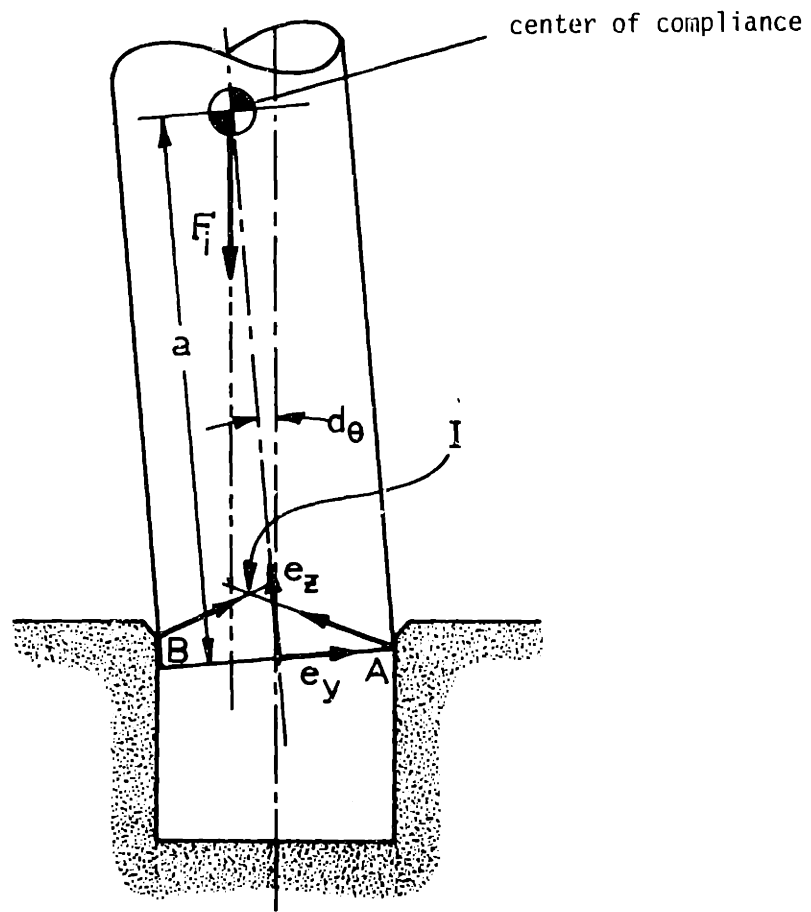


Figure 3.8. Moment caused by the insertion force when the center of compliance is displaced from the assembly interface.

$$-1 < \frac{M/F_z r}{\lambda} + \frac{F_\ell/F_z}{\lambda/(\lambda+1)\mu} < +1$$

$$M = F_z a \epsilon_\theta - F_\ell \mu r$$

$$\therefore -1 < \frac{\left(\frac{a \epsilon_\theta}{r} - \frac{F_\ell \mu}{F_z}\right)}{\lambda} + \frac{\left(\frac{F_\ell}{F_z}\right)}{\lambda/(\lambda+1)\mu} < +1$$

With F_z set to infinity

$$-1 < \frac{a \epsilon_\theta}{r \lambda} < +1$$

$$\lambda = \frac{\ell}{2r\mu} = \frac{\zeta}{2\epsilon_\theta r \mu}$$

$$\therefore -1 < \frac{2\epsilon_\theta^2 \mu a}{\zeta} < +1$$

Assumed Conditions

Angular error, ϵ_θ	0.01 rad
Coefficient of friction, μ	0.2
Clearance, ζ	10 microns (10^{-5} m)

Results

$$-0.25 \text{ m} < a < +0.25 \text{ m}$$

Table 3.3. Jamming conditions resulting from a moment caused by the insertion force.

The conditions would be somewhat more severe if the lateral error was non-zero. The details of the calculations are given in Table 3.3. A more complete explanation of this phenomena can be found in reference [35].

The implication of the above theory is that the compliance parameters can be specified if the expected errors and clearance and maximum desired contact forces are known. In general, the forces will be lowest with the center of compliance at or near the assembly interface. The location of the center of compliance becomes more critical with smaller clearances and larger positional errors.

3.1.4. Position Information

Positional errors can be determined once the assembly or mating of the parts has been initiated if the 6 x 6 compliance matrix is known and if a sensor is used that is capable of measuring the 6-dimensional force vector at the assembly interface. The displacement of the end of the shaft from the unperturbed position is simply the compliance matrix referenced to the end of the shaft multiplied by the measured force vector at this point:

$$D = CF \quad 3.2$$

Once the shaft has started to slide down the chamfer on the hole or has entered the hole, these displacements are approximately the positional errors between the two parts. There will be a residual error that can not be determined due to the clearance between the parts.

This information could be used as a force feedback signal to servo the assembly machine drives. The information obtained by multiplying the force vector by the compliance matrix would be better than the raw force vector information, as the magnitudes of the displacements would be known. However, the major object of designing the compliance system was to avoid the need for force feedback. This information could still be used for several purposes other than on-line force feedback. It could be filtered and used to remove long-term consistent errors. This would remove some of the burden on accurately specifying or teaching the initial location of the parts as a consistent error would be removed after a number of cycles of the assembly machine. The position information also could be used during the teaching or

specifying of the location of the parts and fixtures. Presently, the teaching is accomplished using visual cues. There is some difficulty in being able to see when the parts are properly aligned in several planes.

3.2. Limitations Caused by Impact Forces and Dynamics

At high insertion speeds, the contact forces and the resulting dynamics caused by the parts impacting each other become relatively more important than the quasi-static forces caused by positional errors deflecting the compliance.

3.2.1. Contact Forces Caused by an Impact

The contact forces resulting from an impact were obtained using the Hertzian stress formulas by equating the work done during an impact to the kinetic energy before the impact. Assuming that the impact is elastic and that there is no other internal mechanism for absorbing energy, the work done by the impact is the contact force integrated over the indentation depth. The details of this integration are presented in Appendix B: Impact Forces.

Because a very small area is initially involved in what is a point or a line contact, the local contact stresses for even very small loads or very low velocity collisions can cause the compressive yield strength to be exceeded. This does not necessarily mean that significant damage will be caused, as this stress is highly localized. It does indicate, however, that the collision of one part impacting upon another during assembly may not be entirely elastic.

The equations developed in Appendix B were used to compute the maximum contact force and the maximum compressive stress that occurs when a ball bearing is inserted into an alternator housing with typical conditions using the programmable assembly machine (see Table B.1, Appendix B for details). The maximum computed contact force was 1.76×10^3 N (395 lb_f) with a Hertzian stress of 9.4×10^9 Pa (1.36×10^6 psi). Although this exceeds the elastic limit of the die-cast aluminum housing, the affected area is small and is on a nonfunctional surface. The effect was qualitatively verified by dropping the bearing onto an aluminum plate from a height (~ 45 mm or 1.8 in) that caused the bearing to have the same energy at impact as the sus-

pended mass of the compliance system. This caused a small permanent indentation, indicating that the collision can not be modeled as an elastic impact.

3.2.2. Impact Dynamics

When two parts contact on the chamfers at a low insertion speed due to a lateral misalignment, the lateral component of the contact force will cause the part to move sideways as it slides across the chamfer assuming that the center of compliance is at or near the contact point. The impulse that occurs when the parts impact at higher speeds will cause a motion of or about the center of gravity. If the resultant motion is of sufficient amplitude, the part will bounce across the chamfer and hit the chamfer on the other side of the hole. This will cause a second impact which can start a chattering motion as the part bounces from one side to the other.

A second potential problem is the motion that results from two-point contact. Two-point contact occurs when a part is inserted in a hole that is angularly misaligned with the part. At low insertion speeds, the moments resulting from the two-point contact will cause the part to rotate about the contact points and come into alignment with the hole. At higher speeds, the impact will cause a significant rotational velocity about the contact points. As this initial angular velocity is greater than is required when the part is further in the hole, it is possible that the part will bounce to the other side of the hole and undergo a second two-point impact. If it impacts sufficiently hard, a series of two-point contacts can be set up.

In both cases, the body acted upon is assumed to be the segment of the compliance system supported by the compliance including the part-gripping tool and the parts. The spring forces are those associated with the compliance and are assumed to be acting at the assembly interface or at the point of contact.

Equations of motions for both problems were obtained by considering the impact to cause an instantaneous impulse. For the single-point impact on a chamfer, the impulse was obtained as a function of the coefficient of restitution by finding the energy before and after the impulse. The dynamics of the body are described by a

pair of coupled differential equations:

$$I\ddot{\theta} = K_{\theta}\theta - \ell K_x(\ell\dot{\theta} + \dot{x}) \quad 3.25$$

$$m\ddot{x} = -K_x(\ell\dot{\theta} + \dot{x}) \quad 3.26$$

with initial conditions:

$$\theta = 0, \dot{\theta} = (1 + R_c) \frac{md + md^2}{I} v_i \sin\theta \quad 3.27$$

$$x = 0, \dot{x} = (1 + R_c) \frac{I + md^2}{I} v_i \sin\theta \cos\theta \quad 3.28$$

where K_x and K_{θ} are the spring constants of the compliance device, m is the suspended mass, I is the moment of inertia about the center of this mass, v_i is the insertion velocity, R_c is the coefficient of restitution, ℓ is the distance from the center of compliance to the center of mass, and d is the distance from the line of action of the impulse to the center of mass.

The solution of the equations will give the maximum displacement as a function of the spring constants and the impact velocity. Given certain spring constants and a maximum permissible displacement, the maximum insertion velocity can be found. A solution was found in two ways. A numerical solution of the coupled differential equations was found for a given set of conditions using a fourth-order Runge-Kutta digital simulation. An approximate solution was found using energy considerations.

The approximate solution is found by solving for the maximum insertion velocity given a permissible lateral displacement (generally the distance from the point of impact to the far side of the hole). First, a solution is found by setting θ and $\dot{\theta}$ to zero:

$$v_{ix} \leq \frac{I}{1 + R_c} \left(\frac{I + md^2}{I} \right) \left(\frac{\delta}{\sin\theta \cos\theta} \right) \sqrt{\frac{K_x}{m}} \quad 3.29$$

Next, a solution is found by setting x and \dot{x} to zero:

$$v_{i\theta} \leq \frac{1}{1 + R_c} \left(\frac{I + md^2}{md} \right) \left(\frac{1}{\sin\theta} \right) \left(\frac{\delta}{\ell} \right) \sqrt{\frac{K_{\theta} + K_x \ell^2}{I}} \quad 3.30$$

These two solutions are then combined using the following expression to find an

approximate value for the maximum insertion velocity:

$$v_i = \frac{1}{\frac{1}{v_{ix}} + \frac{1}{v_{i\theta}}} \quad 3.31$$

This value is not an absolute maximum value for the insertion velocity. It only indicates when problems with chattering should be expected and what parameters influence this problem.

Approximate solutions of v_i obtained for typical assembly conditions were used as initial values for digital equations. The numerical solutions were in close agreement to the approximate solutions. Details on obtaining the differential equations and the initial conditions and on the techniques used in solving them are given in the first section of Appendix C: Impact Dynamics.

A more complete digital simulation was written to model multiple impacts on the chamfers and single-point impacts once the shaft enters the hole. Details on this simulation along with representative output plots are also presented in the first section of Appendix C.

An exact solution was found for the maximum value that the insertion velocity could have without causing a secondary two-point contact when the part is angularly misaligned with the hole:

$$v_i \leq 1.5063 \frac{\zeta}{\epsilon_\theta} \sqrt{\frac{K_\theta}{I_p}} \quad 3.32$$

where ζ is the clearance between the parts, ϵ_θ is the angular error between the parts, K_θ is the rotational stiffness of the compliance, and I_p is the moment of inertia of the suspended mass about a point between the two contact points. As before, this value is not an absolute maximum insertion velocity. It only indicates when a problem may occur with the part bouncing from one side to the other and what parameters influence this problem. The details on obtaining this expression and an example using it to solve for the maximum insertion velocity when a ball bearing is inserted into an automobile alternator housing are given in the second section of Appendix C.

4. EXPERIMENTAL APPARATUS AND PROCEDURES

Two complete compliance systems were designed and constructed. The first system used a cantilever beam spring to provide compliance. The second compliance system had a deformable structure with the center of compliance designed to be at the assembly interface. See Appendix D for details on the compliance design. Both systems were designed with a compliance lock and an automatic tool-change mechanism.

The compliance systems were designed to be mounted on a four-degree-of-freedom manipulator arm for the assembly of real parts. However, experiments to measure assembly forces were conducted with the compliance system attached to a six-axis force sensor and mounted in the spindle of a Bridgeport vertical milling machine (Figures 4.1 through 4.3). See Appendices F and G for details on the force sensor design and the calibration procedure. The milling machine and a precision machinist tilting rotary table were used as test fixtures to accurately set up known lateral and angular errors or offsets. To eliminate the effect of the milling machine lead-screw backlash, a spring-loaded dial gauge was used to measure lateral displacement.

Experimental data was taken by recording forces and moments while pushing the parts together by manually lowering the milling machine spindle or quill. The amplified and filtered force sensor signals and the vertical displacement signal were multiplexed and converted from analog to digital signals and processed in a minicomputer. The force sensor signals were multiplied by a 6 x 6 calibration matrix to resolve and scale the actual forces and torques. The displacement signal was multiplied by a constant to obtain an output scaled in millimeters.

Data was taken every one hundred milliseconds during a five-second interval for most of the experiments. At the end of the experimental run, the data was labeled and dumped onto a disc file. The data from earlier experiments was printed and selected runs were plotted by hand. A computer-driven plotter was used to plot the data from the later experiments. Typical plots of the data are included in the following section.

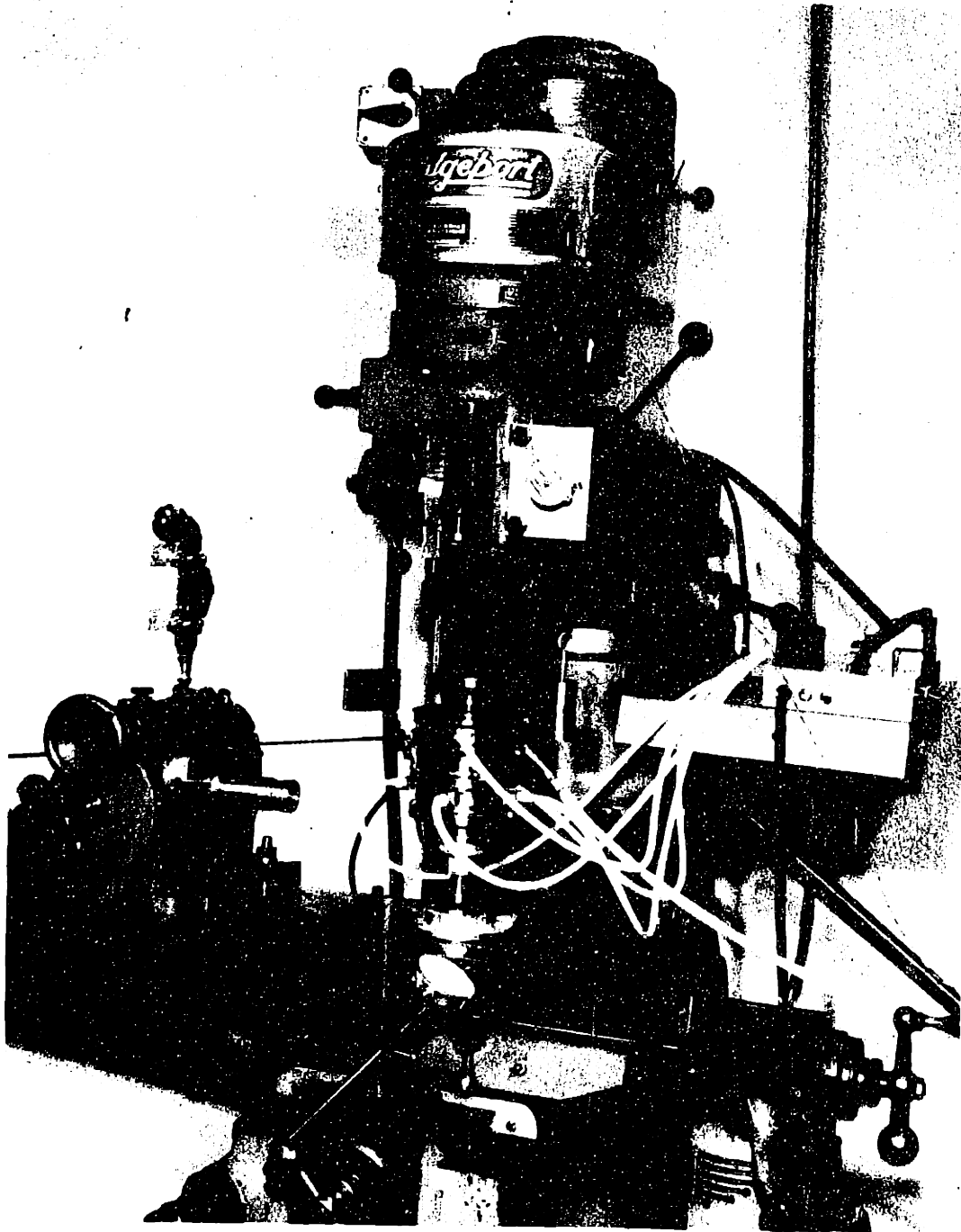


Figure 4.1. Overall view of the milling machine setup with the second compliance system mounted in the milling machine spindle.

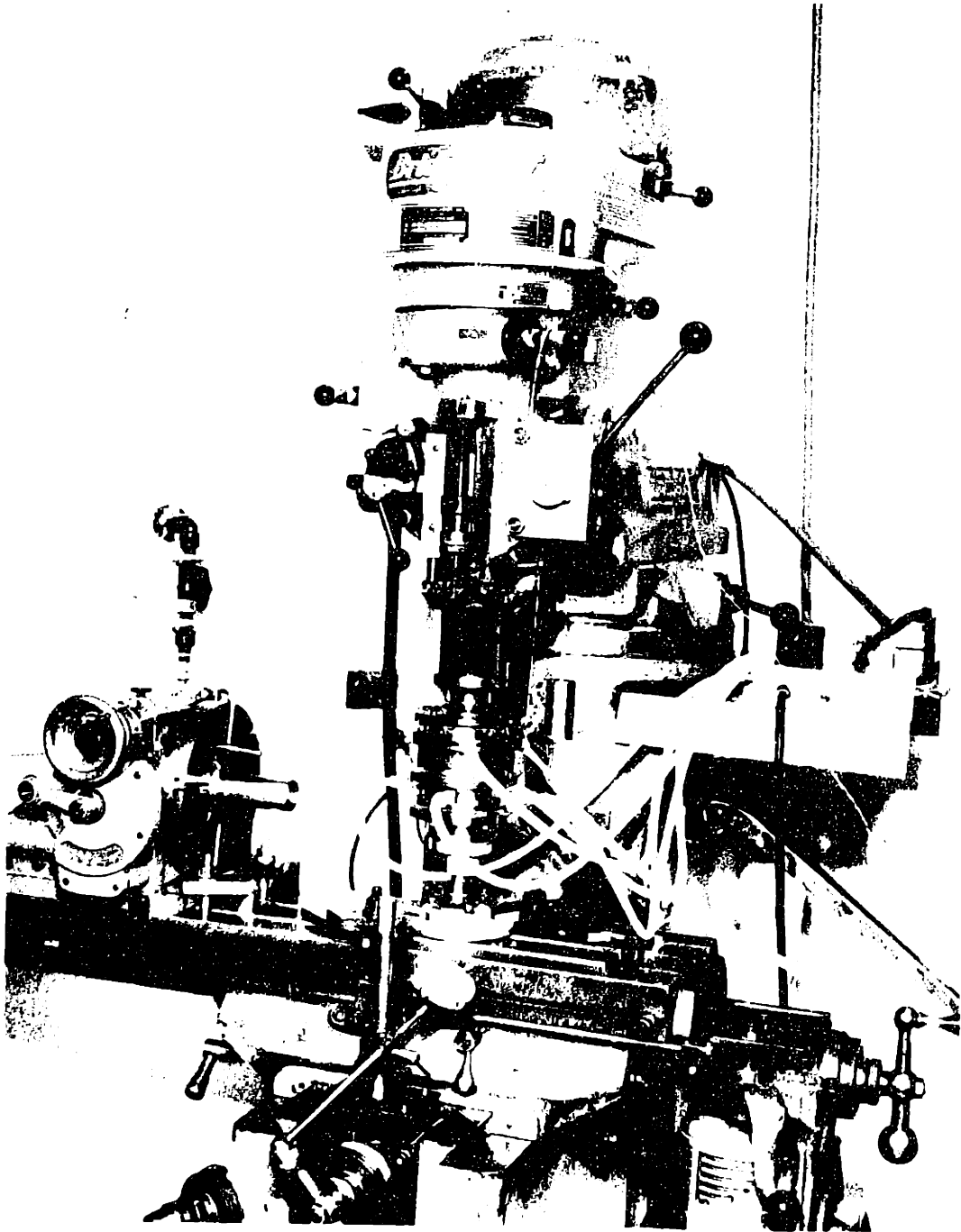


Figure 4.1. Overall view of the milling machine setup with the second compliance system mounted in the milling machine spindle.

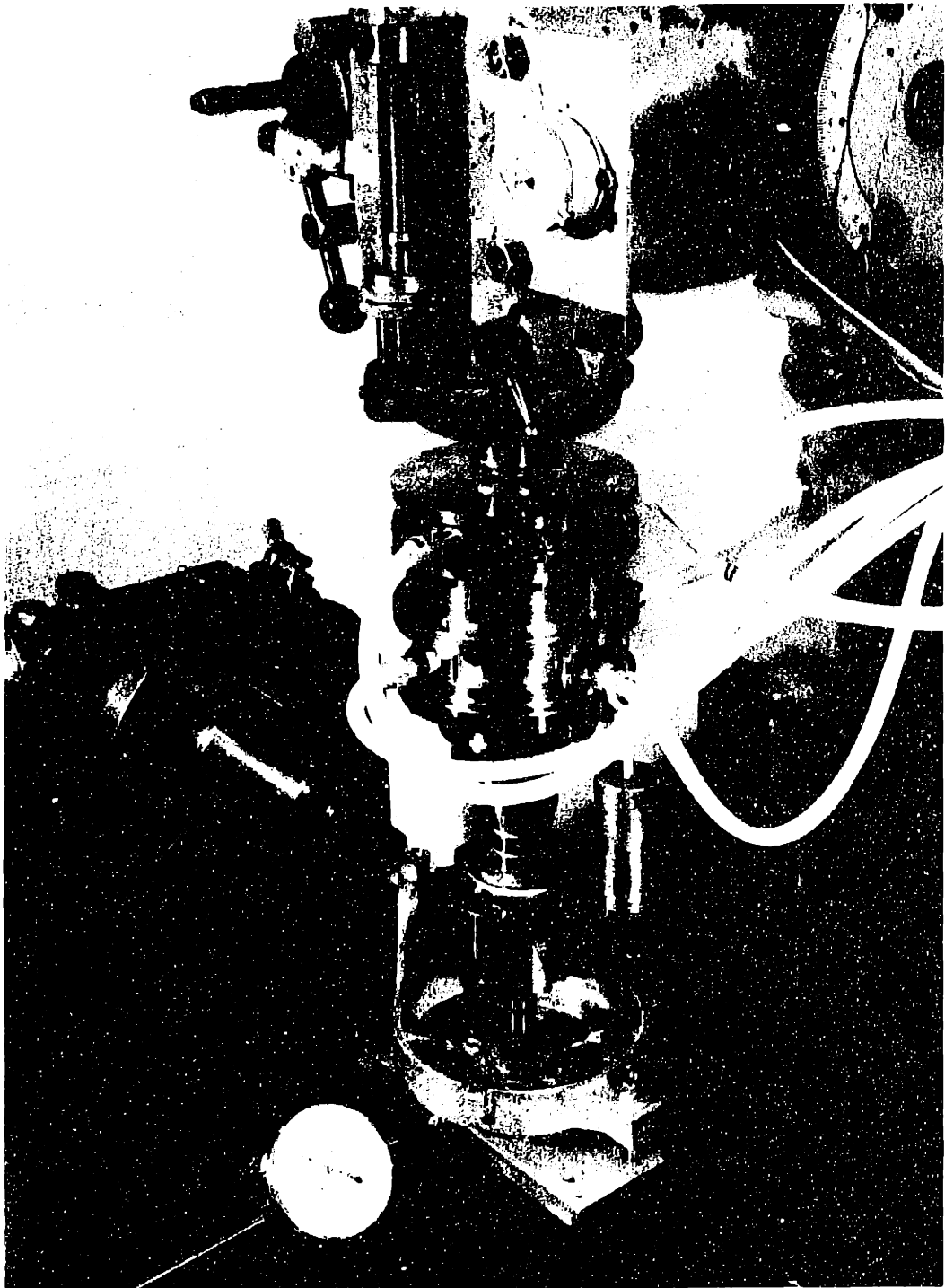


Figure 4.2. Close-up view of the insertion of the automobile alternator rotor into a ball bearing using the second compliance system.

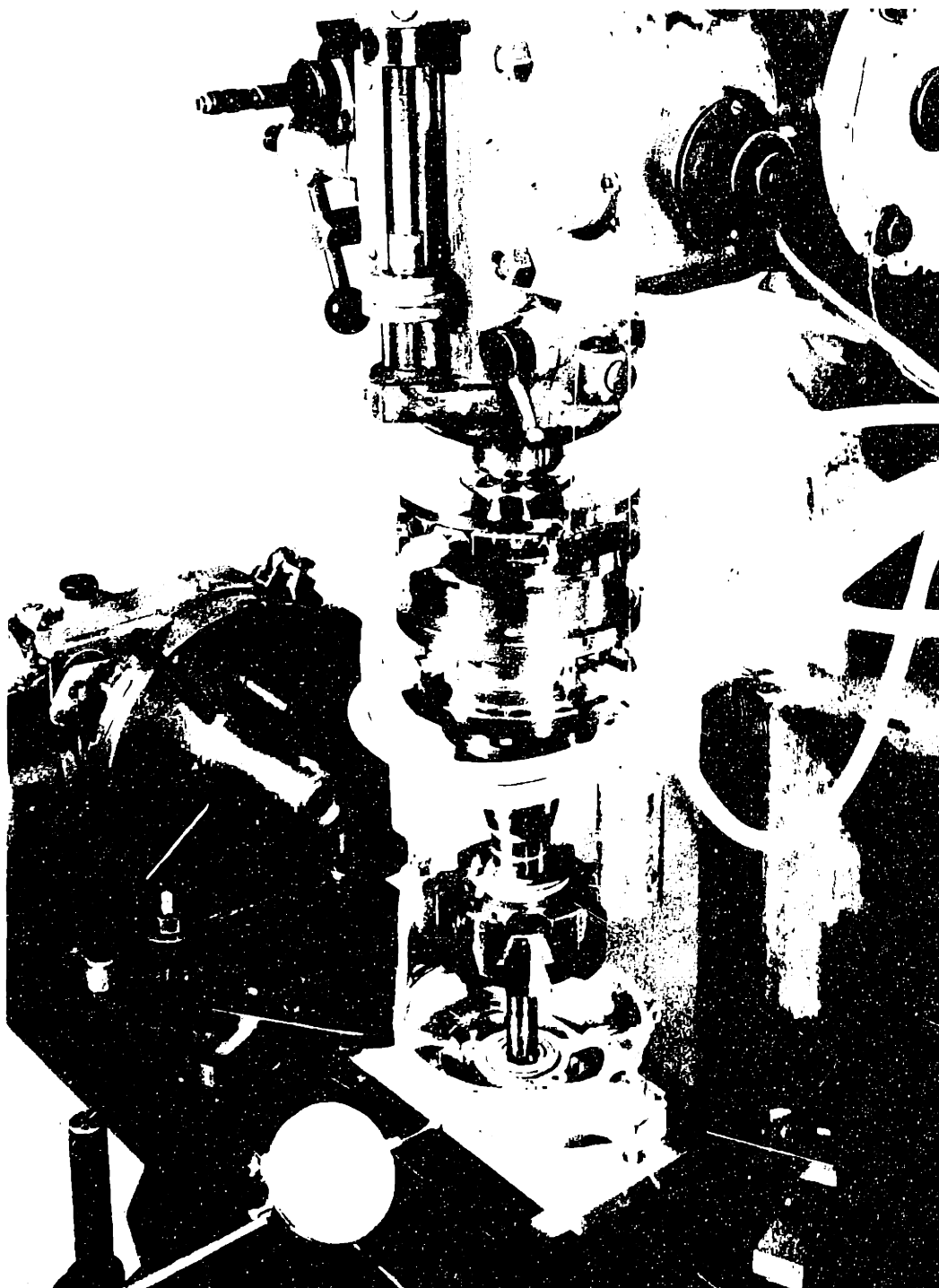


Figure 4.2. Close-up view of the insertion of the automobile alternator rotor into a ball bearing using the second compliance system.

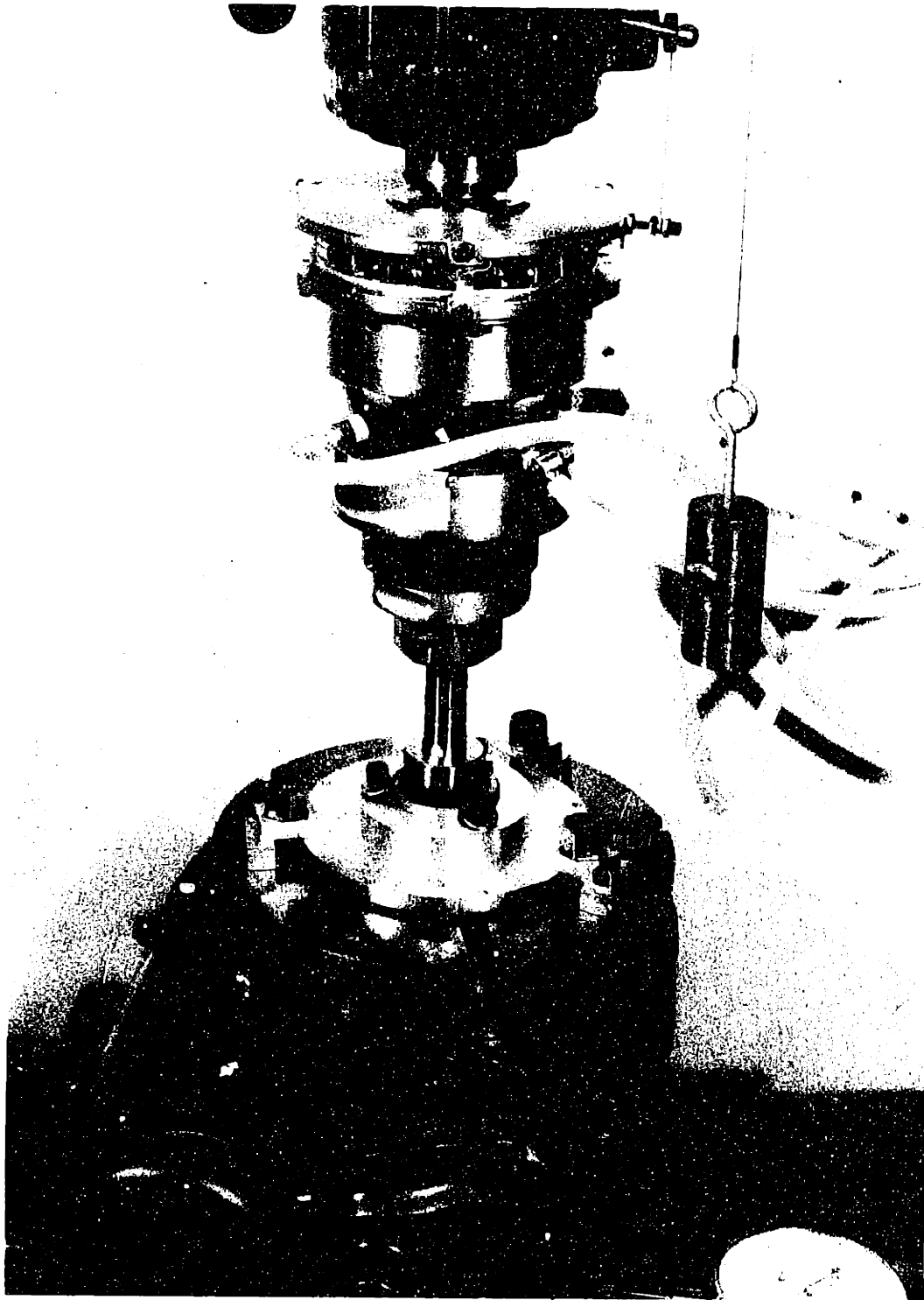


Figure 4.3. Close-up view of the insertion of the steel test plug into a drill bushing using simplified apparatus and the more sensitive aluminum six-axis force sensor.

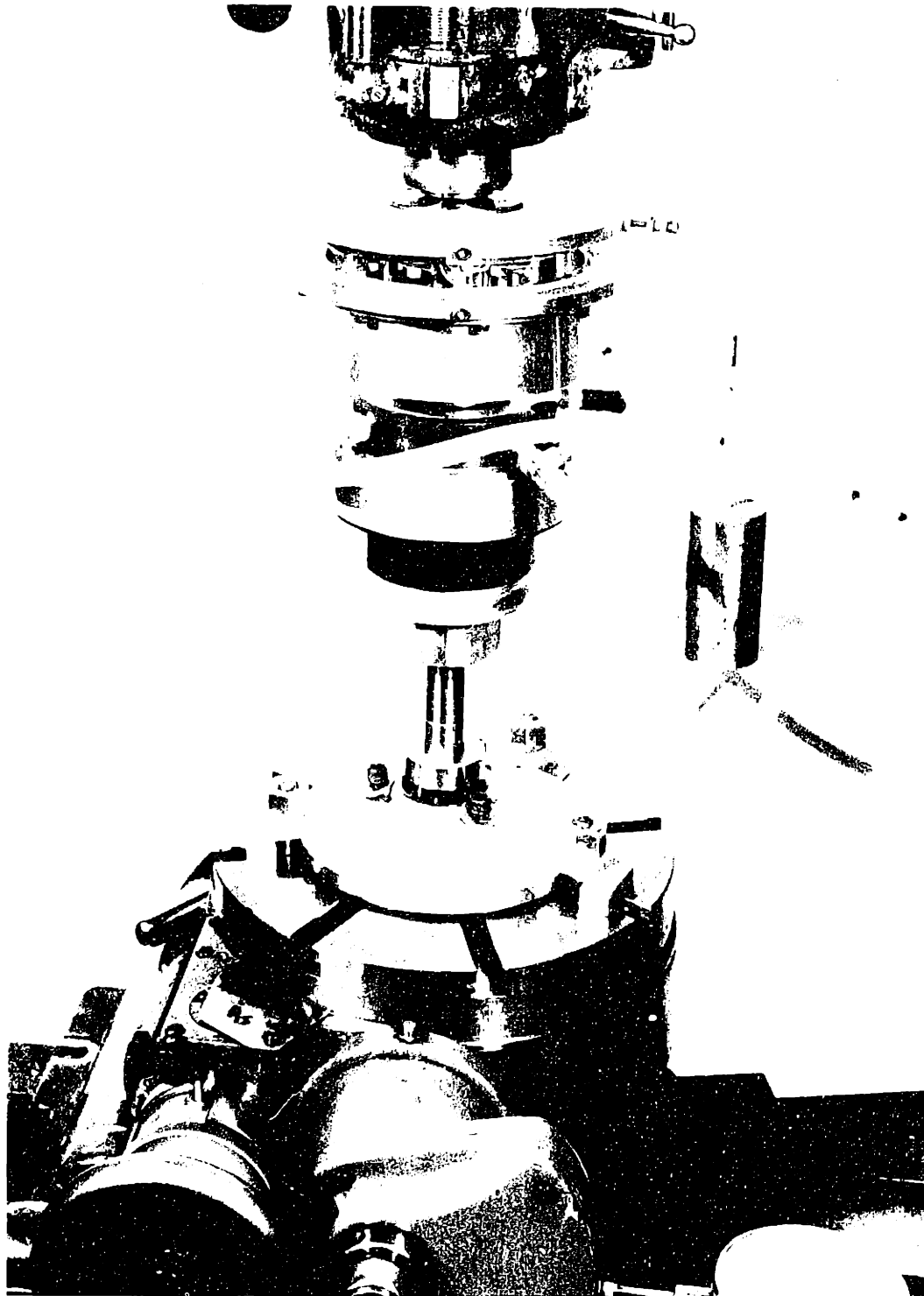


Figure 4.3. Close-up view of the insertion of the steel test plug into a drill bushing using simplified apparatus and the more sensitive aluminum six-axis force sensor.

5. RESULTS

Results from the initial assembly force experiments with the first compliance system using a cantilever beam spring to provide the compliance are presented in the first section. The second section contains the results from later assembly force experiments with the second compliance system using a deformable structure to provide the compliance.

5.1. Results Using the Cantilever Beam Compliance

The initial series of experiments involved measuring the forces and moments while inserting steel shafts or pegs into a hole in a meehanite (a type of high-strength cast iron) plate. The hole was 12.70 mm (0.5000 in) in diameter and drilled through a 25mm (1.0 in) thick plate. The steel shafts or pegs were made with diameters of 12.69, 12.67, 12.66 and 12.65mm (0.4995, 0.4990, 0.4985, and 0.4980 inch). Therefore the clearance ratios (clearance divided by hole diameter) available were 0.001, 0.002, 0.003, and 0.004. All the parts had ground finishes and 45° chamfers.

A number of tests were run varying the lateral and angular offsets and the clearance ratio. The lateral offsets were varied from -1.0 mm to +1.0 mm (-0.040 inch to +0.040 inch) while the angular offsets were varied from -5.0 mrad to +5.0 mrad. The center of compliance for these experiments was located 200 mm (7.87 in) from the end of the shaft. The rotational compliance was approximately 2.5 mrad/Nm (3.4 mrad/ft-lb) while the lateral compliance at the center of compliance was negligible. At the assembly interface, the effective lateral compliance was 0.1 mm/N (0.018 in/lb). Figures 5.1 through 5.4 are plots of typical force and moment data. Note that the separate phases of chamfer crossing single-point contact and two-point contact are clearly discernable. Also note that in Figure 5.4 the lateral force is negative during the single-point contact phase and becomes positive during the two-point contact phase.

Experiments were also run with random lateral and angular positional offsets. These unknown random errors were then removed manually during the insertion of the shaft by using the force and moment data as a guide while the shaft was slowly in-

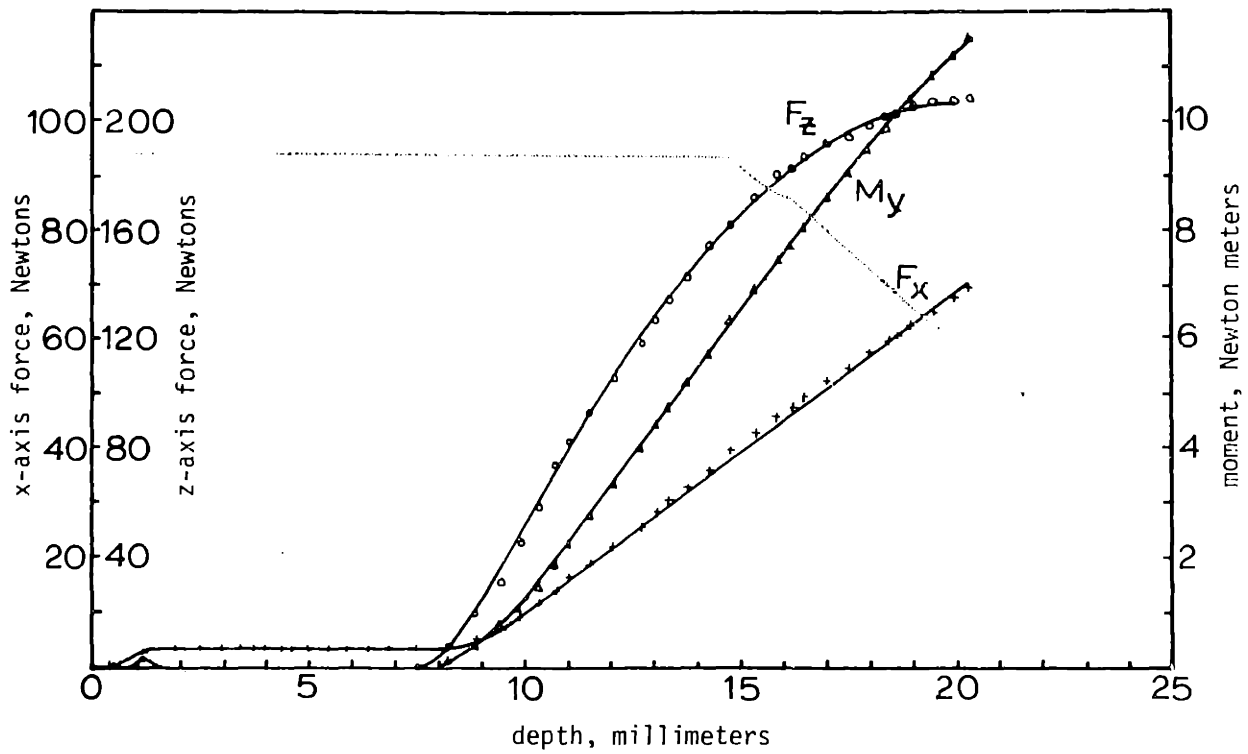


Figure 5.1. Force and moment data; 0.6 mm x-axis offset, 0.002 clearance ratio.

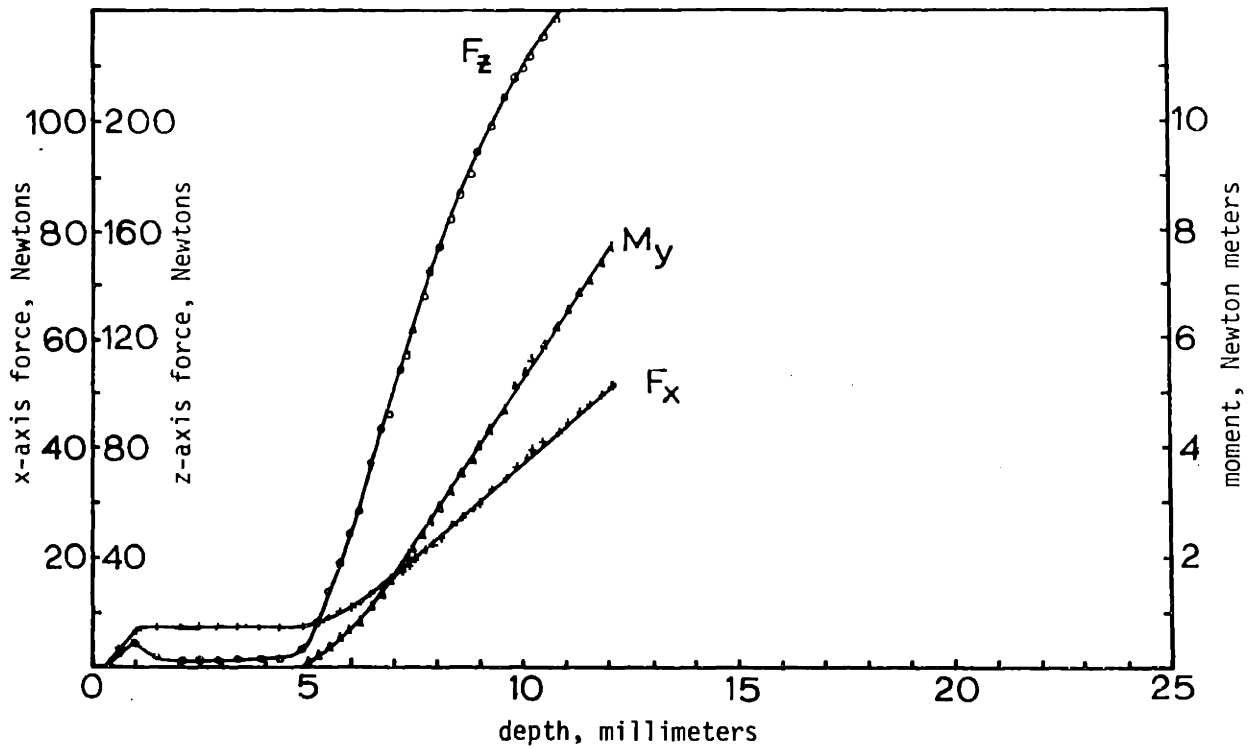


Figure 5.2. Force and moment data, 0.6 mm x-axis offset, 0.001 clearance ratio.

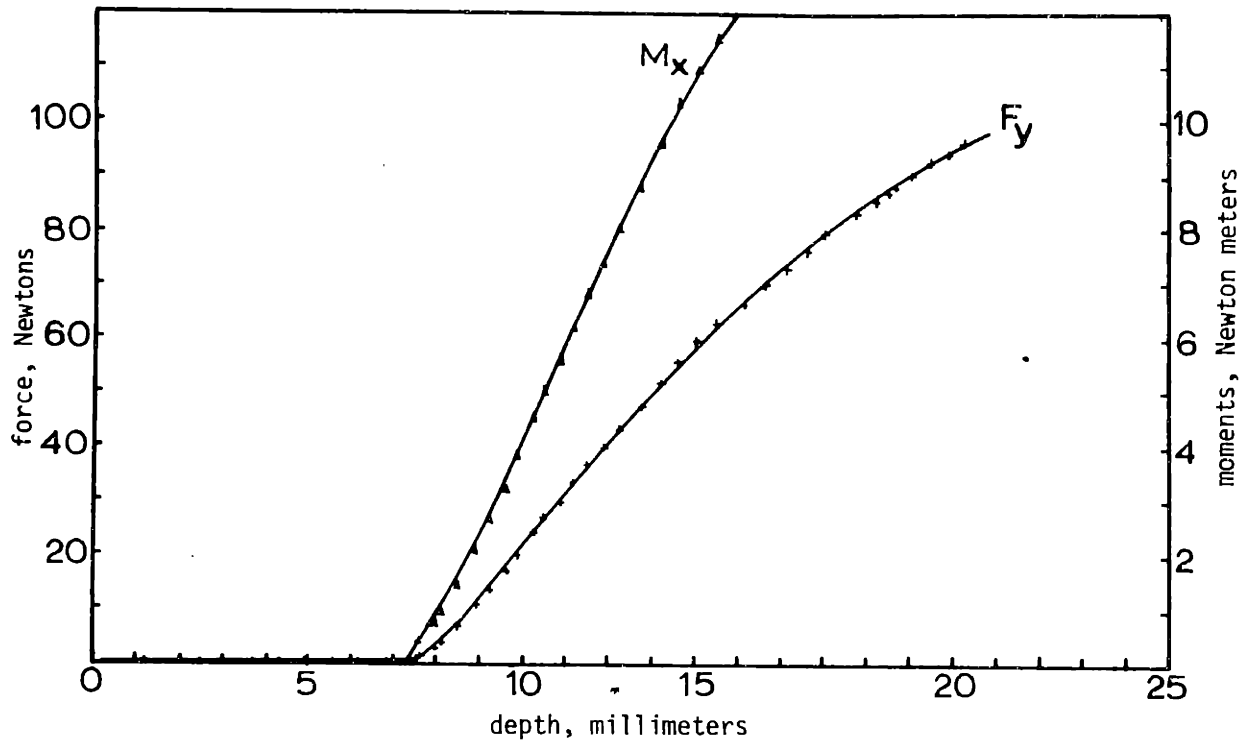


Figure 5.3. Force and moment data; zero lateral offset, +3.0 mrad angular offset, 0.002 clearance ratio.

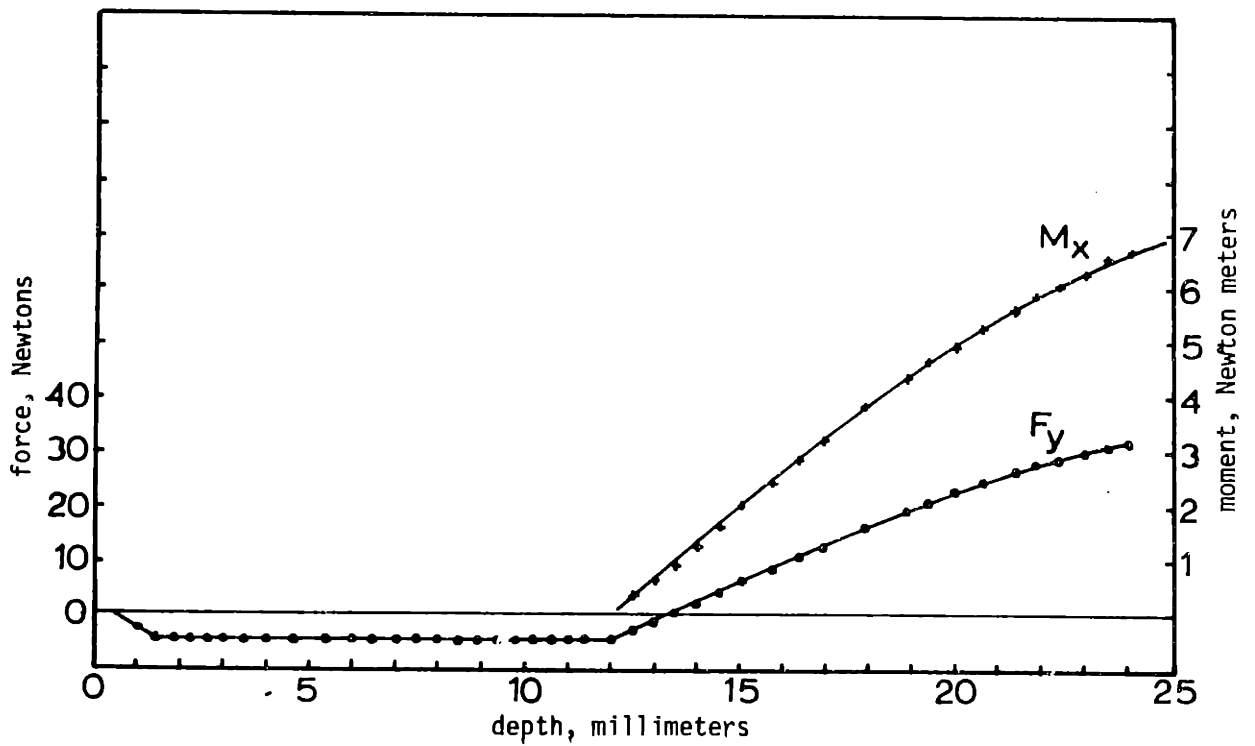


Figure 5.4. Force and moment data; -0.4 mm lateral offset, +3.0 mrad angular offset, 0.002 clearance ratio.

serted into the hole. The object was to prove that the data generated was unambiguous and could be used for active force feedback strategies.

5.2 Results Using the Deformable Structure Compliance

Forces and moments were measured in experiments using the compliant system to both assemble a number of real parts and to insert a precision test plug into a hole under varying conditions. Experiments with actual parts included inserting a ball bearing into an automobile alternator housing, inserting an alternator rotor into the ball bearing and inserting a ball bearing from a fraction horsepower electric motor into a steel bushing. The alternator parts used in these experiments were the same type as those used in the assembly of an automobile alternator for the programmable assembly demonstration project. For a detailed discussion of this project, see Appendix A: Programmable Assembly Demonstration Project. The hardened and ground steel test plug was made to the same external dimensions (35.00 mm O.D. x 12.00 mm width) as the ball bearing from the electric motor. This plug was inserted into a hardened and ground steel drill bushing with a clearance of 0.025 mm (0.001 inch).

The center of compliance of the deformable structure mounted on the six-axis force sensor was located approximately 145 mm (5.7 inch) from the top of the structure. The lateral stiffness (inverse of compliance) was approximately 12 N/mm (68 lb_f/inch) while the rotational stiffness was approximately 0.45 Nm/mrad (4.0 in.-lb_f/mrad).

Figures 5.5 through 5.9 are plots of the force and moment data obtained while inserting the hardened and ground steel test plug into the drill bushing with the assembly interface at the center of compliance. In the first three figures, the x-axis offset is increased in increments of 0.25 mm (0.010 inch). The lateral force profiles are quite smooth and are linearly proportional to the lateral offset during the entire insertion. There is no evidence of two-point contact. In the fourth test (Figure 5.8), the drill bushing was given an angular offset of 5.0 milliradians in the θ_y direction with zero lateral offset. There was no contact until a

depth of approximately 6 millimeters when two-point contact occurred. The lateral force remained negligible. In the fifth test of this series (Figure 5.9), a lateral offset of 0.50 mm (0.020 inch) was added to the 5.0 milliradian angular offset. The effect is very nearly a simple addition of the results of the second test and the fourth test. An initial single-point contact occurred with a typical chamfer crossing. At a depth of approximately 6 millimeters, two-point contact occurred. The two-point contact caused a large rise in the insertion force as the reaction forces to the moment were separated by a maximum distance of only 12 millimeters and were therefore quite large.

The conditions for the force and moments plots in Figures 5.10, 5.11 and 5.12 were the same as for Figures 5.7, 5.8, and 5.9 except that the assembly interface has been moved to a point +50mm (+2.0 inch) away from the center of compliance (in the direction closer to the compliant structure). For the first part of the insertion, the forces and moments plotted in Figure 5.10 for a lateral offset of 0.75 mm are quite similar to those plotted in Figure 5.7. However, at a depth of approximately 8 millimeters, two-point contact occurs with an increasing positive moment and a rapidly increasing insertion force. The forces and moment plotted in Figure 5.11 for an angular offset are similar to forces and moment plotted in Figure 5.8 except that the sign of the lateral force is negative. The plots in Figure 5.12 for the combined lateral and angular offset are also quite similar to the plots in Figure 5.9 with a slightly higher maximum insertion force.

The conditions for the forces and moment plotted in Figures 5.13, 5.14, and 5.15 were similar to those for figures 5.10, 5.11, and 5.12 except this time the assembly interface was moved to a point -50 mm (-2.0 inch) away from the center of compliance (in the direction away from the compliant structure). The forces and moment for an angular offset plotted in Figure 5.14 were somewhat greater than those plotted in Figure 5.11. Also the sign of the x force is positive. With the combined lateral and angular offset, the two-point contact occurred sooner in Figure 5.15 than in Figure 5.12 with larger forces and a larger moment.

Figures 5.16 and 5.17 are plots of the forces and the moment for the insertion of a ball bearing into the drill bushing with the assembly interface -50mm from the center of compliance. The conditions for the two tests were the same as the conditions for the tests plotted in Figures 5.13 and 5.14. With a lateral offset, the major difference between the data plotted in Figure 5.16 and that plotted in Figure 5.13 is that there is no evidence of two-point contact in Figure 5.16. With an angular offset, there are virtually no forces or moments (Figure 5.17). This phenomena is due to the inherent angular compliance in ordinary (radial) ball bearings.

Figures 5.18 and 5.19 are plots of the force and moment data for the insertion of the test plug into the drill bushing with the assembly interface -100 mm (3.9 inch) from the center of compliance. The forces and moment for a lateral offset are plotted in Figure 5.18. The lateral force prior to two-point contact is less than it was in similar tests with assembly interface closer to the center of compliance. After two-point contact, the force and the moment rise faster than in the previous tests. The forces and moment for an angular offset are considerably higher than those in the previous tests (Figure 5.19).

In the final series of tests for inserting the steel plug into the drill bushing, the assembly interface was -150 mm (-5.9 inch) from the center of compliance (Figures 5.20, 5.21, and 5.22). The forces plotted in Figure 5.20 for the same 0.75 mm lateral offset used previously (Figures 5.7, 5.10, 5.13, and 5.18) are lower prior to the onset of two-point contact and rise more rapidly after two-point contact occurs. The moment also rises rapidly after the occurrence of two-point contact. The forces and moments plotted in Figure 5.21 for a 5.0 milliradian angular offset are also higher than those obtained in the previous tests with the same angular offset (Figures 5.8, 5.11, 4.14, and 5.19). With a combined lateral and angular offset it was, for the first time necessary to rescale the x force and the y moment (Figure 5.22). Also, for the first time, the insertion force exceeded 100 Newtons (22.5 lb_f).

Experiments inserting the ball bearing into the alternator housing and inserting the alternator rotor into the ball bearing were run using the same part-

gripping tools used for the assembly demonstration project. With these tools, the distance from the center of compliance to the assembly interface was approximately -55mm (-2.2 inch) for inserting the ball bearing into the housing and approximately -200 millimeters (-7.9 inch) for inserting the rotor into the ball bearing, (the negative direction is vertically down or away from the compliant structure).

In Figures 5.23 and 5.24, the x-axis lateral force, the z-axis insertion force, and the moment about y axis are plotted into the alternator housing. The offset or positional error was 0.5 mm (0.020 inch) for Figure 5.23 and 0.75 mm (0.030 inch) for Figure 5.24. The housing had previously been used in the assembly demonstration project and had been subjected to numerous insertions. As can be seen from the figures, the lateral force rises to an amount proportional to the lateral offset as the bearing crosses the chamfer. The insertion force rises as the bearing crosses the chamfer and then falls back to a level approximately equal to the lateral forces times the coefficient of friction.

In Figure 5.25, the same forces and moment are plotted against insertion depth for the insertion of a ball bearing into a new alternator housing. The other conditions are the same as the conditions for Figure 5.24. The lateral force is similar in profile to the lateral force in Figure 2.24 except for one small perturbation. The insertion force profile is quite ragged although the maximum force still occurs at the chamfer crossing. Force and moment data was also recorded for a second and third consecutive insertion. The lateral force plotted in Figure 2.26 does not show any abnormalities. The spikes in the insertion force are considerably reduced although the average insertion force after the chamfer crossing is still approximately twice as high as the insertion force plotted in Figure 5.24. The plot of the insertion force for the third insertion in Figure 5.27 is noticeably smoother.

A total of four experiments were made inserting a ball bearing into a previously unused alternator housing. The second and third experiments were not as dramatic as the first one. In the fourth test, the insertion force at one point exceeded 120 Newtons (27 lb_f) while the insertion force in the previous tests had not exceeded 10 Newtons (2.2 lb). The insertion force still exceeded 15 Newtons at this

point on the second insertion. The forces and moment for these runs are plotted in Figures 5.28 and 5.29. The insertion force alone is rescaled and plotted for the first, second, and third insertion in Figure 5.30. There was still a noticeable spike in the insertion force on the third run. A visual inspection of the part after the test did not disclose the cause of the problem.

The lateral force, the insertion force, and the moment are plotted against insertion depth for the insertion of the rotor shaft into the ball bearing in Figure 5.31, 5.32, and 5.33. In the first run, a rotor that had been well burnished from numerous insertions was used. There are several interesting phenomena to note. For the same 0.75 mm offset, the forces for the insertion of the rotor into the bearing are lower than the forces for the insertion of the bearing into the housing. This is explained by the fact that although a ball bearing is quite stiff in the radial direction, it has considerable angular compliance. If the angle of the shaft is not constrained, the effective lateral compliance increases as the distance from the center of compliance increases. Part of the lateral deflection is due to the angular deflection multiplied by the distance from the center of compliance. Because the initial 15 millimeters (0.6 inch) of the shaft are threaded, the force profiles are considerably more ragged than the profiles for the insertion of the ball bearing into the housing.

In Figure 5.32, a new shaft was inserted into the bearing under otherwise similar conditions. The initial force profiles during the insertion of the threaded section are quite similar to the profiles in the previous plot. When the straight part of the shaft was encountered, there was a rapid rise in the insertion force. During the second insertion of the same shaft into the bearing (Figure 5.33) the insertion force was much lower. This test was repeated with a second new rotor with quite similar results. The probably cause of the high insertion force for the initial insertion is a burr caused by undercutting the threads.

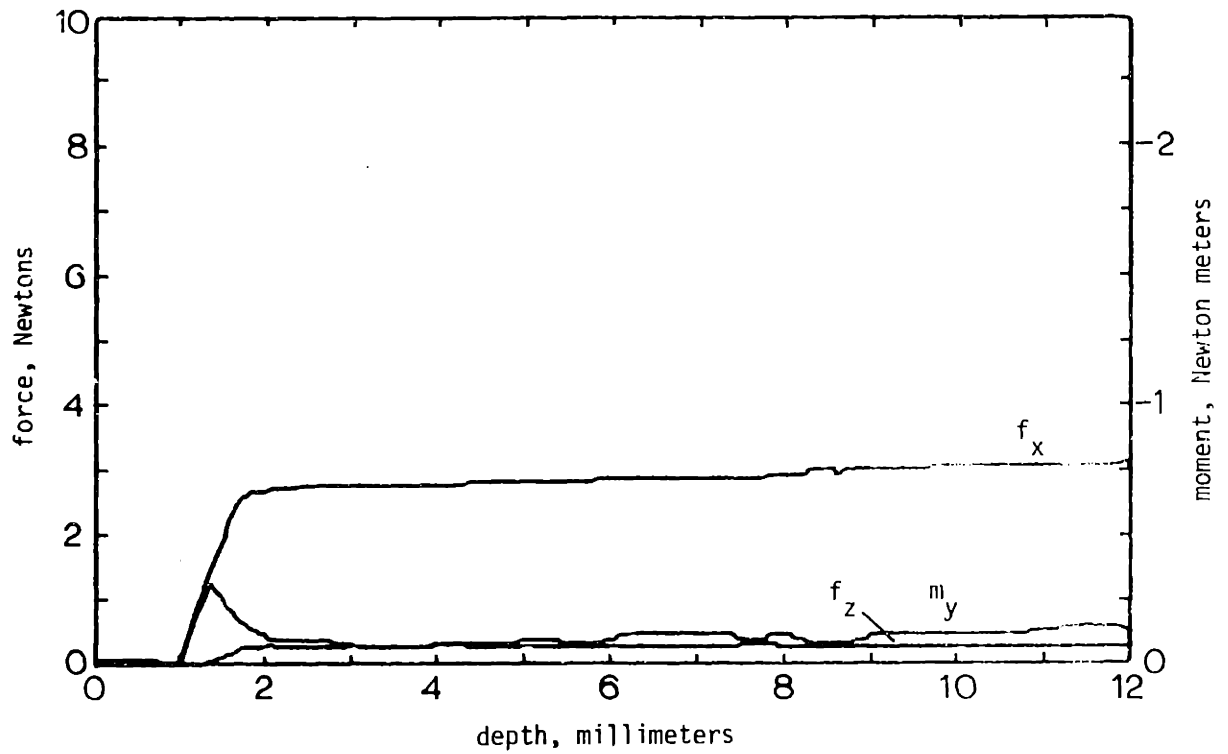


Figure 5.5. Force and moment data; insertion of a 35.00 mm diameter hardened steel plug into a 35.02 mm diameter drill bushing, center of compliance at the assembly interface, 0.25 mm x-axis offset.

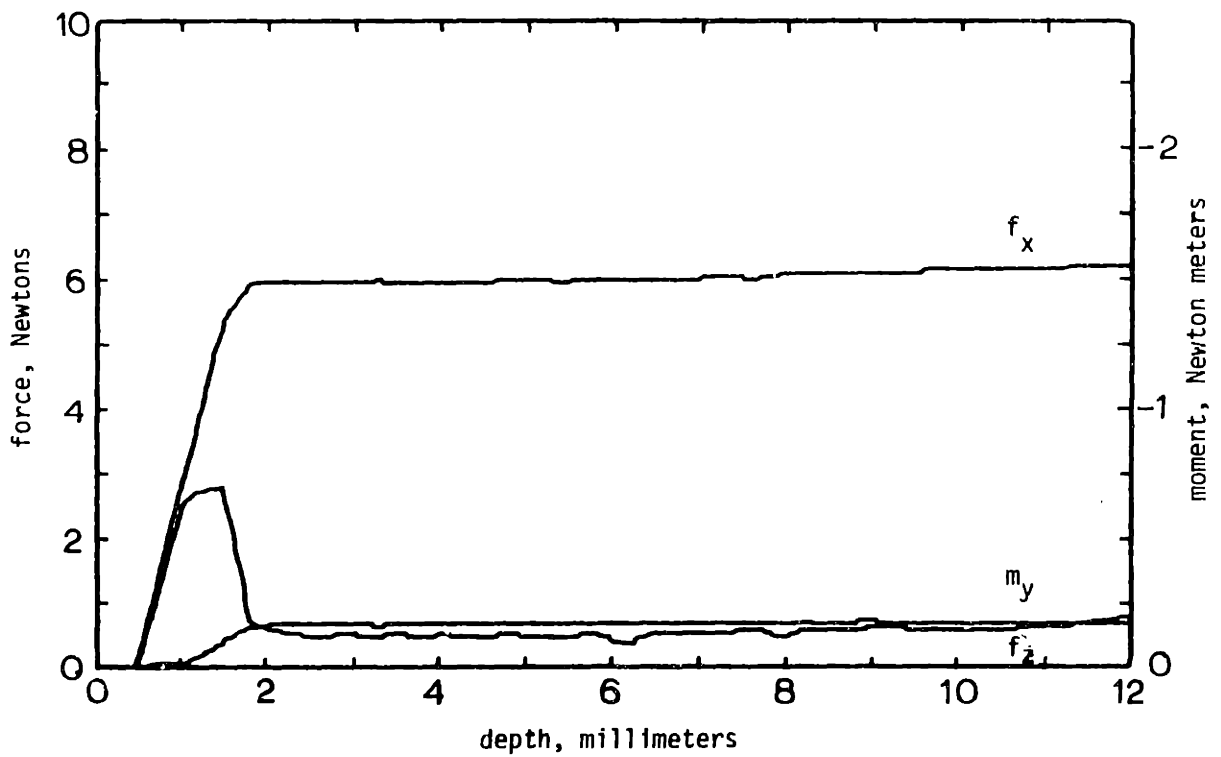


Figure 5.6. Force and moment data; insertion of a 35.00 mm diameter hardened steel plug into a 35.02 mm diameter drill bushing, center of compliance at the assembly interface, 0.50 mm x-axis offset.

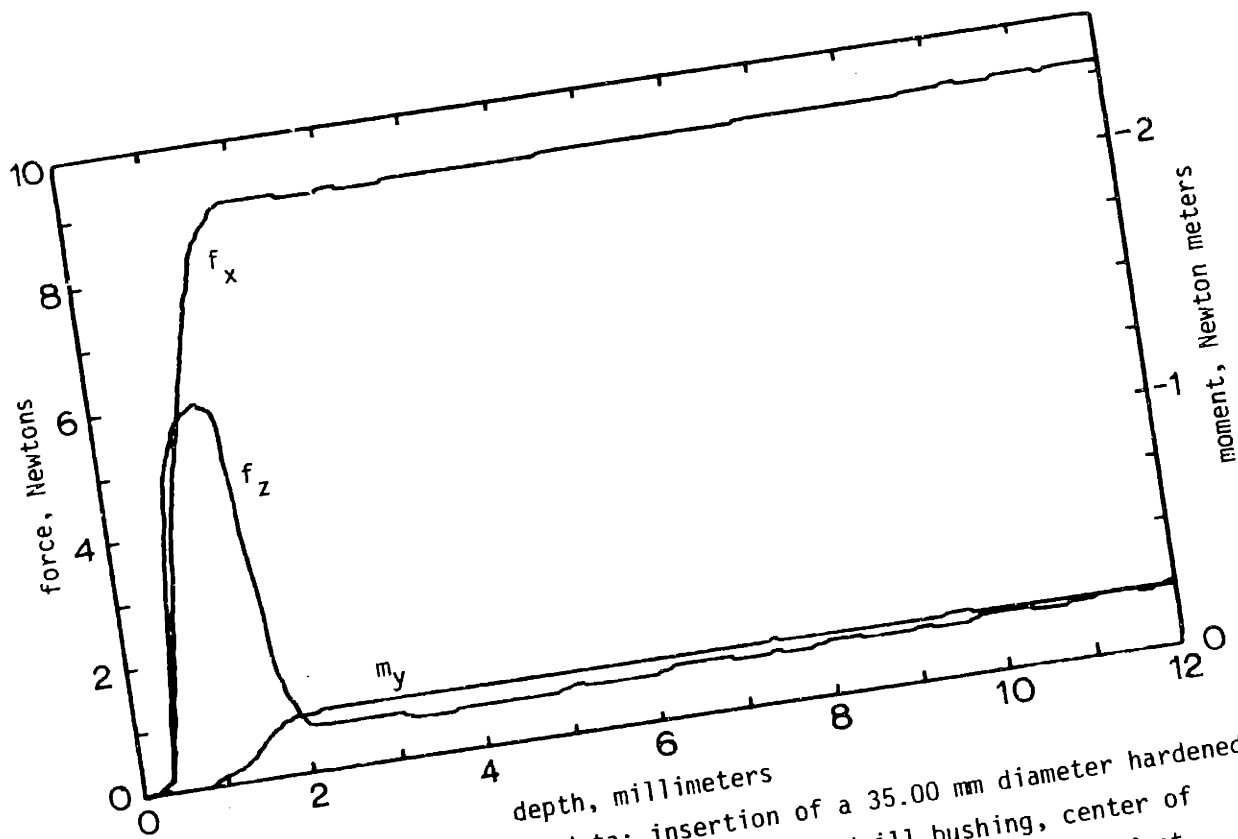


Figure 5.7. Force and moment data; insertion of a 35.00 mm diameter hardened steel plug into a 35.02 mm diameter drill bushing, center of compliance at the assembly interface, 0.75 mm x-axis offset.

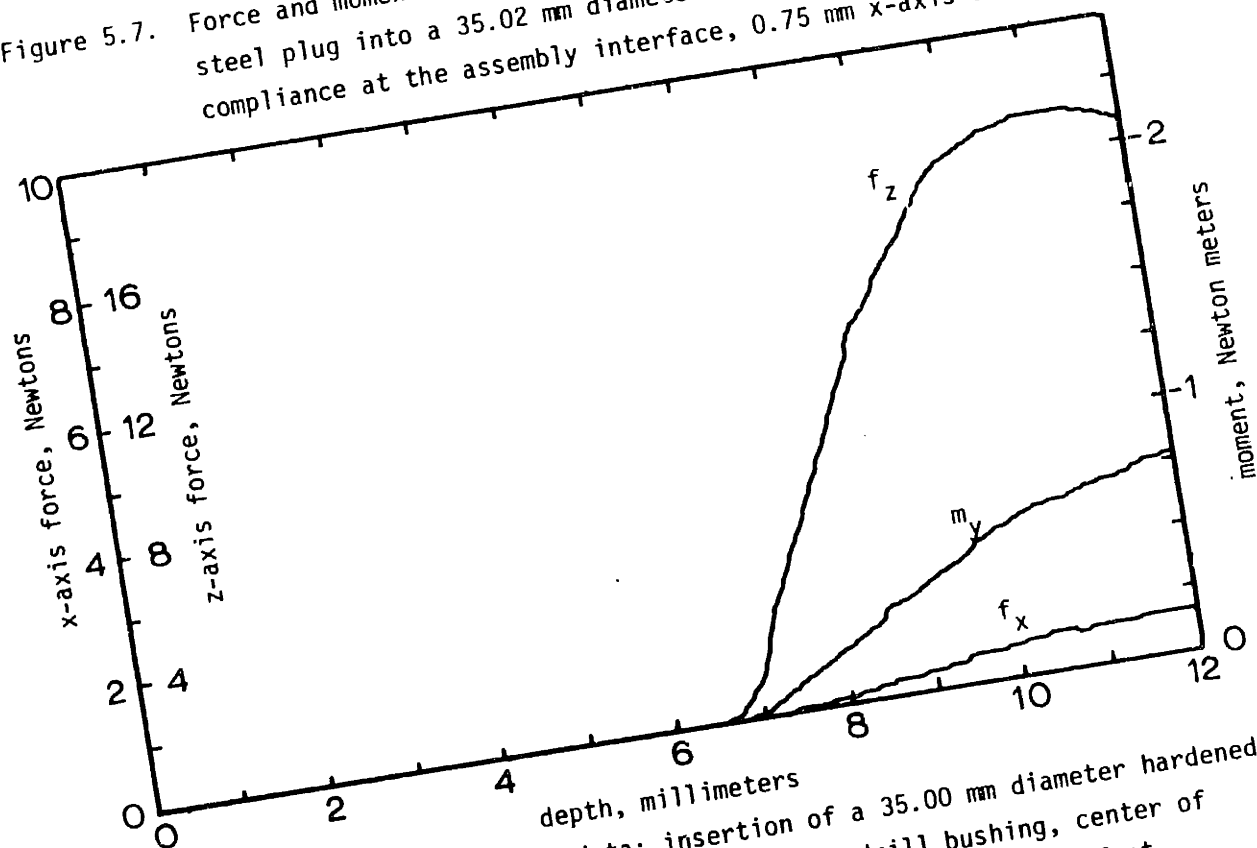


Figure 5.8. Force and moment data; insertion of a 35.00 mm diameter hardened steel plug into a 35.02 mm diameter drill bushing, center of compliance at the assembly interface, 5.0 mrad θ_y offset.

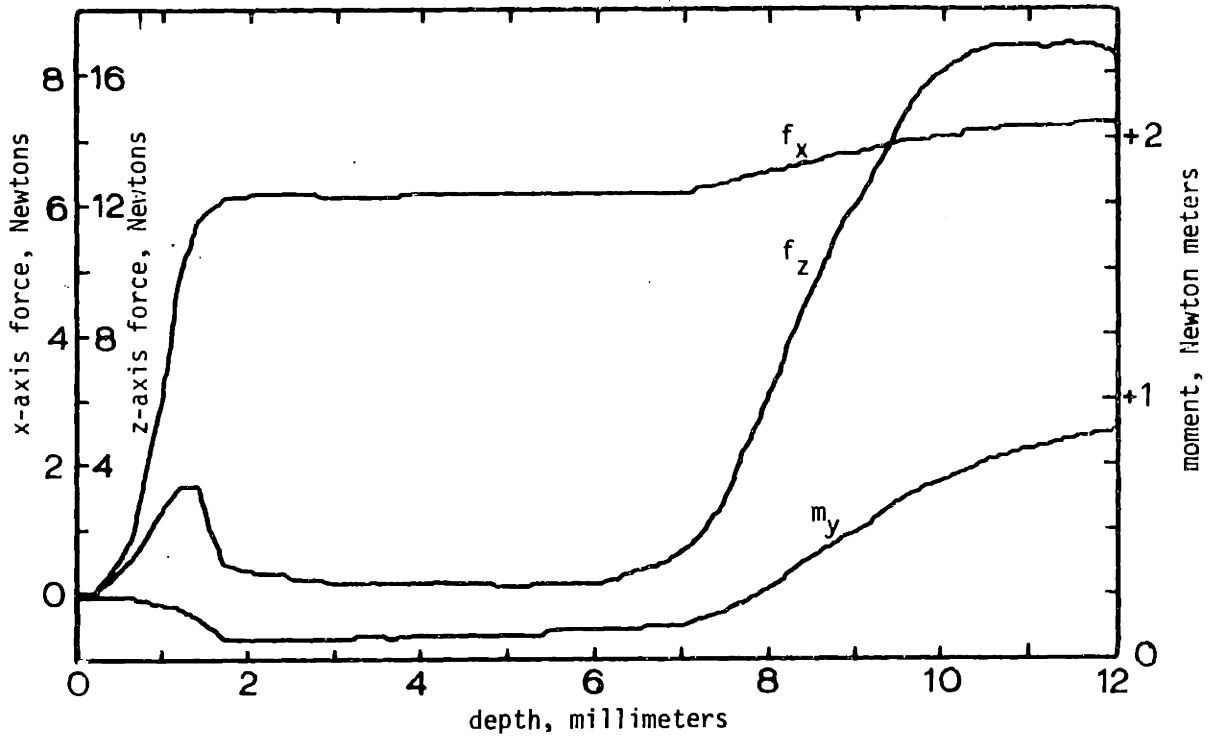


Figure 5.9. Force and moment data; insertion of a 35.00 mm diameter hardened steel plug into a 35.02 mm diameter drill bushing, center of compliance at the assembly interface, 0.50 mm x-axis and 5.0 mrad θ_y offset.

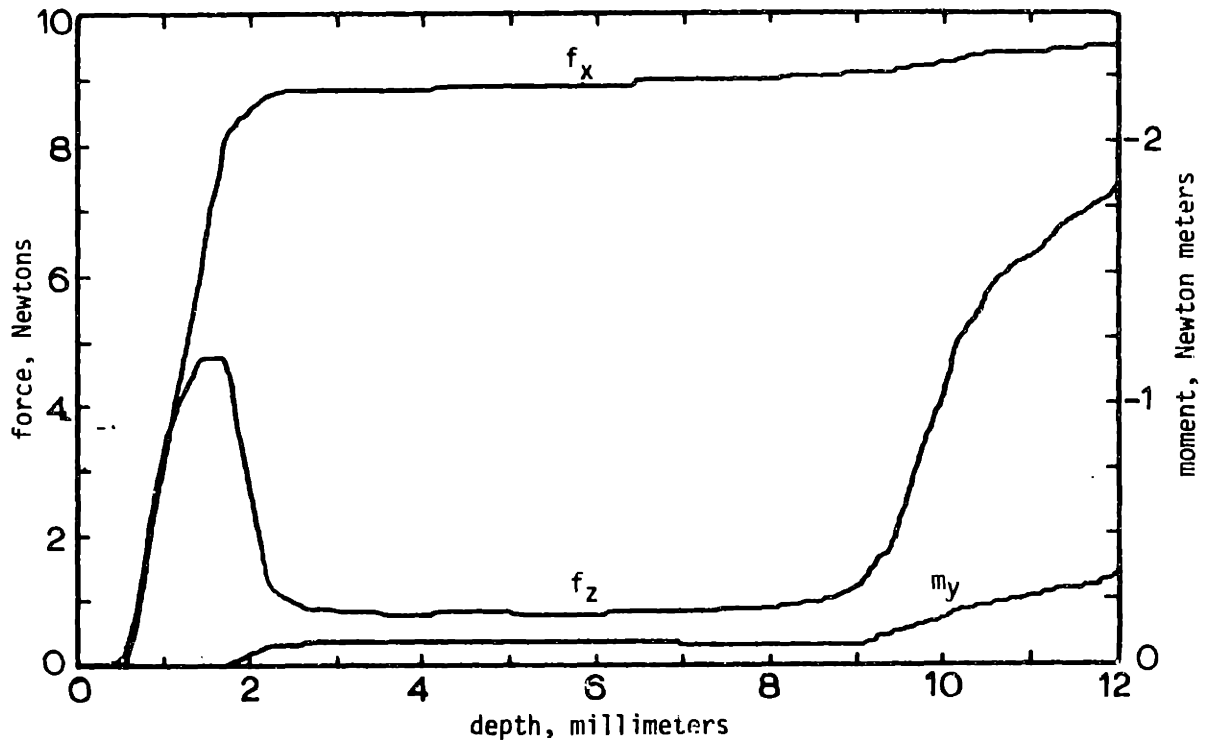


Figure 5.10. Force and moment data; insertion of a 35.00 mm diameter hardened steel plug into a 35.02 mm diameter drill bushing, center of compliance +50 mm from the assembly interface, 0.75 mm x-axis offset.

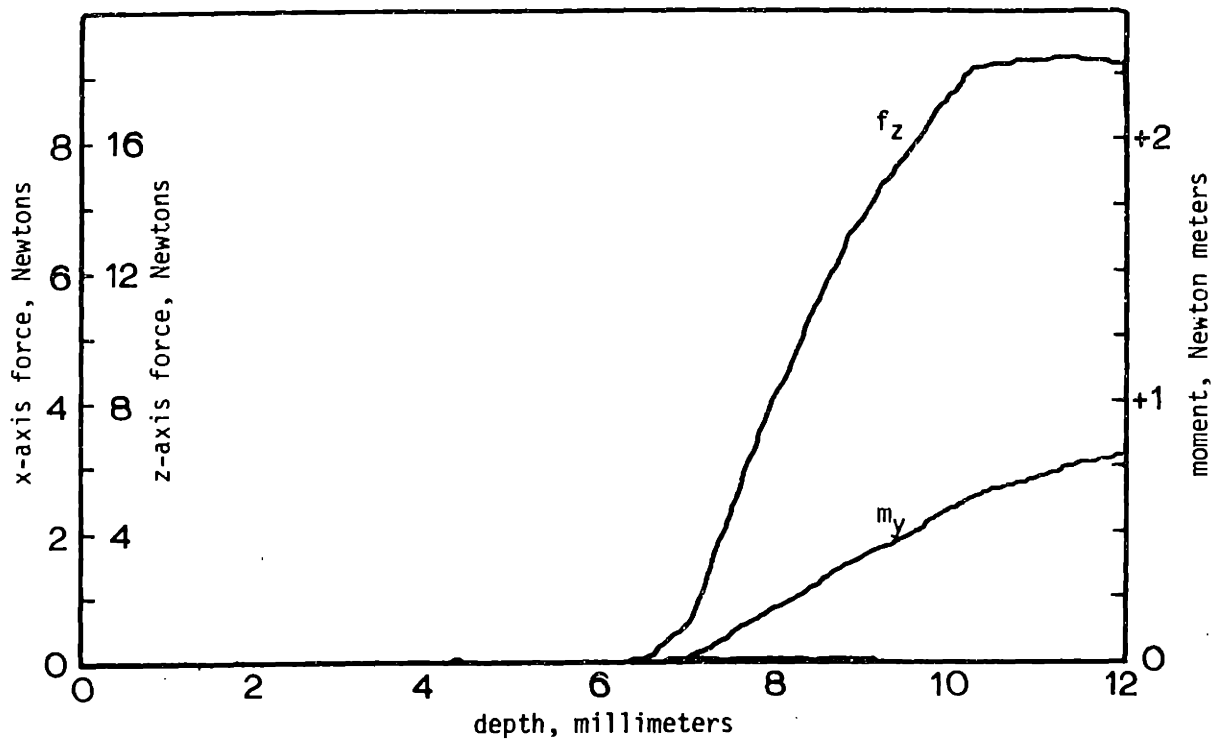


Figure 5.11. Force and moment data; insertion of a 35.00 mm diameter hardened steel plug into a 35.02 mm diameter drill bushing, center of compliance +50 mm from the assembly interface, 5.0 mrad θ_y offset.

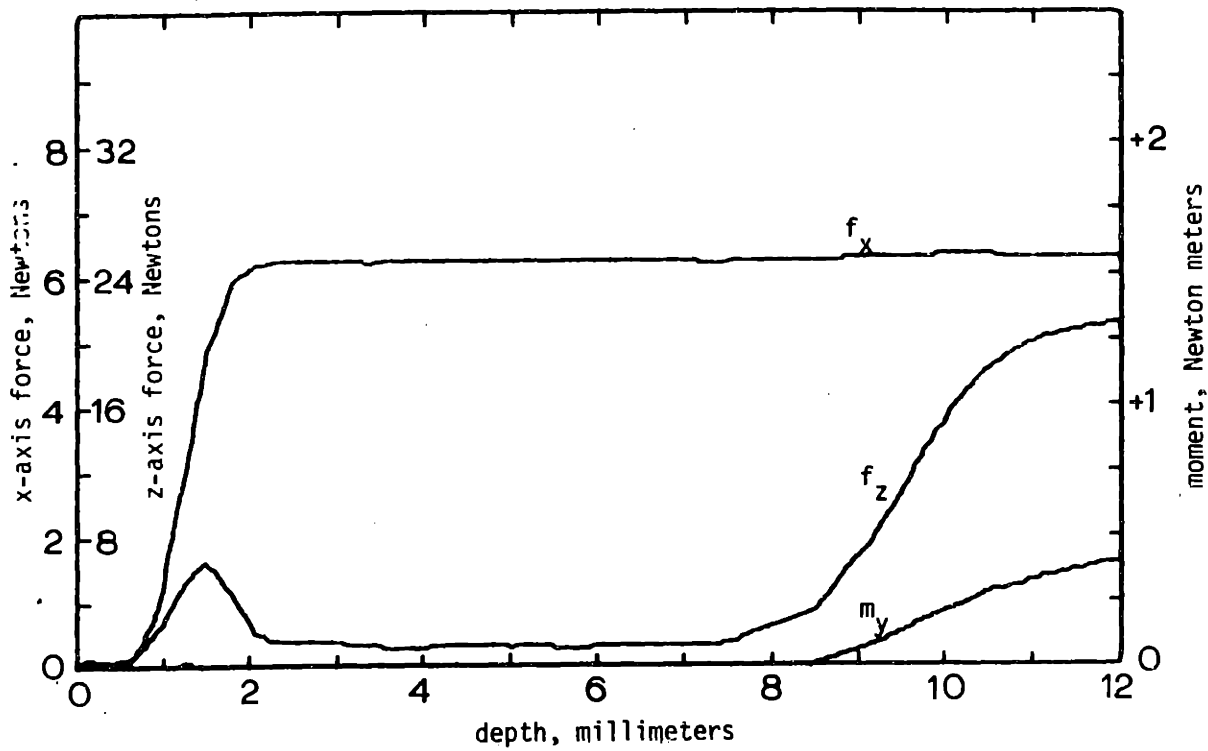


Figure 5.12. Force and moment data; insertion of a 35.00 mm diameter hardened steel plug into a 35.02 mm diameter drill bushing, center of compliance +50 mm from the assembly interface, 0.50 mm x-axis and 5.0 mrad θ_y offsets.

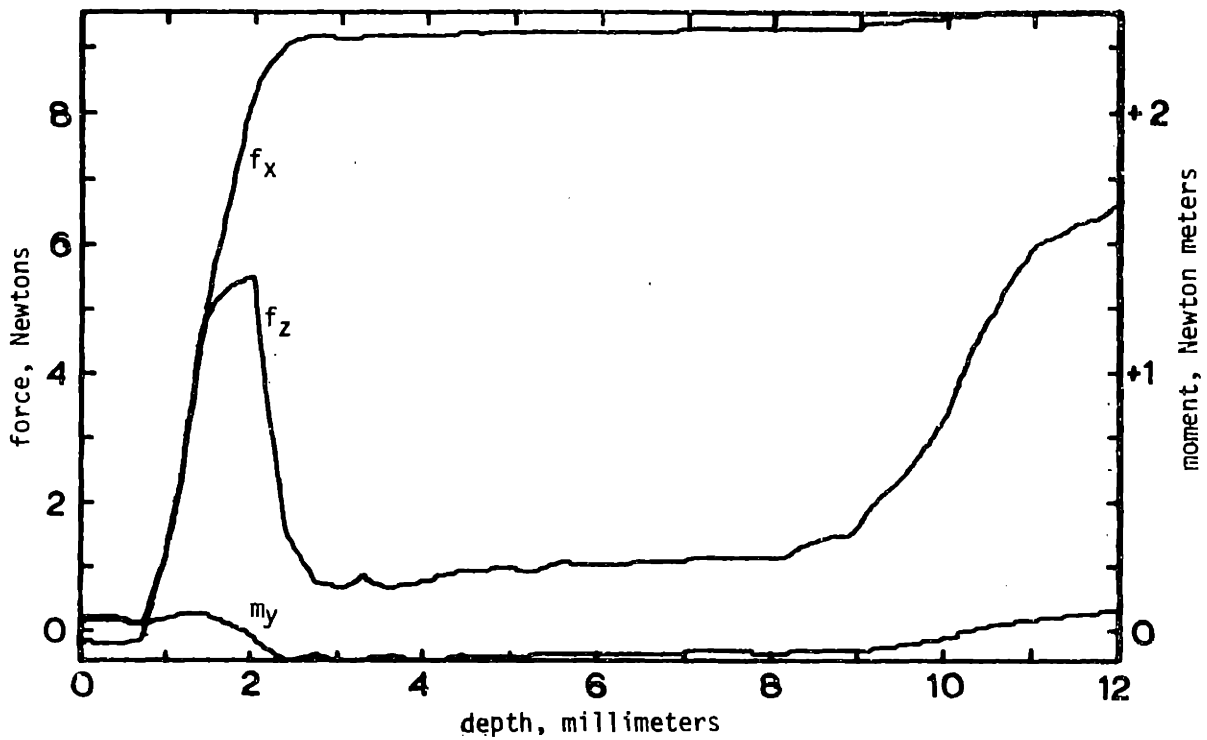


Figure 5.13. Force and moment data; insertion of a 35.00 mm diameter hardened steel plug into a 35.02 mm diameter drill bushing, center of compliance -50 mm from the assembly interface, 0.75 mm x-axis offset.

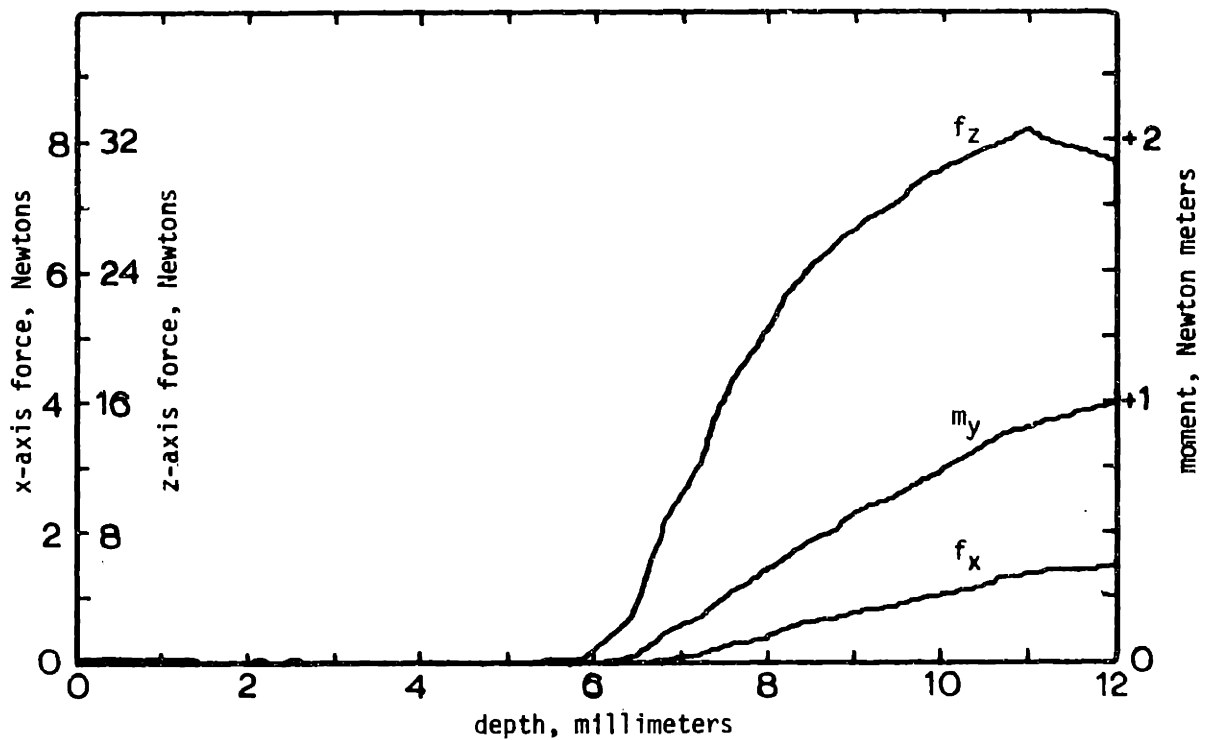


Figure 5.14. Force and moment data; insertion of a 35.00 mm diameter hardened steel plug into a 35.02 mm diameter drill bushing, center of compliance -50 mm from the assembly interface, 5.0 mrad θ_y offset.

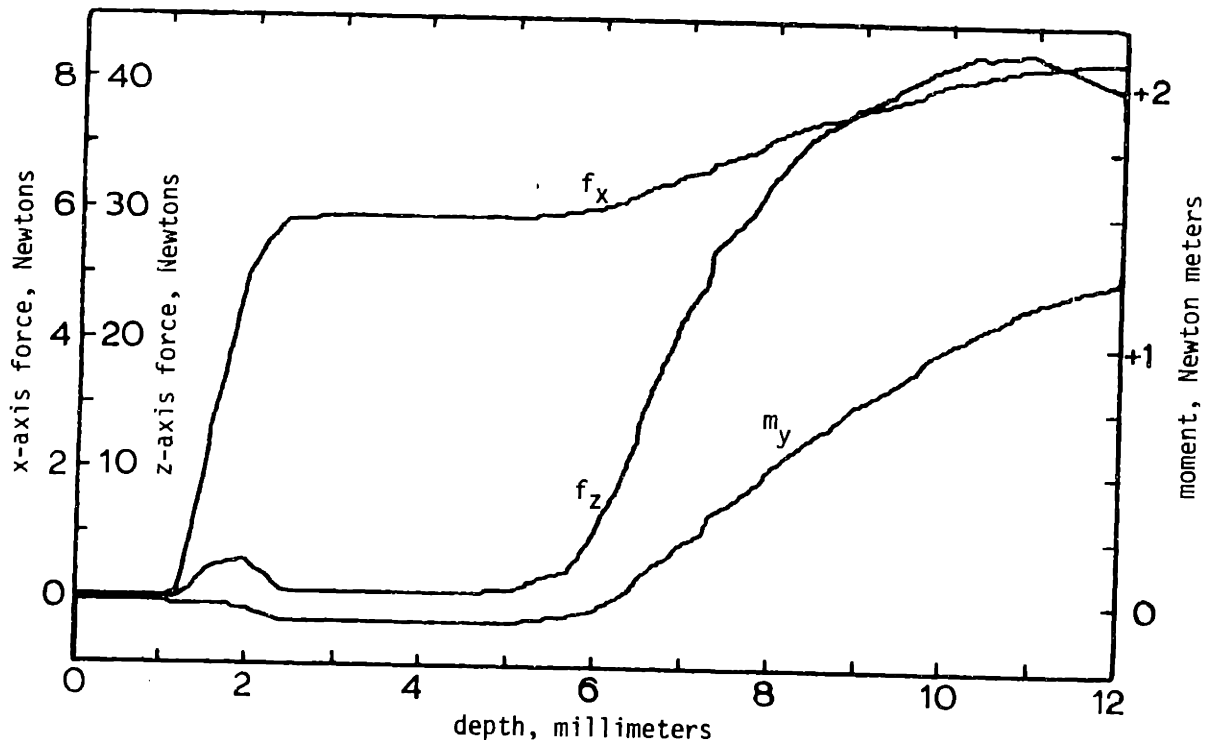


Figure 5.15. Force and moment data; insertion of a 35.00 mm diameter hardened steel plug into a 35.02 mm diameter drill bushing, center of compliance -50 mm from the assembly interface, 0.50 mm x-axis and 5.0 mrad θ_y offsets.

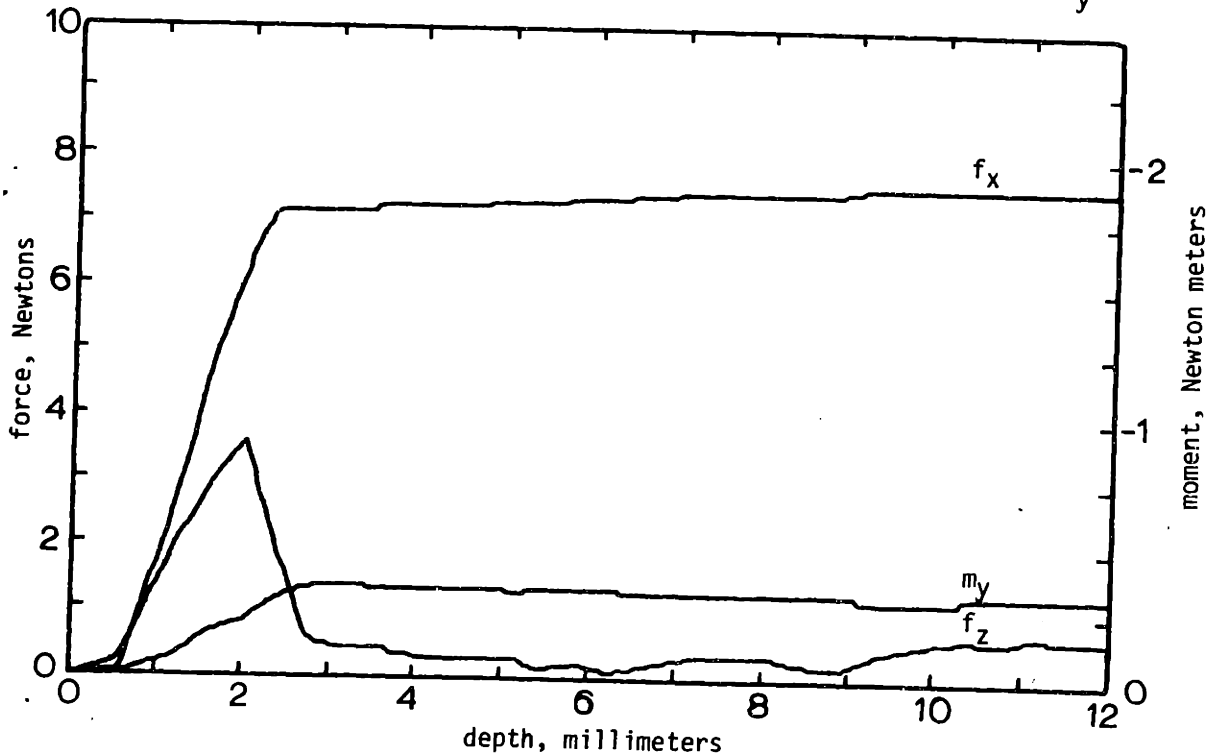


Figure 5.16. Force and moment data; insertion of a ball bearing with a 35.00 mm diameter into a 35.02 mm diameter drill bushing, center of compliance -50 mm from the assembly interface, 0.75 mm x-axis offset.

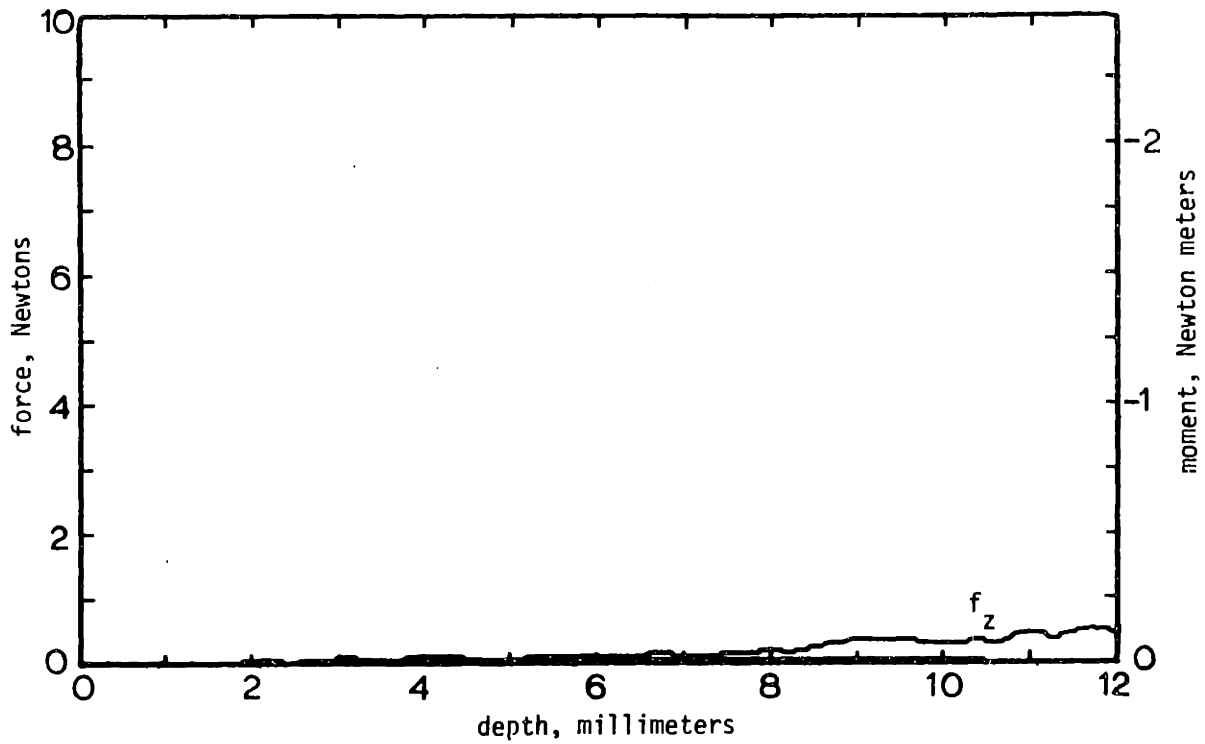


Figure 5.17. Force and moment data; insertion of a ball bearing with a 35.00 mm diameter into a 35.02 mm diameter drill bushing, center of compliance -50 mm from the assembly interface, 5.0 mrad θ_y offset.

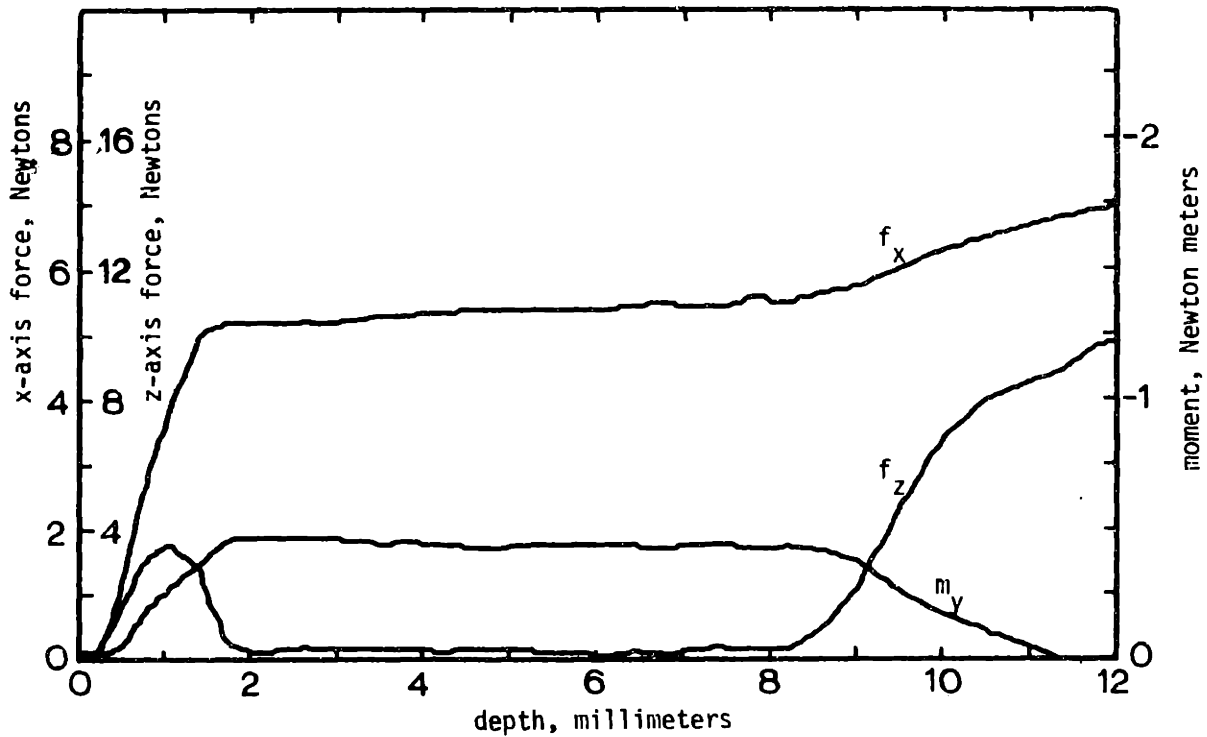


Figure 5.18. Force and moment data; insertion of a 35.00 mm diameter hardened steel plug into a 35.02 mm diameter drill bushing, center of compliance -100 mm from the assembly interface, 0.75 mm x-axis offset.

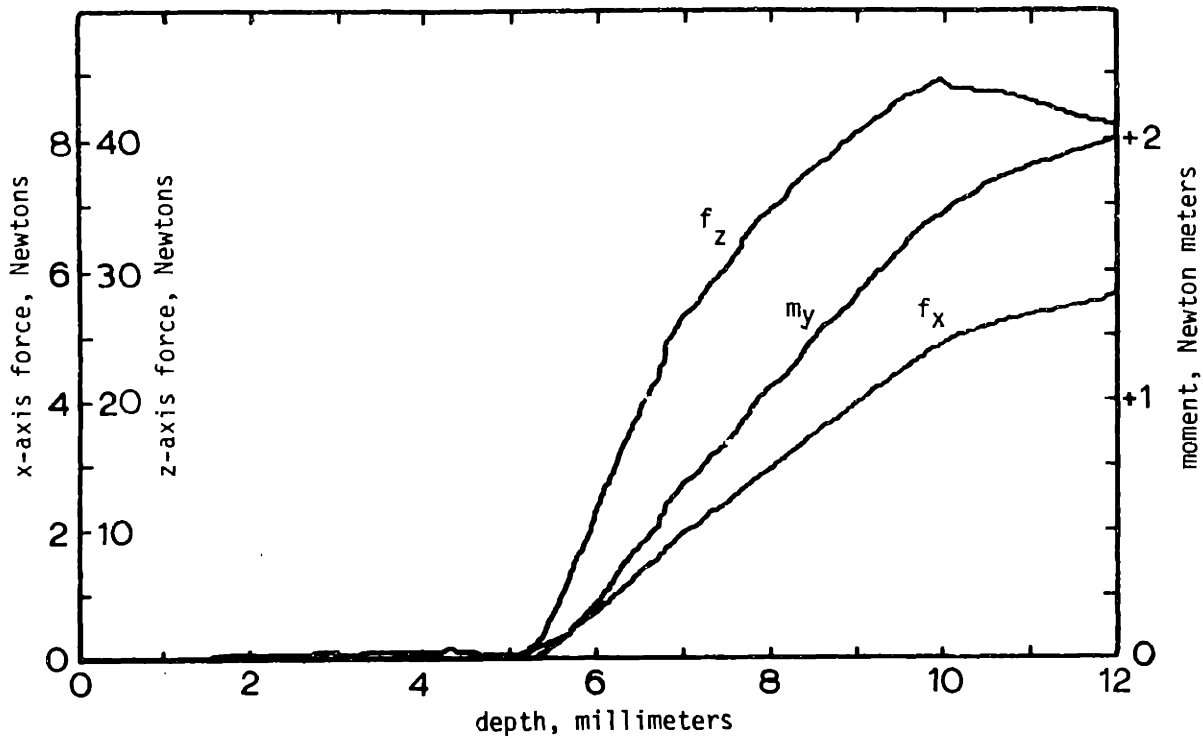


Figure 5.19. Force and moment data; insertion of a 35.00 mm diameter hardened steel plug into a 35.02 mm diameter drill bushing, center of compliance -100 mm from the assembly interface, 5.0 mrad θ_y offset.

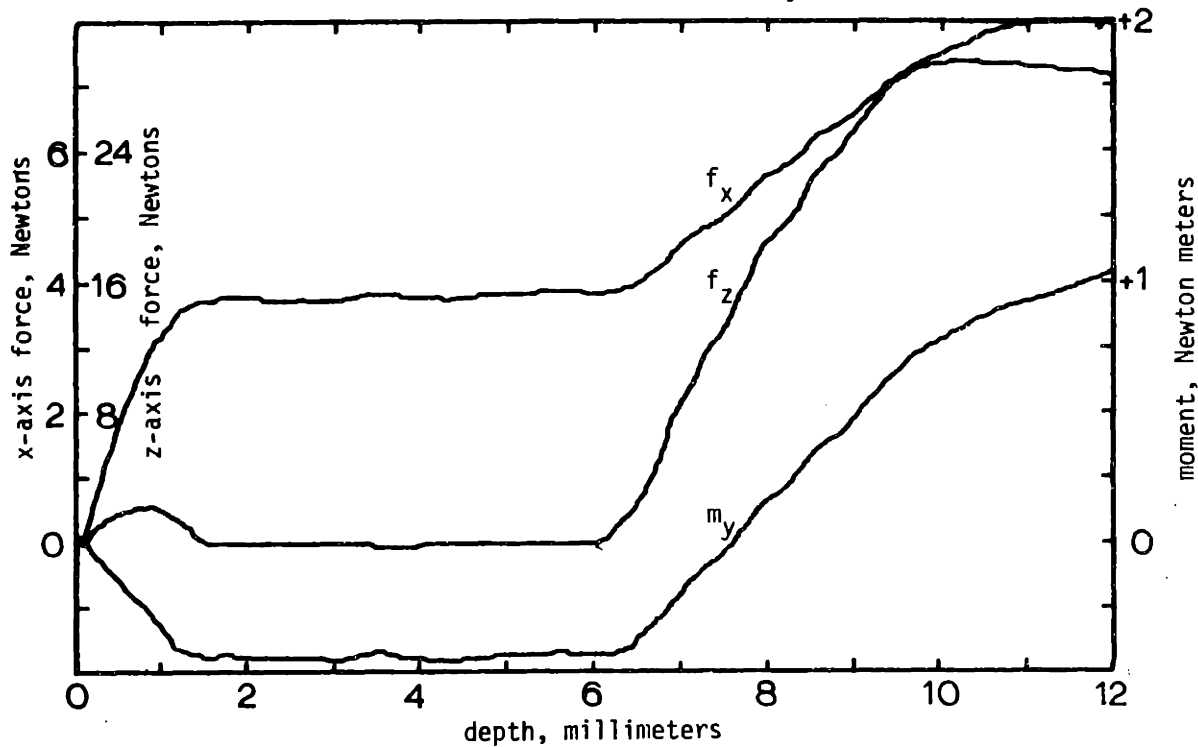


Figure 5.20. Force and moment data; insertion of a 35.00 mm diameter hardened steel plug into a 35.02 mm diameter drill bushing, center of compliance -150 mm from the assembly interface, 0.75 mm x-axis offset.

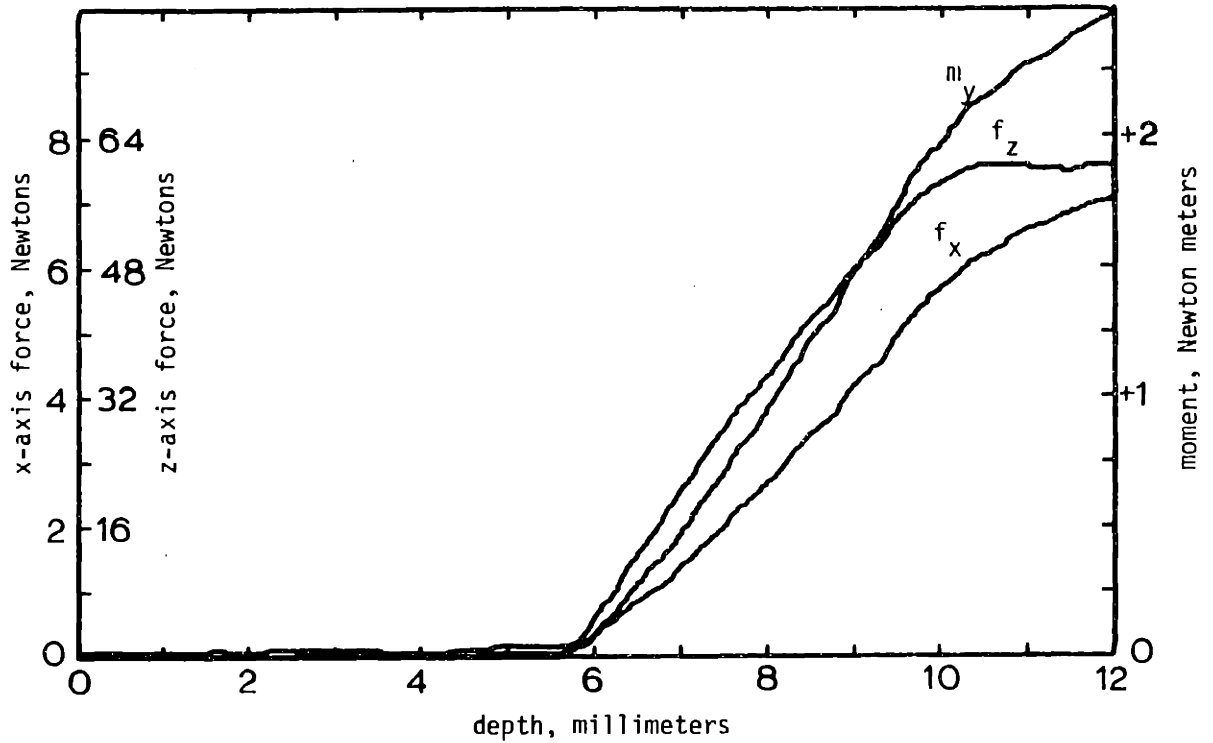


Figure 5.21. Force and moment data; insertion of a 35.00 mm diameter hardened steel plug into a 35.02 mm diameter drill bushing, center of compliance -150 mm from the assembly interface, 5.0 mrad θ_y offset.

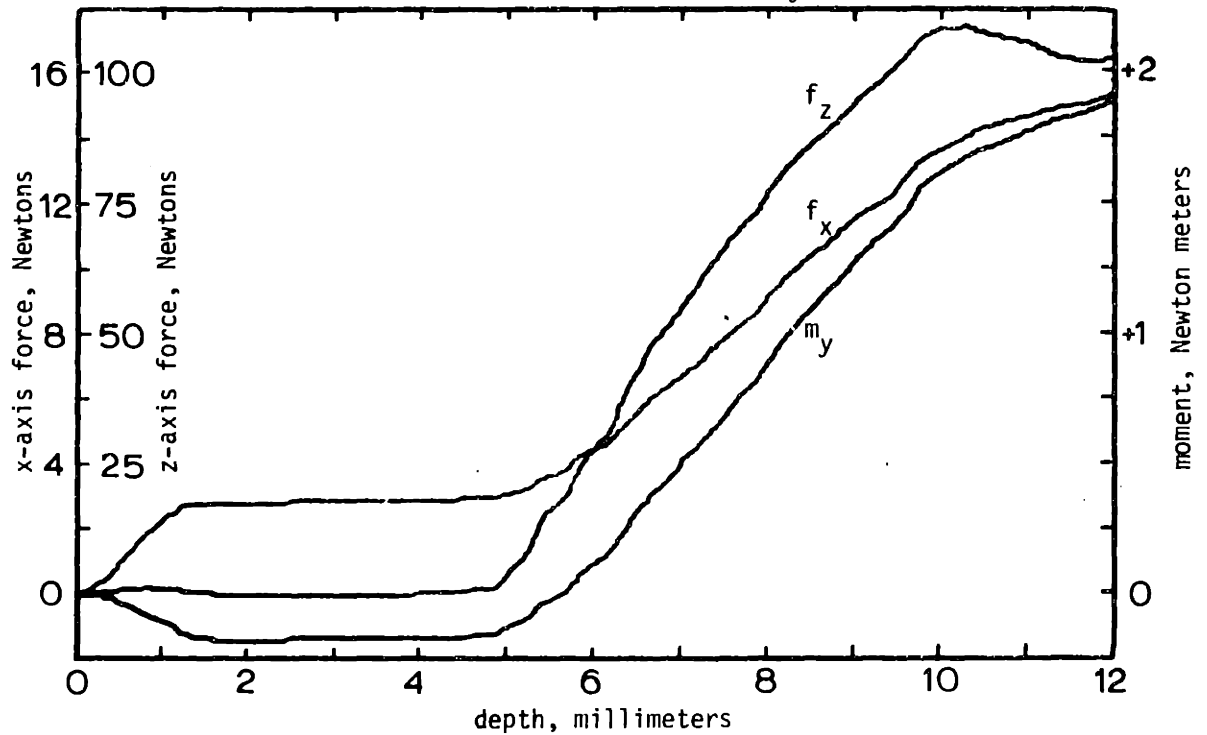


Figure 5.22. Force and moment data; insertion of a 35.00 mm diameter hardened steel plug into a 35.02 mm diameter drill bushing, center of compliance -150 mm from the assembly interface, 0.75mm x-axis and 5.0 mrad θ_y offsets.

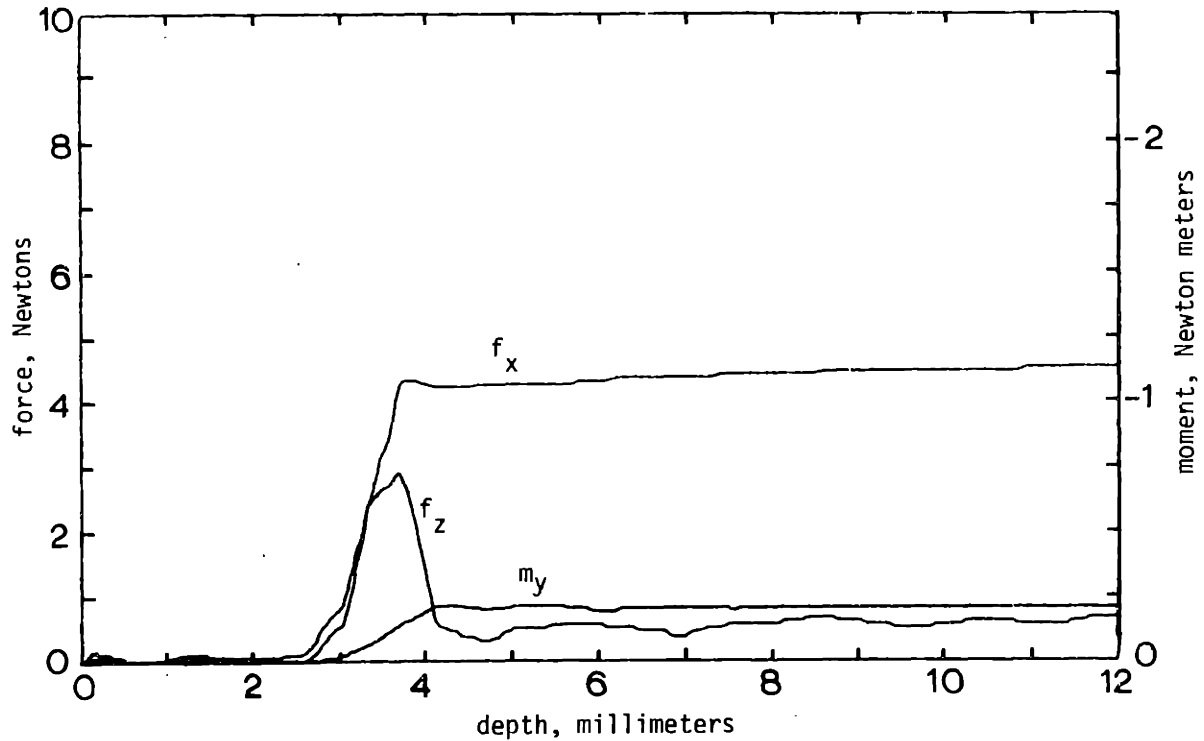


Figure 5.23. Force and moment data; insertion of a ball bearing with a 40 mm outer diameter into an alternator housing with a burnished hole, 0.5 mm x-axis offset.

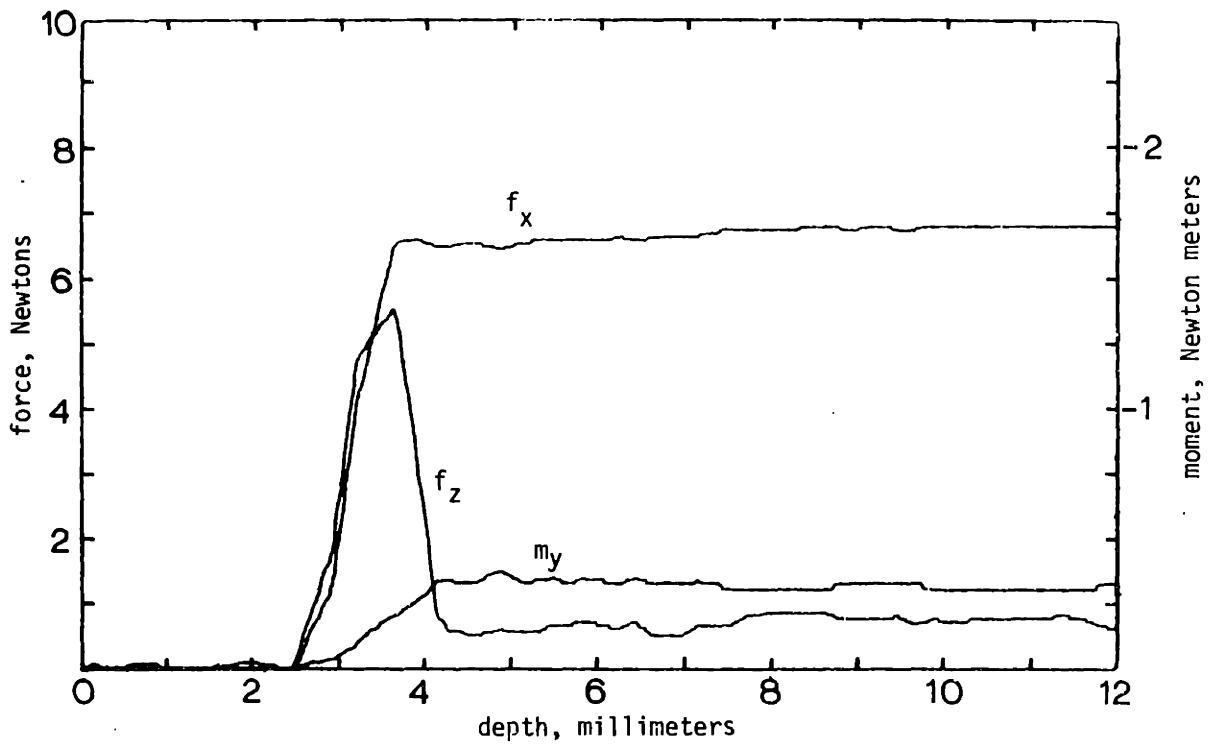


Figure 5.24. Force and moment data; insertion of a ball bearing with a 40 mm outer diameter into an alternator housing with a burnished hole, 0.75 mm x-axis offset.

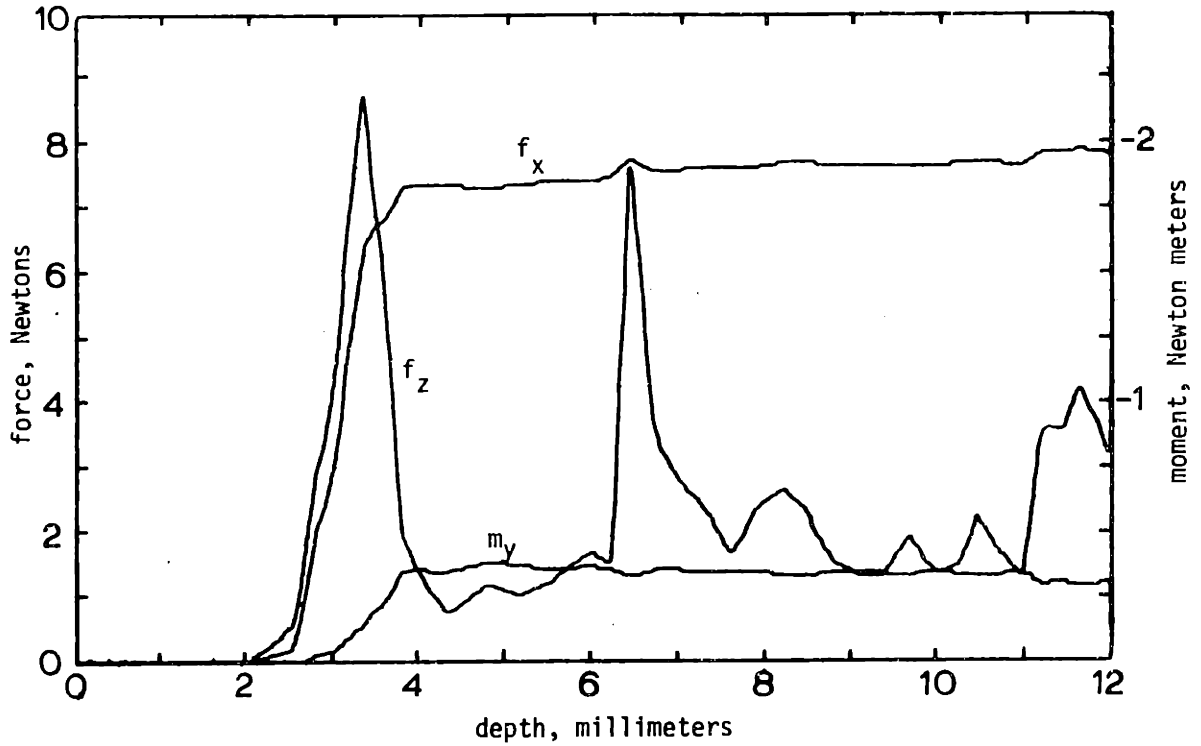


Figure 5.25. Force and moment data; first insertion of a ball bearing with a 40 mm outer diameter into a new alternator housing, 0.75 mm x-axis offset.

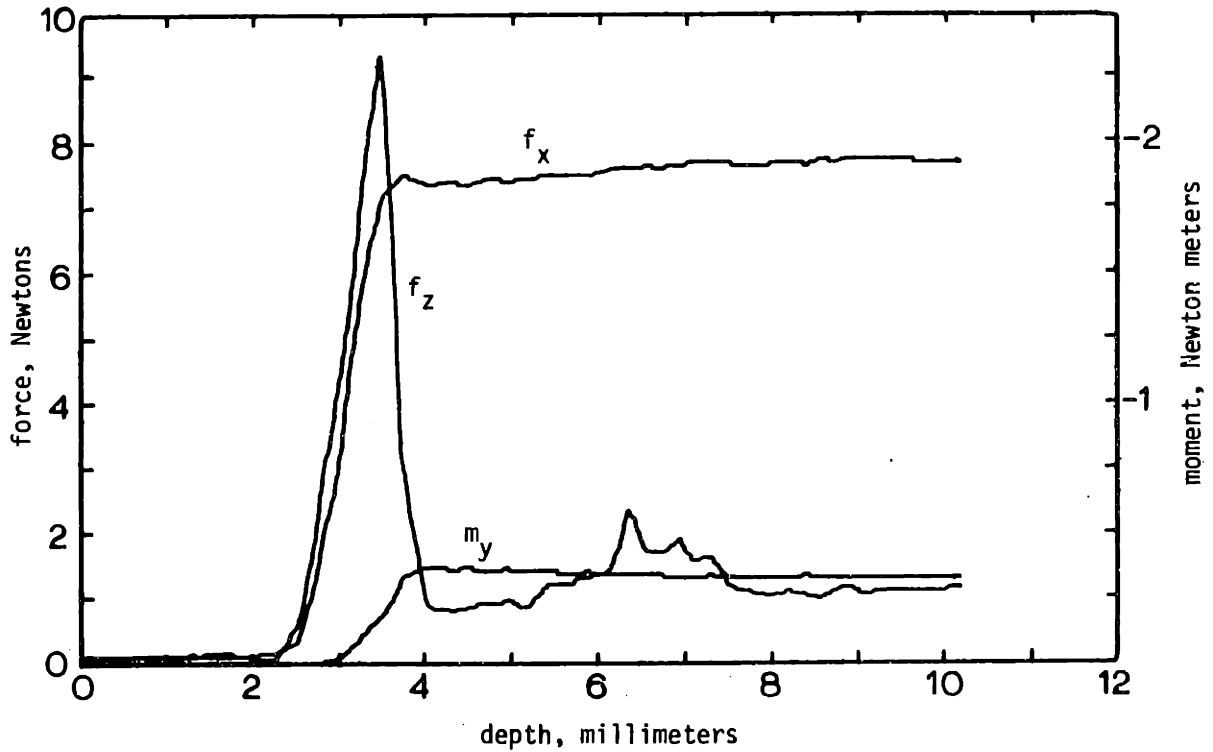


Figure 5.26. Force and moment data; second insertion of a ball bearing with a 40 mm outer diameter into a new alternator housing, 0.75 mm x-axis offset.

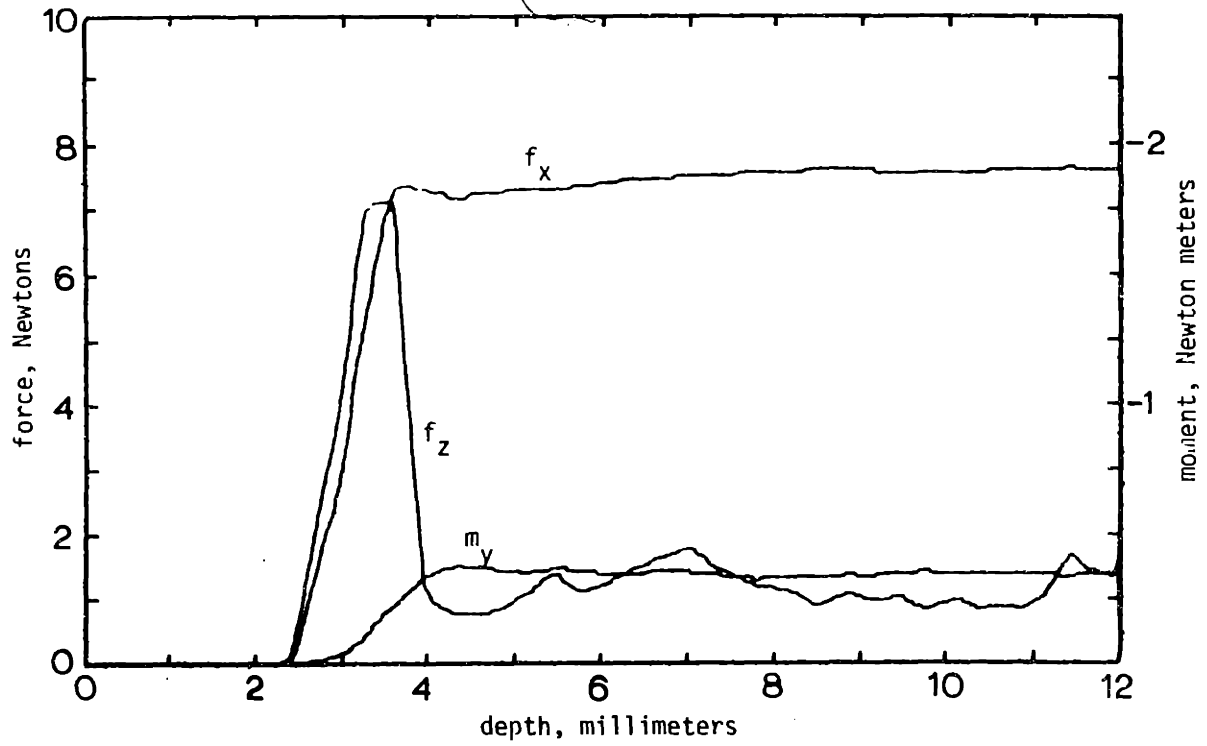


Figure 5.27. Force and moment data; third insertion of a ball bearing with a 40 mm outer diameter into a new alternator housing, 0.75 mm x-axis offset.

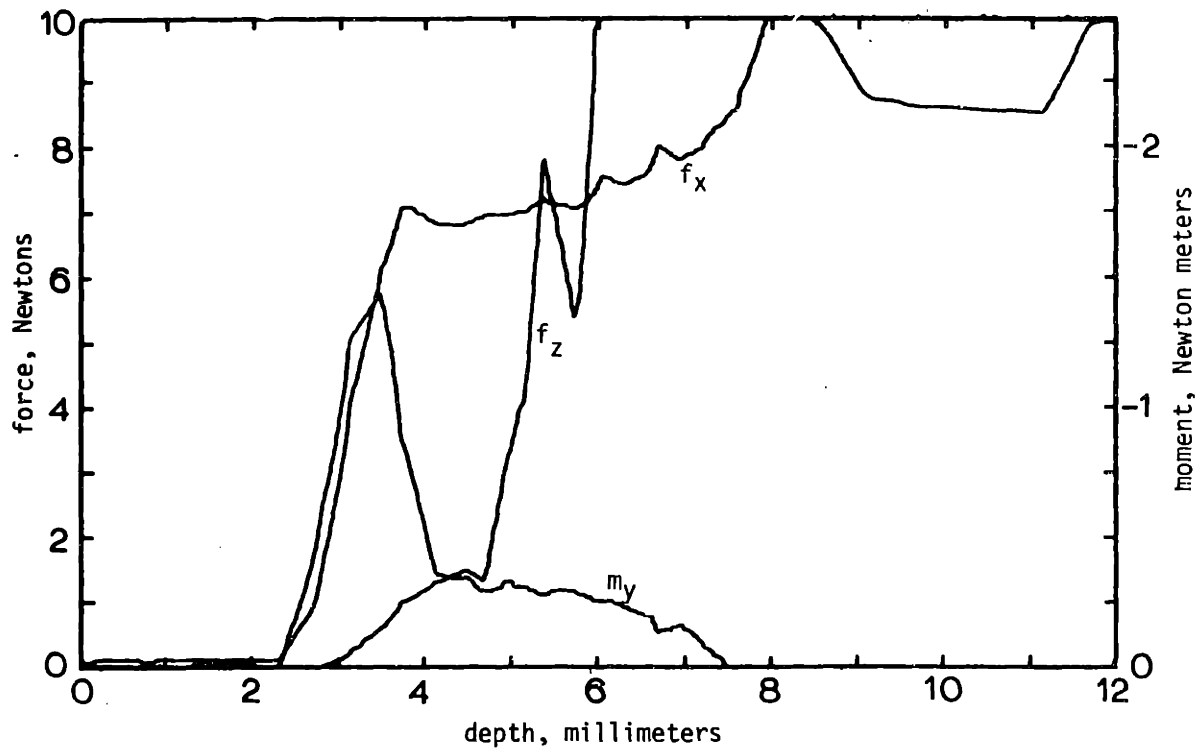


Figure 5.28. Force and moment data; first insertion of a ball bearing with a 40 mm outer diameter into a new alternator housing, 0.75 mm x-axis offset.

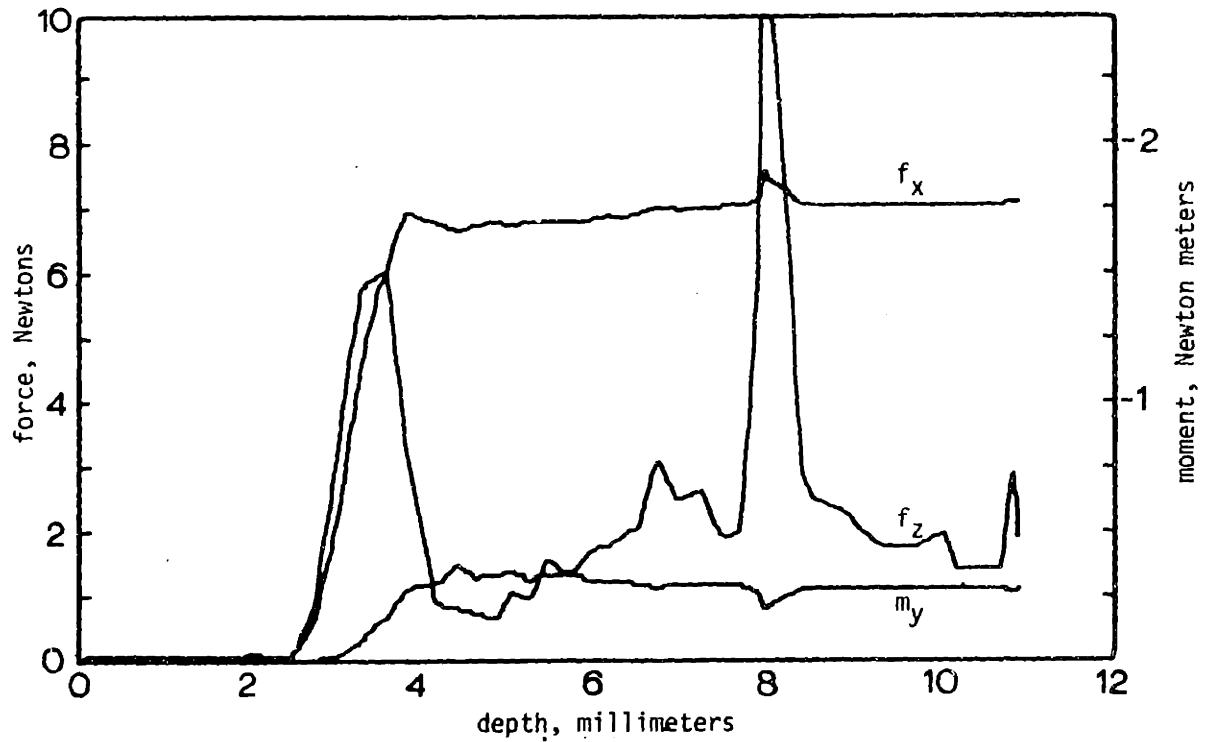


Figure 5.29. Force and moment data; second insertion of a ball bearing with a 40 mm outer diameter into a new alternator housing, 0.75 mm x-axis offset.

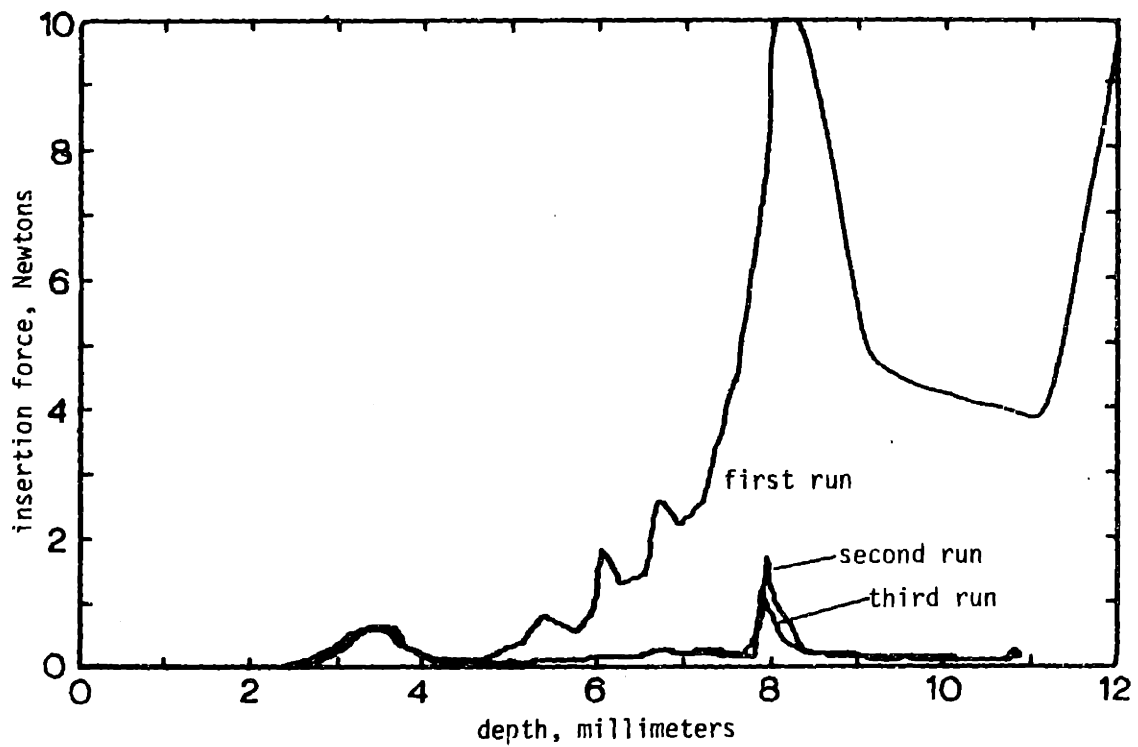


Figure 5.30. Insertion forces for the first three insertions of a ball bearing with a 40 mm outer diameter into a new alternator front housing.

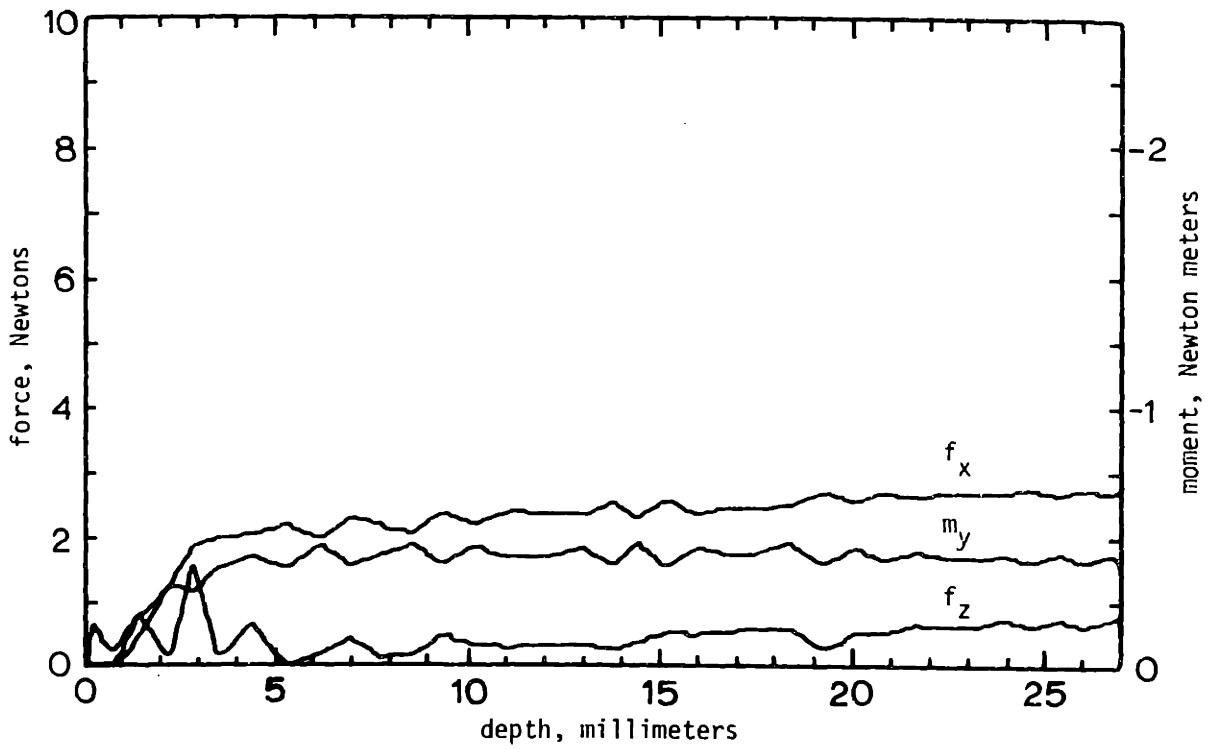


Figure 5.31. Force and moment data; insertion of a well-polished alternator rotor shaft into a 17 mm ball bearing, 0.75 mm x-axis offset.

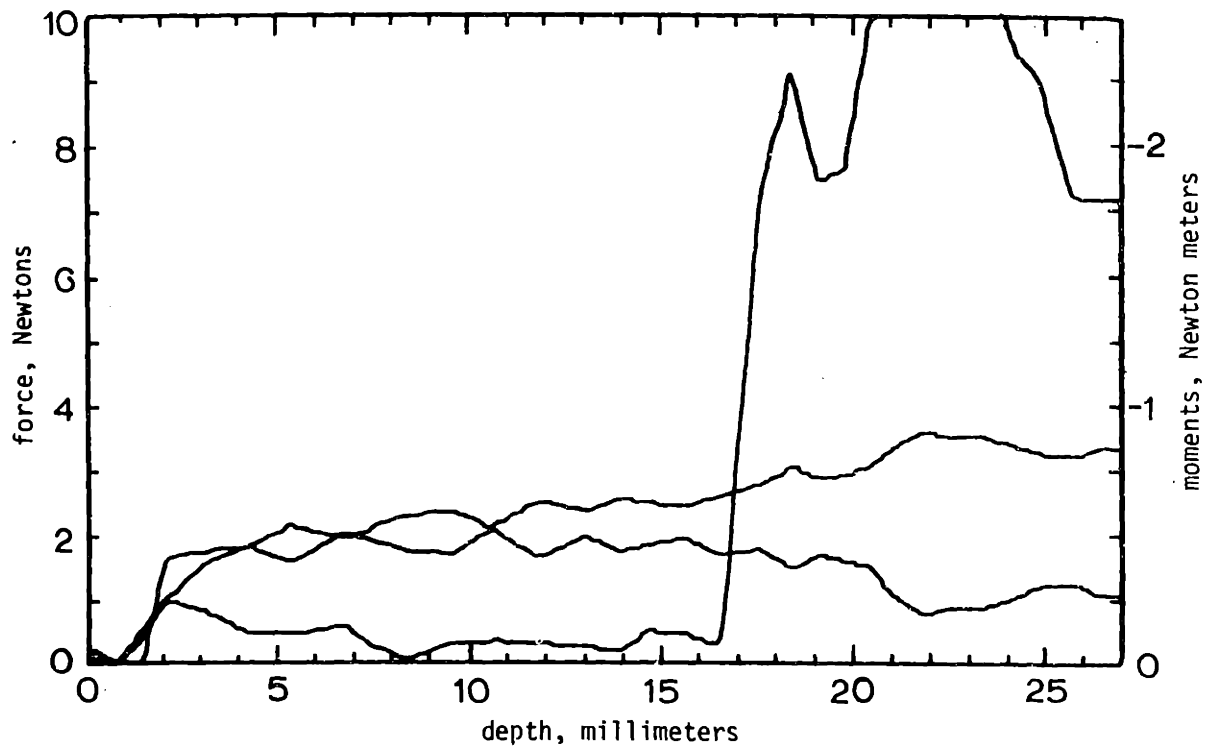


Figure 5.32. Force and moment data; first insertion of a new alternator rotor shaft into a 17 mm ball bearing, 0.75 mm x-axis offset.

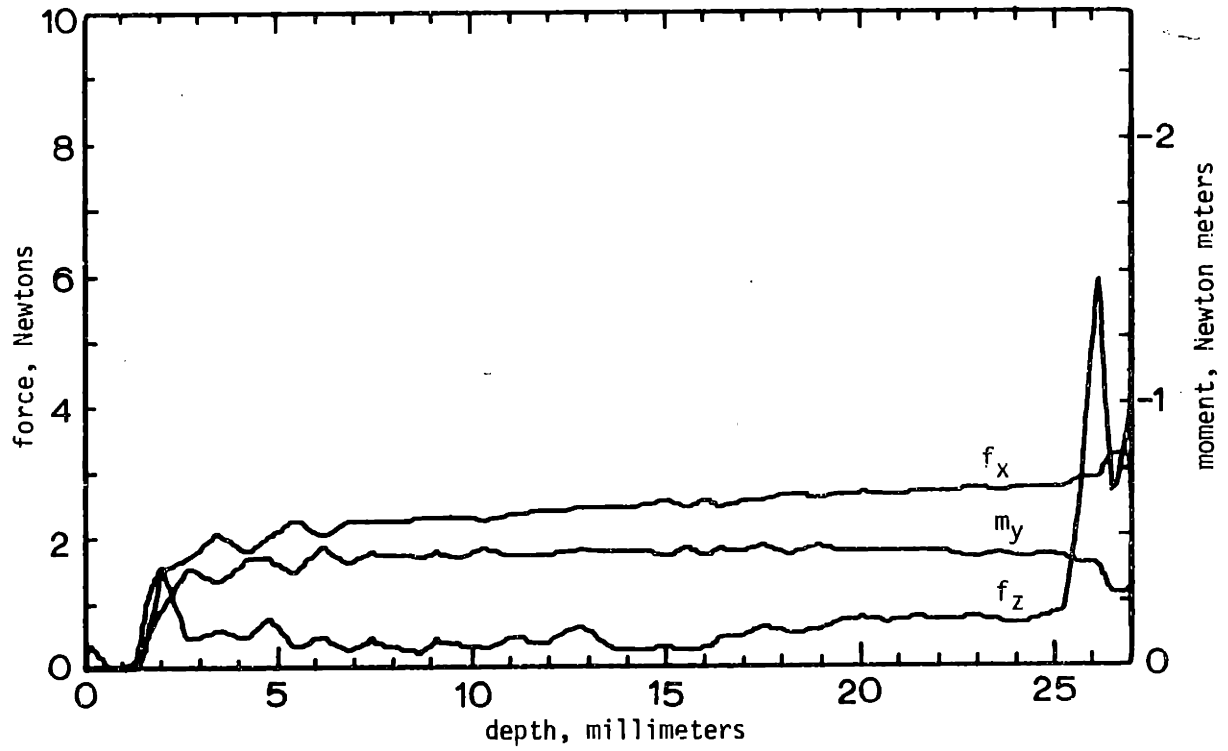


Figure 5.33. Force and moment data; second insertion of a new alternator rotor shaft into a 17 mm ball bearing, 0.75 mm x-axis offset.

6. CONCLUSIONS AND RECOMMENDATIONS

Conclusions are drawn from three sets of experiments: first, from the assembly force and moment measurement experiments using the system with the cantilever beam compliance; second, from later assembly force and moment measuring experiments using the system with a deformable structure compliance; and, third, from assembly experiments using the second system on the programmable assembly machine. A number of conclusions from the experiments using the first system were incorporated into the design of the second compliance system.

6.1. Conclusions from Experiments Using the Cantilever Beam Compliance

The first compliance system was used successfully to insert a series of close-fitting shafts into a hole with varying initial lateral and angular errors, thus demonstrating the use of compliance for automatic assembly. In the absence of two-point contact, the forces for a typical insertion were quite low. With two-point contact, the lateral force, the insertion force, and the moment rose rapidly although jamming was not observed.

Requiring that two-point contact not occur during the insertion places fairly severe restrictions on the permissible angular errors between the parts and on the required clearance between the parts. Therefore, while the first compliance system worked, it was not the optimum design for the assembly of parts with close fits or with large positional errors and, in particular, large angular errors. It was concluded that a better design would be a device that yielded lateral displacements in response to lateral forces at the assembly interface and yielded rotational displacement in response to moments at the assembly interface. That is, the center of compliance should be at or near the assembly interface and the device should be both laterally and rotationally compliant. As designed, the cantilever beam compliance had a center of compliance approximately 200 millimeter (7.9 inches) from the assembly interface and had virtually no lateral compliance.

The data taken during the experiments are clean and repeatable. The separate phases of chamfer crossing, single-point contact, and two-point contact are clearly

discernible. During single-point contact, the lateral force is proportional to the lateral error. Once two-point contact has occurred, the moment data is unambiguous and proportional to the angular error. Therefore the data could have been used to servo the arm to minimize the forces caused by two-point contact. Although this was not done, the data was used successfully to simulate force feedback by manually removing random unknown lateral and angular errors during experiments using the milling machine.

6.2. Conclusions from Experiments Using the Deformable Structure Compliance

The second compliance system was used successfully to assemble close-fitting parts from an automobile alternator (nominal clearance of 0.01 mm or 0.0004 inch) both during experiments measuring quasi-static assembly forces and during experiments assembling the parts with a four-axis programmable assembly machine. The insertion of a ball bearing into an alternator housing using the assembly machine was accomplished in approximately 0.2 seconds, the speed of the insertion being limited by the dynamics of the assembly machine, not the compliance system. Using this system, the entire final assembly of the alternator (17 parts) was accomplished in approximately 2 minutes and 30 seconds. The second compliance system was also used successfully to insert a hardened and ground steel test plug into a drill bushing during force and moment measuring experiments using the milling machine. This test of the apparatus is more stringent because the test plug does not have the angular compliance exhibited by the ball bearing.

The assembly force data from insertion of the steel test plug into the drill bushing confirms the prediction of the quasi-static theory that the forces and moments for a given positional error will be minimized when the assembly interface is at or near the center of compliance. The jamming theory predicts that the optimum placement for the center of compliance is the intersection of the reaction force vectors for the initial two-point contact (point I in Figure 3.4). However, for the nominal compliance values, clearances, and positional offsets used in the experiments in this thesis, the exact placement is not critical.

Varying the placement of the assembly interface ± 50 mm (± 2.0 inch) with respect to the center of compliance did not cause the insertion force during any of the tests with the steel plug to exceed twice the maximum value obtained during similar tests with the assembly interface located at the center of compliance. As a radial ball bearing has sufficient angular compliance to cause the effective center of compliance to be near the assembly interface, the location of the center of compliance of the deformable structure is relatively unimportant for the insertion of the ball bearing into the alternator housing or the insertion of the rotor into the ball bearing. The insertion of the ball bearing and the insertion of the rotor are also insensitive to angular offsets. This fact is demonstrated in Figure 5.28.

The assembly forces for parts with smooth surfaces were close to the predicted values. However, for parts with machining marks and small burrs, the forces varied considerably, particularly for the first insertion (for most assembly operations, only the first insertion is important).

Using a properly engineered compliance system for automatic assembly instead of using force feedback or active accommodation has a number of important advantages. A force sensor is not required nor is any additional computational power required. As the compliant structure or mechanism allows small corrective motions, many assembly operations can be performed using a programmable assembly machine with fewer than six degrees of freedom (generalized force feedback requires a minimum of six active degrees of freedom). The speed at which the assembly can be accomplished is limited only by the impact dynamics and the speed of the assembly machine.

The only disadvantages of using compliance instead of force feedback are that chamfered edges are required to provide the lateral forces to obtain an initial alignment and that the compliance parameters can not be varied during the assembly or parts mating (with active force feedback, it is possible to vary the servo gains). However, with the compliance-locking mechanism activated, the system is held rigid. This allows the compliance system which otherwise has a low natural frequency to be positioned using high velocities and accelerations.

While the compliance system was developed for use in programmable automatic assembly, it could also be used in conjunction with transfer-line or fixed automation. Using compliance, it should be possible to reduce the design, tolerance, alignment, and debugging requirements and to perform tasks that could not otherwise be performed automatically due to tolerance stack-up problems.

6.3. Recommendations for Further Work

Further work would be useful in several different areas. In the mechanical design area, the compliance device should be redesigned to increase the strength while retaining or increasing the present compliance values. This can be easily accomplished by increasing the length of the compliant members. It would be preferable, however, to keep the system compact. It also would be desirable to design a compliance system with damping. Because energy is dissipated with friction and during impacts with coefficients of restitution less than unity, the damping is not normally needed during the assembly or parts mating. However, prior to the insertion, it is possible to excite the compliance device with the assembly machine, with operating the tools, and with operating the compliance lock. Added damping would help to alleviate this problem. A compliance system with damping could possibly be used without a compliance lock on transfer lines or fixed automatic machines for simple vertical insertions.

There is also interest in using compliance to aid in performing assembly operations with interference, or force, fits. A compliance system needs to be designed that will withstand the higher force loadings necessary for interference fits. The accuracy of the location of the center of compliance will be more important for interference fits.

The present system requires that one or both of the parts be chamfered to start the insertion or assembly operation. A simple passive technique not involving a search is needed that will start the insertion without chamfers when the positional errors are larger than the clearance but still small compared to the diameter of the hole.

A more complete theoretical model of impact interaction should be developed. Higher insertion speeds are not needed for the present programmable assembly machine but might be desirable if the device was used with high-speed fixed automation machinery. The present model treats the impact as an impulse. It would be desirable to model the impact as a force over a finite period of time. The effect of a non-unity coefficient of restitution was modeled, assuming an impulse, but the effects of friction and squeeze film damping were not modeled.

The experimental setup should be modified for dynamic or impact testing to verify the theoretical models or to develop an empirical model. The present setup using a milling machine could be modified by adding a pneumatic piston and a hydraulic speed-check to drive the milling machine quill. A better but more complicated modification would be to add a servo controlled hydraulic drive.

A six-degree-of-freedom actively servoed device capable of making small, high-speed, high resolution motions could be built to be used as a test device. Any generalized compliance could be synthesized using this device. The device also could be used to study active or a combination of active and passive assembly strategies.

REFERENCES

- [1] R.G. Abraham and L.Y. Shum, "Robot-Arc Welder with Contouring Teach Mode", Proceedings of the 5th International Symposium on Industrial Robots, Chicago, Illinois, Sept. 1975, pp. 239-258.
- [2] R.G. Abraham, et.al., "Programmable Assembly Technology Transfer to Industry", Project Reports, NSF Grant ISP 76-24164.
- [3] R.G. Abraham, R.J.S. Stewart, L.Y. Shum, "State-of-th-Art in Adaptable-Programmable Assembly Systems", NSF Grant ISP 76-24164, May 1977.
- [4] J.S. Albus and J.M. Evans, "Robot Systems", Scientific American, Vo. 234, No. 2, pp 77-86B, Feb. 1976.
- [5] J.S. Albus and J.M. Evans, "A Hierarchical Structure for Robot Control", Proceedings of the 5th International Symposium on Industrial Robots, Chicago, Illinois, Sept. 1975, pp. 231-238.
- [6] T.O. Binford, D.D. Grossman, E. Miyamoto, R.A. Finkle, B.E. Shimano, M.S. Mujtaba, and T.A. Gafford, "Exploratory Study of Computer Integrated Assembly Systems", Second Project Report, Sept. 1974 to Nov. 1975, NSF Grant APR 74-0139A04, Artificial Intelligence Laboratory, Stanford University.
- [7] T.O. Binford, D.D. Grossman, C.R. Liu, R.C. Bolles, R.A. Finkle, M.S. Mujtaba, M.D. Roderick, B.E. Schimano, R.H. Taylor, R.H. Grossman, J.P. Jarvis, V.D. Scheinman, and T.A. Gafford, "Exploratory Study of Computer Integrated Assembly Systems", Third Project Report, Dec. 1975 to July 1976, NSF Grant APR 74-0139A04, Artificial Intelligence Laboratory, Stanford University.
- [8] J. Birk, R. Kelley, D. Seres, R. Brand, N. Chen, K. Silvestro and L. Wilson, "Robot Computation for Orienting Workpieces," First Project Report April 1975, NSF Grant APR 74-13935, University of Rhode Island.
- [9] J. Birk, R. Kelley, V. Badami, R. Brand, N. Chen, D. Seres, R. Silva, and L. Wilson, "Robot Computation for Orienting Workpieces", Second Project Report, Dec 1975 to Aug 1976, NSF Grant APR 74-13935, University of Rhode Island.

- [10] R.C. Bolles and R. Paul, "The Use of Sensory Feedback in a Programmable Assembly System", Stanford University, Artificial Intelligence Laboratory Memo, AIM-220, Oct. 1973.
- [11] G. Boothroyd, et.al., Handbook on Feeding and Orienting Parts, University of Massachusetts, 1975.
- [12] G. Boothroyd, C. Poli, and L.E. Murch, "Group Technology Applied to the Automatic Handling of Small Parts", Fourth NSF/RANN Grantees' Conference on Production Research and Technology, IIT Research Institute, Chicago, Illinois, Nov 1976, pp 105-112.
- [13] A. d'Auria and M. Salmon, "SIGMA - An Integrated General Purpose System for Automatic Manipulation", Proceedings of the 5th International Symposium on Industrial Robots, Chicago, Illinois, Sept 1975, pp. 185-202.
- [14] S.H. Drake, "Proposed Experiment to Either Prove or Disprove the Need for a Servoed Small Motion Device", CS Draper Laboratory, MAT Memo #319, April 1975.
- [15] S.H. Drake, P.C. Watson, and S.N. Simunovic, "High Speed Robot Assembly of Precision Parts Using Compliance Instead of Sensory Feedback", to be presented at the 7th International Symposium on Industrial Robots, Tokyo, Japan, Oct. 1977.
- [16] T. Goto, T. Inoyama, and K. Takeyasu, "Precise Insert Operation by Tactile Controlled Robot "HI-TI-HAND" Expert 2", Proceedings of the 4th International Robots, Tokyo, Japan, Nov. 1974, pp 209-218
- [17] T. Goto, T. Inoyama and K. Takeyasu, "Precision Insertion Control Robot and Its Application", presented at the 14th Biennial ASME Mechanism Conference, Montreal, Canada, Sept 1976.
- [18] R.C. Groome, "Force Feedback Steering of a Teleoperator System", SM Thesis, MIT, Department of Aeronautics and Astronautics, Aug. 1972.
- [19] W.B. Heginbotham, C.J. Page, and A. Pugh, "Robot Research at the University of Nottingham," Proceedings of the 4th International Symposium on Industrial Robots, Tokyo, Japan, Nov. 1974, pp. 53-64.

- [20] H. Inoue, "Force Feedback in Precise Assembly Tasks", Artificial Intelligence Laboratory, Memo No. 308, MIT, Aug 1974.
- [21] P.M. Lynch, "Economic-Technological Modeling and Design Criteria for Programmable Assembly Machines", PhD Thesis, MIT, Department of Mechanical Engineering, June 1976.
- [22] J.L. Nevins, D.E. Whitney, A.E. Woodin, S. Drake, M. Lynch, D. Seltzer, R. Sturges, and P. Watson, "A Scientific Approach to the Design of Computer Controlled Manipulators", C.S. Draper Laboratory Report R-837, ARPA Contract DAH-C-15-73-C-0278, Aug 1974.
- [23] J.L. Nevins, D.E. Whitney, H.J. Doherty, D. Killoran, P.M. Lynch, D.S. Seltzer, S.N. Simunovic, R. Sturges, P.C. Watson, and E.A. Woodin, "Exploratory Research in Industrial Modular Assembly", C.S. Draper Laboratory Report R-800, First Project Report NSF Grant GI-39432X, May 1974.
- [24] J. Nevins, D. Whitney, M. Lynch, S. Simunovic, S. Drake, M. Jilanti, D. Killoran, D. Seltzer, P. Watson, and A. Woodin, "Exploratory Research in Industrial Modular Assembly", C.S. Draper Laboratory Report R-850, Second Project Report NSF Grant APR 74-18173 A01 and GI-39432X, Dec. 1974.
- [25] J. Nevins, D. Whitney, S. Drake, D. Killoran, A. Kondoleon, P. Lynch, S. Simunovic and S. Wang, "Exploratory Research in Industrial Modular Assembly", C.S. Draper Laboratory Research Report R-921, Third Project Report NSF Grant APR 74-18173 A02, Oct. 1975.
- [26] J. Nevins, D. Whitney, S. Drake, D. Killoran, A. Kondoleon, P. Lynch, S. Simunovic and S. Wang, "Exploratory Research in Industrial Modular Assembly", C.S. Draper Laboratory Report R-996, Fourth Project Report, NSF Grant APR 74-18173 A03, Aug. 1976.
- [27] R.J. Roark and W.C. Young, Formulas for Stress and Strain, McGraw-Hill Book Company, New York, 1975, pp 513-522.

- [28] C. Rosen and D. Nitzan et.al., "Exploratory Research in Advanced Automation", Project Reports 1 through 5, NSF Grants GI-38100X and GI-38100X1, Stanford Research Institute, Dec 73 through Jan 76.
- [29] C. Rosen and D. Nitzan, "Programmable Industrial Automation", IEEE Transactions on Computers, Vol. C-25, No. 12, Dec 1976, pp. 1259-1270.
- [30] C. Rosen and D. Nitzan et.al., "Machine Intelligence Research Applied to Industrial Automation", Project Report, NSF Grant APR 75-13074, Stanford Research Institute, Nov 1976.
- [31] G. Schneider, "Entwicklung und Bau einer sich selbst steuernden Roboterhand", Institut für Industrielle Fertigung and Fabrikbetrieb, Der Universität Stuttgart, March 1976.
- [32] K. Seko and H. Toda, "Development and Application Report on the Arc Welding and Assembly Operation by the High Performance Robot", Proceedings of the 4th International Symposium on Industrial Robots, Tokyo, Japan, Nov 1974, pp. 487-596.
- [33] D. Seres, R. Kelley, and J. Birk, "Visual Robot Instruction", Proceedings of the 5th International Symposium on Industrial Robots, Chicago, Illinois, Sept 1975, pp. 113-126.
- [34] S.N. Simunovic, "Force Information in Assembly Processes", Proceedings of the 5th International Symposium on Industrial Robots, Chicago, Illinois, Sept 1975, pp. 415-431.
- [35] S.N. Simunovic, "An Information Approach to Parts Mating", PhD Thesis, MIT Department of Mechanical Engineering, to be presented Spring 1978.
- [36] United States Patent No. 3,828,674, "Automatic Assembly Control Method and Device Therefore", July 23, 1974.
- [37] P.C. Watson and S.H. Drake, "Pedestal and Wrist Force Sensors for Automatic Assembly", Proceedings 5th International Symposium on Industrial Robots, Chicago, Illinois, Sept 1975, pp. 501-511.

- [38] D.E. Whitney, "The Mathematics of Coordination Control of Prosthetic Arms and Manipulators", ASME Journal of Dynamic Systems, Measurement and Control, Dec. 1972, pp. 303-309.
- [39] D.E. Whitney, "Force Feedback Control of Manipulator Fine Motions," Transactions of the ASME, Journal of Dynamic Systems, Measurement and Control, June 1977, pp. 91-97.
- [40] P.M. Will, "Computer Controlled Mechanical Assembly", Proceedings 5th International Symposium on Industrial Robots, Chicago, Illinois, Sept 1975, pp 153-170.
- [41] P.M. Will, and D.D. Grossman, "An Experimental System for Computer Controlled Mechanical Assembly", IEEE Transactions on Computers Vol C-24, No. 9, Sept 1975, pp. 879-888.
- [42] A.E. Woodin, et.al., "Development of Multi-Moded Remote Manipulator System", First Annual Report, C.S. Draper Laboratory Report C-3790, MIT, NASA Contract No. SNPN-54, Jan 1972.
- [43] A.E. Woodin, et.al., "Development of Multi-Moded Remote Manipulator System", Second Annual Report, Report C-3901, MIT, NASA Contract No. SNPN-54, March 1973.

APPENDIX A: PROGRAMMABLE ASSEMBLY DEMONSTRATION PROJECT

To both demonstrate the idea of using compliance in lieu of force feedback and the idea of programmability in automatic assembly, parts of an automobile alternator were assembled with a four-degree-of-freedom manipulator arm that was built as a prototype programmable assembly machine. This machine is electrically actuated with D.C. servo motors and originally had six degrees of freedom. It was modified by removing the last two degrees of freedom on the wrist and adding the compliance system. The machine operates in a cylindrical coordinate space with a base rotation of 180 degrees, a vertical travel of 0.5 m (20 in), and an in-out travel from a radius of 0.56 m (22 in) to 1.1 m (43 in). The wrist has a total rotation of 360 degrees. Figures A.1 and A.2 are overall views of the assembly machine setup.

The compliance system comprises a deformable structure to provide the desired compliance, a compliance-locking mechanism, and an automatic tool-changing mechanism (Figure A.3). Provision is also made for including a six-axis force sensor in the system. However, the force sensor is not normally used during assembly. The compliance is locked with a pneumatically actuated single-taper collet with a large expansion/contraction range. This collet also acts as a limit stop for the compliance in the unlocked state. The compliance is normally locked while the pieces to be assembled are being transported and positioned and is normally unlocked immediately before the assembly or mating of the parts. The compliance is also unlocked during a tool change when a new tool is being either placed in the tool rack or removed from it.

The automatic tool-changing mechanism is incorporated into the system to facilitate the use of different tools needed for the programmable assembly demonstration. Functionally, the tool changer is similar to those used on many numerically controlled machine tools. A major design difference is that the assembly arm performs the tool change whereas numerically controlled machine tools use an auxiliary mechanism to transfer the tool from the rack to the machine spindle. Instead of the truncated cone shape commonly used for NC milling machine tools, a cylindrical tool stub shape is used to allow more of the tool-actuating mechanism

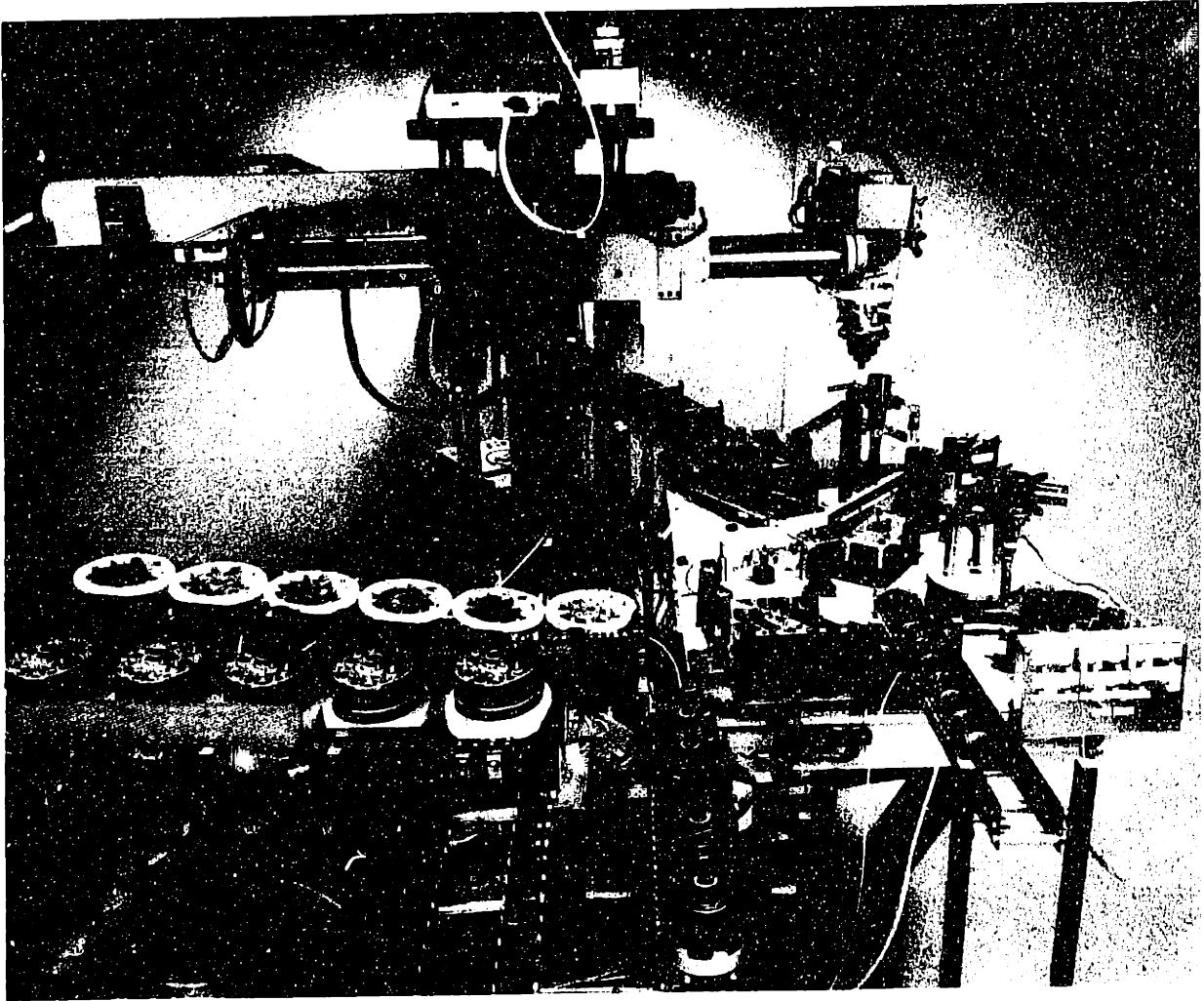


Figure A.1. Photograph of the complete programmable assembly machine setup.

to be located in the stub. A pneumatically actuated collet mechanism is used to grip the tools. Figure A.4 shows a tool changer operation.

The automobile alternator was selected from a short list of possible small automobile assemblies because all the assembly operations can be accomplished with a single four-degree-of-freedom assembly machine. The stator, diode assembly, brush assembly, and rear housing are preassembled and handled as a subassembly during final assembly, making it possible to assemble all the parts along a single axis. Although the automobile alternator is mass produced, it is similar to fractional and small integral horsepower electric motors that are assembled in batch lots

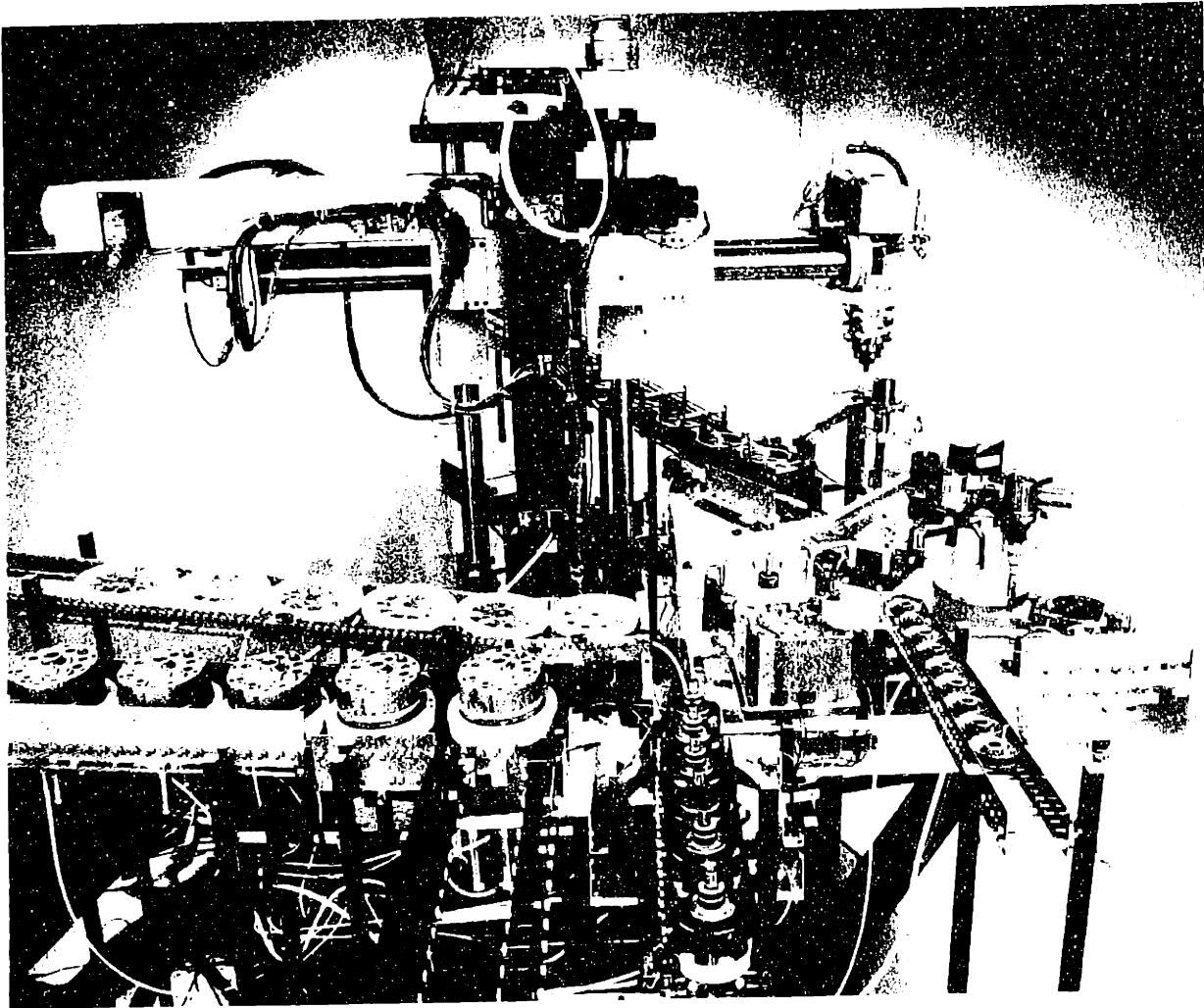


Figure A.1. Photograph of the complete programmable assembly machine setup.

to be located in the stub. A pneumatically actuated collet mechanism is used to grip the tools. Figure A.4 shows a tool changer operation.

The automobile alternator was selected from a short list of possible small automobile assemblies because all the assembly operations can be accomplished with a single four-degree-of-freedom assembly machine. The stator, diode assembly, brush assembly, and rear housing are preassembled and handled as a subassembly during final assembly, making it possible to assemble all the parts along a single axis. Although the automobile alternator is mass produced, it is similar to fractional and small integral horsepower electric motors that are assembled in batch lots

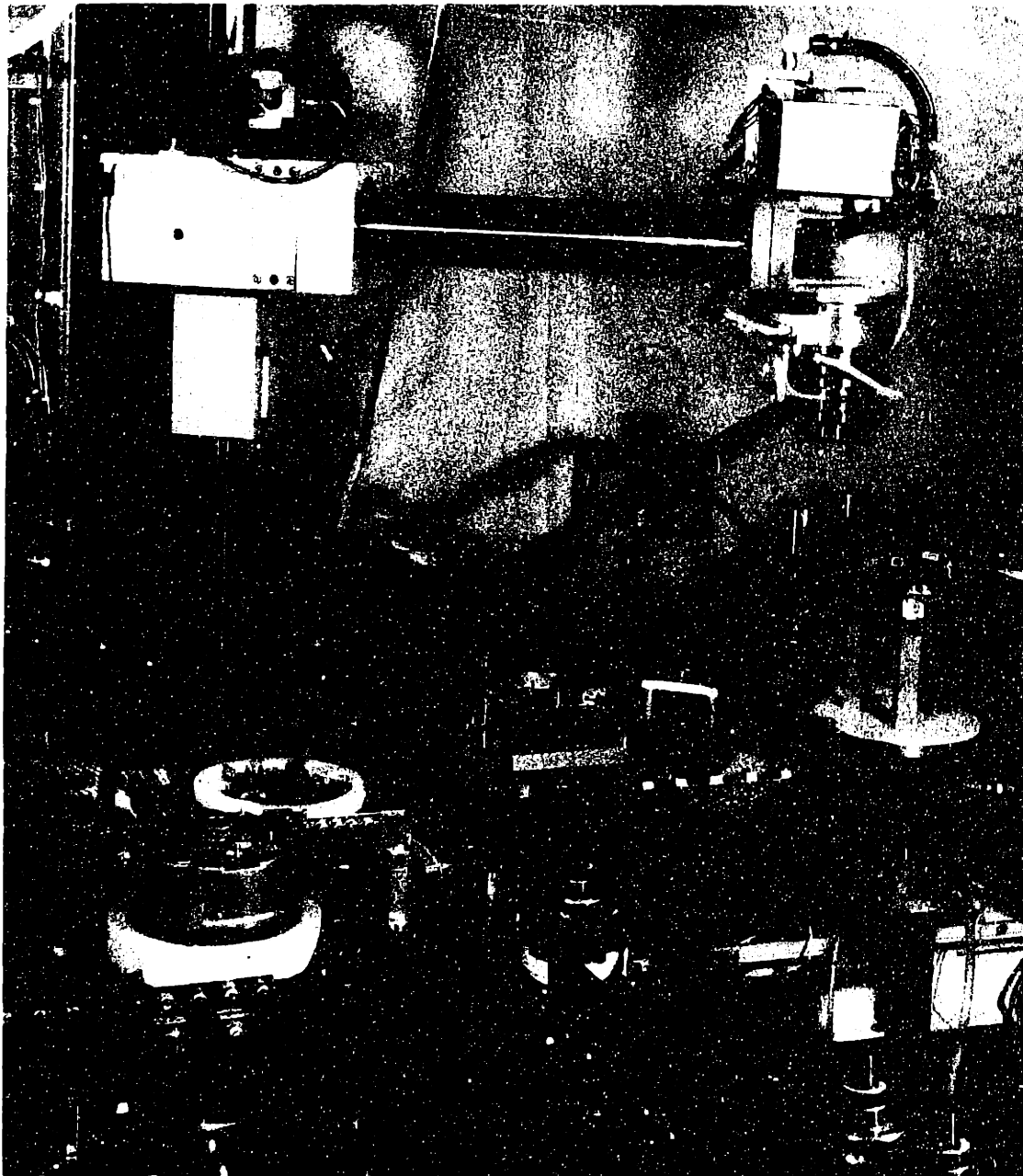


Figure A.2. Photograph of the programmable assembly machine work area.

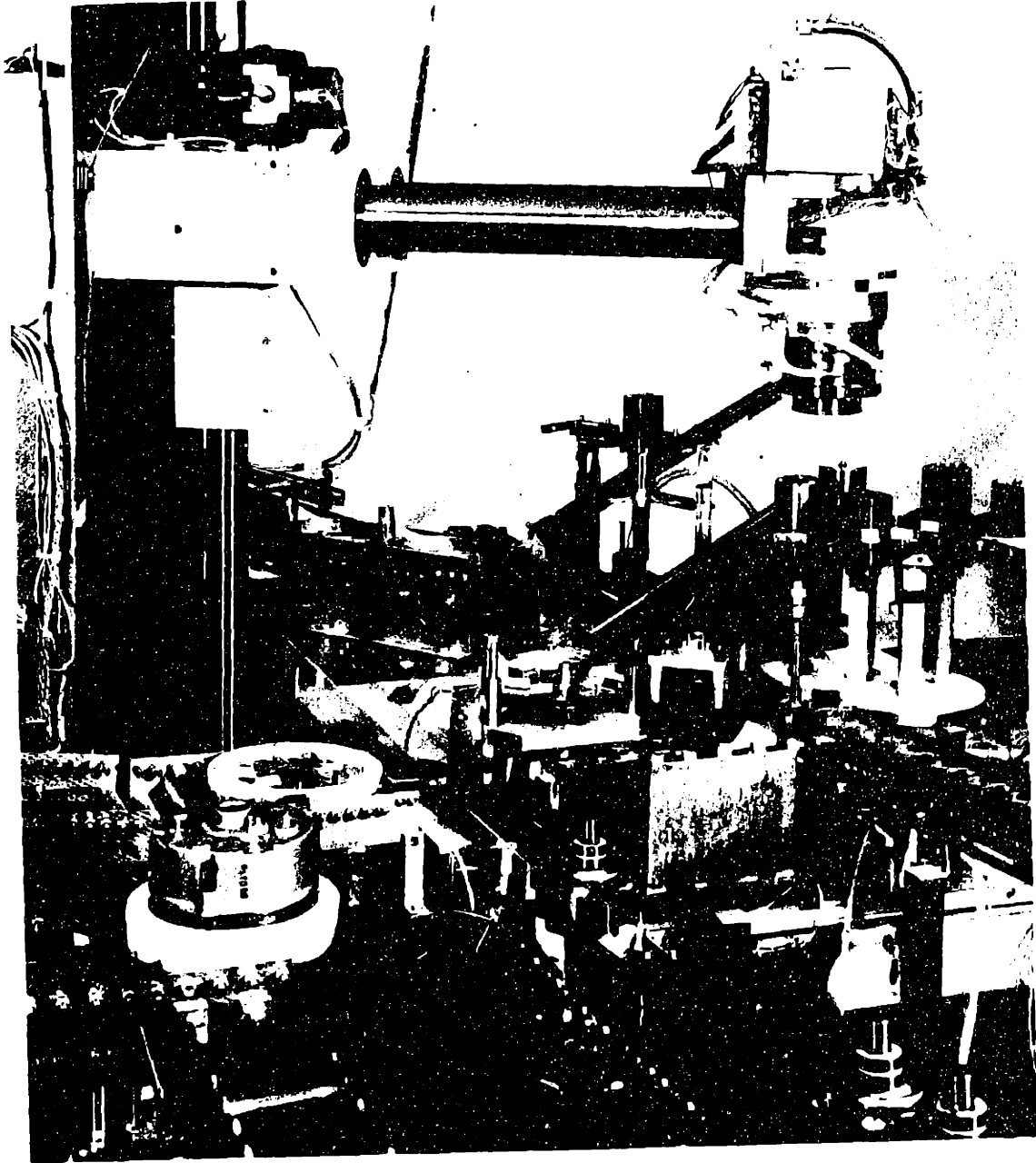


Figure A.2. Photograph of the programmable assembly machine work area.

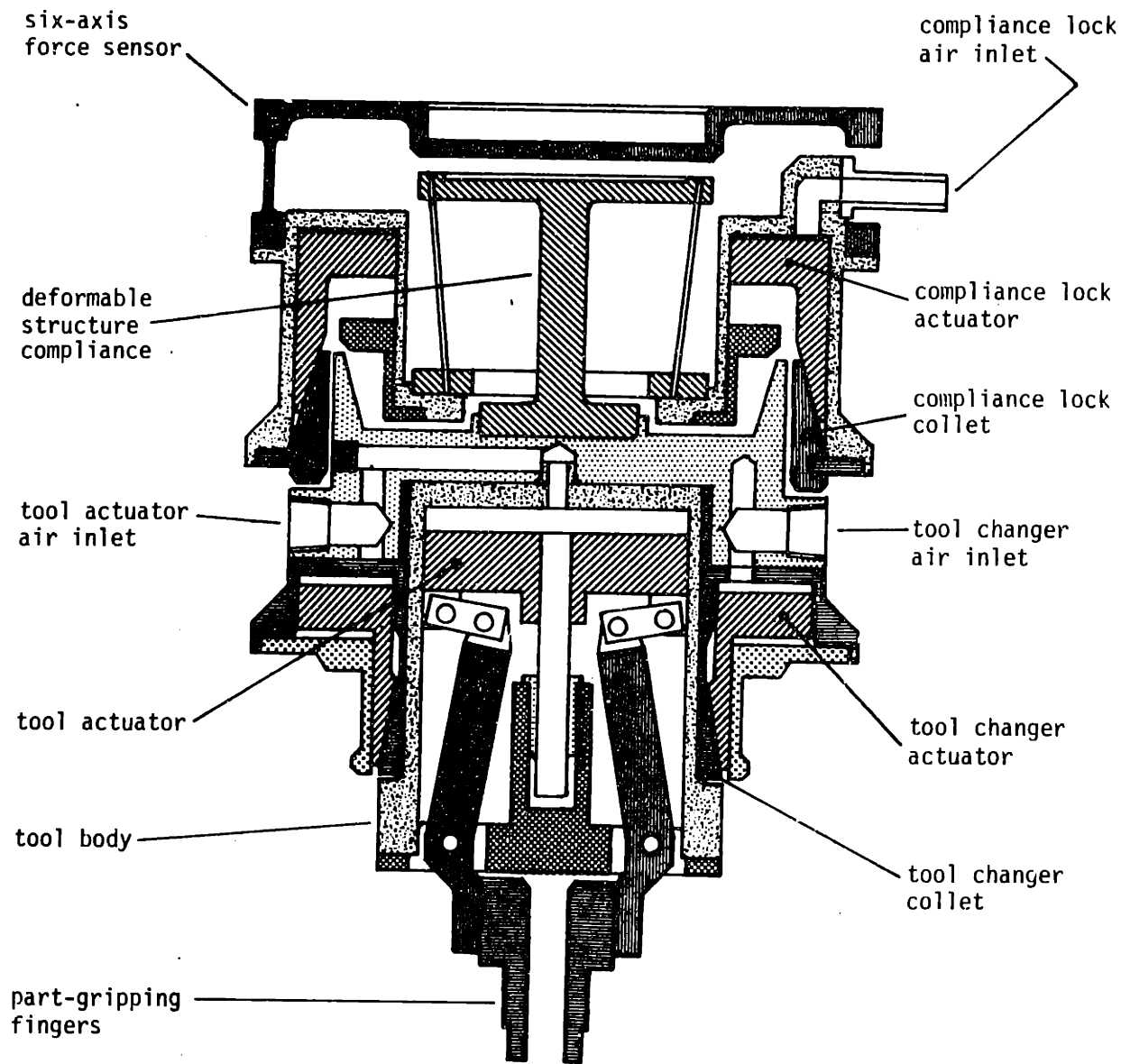


Figure A.3. Cross-sectional drawing of the complete compliance system (shown with a six-axis force sensor).

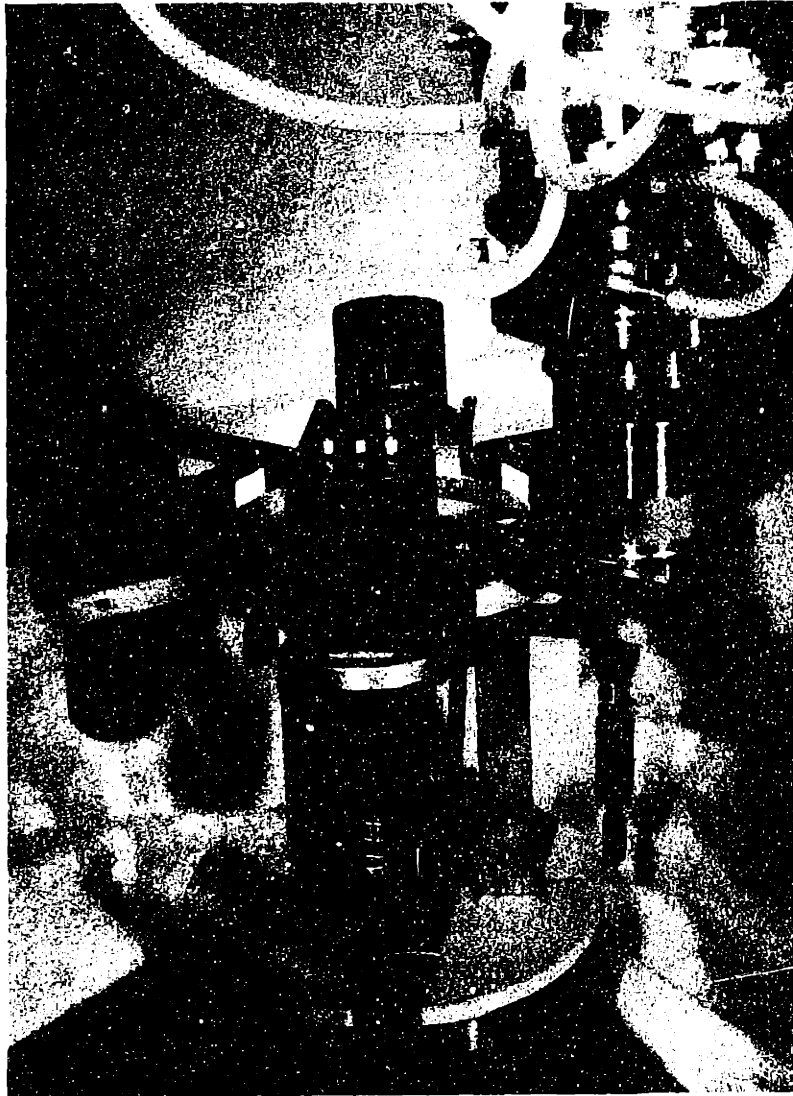


Figure A.4. Photograph illustrating a tool-change operation.

because of the number of variations. The alternator is produced in a number of variations but, with the exception of the pulley, the variations do not affect the assembly operation.

The seventeen parts of the automobile alternator are assembled using six different tools. Three of these tools are used to drive threaded fasteners. The nut, lockwasher, pulley, fan, two spacers, bearing, front housing, and bearing retainer plate are handled by an expanding three-finger tool. The fingers or jaws have four steps to accommodate the different part diameters. The rotor is handled with a contracting collet tool that uses commercially available collets. The rear

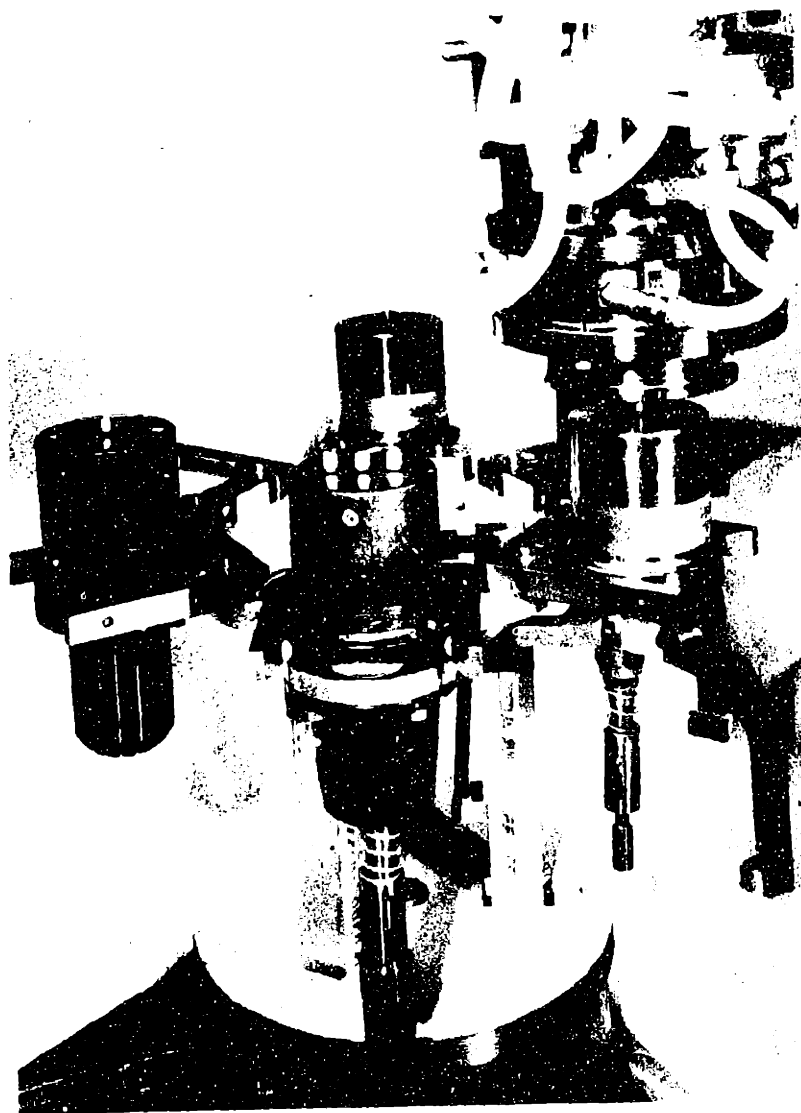


Figure A.4. Photograph illustrating a tool-change operation.

because of the number of variations. The alternator is produced in a number of variations but, with the exception of the pulley, the variations do not affect the assembly operation.

The seventeen parts of the automobile alternator are assembled using six different tools. Three of these tools are used to drive threaded fasteners. The nut, lockwasher, pulley, fan, two spacers, bearing, front housing, and bearing retainer plate are handled by an expanding three-finger tool. The fingers or jaws have four steps to accommodate the different part diameters. The rotor is handled with a contracting collet tool that uses commercially available collets. The rear

housing/stator subassembly and the final assembly are handled with a large contracting three-finger tool. The parts are shown in Figure A.5, while the tools are shown in Figure A.6.

The assembly sequences involve building one subassembly comprising the front housing, ball bearing, bearing retainer plate, and three short screws on an auxiliary assembly fixture or nest. The rest of the assembly sequence involves stacking the remaining parts and the front housing subassembly on the main assembly fixture or nest. A spring-loaded plunger is used to retain the fan and the spacers in alignment until the rotor is added. (Figure A.7). The entire sequence requires sixteen assembly operations and eight tool changes (See Table A.1). Note that instead of driving the nut onto the rotor, the rotor is turned while the nut is held fixed. The only required modification to the alternator parts was chamfering one edge on the rotor (Figure A.8). The three short screws for the bearing retainer plate were blown down a tube from the feeder escapement. While the long screws for the final assembly could be fed in a similar manner, they were simply placed in the holes in the rear housing and fed along with the housing.

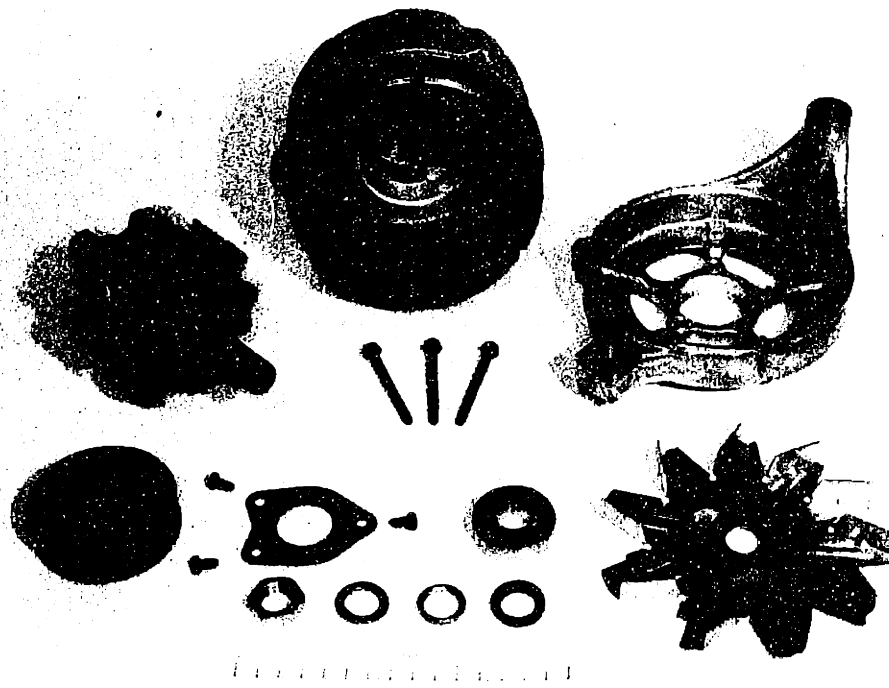


Figure A.5. Parts of the automobile alternator.

INTENTIONAL DUPLICATE EXPOSURE

housing/stator subassembly and the final assembly are handled with a large contracting three-finger tool. The parts are shown in Figure A.5, while the tools are shown in Figure A.6.

The assembly sequences involve building one subassembly comprising the front housing, ball bearing, bearing retainer plate, and three short screws on an auxiliary assembly fixture or nest. The rest of the assembly sequence involves stacking the remaining parts and the front housing subassembly on the main assembly fixture or nest. A spring-loaded plunger is used to retain the fan and the spacers in alignment until the rotor is added. (Figure A.7). The entire sequence requires sixteen assembly operations and eight tool changes (See Table A.1). Note that instead of driving the nut onto the rotor, the rotor is turned while the nut is held fixed. The only required modification to the alternator parts was chamfering one edge on the rotor (Figure A.8). The three short screws for the bearing retainer plate were blown down a tube from the feeder escapement. While the long screws for the final assembly could be fed in a similar manner, they were simply placed in the holes in the rear housing and fed along with the housing.

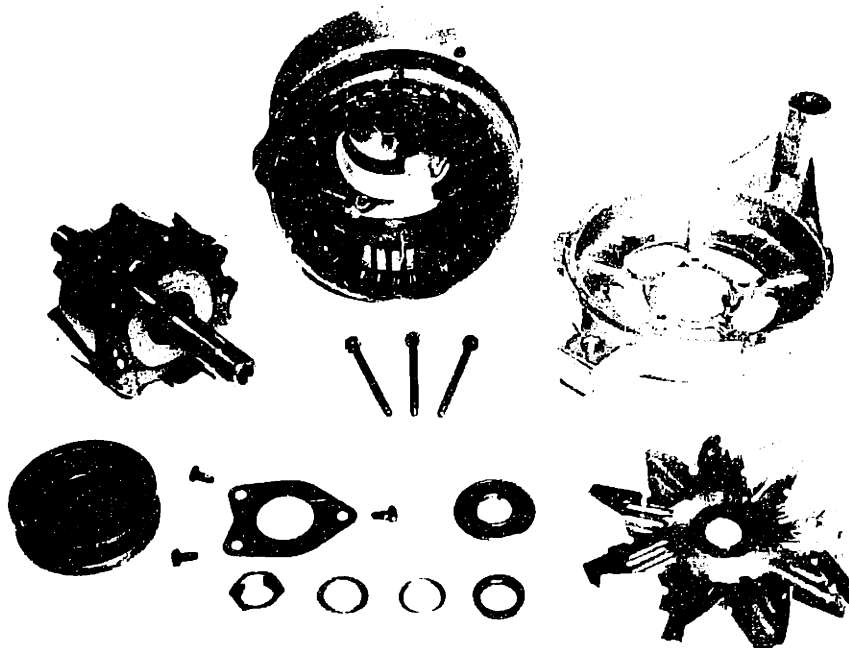


Figure A.5. Parts of the automobile alternator.

C-1	TOOL CHANGE - EXPANDING THREE-FINGER TOOL
A-1	PLACE NUT ON MAIN NEST
A-2	PLACE LOCK WASHER ON MAIN NEST
A-3	PLACE PULLEY ON MAIN NEST
A-4	PLACE FAN ON MAIN NEST
A-5	PLACE FAN SPACER ON MAIN NEST
A-6	PLACE FRONT HOUSING ON AUXILLIARY NEST
A-7	INSERT BALL BEARING INTO FRONT HOUSING
A-8	PLACE BEARING RETAINER PLATE ON AUXILLIARY NEST
C-2	TOOL CHANGE - AUTOFEED SCREWDRIVER
A-9	DRIVE 3 BEARING RETAINER SCREWS
C-3	TOOL CHANGE - EXPANDING THREE-FINGER TOOL
A-10	PLACE FRONT HOUSING SUBASSEMBLY ON MAIN NEST
A-11	PLACE BEARING SPACER ON MAIN NEST
C-4	TOOL CHANGE - CONTRACTING COLLET TOOL
A-12	INSERT ROTOR INTO PART STACK
C-5	TOOL CHANGE - NUTRUNNER
A-13	DRIVE ROTOR INTO NUT
C-6	TOOL CHANGE - LARGE CONTRACTING THREE-FINGER TOOL
A-14	PLACE REAR HOUSING / STATOR SUBASSEMBLY ONTO FRONT HOUSING
C-7	TOOL CHANGE - SCREWDRIVER
A-15	DRIVE 3 HOUSING ASSEMBLY SCREWS
C-8	TOOL CHANGE - LARGE CONTRACTING THREE-FINGER TOOL
A-16	REMOVE COMPLETED ASSEMBLY

Table A.1. Sequence of operations for the automobile alternator assembly using the programmable assembly machine.

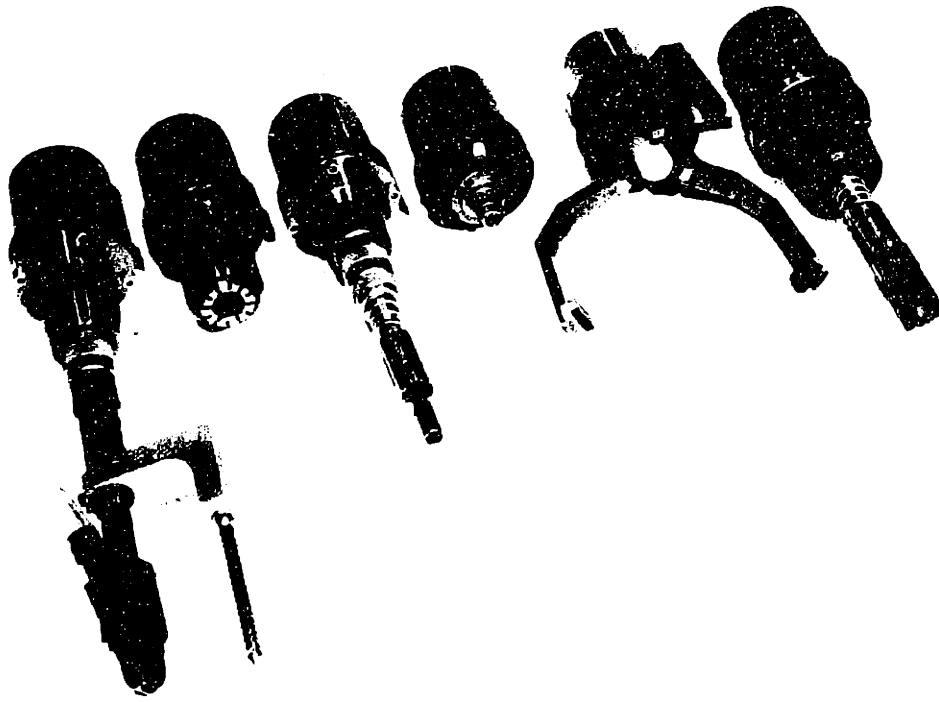


Figure A.6. Tools used in the assembly of the automobile alternator. From left to right, screwdriver with automatic screw feed used to drive the short screws, contracting collet tool, screwdriver used to drive the long screws, expanding three-finger tool, large contracting three-finger tool, nutrunner used to torque the rotor onto the nut.

Simple parts feeders were designed and constructed so that at least six-to-eight complete alternators could be assembled sequentially to simulate a production run. The larger parts are fed using roller conveyors. Parts without suitable surfaces for being fed in this manner or that are unstable are placed on individual plastic pallets. Most of the smaller parts are fed on simple gravity tracks.

The assembly fixtures, the tool holders, and most of the parts feeders are mounted on ball plunger and detent break-aways. These devices will allow the assembly fixtures, the tool racks, or the feeders to break away in any direction if a certain force or torque limit is exceeded. As these break-aways are preloaded, the initial deflection with force is minimal. Microswitches are used to shut down the assembly machine if any of the devices are tripped. A microswitch and the break-aways supporting the main nest can be seen in Figure A.7.

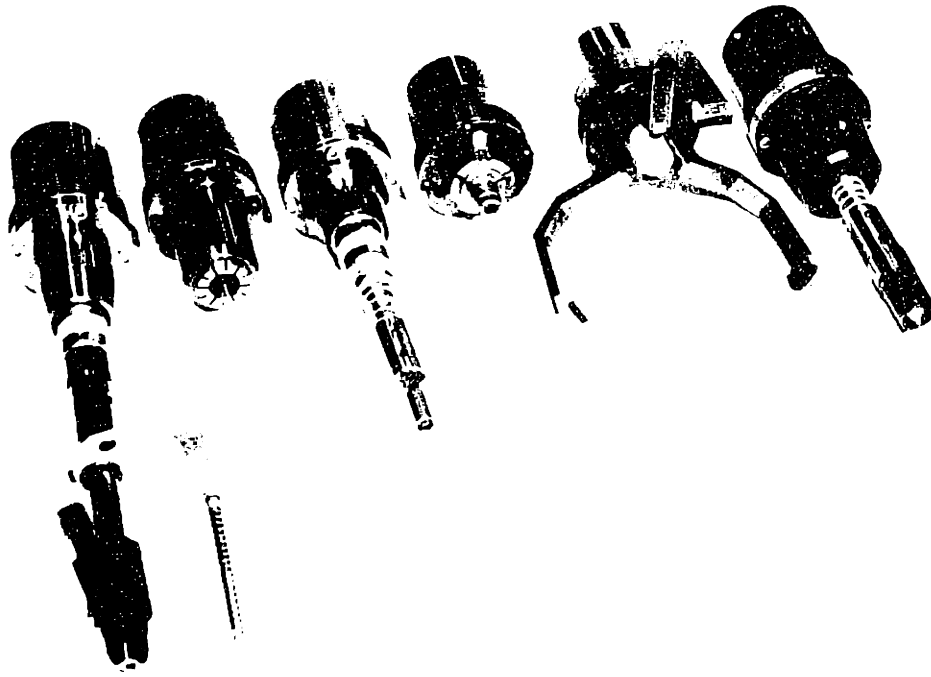


Figure A.6. Tools used in the assembly of the automobile alternator. From left to right, screwdriver with automatic screw feed used to drive the short screws, contracting collet tool, screwdriver used to drive the long screws, expanding three-finger tool, large contracting three-finger tool, nutrunner used to torque the rotor onto the nut.

Simple parts feeders were designed and constructed so that at least six-to-eight complete alternators could be assembled sequentially to simulate a production run. The larger parts are fed using roller conveyors. Parts without suitable surfaces for being fed in this manner or that are unstable are placed on individual plastic pallets. Most of the smaller parts are fed on simple gravity tracks.

The assembly fixtures, the tool holders, and most of the parts feeders are mounted on ball plunger and detent break-aways. These devices will allow the assembly fixtures, the tool racks, or the feeders to break away in any direction if a certain force or torque limit is exceeded. As these break-aways are preloaded, the initial deflection with force is minimal. Microswitches are used to shut down the assembly machine if any of the devices are tripped. A microswitch and the break-aways supporting the main nest can be seen in Figure A.7.

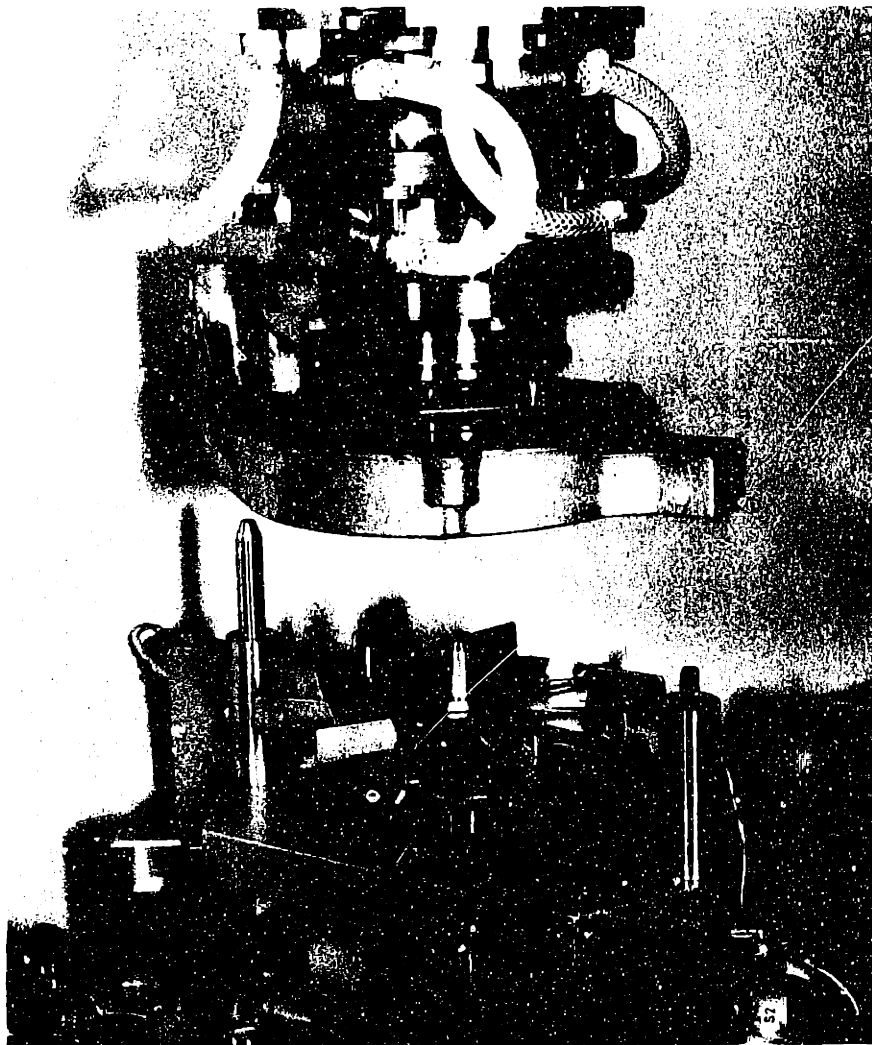


Figure A.7. Front housing subassembly being inserted on the main nest.
Note the plunger holding the fan and fan spacer in place.

The assembly is completed in approximately 2 minutes 30 seconds. The average assembly time could be shortened by building more than one alternator at a time and thus spreading the tool change time over several assemblies. More time could be saved by using multiple-head screwdrivers and driving three screws at once. However, if a serious attempt was made to design an economically viable reprogrammable assembly machine to assemble an item that is produced in a volume large enough such that the entire output could not be assembled with one multi-degree-of-freedom arm, a different assembly machine configuration would probably be chosen. When production volume cannot be attained on one machine, there is a choice between building

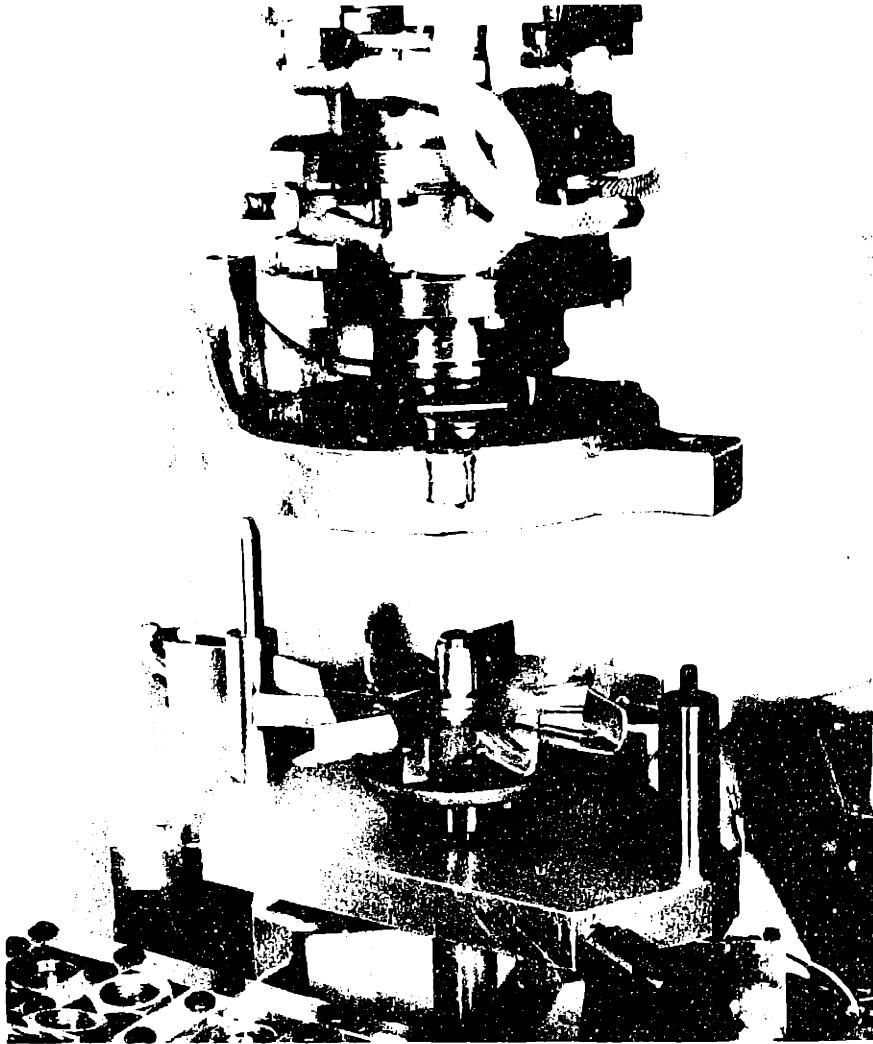


Figure A.7. Front housing subassembly being inserted on the main nest.
Note the plunger holding the fan and fan spacer in place.

The assembly is completed in approximately 2 minutes 30 seconds. The average assembly time could be shortened by building more than one alternator at a time and thus spreading the tool change time over several assemblies. More time could be saved by using multiple-head screwdrivers and driving three screws at once. However, if a serious attempt was made to design an economically viable reprogrammable assembly machine to assemble an item that is produced in a volume large enough such that the entire output could not be assembled with one multi-degree-of-freedom arm, a different assembly machine configuration would probably be chosen. When production volume cannot be attained on one machine, there is a choice between building

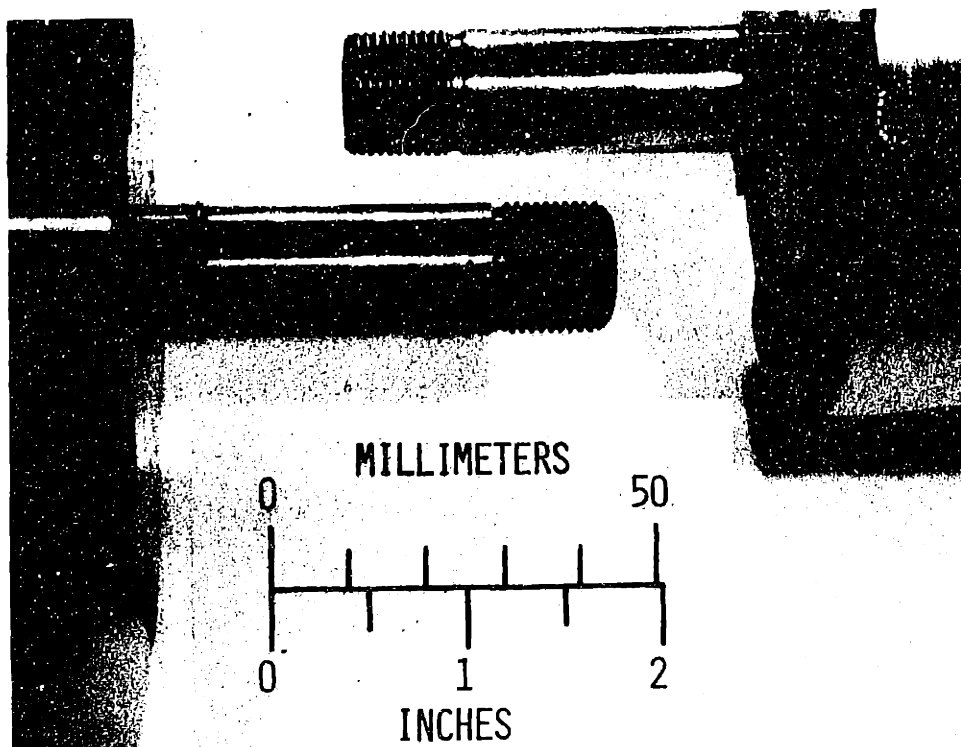


Figure A.8. Modification to the alternator rotor. Note the chamfer to the right of the threads on the top rotor. Bottom rotor is not modified.

a number of similar machines that each put together the entire assembly or building an assembly line configuration with a number of relatively simple reprogrammable arms that add one or more parts to the assembly. The advantage of doing the latter is that tool changes can be completely eliminated and, perhaps even more important, the parts feeders do not need to be duplicated for each machine.

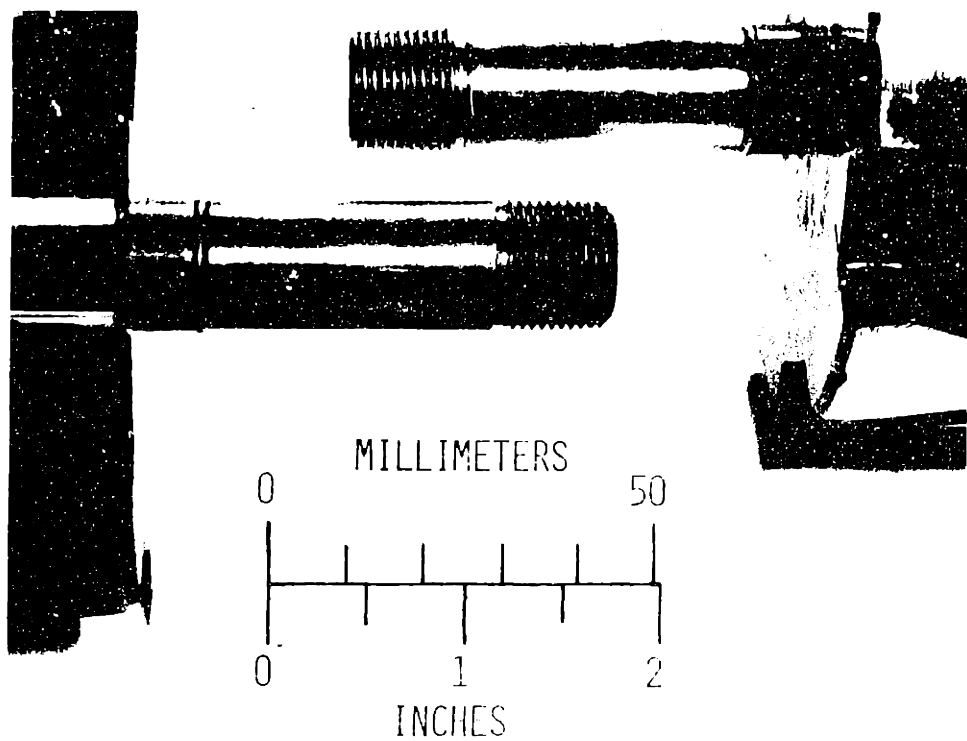


Figure A.8. Modification to the alternator rotor. Note the chamfer to the right of the threads on the top rotor. Bottom rotor is not modified.

a number of similar machines that each put together the entire assembly or building an assembly line configuration with a number of relatively simple reprogrammable arms that add one or more parts to the assembly. The advantage of doing the latter is that tool changes can be completely eliminated and, perhaps even more important, the parts feeders do not need to be duplicated for each machine.

APPENDIX B: IMPACT FORCES

The contact forces resulting from an impact can be obtained from the Hertzian stress formulas by equating the work done during the impact to the kinetic energy before the impact. The mass used in the kinetic energy calculation is the total mass suspended by the compliance. It is assumed that during the impact the compliance isolates this mass from the remaining mass of the assembly machine.

The work done by the impact is simply the contact force integrated over the indentation depth. Assuming the impact is elastic and there are no other internal mechanisms for absorbing energy, the Hertzian stress formulas can be used to obtain the contact force as a function of the indentation depth [27]. For the case of a sphere of radius r impacting on a flat plate, the indentation as a function of the load or force, F , on the sphere is:

$$y = 0.825 \left[\frac{F^2 C_E^2}{r} \right] \quad \text{B.1}$$

where:

$$C_E = \frac{1-\nu_1^2}{E_1} + \frac{1-\nu_2^2}{E_2} \quad \text{B.2}$$

E_1 and E_2 and ν_1 and ν_2 are the Young's moduli and the Poissons' ratios for the two materials. Therefore the force as a function of the indentation depth is:

$$F = 1.334 \frac{y^{2/3} r^{1/2}}{C_E} \quad \text{B.3}$$

The work done during the impact is:

$$W = 1.334 \frac{r^{1/2}}{C_E} \int_0^{d_i} y^{2/3} dy \quad \text{B.4}$$

Performing this integration and equating the result to the kinetic energy before impact, an expression for the maximum indentation depth, d_i , is obtained:

$$d_i = 0.975 \left[\frac{m v_i^2 C_E}{r^{1/2}} \right]^{2/5} \quad \text{B.5}$$

where m is to total suspended mass supported by the compliance and v_i is the insertion velocity at impact. Using this expression in equation B.3, the maximum impact force is:

$$F_i = 1.284 \left[\frac{m^3 v_i^6 r}{C_E^2} \right]^{1/5} \quad \text{B.6}$$

This expression is used as the force in the Hertzian stress formula to find the maximum stress caused by the impact:

$$\sigma_i = 0.578 \left[\frac{F_i}{r^2 C_E^2} \right]^{1/3} \quad \text{B.7}$$

The impact of a part with a rounded edge upon a chamfered hole is treated in a similar manner utilizing the formulas for the general case of two bodies in contact [27]. In place of equation B.1., the expression for the indentation depth is:

$$y = \lambda \left[\frac{F^2 C_E^2}{K_D} \right]^{1/3} \quad \text{B.8}$$

where K_D is obtained using the expression:

$$K_D = \frac{1.5}{\frac{1}{r_1} + \frac{1}{r_2} + \frac{1}{r_1'} + \frac{1}{r_2'}} \quad \text{B.9}$$

and λ is a tabulated function of $\cos \theta$ which is given by the expression:

$$\cos \theta = \frac{K_D}{1.5} \sqrt{\left(\frac{1}{r_1} - \frac{1}{r_1'}\right)^2 + \left(\frac{1}{r_2} - \frac{1}{r_2'}\right)^2 + 2\left(\frac{1}{r_1} - \frac{1}{r_1'}\right)\left(\frac{1}{r_2} - \frac{1}{r_2'}\right) \cos 2\theta} \quad \text{B.10}$$

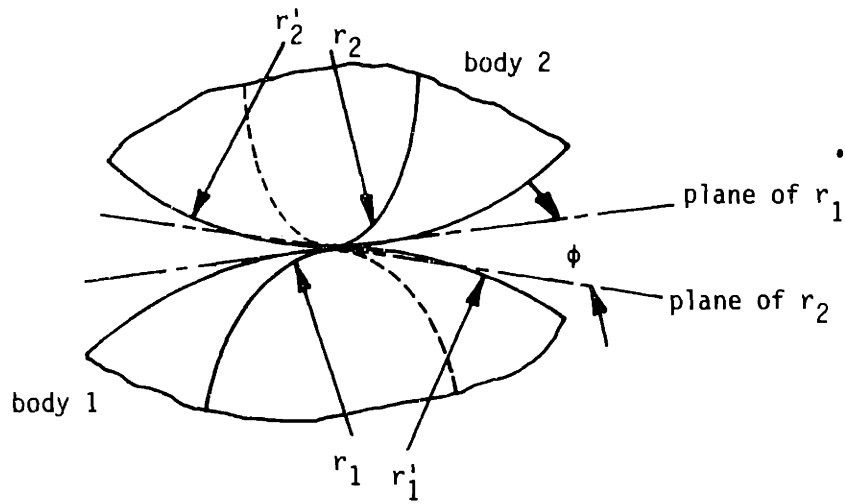
The radii of curvature r_1 , r_1' , r_2 and r_2' and the angle θ are as defined in Figure B.1 with positive values for convex surfaces and negative values for concave surfaces. The table for the values of λ is also included in Figure B.1.

From equation B.8, the force as a function of the indentation depth is:

$$F = \frac{K_D^{1/2} y^{3/2}}{C_E \lambda^{3/2}} \quad \text{B.11}$$

Integrating this expression over the indentation depth as before to find the work, equating the work to the kinetic energy before the impact and solving for the maximum indentation depth:

$$d_i = 1.093 \left[\frac{\lambda^3 C_E^2 m^2 v_i^4}{K_D} \right]^{1/5} \quad \text{B.12}$$



Cos θ	α	β	λ	Cos θ	α	β	λ
0.00	1.000	1.000	0.750	0.80	2.292	0.544	0.594
0.10	1.070	0.936	0.748	0.85	2.600	0.507	0.559
0.20	1.150	0.878	0.743	0.90	3.093	0.461	0.510
0.30	1.242	0.822	0.734	0.92	3.396	0.438	0.484
0.40	1.351	0.769	0.721	0.94	3.824	0.412	0.452
0.50	1.486	0.717	0.703	0.96	4.508	0.378	0.410
0.60	1.661	0.664	0.678	0.98	5.937	0.328	0.345
0.70	1.905	0.608	0.644	0.99	7.774	0.287	0.288
0.75	2.072	0.578	0.622				

Figure B.1. Definition of parameters for Hertzian stress between two generalized bodies.

This expression is then used in equation B.11 to find the maximum impact force;

$$F_i = 1.142 \left[\frac{K_D m^3 v_i^6}{\lambda^3 C_E^2} \right]^{1/5} \quad \text{B.13}$$

The maximum compressive stress can be found by using this result in the equation:

$$\sigma_i = \frac{1.5F_i}{ab} \quad \text{B.14}$$

where a is obtained using the expression:

$$a = \alpha \left[FK_D C_E \right]^{1/3} \quad \text{B.15}$$

and b is obtained using the expression:

$$b = \beta \left[\frac{FK_C C_E}{C} \right]^{1/3} \quad \text{B.16}$$

Values for α and β are tabulated as a function of $\cos \theta$ and are included in Figure B.1.

The above equations were used to compute the contact force, the compressive stress, the indentation and the area of indentation that occurs when a ball bearing is inserted into an alternator housing with typical conditions using the programmable assembly machine. The conditions and the results are listed in Table B.1. The results indicate that the elastic limit is exceeded. This was verified qualitatively by dropping the bearing at a 45° angle onto an aluminum plate from a height that caused the bearing to have the same energy at impact as the suspended mass of the compliance wrist system. The aluminum plate was permanently indented.

As can be seen from the form of the equations, the maximum Hertzian stress between a specified pair of materials is a stronger function of the radii of curvature at the contact point than the contact force as:

$$\sigma_i \propto \left[\frac{F}{K_D^2} \right]^{1/3} \quad \text{B.17}$$

or, for a sphere on a plate, K_D is replaced with r :

$$\sigma_i \propto \left[\frac{F}{r^2} \right]^{1/3} \quad \text{B.18}$$

The lowest Hertzian stress will occur when two flat chamfers impact upon each other.

Assumed Impact Conditions

Velocity at impact	120 mm/sec (4.75 in/sec)
Ball bearing race edge radius, r_1	2.0 mm (0.080 in)
Ball bearing race radius, r_1'	18.0 mm (0.71 in)
Hole chamfer radius, r_2	flat or infinite radius
Hole radius, r_2'	20.5 mm (0.81 in)
K_D	2.96 mm (0.117 in)
$\cos \theta$	0.882
α	2.92
β	0.477
λ	0.527
C_E (steel race, aluminum hole)	$17.48 \times 10^{-12} \text{ m}^2/\text{N}$ ($120 \times 10^{-9} \text{ in}^2/\text{lb}_f$)

Calculated Results

Maximum contact force	1.76 x 10 ³ N (395 lb _f)
Contact patch dimensions	1.314 mm x 0.214 mm (0.052 in x 0.008 in)
Maximum indentation	0.036 mm (0.0015 in)
Hertzian stress	9.4 x 10 ⁹ Pa (1.36 x 10 ⁶ psi)

Table B.1. Calculated maximum contact force and Hertzian stress for the insertion of a ball bearing into an automobile alternator housing.

APPENDIX C: IMPACT DYNAMICS

C.1. Dynamics of a Single-Point Impact on a Chamfer

When two parts contact on the chamfers at a low insertion speed due to a lateral misalignment, the lateral component of the contact force will cause the parts to move sideways relative to each other as they slide across the chamfers assuming that the center of compliance is at or near the contact point. The impulse that occurs when the parts impact at higher speeds will cause a motion of and about the center of gravity of the compliance system. If the resultant motion is of sufficient amplitude, the part held by the compliance will bounce across the chamfers and either hit the far side of the hole or hit the chamfer on the other side of the hole. In either case, this will cause a second impact which can set up a chattering motion as the part bounces from one side of the hole to the other.

It is assumed that the motion of the body after a single-point contact is caused by an instantaneous impulse that occurs when the two parts impact. The initial contact is assumed to occur between the chamfers of the parts. The body acted upon is assumed to be the segment of the compliant wrist assembly that is supported by the compliance including the part-gripping tool and the part. The spring forces are those associated with the compliance and are assumed to be acting at the assembly interface or the point of contact.

The kinetic energy before the impact is:

$$E = \frac{mv_i^2}{2} \quad \text{C.1}$$

where m is the total suspended mass and v_i is the velocity at impact. Immediately after impact the kinetic energy is:

$$E = \frac{mv_z^2}{2} + \frac{mv_x^2}{2} + \frac{I\omega^2}{2} \quad \text{C.2}$$

where v_z is the new velocity in the insertion direction, v_x is the lateral velocity of the center of gravity, and ω is the angular velocity about this point. I is the moment of inertia of the suspended mass. The new velocities are related to the impulse by the equations:

$$v_z = v_i - \frac{J \sin \theta}{m} \quad C.3$$

$$v_x = \frac{J \cos \theta}{m} \quad C.4$$

$$\omega = \frac{J d_\ell}{I} \quad C.5$$

where θ is the angle of the chamfer, ℓ is the distance from the center of mass to the impact point, r is the radius of the shaft or part being inserted, and d_ℓ is the distance from the line of action of the impulse to the center of mass (see Figure C.1):

$$d_\ell = \ell \cos \theta - r \sin \theta \quad C.6$$

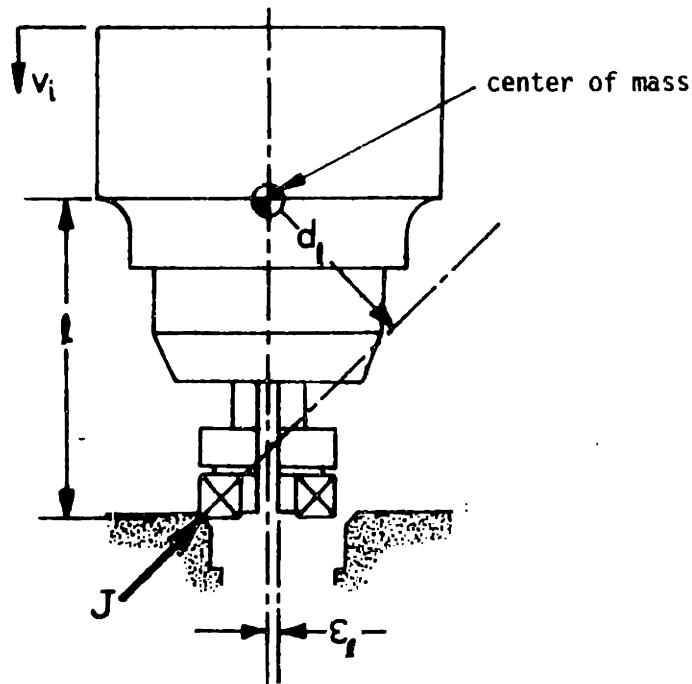


Figure C.1. Part impacting chamfer at finite velocity with resulting impulse not thru the center of mass.

Substituting expression C.3, C.4, and C.5 into the equation for the energy after impact:

$$E' = \frac{m}{2} \left(v_I - \frac{J}{m} \sin\theta \right)^2 + \frac{J^2 \cos^2\theta}{2m} + \frac{J^2 d^2}{2I} \quad C.7$$

The magnitude of the impulse, J , will depend on the coefficient of restitution. The coefficient of restitution is defined as the ratio of the velocities before impact to the components of velocity after impact along the line of impact. In a completely elastic impact, the coefficient of restitution is unity and the energy after the impact is equal to the energy before the impact. In a completely inelastic impact, the coefficient of restitution is zero and the energy after the impact is at a minimum. The maximum value of J is found by equating the kinetic energy before the impact to the kinetic energy after impact:

$$\frac{m}{2} \left(v_I - \frac{J}{m} \sin\theta \right)^2 + \frac{J^2 \cos^2\theta}{2m} + \frac{J^2 d^2}{2I} = \frac{mv_I^2}{2} \quad C.8$$

Solving this equation for J :

$$J = 2v_I \sin\theta \left(\frac{mI}{I + md^2} \right) \quad C.9$$

The minimum value for J is found by differentiating the kinetic energy with respect to J and setting this result to zero:

$$\frac{dE}{dJ} = -v \sin\theta + \frac{J \sin^2\theta}{m} + \frac{J \cos^2\theta}{m} + \frac{Jd^2}{I} = 0 \quad C.10$$

Solving this for J :

$$J = v_I \sin\theta \left(\frac{mI}{I + md^2} \right) \quad C.11$$

After impact, the body is constrained only by the spring forces provided by the compliance device. As the spring force in the lateral direction acts at the assembly interface at a distance ℓ from the center of gravity, the pair of differential equations that describe the lateral motion of the center of gravity and the rotary motion about the center of gravity are coupled:

$$I\ddot{\theta} = K_{\theta}\theta - \ell K_x(\ell\theta + x) \quad C.13$$

$$m\ddot{x} = K_x(\ell\theta + x) \quad C.14$$

The initial conditions for these equations are:

$$\theta = 0, \dot{\theta} = (1 + R_c) \left(\frac{md_{\ell}}{I + md_{\ell}^2} \right) v_i \sin\theta \quad C.15$$

$$x = 0, \dot{x} = (1 + R_c) \left(\frac{I}{I + md_{\ell}^2} \right) v_i \sin\theta \cos\theta \quad C.16$$

where K_x and K_{θ} are the spring constants of the compliance device, and R_c is the coefficient of restitution.

The solution of the equations will give the maximum displacement as a function of the spring constants and the impact velocity. Given certain spring constants and a maximum displacement, the maximum insertion velocity can be found. A solution was found in two ways. An exact solution of the coupled different equations was found for a given set of conditions using a fourth-order Runge-Kutta digital simulation. An approximate solution was found using energy considerations.

The approximate solution is found by solving for the maximum insertion velocity given a permissible lateral displacement δ (generally the distance from the point of impact to the far side of the hole). A first solution is found by setting θ and $\dot{\theta}$ to zero. With θ and $\dot{\theta}$ set to zero, the kinetic energy is:

$$E = \frac{mv_x^2}{2} \quad C.17$$

Equating the kinetic energy to the work done on the compliance in displacing the part through a distance δ and solving for v_x :

$$v_x = \delta \sqrt{\frac{K_x}{m}} \quad C.18$$

Using equations C.4 and C.12:

$$v_i = \frac{1}{1 + R_c} \left(\frac{I + md_\ell^2}{I} \right) \frac{\delta}{\sin\theta \cos\theta} \sqrt{\frac{K_x}{m}} \quad \text{C.19}$$

As the effect of θ and $\dot{\theta}$ was ignored, v_i must be smaller than this value.

In a similar manner, setting x and v_x to zero, the kinetic energy is:

$$E = \frac{I\dot{\theta}^2}{2} \quad \text{C.20}$$

Equating this energy to the work done on the compliance in rotating the part through an angle δ/ℓ and solving for $\dot{\theta}$:

$$\dot{\theta} \leq \frac{\delta}{\ell} \sqrt{\frac{K_\theta + K_x \ell^2}{I}} \quad \text{C.21}$$

Using equations C.5 and C.12:

$$v_i = \frac{1}{1 + R_c} \left(\frac{I + md_\ell^2}{md} \right) \left(\frac{1}{\sin\theta} \right) \frac{\delta}{\ell} \sqrt{\frac{K_\theta + K_x \ell^2}{I}} \quad \text{C.22}$$

As the effect of x and v_x were ignored in this argument, v_i must also be smaller than this value. As it is known that v_i must be smaller than the value obtained by ignoring the θ deflection and smaller than the value ignoring the x deflection, an approximate value for v_i can be obtained from the relationship:

$$v_i = \frac{1}{\frac{1}{v_{ix}} + \frac{1}{v_{i\theta}}} \quad \text{C.23}$$

where v_{ix} is the value obtained from setting θ and $\dot{\theta}$ to zero and $v_{i\theta}$ is the value obtained from setting x and v_x to zero. This value of v_i is not an absolute maximum value for an insertion velocity. It only indicates when problems with chattering should be expected and what parameters influence this problem.

Values for v_{ix} and $v_{i\theta}$ are obtained for the case of inserting a ball bearing into the front housing of the automobile alternator used in the programmable assembly demonstration, first assuming an elastic impact and then, more realistically, assuming the coefficient of restitution equals 0.3. Assuming an elastic impact, the maximum value of v_i is 37mm/sec (1.46 in/sec). With a coefficient of restitution of 0.3, the maximum value of v_i is 56mm/sec (2.21 in/sec). Details of the assumed

Assumed Conditions

Suspended mass, m	4.060 Kg (8.94 lb _m)
Moment of inertia, I	7.137×10^{-3} Kg m ² (24.4 lb _m in ²)
Length, l	95 mm (3.74 in)
Length, d	53 mm (2.09 in)
Spring constant, K_x	10^4 N/m (57 lb _f /in)
Spring constant, K_θ	400 N m/rad (3.55×10^3 lb _f in/rad)
Initial lateral error, δ	0.5 mm (0.020 in)

Results Assuming an Elastic Impact

v_{ix}	65 mm/sec (2.56 in/sec)
$v_{i\theta}$	84 mm/sec (3.30 in/sec)
v_i	37 mm/sec (1.46 in/sec)

Results Assuming a Coefficient of Restitution of 0.3

v_{ix}	100 mm/sec (3.93 in/sec)
$v_{i\theta}$	129 mm/sec (5.08 in/sec)
v_i	56 mm/sec (2.21 in/sec)

Table C.1. Maximum values of v_i that will not result in a secondary impact.

conditions and results are listed in Table C.1.

These approximate values for v_i are then used as initial conditions for a digital simulation using a fourth-order Runge-Kutta solution to the differential equations. The simulation gives a detailed description of the motion of the part at the assembly interface. The parameter of particular interest is the maximum amplitude of the lateral displacement. The results in Figure C.2 shown the numerical solution to be in close agreement with the approximate solution. The maximum amplitude of the lateral displacement is approximately 0.45mm (0.18 in), compared to the assumed value of 0.50mm (0.020 in) for the approximate solution.

The body will not continue to oscillate as shown in Figure C.2. If a line representing the profile of the chamfer and the hole is drawn on this figure, it is obvious that unless the part bounces just the right amount and enters the hole after the initial impact, it will impact the chamfer again either on one side of the hole

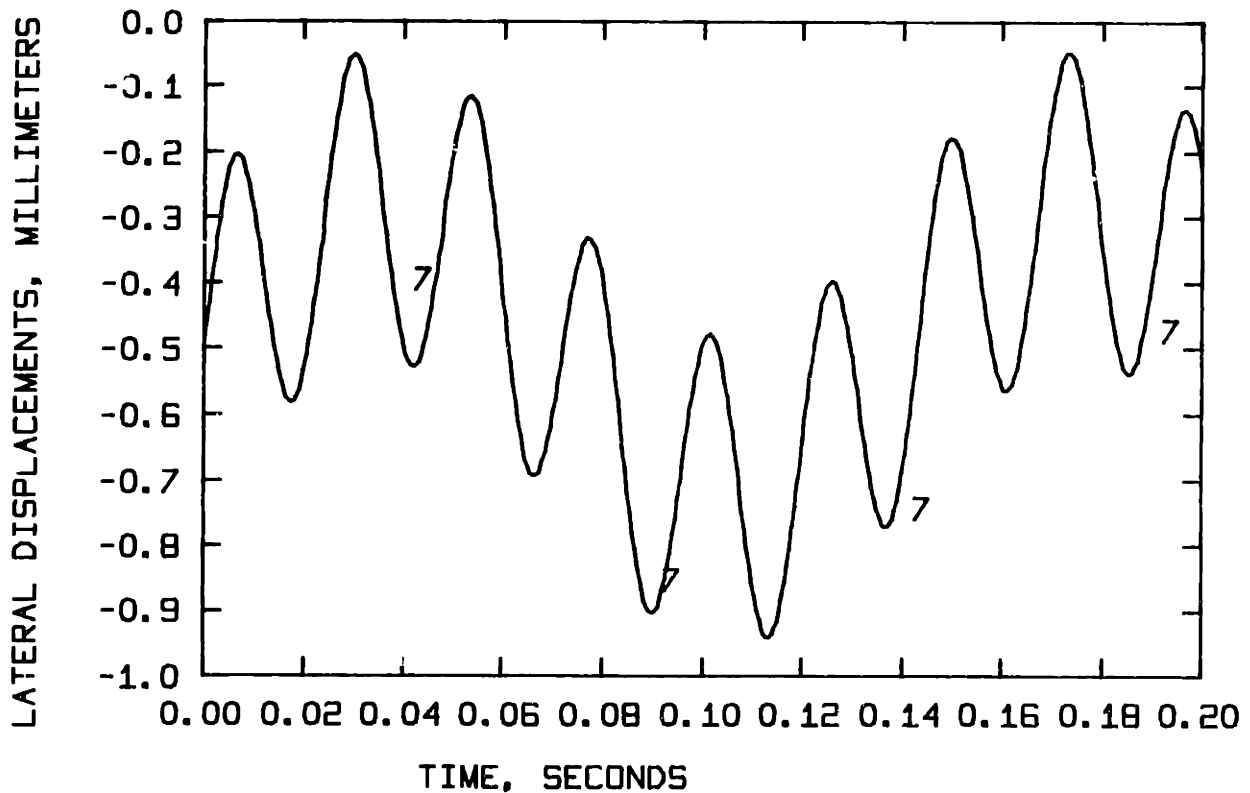


Figure C.2. Free body oscillation of the compliance system resulting from a single impulse at the center of compliance.

or the other. A more complete digital simulation was written to model this. The inputs are the initial position error between the part and the hole, the clearance between the part and the hole, the insertion velocity, the angle of the chamfer, the coefficient of restitution and the radius of the part along with the spring constants and the mass and inertia of the compliant wrist system. The program computes and records the magnitude of the impulse for each impact. The trajectory of the part along with the outline of the chamfer and the hole are plotted. For simplicity, only the center line position at the end of the part is plotted. Therefore, the distance between the two lines representing the walls of the hole is the clearance between the part and the hole.

Representing plots for several different conditions are shown in Figures C.3 through C.8. The geometric data for these runs was taken from the insertion of the ball bearing into the alternator housing. If the coefficient of resitution is significantly less than one, the system is well damped without external damping once the parts are in contact. The parts will slide instead of bouncing after an impact if the coefficient of restitution is sufficiently small. This phenomena is seen in Figures C.7 and C.8.

A rule of thumb for using this simulation to select a maximum value of v_i is to limit the impacts to the chamfer on one side of the hole. This assumes that values for the spring constants, the mass and inertia, and the probable positional error are fixed. It should be emphasized that neither this value of v_i nor the value found using the other technique is an absolute maximum value for the insertion speed. No attempt was made to optimize the experimental apparatus used in the programmable assembly demonstration project for high-speed insertions. The insertion that is used as an example has been performed with a maximum impact speed of approximately 120mm/sec (4.72 in/sec). There is relatively little to be gained in making this insertion faster as most of the assembly time is expended in picking up and transporting the parts and in changing tools. The insertion speed would be more important for a compliant system designed to be used on a transfer line or fixed automation machine.

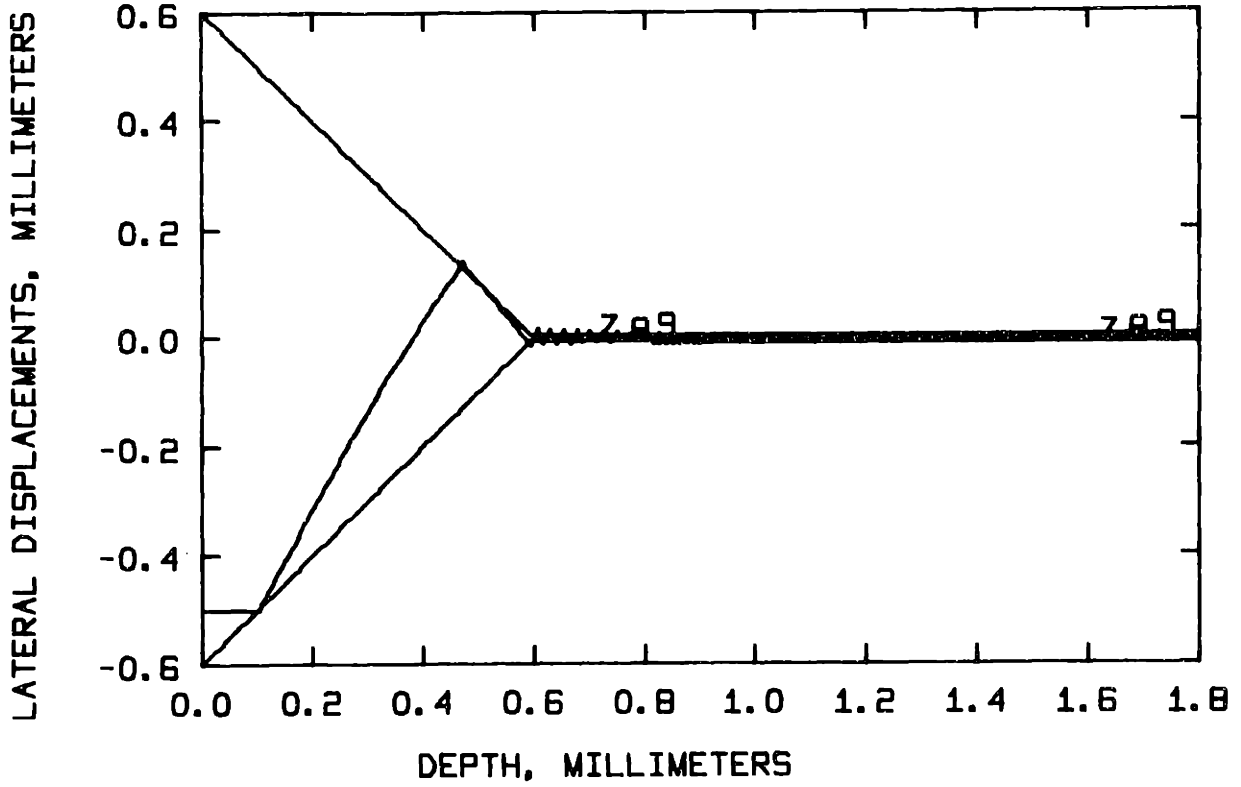


Figure C.3. Digital simulation of bearing bounce during insertion. Impact velocity, 120mm/sec; coefficient of restitution, 0.95.

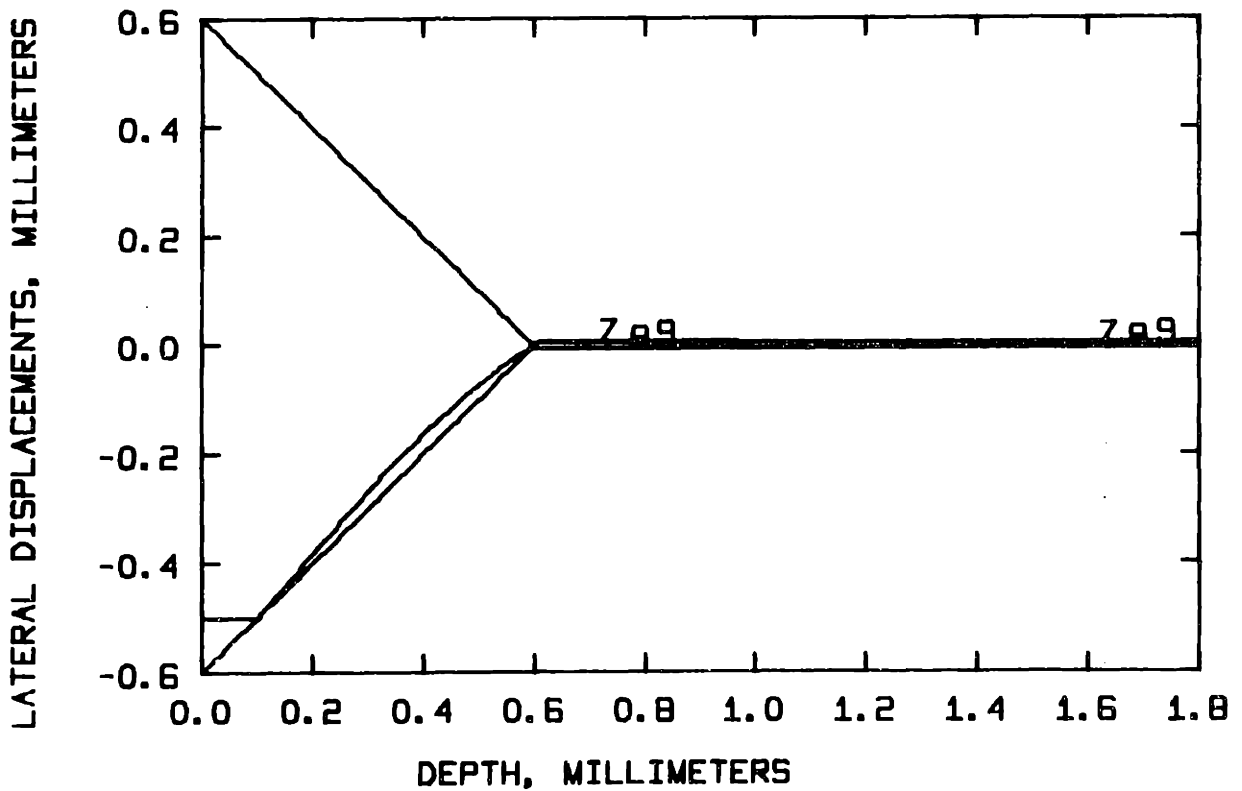


Figure C.4. Digital simulation of bearing bounce during insertion. Impact velocity, 120mm/sec; coefficient of restitution, 0.3.

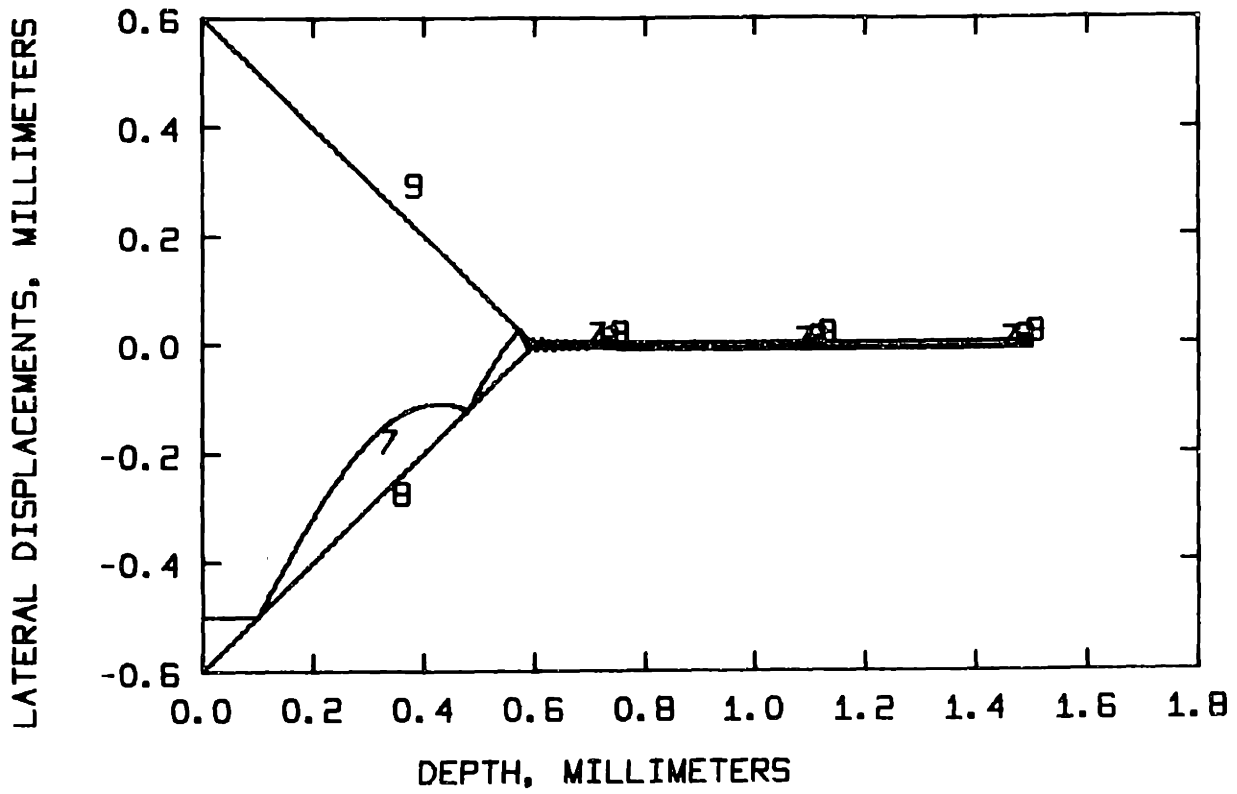


Figure C.5. Digital simulation of bearing bounce during insertion. Impact velocity, 50 mm/sec; coefficient of restitution, 0.95.

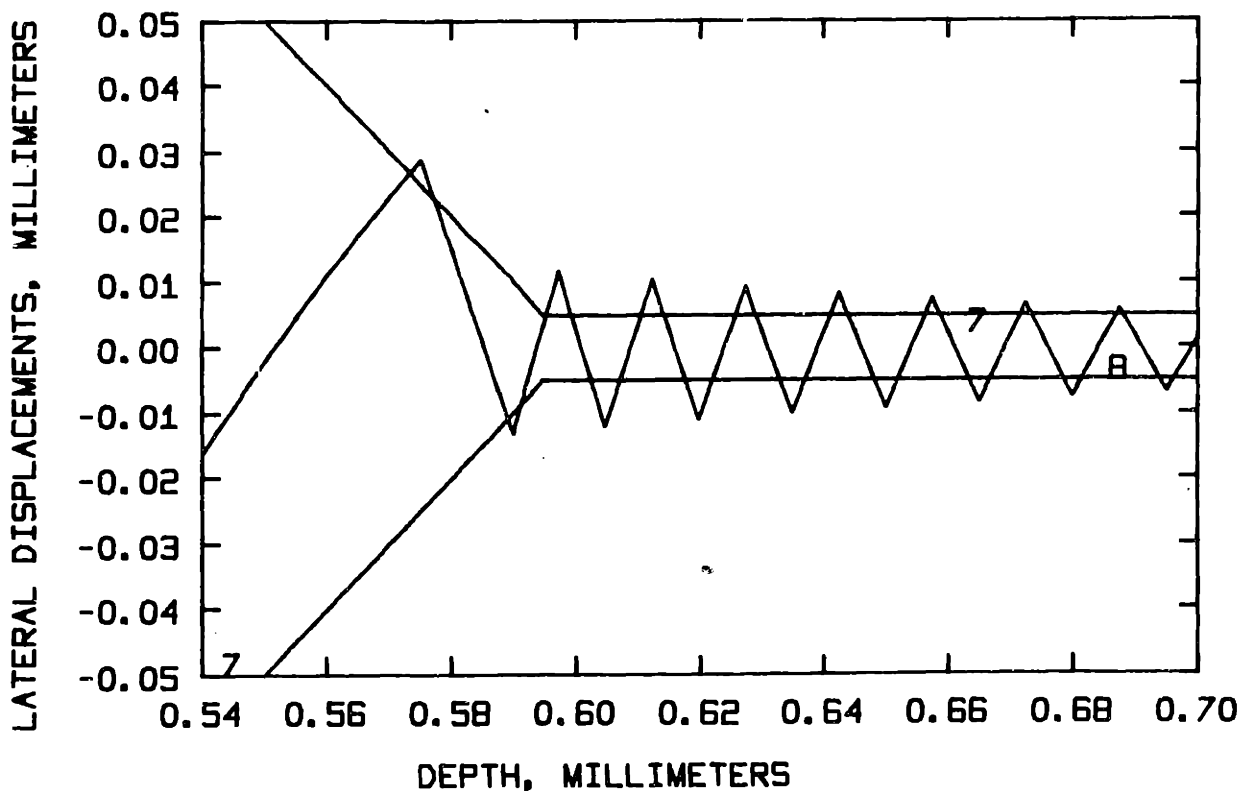


Figure C.6. Enlarged section of figure C.5 showing detail of interaction between bearing and housing during insertion.

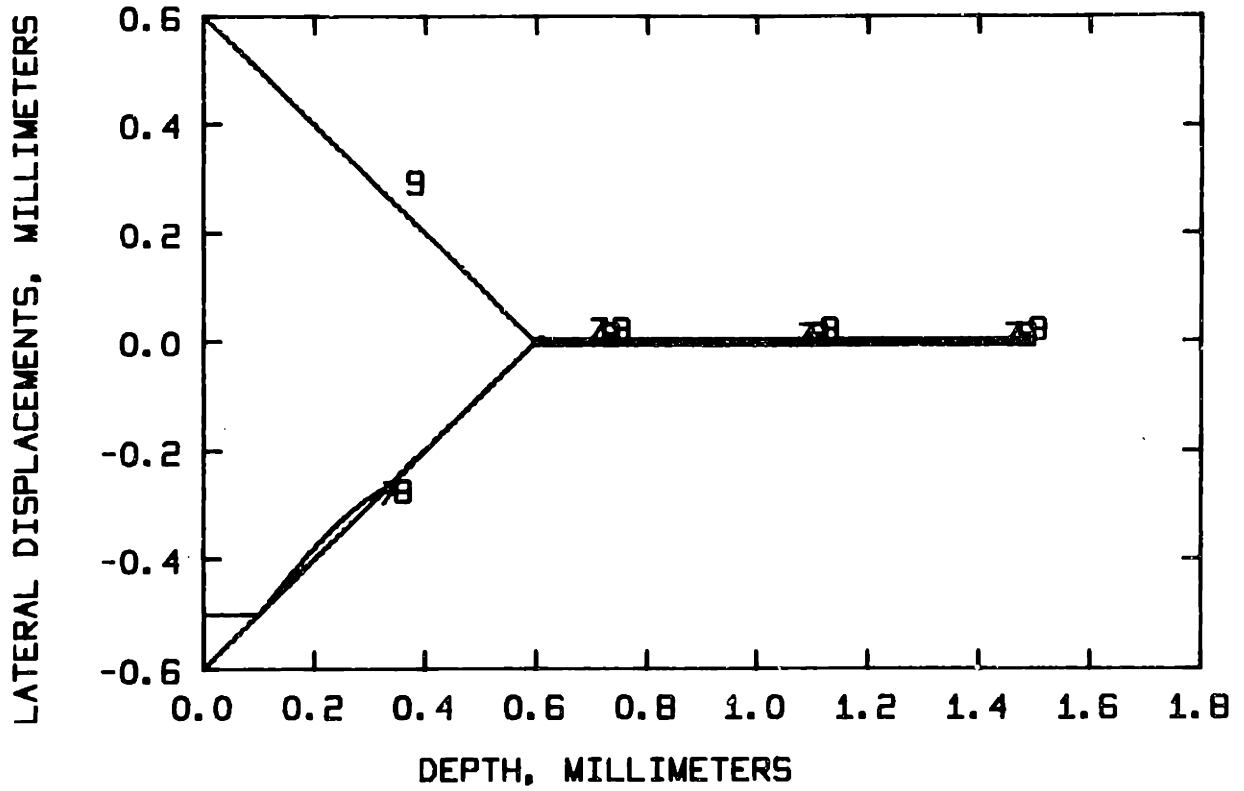


Figure C.7. Digital simulation of bearing bounce during insertion. Impact velocity, 50 mm/sec; coefficient of restitution, 0.3.

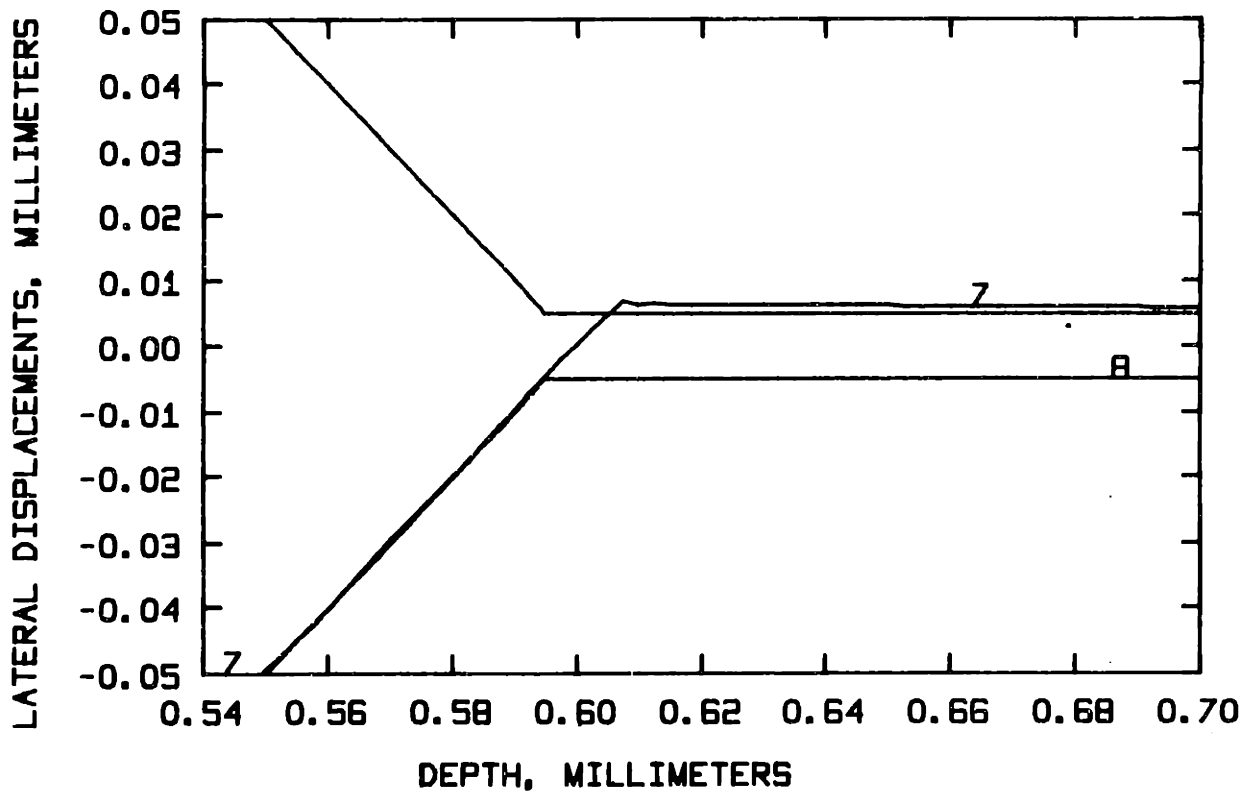


Figure C.8. Enlarged section of figure C.7 showing detail of interaction between bearing and housing during insertion.

C.2. Dynamics of Two-Point Contact

Two-point contact occurs when a part is inserted into a hole that is angularly misaligned with the part (Figure C.9). At low insertion speeds, the moments resulting from the two-point contact will cause the part to rotate about the contact points and come into alignment with the hole. At higher speeds, the two-point impact will cause a significant rotational velocity about the contact points. Because this initial angular velocity is greater than is required when the part is further in the hole, it is possible that the part will bounce to the other side of the hole and undergo another two-point impact. If it impacts sufficiently hard, a series of two-point contacts can be set up.

If the clearance is represented as ζ and the angular error as ϵ_θ , the initial two-point contact will occur at a depth, γ , of:

$$\gamma = \frac{\zeta}{\epsilon_\theta}$$

C.24

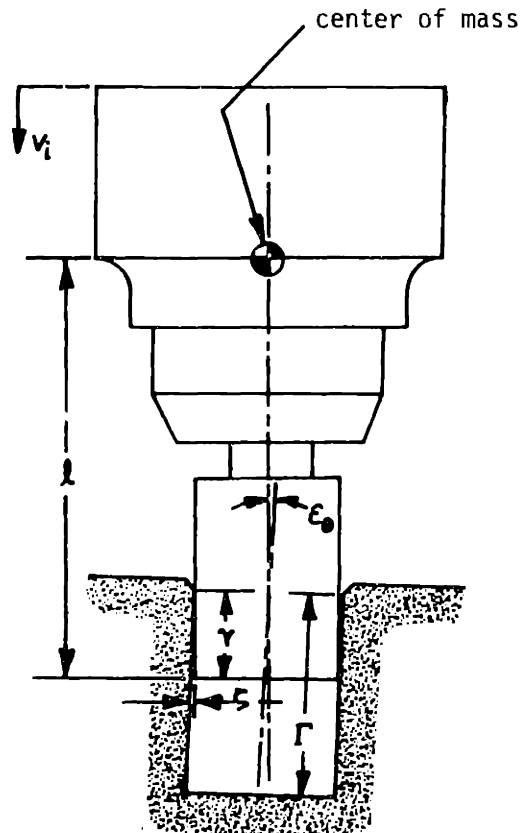


Figure C.9. Part undergoing two-point impact at finite velocity.

The angle between the shaft and the hole at this depth is:

$$\theta = \frac{|\epsilon_{\theta}|}{\epsilon_{\theta}} \zeta \gamma^{-1} \quad \text{C.24}$$

The rate at which this angle changes with respect to the insertion depth is:

$$\frac{d\theta}{d\gamma} = - \frac{|\epsilon_{\theta}|}{\epsilon_{\theta}} \zeta \gamma^{-2} \quad \text{C.25}$$

where the negative value for ϵ_{θ} is chosen to simplify the equations. The sign of initial angular error ϵ_{θ} does not affect the calculated value for the magnitude of v_i .

Differentiating C.26 with respect to time, the angular velocity of the part immediately after the initial two-point contact is geometrically constrained to be:

$$\dot{\theta} = \zeta \gamma^{-2} \dot{\gamma} \quad \text{C.26}$$

As the required angular velocity decreases with the depth, the maximum required angular velocity is the initial angular velocity:

$$\theta = \frac{\epsilon_{\theta}^2 v_i}{\zeta} \quad \text{C.27}$$

where the term v_i has been substituted for $\dot{\gamma}$.

The differential equation describing the motion after the two-point contact is:

$$\ddot{\theta} + \frac{K_{\theta}}{I_p} \theta = 0 \quad \text{C.28}$$

with initial conditions:

$$\theta = 0, \quad \dot{\theta} = \frac{\epsilon_{\theta}^2 v_i}{\zeta} \quad \text{C.29}$$

The moment of inertia, I_p , is taken about the contact points:

$$I_p = I + m\ell^2 \quad \text{C.30}$$

Using the initial conditions to solve for the constants of integration, the solution to the differential equation is:

$$\theta = \frac{\epsilon_{\theta}^2 v_i}{\zeta} \sqrt{\frac{I_p}{K_{\theta}}} \sin \sqrt{\frac{K_{\theta}}{I_p}} t \quad \text{C.31}$$

The maximum displacement occurs at time:

$$t = \frac{\pi}{2} \sqrt{\frac{I_p}{K_{\theta}}} \quad \text{C.32}$$

with an amplitude:

$$\theta = \frac{\epsilon_{\theta}^2 v_i}{\zeta} \sqrt{\frac{I_p}{K_{\theta}}} \quad \text{C.33}$$

This will occur at a depth:

$$\gamma' = \gamma + \frac{v_i \pi}{2} \sqrt{\frac{I_p}{K_{\theta}}} \quad \text{C.34}$$

The maximum total angle that can be tolerated without a secondary two-point contact at this depth is:

$$\theta' = \frac{\zeta}{\gamma} + \frac{\zeta}{\left(\gamma + \frac{v_i \pi}{2} \sqrt{\frac{I_p}{K_{\theta}}} \right)} \quad \text{C.35}$$

The angle that the part has rotated through must be less than or equal to this angle or:

$$\frac{\epsilon_{\theta}^2 v_i}{\zeta} \sqrt{\frac{I_p}{K_{\theta}}} \leq \frac{\zeta}{\gamma} + \frac{\zeta}{\left(\gamma + \frac{v_i \pi}{2} \sqrt{\frac{I_p}{K_{\theta}}} \right)} \quad \text{C.36}$$

Substituting ω for $\sqrt{\frac{K_{\theta}}{I_p}}$, ϵ_{θ} for $\frac{\zeta}{\gamma}$ and regrouping terms on the right,

expression C.36 becomes:

$$\frac{\epsilon_{\theta} v_i}{\gamma \omega} \leq \frac{\frac{2\zeta}{\epsilon_{\theta}} + \frac{\pi v_i}{2\omega}}{\frac{\zeta}{\epsilon_{\theta}} + \frac{\pi v_i}{2\omega}} \quad \text{C.37}$$

Multiplying the term on the left by the denominator on the right and regrouping the terms, it can be seen that this expression is a quadratic expression for $\frac{v_i}{\omega}$:

$$\frac{v_i^2}{\omega^2} + \left(\frac{2-\pi}{\pi}\right) \frac{\zeta v_i}{\epsilon_{\theta} \omega} - \frac{4\zeta^2}{\pi \epsilon_{\theta}} \leq 0 \quad \text{C.38}$$

Solving this expression for $\frac{v_i}{\omega}$:

$$\frac{v_i}{\omega} \leq \frac{\pi}{2} \pm \frac{1}{2} \sqrt{\left(\frac{2-\pi}{\pi}\right)^2 + \frac{16}{\pi} \frac{\zeta}{\epsilon_{\theta}}} \quad \text{C.39}$$

As both v_i and ω must be positive:

$$\frac{v_i}{\omega} \leq 1.5063 \frac{\zeta}{\epsilon_{\theta}} \quad \text{C.40}$$

or:

$$v_i \leq 1.5063 \frac{\zeta}{\epsilon_{\theta}} \sqrt{\frac{K_{\theta}}{I_p}} \quad \text{C.41}$$

The maximum value that v_i could have without setting up a secondary impact was found for the insertion of the ball bearing into the front housing of the automobile alternator. The assumed conditions are listed in Table C.2. With these conditions, the maximum value of v_i that will not result in a secondary impact is 300 mm/sec (11.8 in/sec). As before, this value is not an absolute maximum insertion velocity. It only indicates when problems may occur with the part bouncing from one side of the hole to the other and what parameters affect this problem. These results have not been experimentally verified.

Assumed Conditions

Suspended mass, m	4.060 Kg (8.94 lb_m)
Length, ℓ	90 mm (3.54 in)
Moment of inertia, I	7.137×10^{-3} Kg m^2 (24.4 lb_m in ²)
Moment of inertia, $I_p = I + m\ell^2$	40.02×10^{-3} Kg m^2 (137 lb_m in ²)
Spring constant, K_θ	400 N m/rad (3.55×10^3 lb_f in/rad)
Initial angular error, ϵ	5 mrad (0.29 ^o)
Clearance, ζ	0.02 mm (0.0004 in)

Results

v_i	300 mm/sec (11.81 in/sec)
-------------	---------------------------

Table C.2. Maximum value of v_i that will not result in a secondary two-point contact.

APPENDIX D: COMPLIANCE DESIGN

There is not one optimum compliance design. Rather, there are a large number of different mechanisms or linkages with flexures at the joints, spring-loaded mechanisms or linkages, and deformable structures that can be designed to have the desired properties. This appendix presents some workable design concepts and methods to determine the necessary design parameters.

The three important design parameters for the common task of inserting a round shaft into a round hole are the lateral stiffness, the rotational stiffness, and the center of compliance. The center of compliance is the point in space where a lateral force will cause only a lateral deflection and a moment will cause only a rotational deflection. At this point the compliance matrix is diagonal. A true center of compliance will exist only if the compliance is symmetric about the insertion axis. For applications involving the insertion of a square shaft or a splined shaft into a matching hole or the placement of a part on two or more locating pins, the rotational compliance about the insertion axis is also important. Techniques for experimentally determining the 6 x 6 compliance matrix are given in Appendix E.

The first device built with a center of compliance designed to be at the assembly interface was a mechanism or linkage with flexures at the joints (Figure D.1). It has the advantage that the lateral compliance and the rotational compliance are determined by separate linkages. The center of compliance for small deflections is located at the instantaneous center of the rotational compliance linkage (Figure D.2). As constructed, this mechanism has a number of slender members in compression making it susceptible to both buckling and a spiral collapse instability.

For a lateral deflection δ , each of the flexures at the ends of the links is deflected through an angle δ/l_1 (Figure D.3). Assuming each of the flexures has a rotational stiffness $k_{f\ell}$, the total lateral stiffness of this mechanism is:

$$k_{\ell} = \frac{nk_{f\ell}}{l_1} \tag{D.1}$$

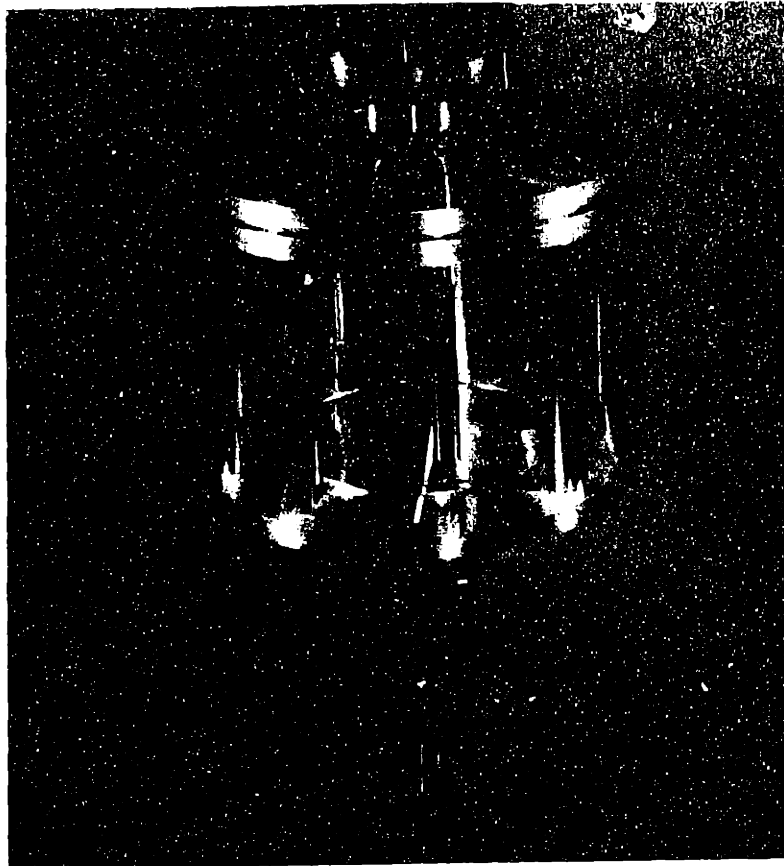


Figure D.1. Original compliance device with the center of compliance at the assembly interface (built by Paul Watson).

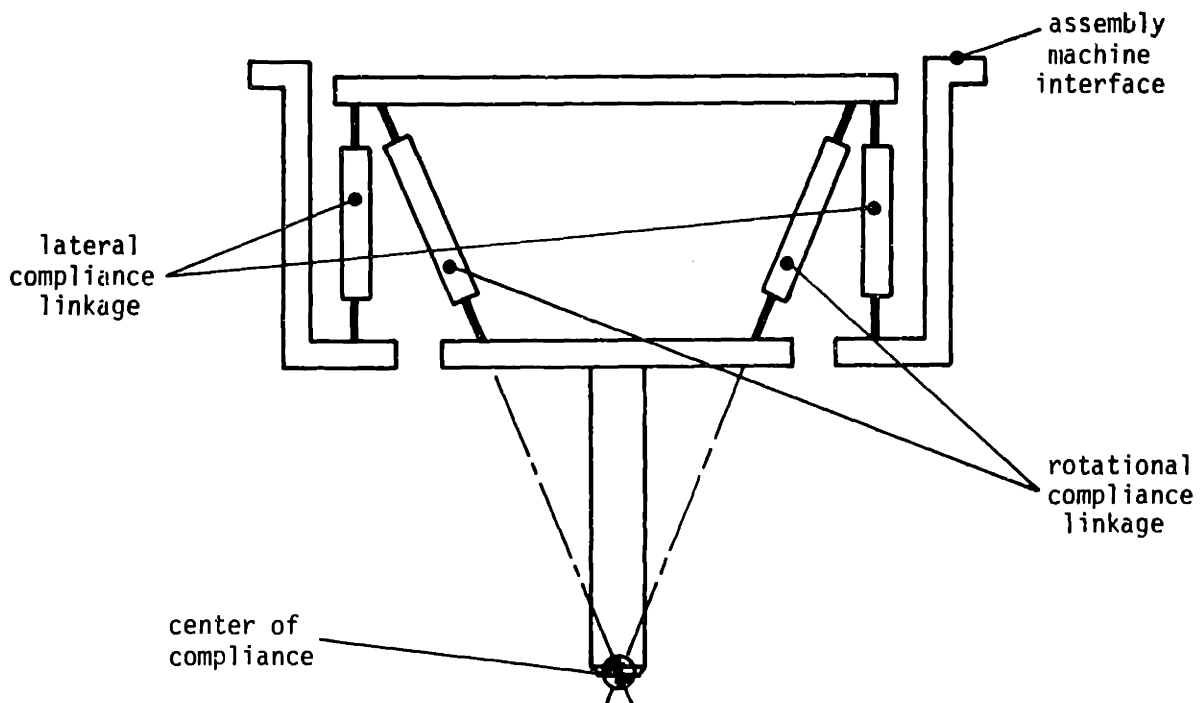


Figure D.2. Schematic representation of the compliance device shown in Figure D.1.

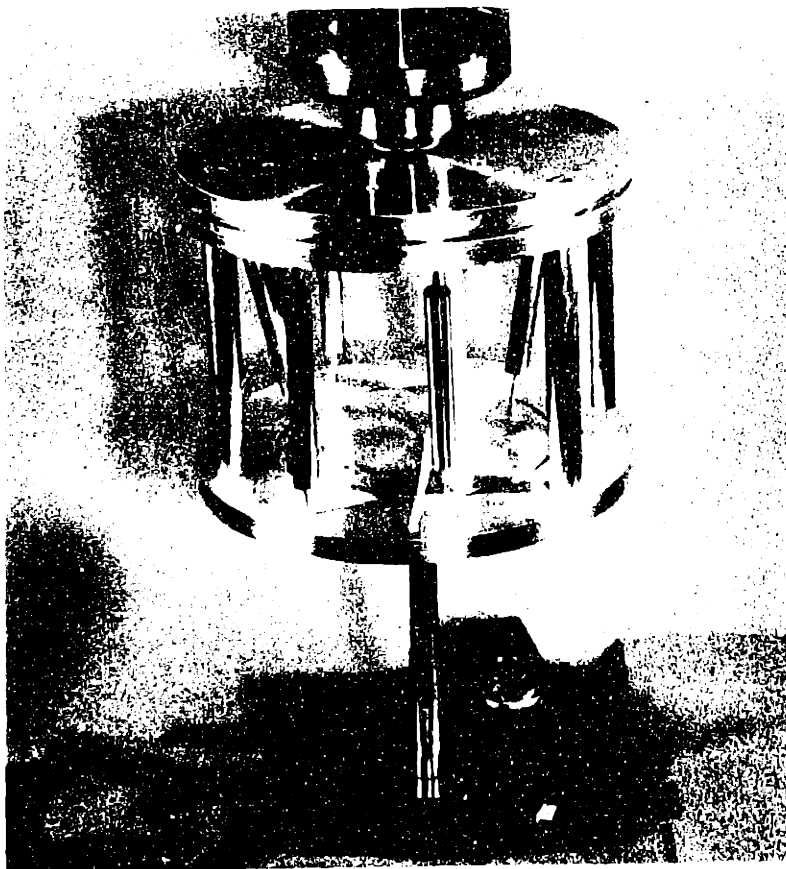


Figure D.1. Original compliance device with the center of compliance at the assembly interface (built by Paul Watson).

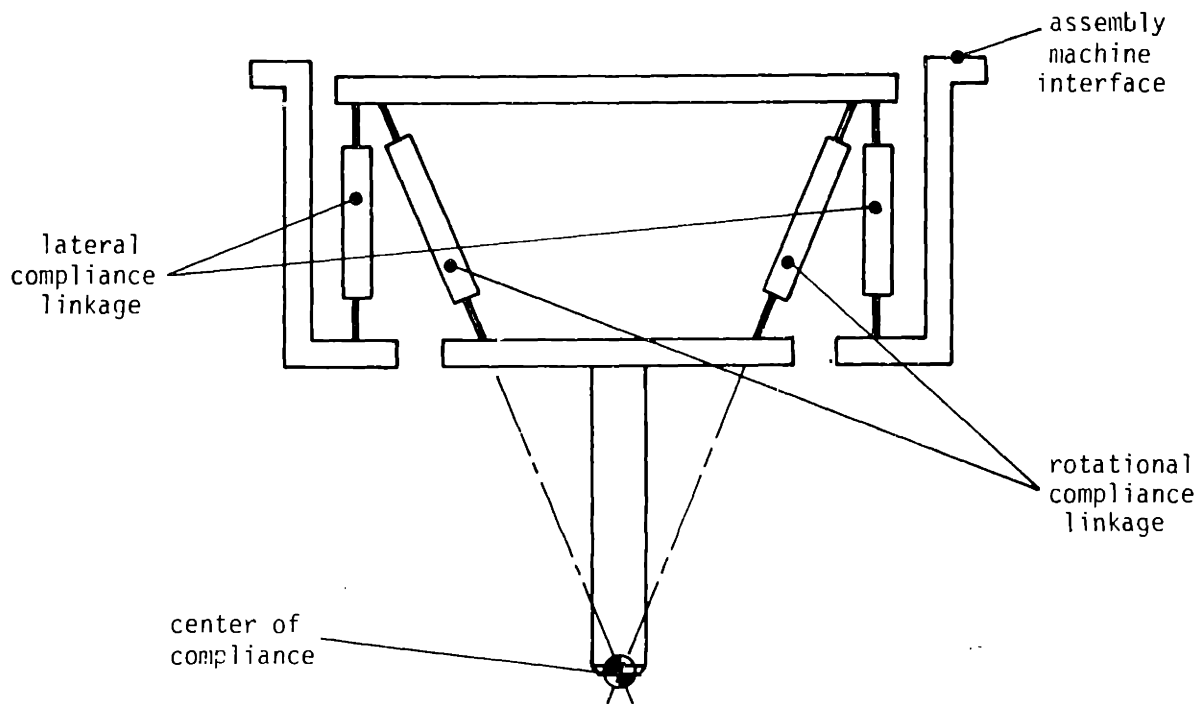


Figure D.2. Schematic representation of the compliance device shown in Figure D.1.

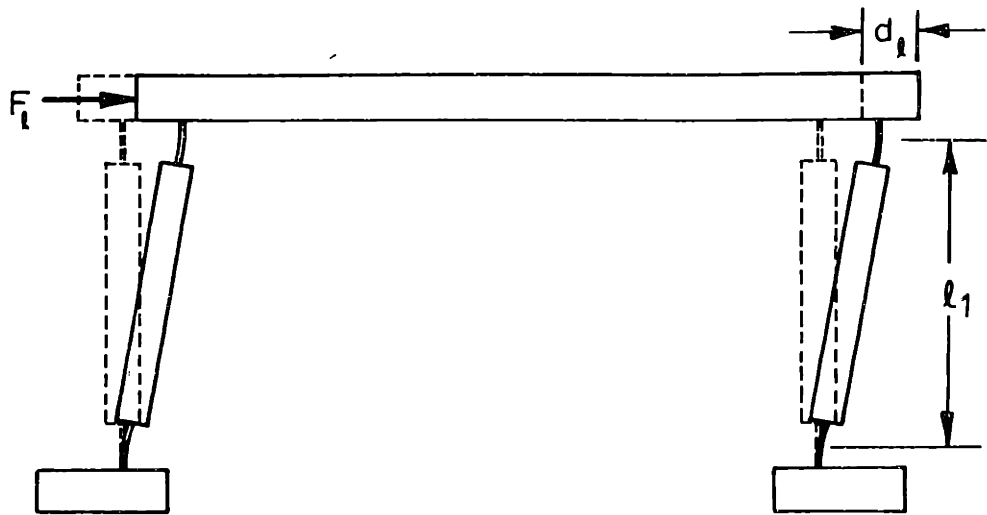


Figure D.3. Deflection of the lateral compliance mechanism part of Figure D.2

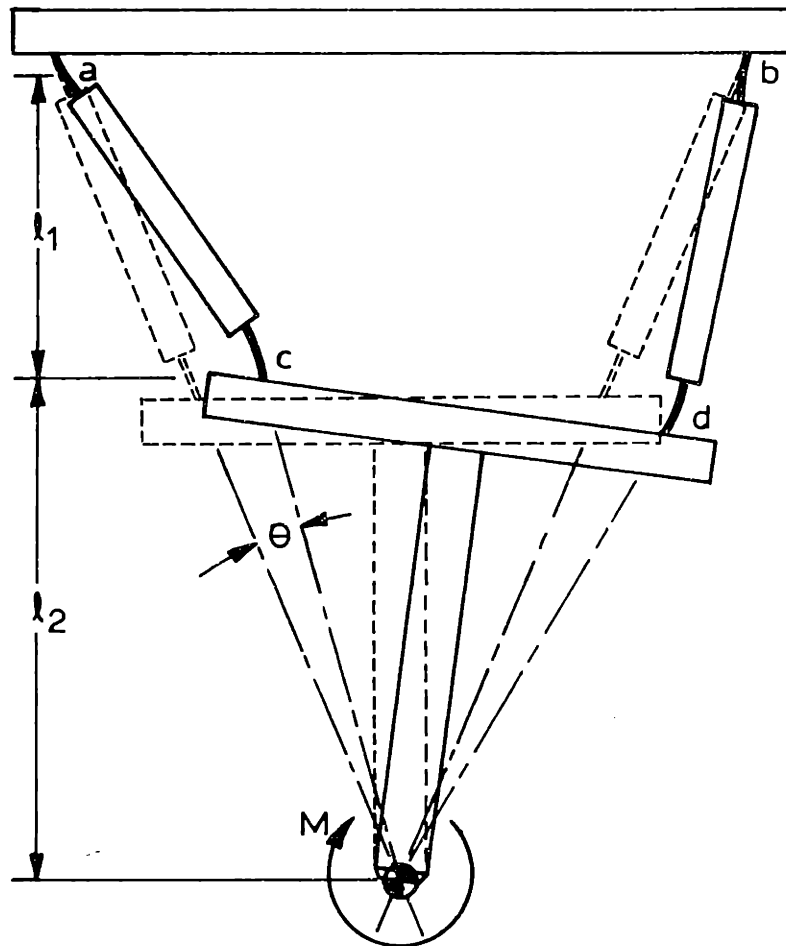


Figure D.4. Deflection of the rotational compliance mechanism part of Figure D.2.

where n is the number of flexures in the mechanism (six for the mechanism shown in Figure D.1). For a rotational deflection θ , the flexures at the top of the rotational compliance structure (points a and b in Figure D.4) are deflected through an angle $\theta \ell_2/\ell_1$, assuming small angle approximations are valid. The flexure at point c is deflected an amount $\theta \ell_2/\ell_1 - \theta$, while the flexure at point d is deflected an amount $\theta \ell_2/\ell_1 + \theta$. As the $-\theta$ and the $+\theta$ terms for points c and d cancel, the total rotational stiffness is:

$$k_{\theta} = nK_{f\theta} \frac{\ell_2}{\ell_1} \quad \text{D.2}$$

where n is again the number of flexures affected, and $k_{f\theta}$ is the rotational compliance of the individual flexures.

Turning this compliant mechanism design upside down (Figure D.5) alleviates some of its problems. The links will be in tension during normal insertion operations, which eliminates both the buckling and the spiral collapse instability.

For experimental verification of the theory and for use in the programmable assembly demonstration project, several distributed compliant structures were designed and built (Figure D.6). While these devices are somewhat more difficult to design because the parameters are coupled, they are compact and easy to fabricate. The slender members are in tension during a normal insertion.

Three parameters need to be specified for the compliance design: the location of the center compliance, the lateral stiffness, and the rotational stiffness. For small angles of deflection, the side structure of the compliance device shown in Figure D.7 has a virtual pivot or instant center at point b while the top structure has a pivot at point a. The center of compliance, point c, is located between these two points, the exact location depending on the relative stiffness between the top structure and the side structure. Three other parameters need to be determined as a function of the center of compliance, the overall lateral stiffness and the overall rotational stiffness: the location of the pivot point or instant center of the side structure, the stiffness of the side structure and the stiffness of the top

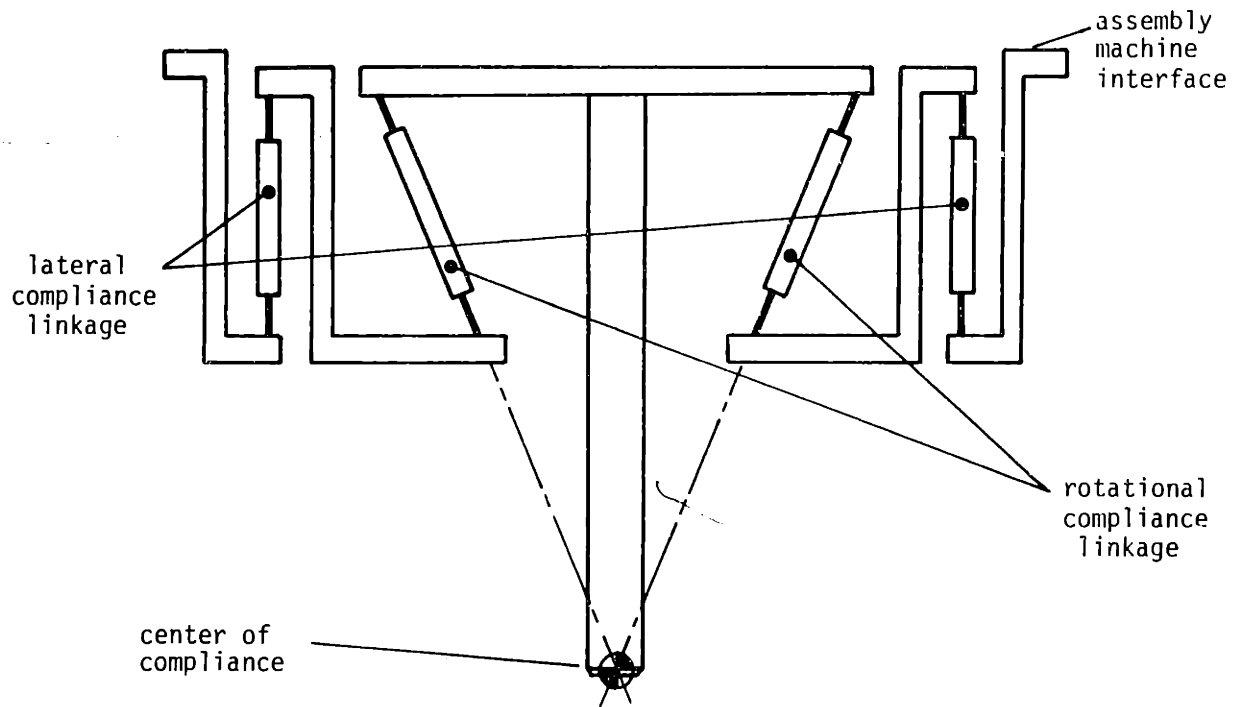


Figure D.5. Schematic representation of a compliance mechanism with all of the links in tension.

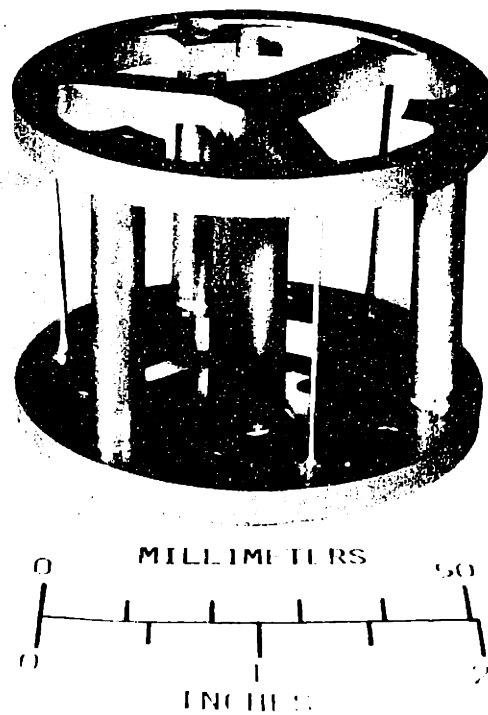


Figure D.6. Photograph of one of the deformable structure compliance devices used in the experimental verification of the theory and in the programmable assembly demonstration project.

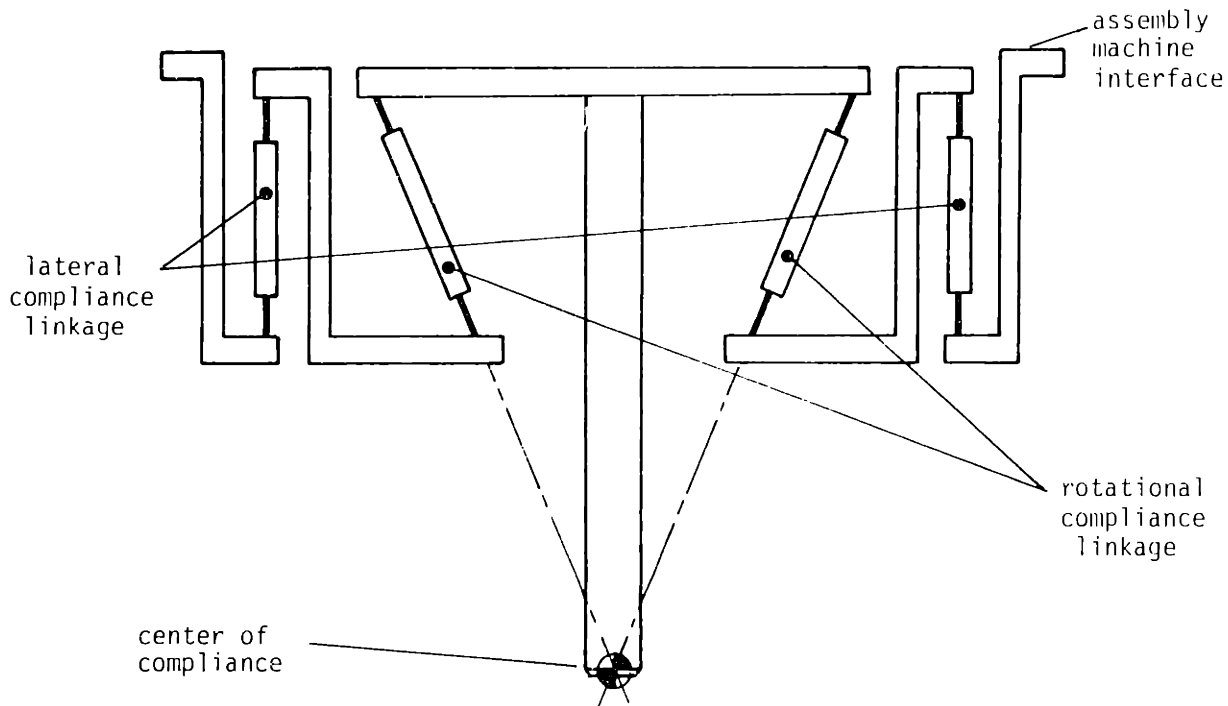


Figure D.5. Schematic representation of a compliance mechanism with all of the links in tension.

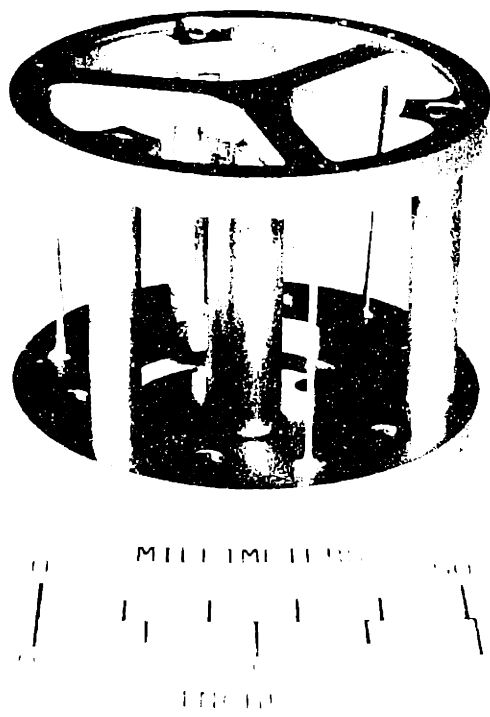


Figure D.6. Photograph of one of the deformable structure compliance devices used in the experimental verification of the theory and in the programmable assembly demonstration project.

structure. Therefore, three independent relationships need to be derived.

At the center of compliance, a lateral force will cause only a lateral deflection. Therefore, referring to Figure D.7, the angular deflection about point a caused by a force applied at the center of compliance, point c, must be equal and opposite to the angular deflection about point b or:

$$\theta_1 = -\theta_2 \quad \text{D.3}$$

If θ_1 is equal and opposite θ_2 at point c, the lateral deflections d_1 and d_2 must be related by:

$$\frac{d_1}{d_2} = \frac{L_1}{L_2} \quad \text{D.4}$$

The total lateral deflection, d , caused by a lateral force applied to the center of compliance is:

$$d = d_1 + d_2 \quad \text{D.5}$$

while the overall lateral stiffness is:

$$k_\ell = \frac{F}{d} \quad \text{D.6}$$

From equations D.4 and D.5 it can be seen that:

$$d_2 = \frac{L_2}{L_1 + L_2} d \quad \text{D.7}$$

Therefore, the lateral stiffness of the side structure is related to the overall lateral stiffness by:

$$k_{\ell 2} = \frac{F}{d_2} = \frac{L_1 + L_2}{L_2} k_\ell \quad \text{D.8}$$

The relationship between the rotational stiffness of the top structure and the overall rotational stiffness can be found by considering the components of lateral deflections due to a lateral force to be angular deflections due to moments about points a and b. The rotational stiffness about point a is:

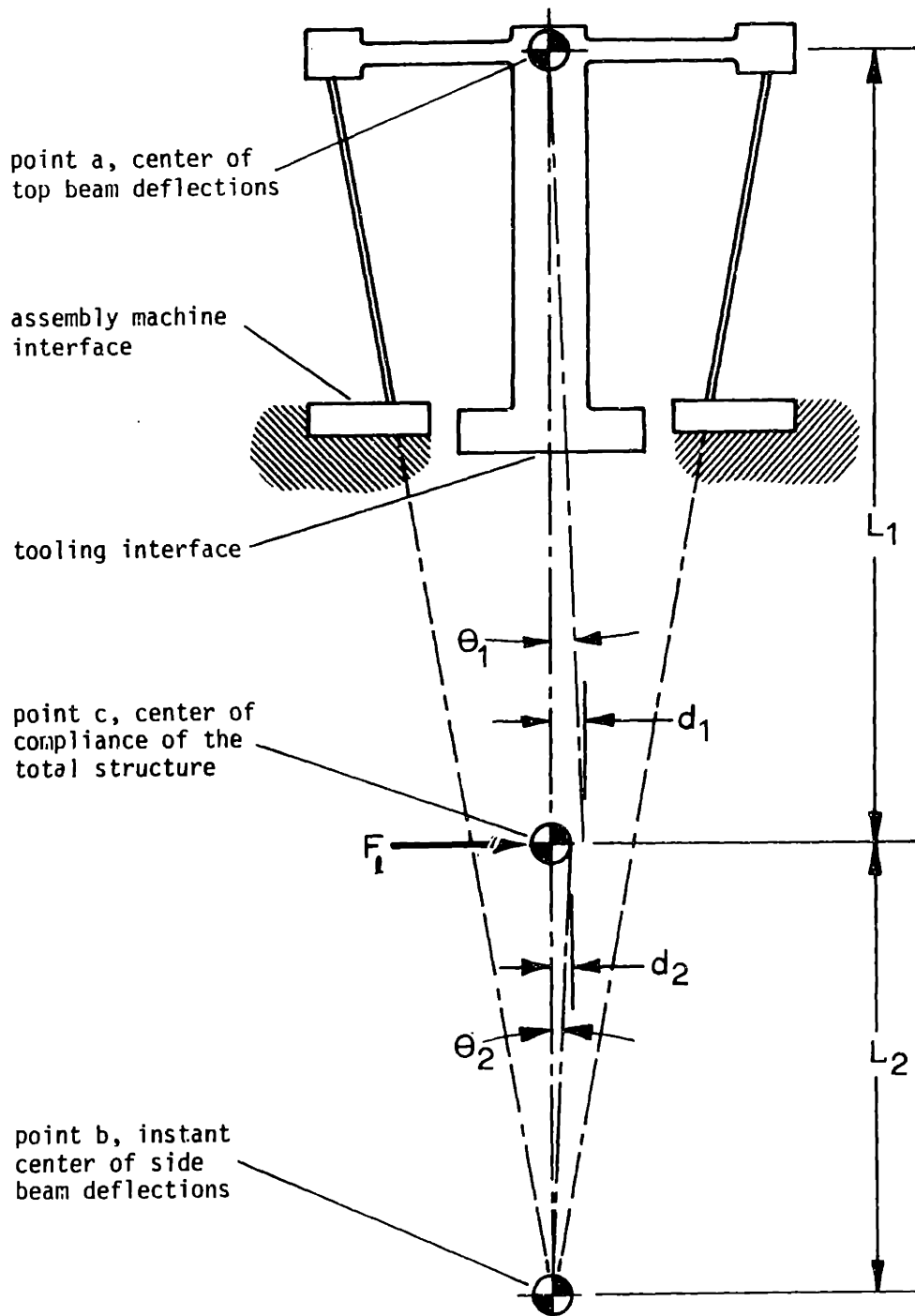


Figure D.7. Schematic drawing of the deformable structure compliance shown in Figure D.6 illustrating the deflections due to a lateral force applied to the center of compliance.

$$k_{\theta 1} = \frac{M_1}{\theta_1} = \frac{FL_1}{\theta_1} \quad \text{D.9}$$

while the rotational stiffness about point b is:

$$k_{\theta 2} = \frac{M_2}{\theta_2} = \frac{-FL_2}{\theta_2} \quad \text{D.10}$$

The overall rotational stiffness is:

$$k_{\theta} = \frac{1}{\frac{1}{k_{\theta 1}} + \frac{1}{k_{\theta 2}}} \quad \text{D.11}$$

Because θ_1 and θ_2 are equal and opposite:

$$k_{\theta 2} = \frac{L_2}{L_1} k_{\theta 1} \quad \text{D.12}$$

Therefore the angular stiffness of the top member is related to the overall angular stiffness by:

$$k_{\theta 1} = \frac{L_1 + L_2}{L_2} k_{\theta} \quad \text{D.13}$$

The third relationship must relate the location of the pivot point for the side structure to the location of the center of compliance, the overall lateral stiffness, and the overall rotational stiffness.

The lateral stiffness of the top structure is:

$$k_{\ell 1} = \frac{F}{d_1} \quad \text{D.14}$$

while the angular stiffness of the top structure is:

$$k_{\theta 1} = \frac{M_1}{\theta_1} = \frac{FL_1^2}{d_1} \quad \text{D.15}$$

Therefore:

$$k_{\theta 1} = L_1^2 k_{\ell 1} \quad \text{D.16}$$

Using equation 11 and finding an expression similar to equation D.8 for $k_{\ell 1}$:

$$k_{\ell 1} = \frac{L_1 + L_2}{L_1} k_{\ell} \quad \text{D.17}$$

equation D.16 becomes:

$$k_{\theta} = (L_1 L_2) k_{\ell} \quad \text{D.18}$$

or

$$L_2 = \frac{k_{\theta}}{L_1 k_{\ell}} \quad \text{D.19}$$

In summary, to design a distributed compliant structure similar to the device shown in Figure D.6, select appropriate values for L_1 , k_{ℓ} and k_{θ} . Solve for L_2 using:

$$L_2 = \frac{k_{\theta}}{L_1 k_{\ell}} \quad \text{D.19}$$

Then find $k_{\ell 2}$ and $k_{\theta 1}$ using:

$$k_{\ell 2} = \frac{L_1 + L_2}{L_2} k_{\ell} \quad \text{D.8}$$

and

$$k_{\theta 1} = \frac{L_1 + L_2}{L_2} k_{\theta} \quad \text{D.13}$$

Note that instead of using equations D.8 and D.13, it is also possible to use equation D.17:

$$k_{\ell 1} = \frac{L_1 + L}{L_1} k_{\ell} \quad \text{D.17}$$

along with an equation that relates the rotational stiffness of the side structure to the overall rotational stiffness:

$$k_{\theta 2} = \frac{L_1 + L_2}{L_1} k_{\theta} \quad \text{D.20}$$

The actual dimensions for the structures are found using simple beam theory. Referring to Figure D.8, it can be shown from symmetry that the vertical deflection of the center point of the top structure caused by a moment is zero. The fact

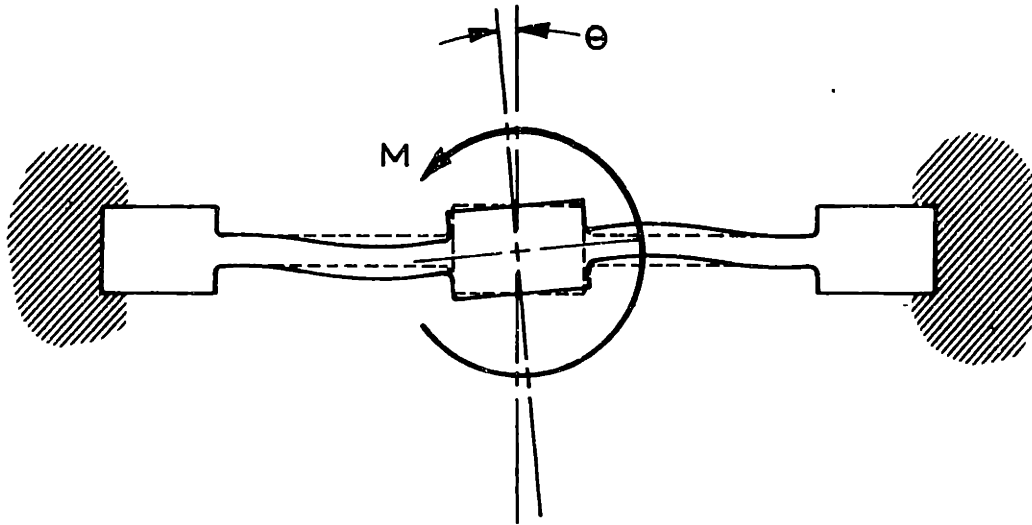


Figure D.8. Idealized deflection of the top structure caused by an applied moment.

that the structure, as built, has threefold geometry with beams located every 120° instead of the planar geometry shown in Figure D.8 does not affect these calculations. It can be shown that, except for small errors caused by the torsional compliance of these beams, each of the two beams located 30° from the centerline contributes one half the stiffness that the beam 90° from the centerline contributes. Therefore the structure in Figure D.8 can be cut at the centerline and each half treated as a simple cantilever beam. The deflection at the end of a cantilever beam caused by a moment is:

$$\delta_M = + \frac{M\ell_1^2}{2E_1I_1} \quad \text{D.21}$$

where M is the moment, ℓ_1 is the length of the cantilever beam, E_1 is Young's modulus, and I_1 is the moment of inertia of the beam cross section for the top structure. The deflection at the end of a cantilever beam caused by a force applied at the end is:

$$\delta_F = + \frac{F\ell_1^3}{3E_1I_1} \quad \text{D.22}$$

As the total deflection must equal zero:

$$\frac{F\ell_1}{3} = \frac{-M}{2} \quad \text{D.23}$$

With a moment M being applied to the beam, the force seen at the end of the beam must be:

$$F = \frac{-3M}{2\ell_1} \quad \text{D.24}$$

The slope or angular deflection at the end of the cantilever beam due to the combined force and moment is:

$$\theta = \frac{M\ell_1}{E_1 I_1} - \frac{3M\ell_1}{4E_1 I_1} = \frac{M\ell_1}{4E_1 I_1} \quad \text{D.25}$$

Therefore, the rotational stiffness of this cantilever beam is:

$$\frac{M}{\theta} = \frac{4E_1 I_1}{\ell_1} \quad \text{D.26}$$

As the other half of the structure contributes an equal stiffness, the total rotational stiffness of the top structure is approximately:

$$k_{\theta_1} = \frac{8E_1 I_1}{\ell_1} \quad \text{D.27}$$

Using equation D.13, the total rotational stiffness k_{θ} is:

$$k_{\theta} = \left(\frac{L_2}{L_2 + L_1} \right) \frac{8E_1 I_1}{\ell_1} \quad \text{D.28}$$

For the design of the compliant structure shown Figure D.6, beams with a rectangular cross section were used. The width of the beams were fixed and the thickness calculated to give the structure the desired rotational stiffness.

The stiffness of the side structure is calculated in an analogous manner. An approximation to the side structure is made. Instead of having the beams converging on point b as shown in Figure D.7, the beams are considered to be parallel as shown in Figure D.9. Due to the parallelogram nature of this structure, it can be argued that the ends of the beams will not undergo any angular deflection when the

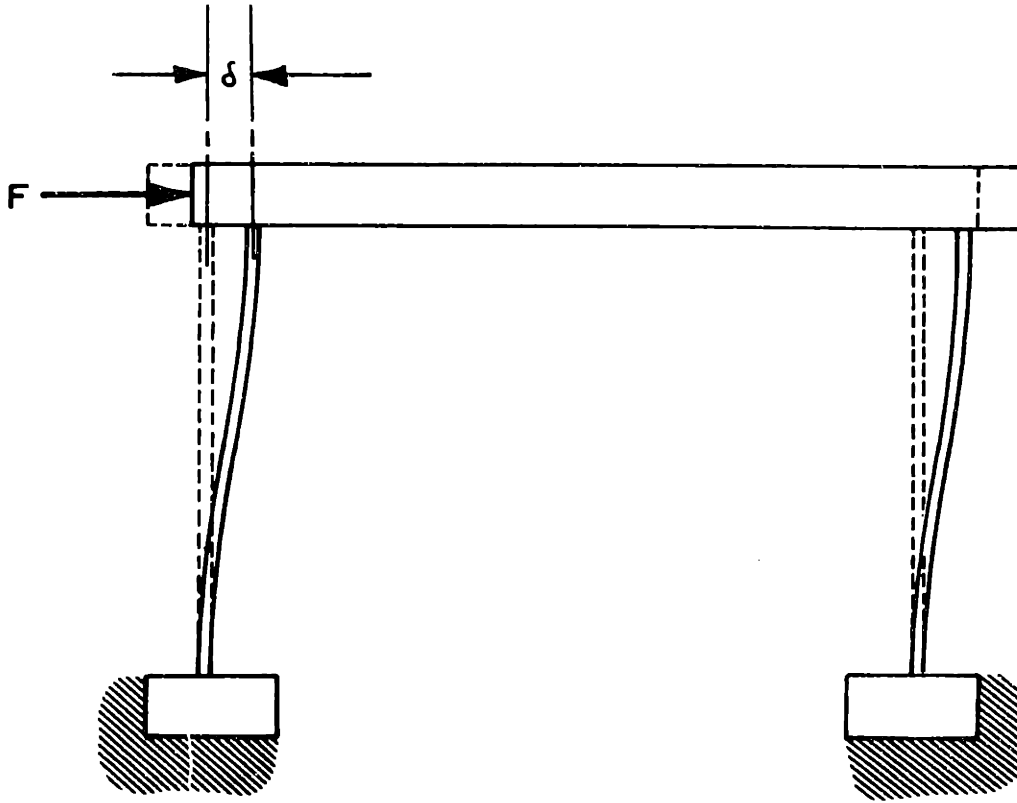


Figure D.9. Idealized deflection of the side structure caused by an applied lateral force.

top of the structure is subjected to a lateral force.

The beams can now be treated as simple cantilever beams and the necessary conditions found that will cause the rotational deflection to be zero. The angular deflection due to a force at the end of the beam is:

$$\theta_F = \frac{F\ell_2^2}{2E_2I_2} \quad \text{D.29}$$

where E_2 , I_2 and ℓ_2 are the Young's modulus, the moments of inertia, and the length of the beams in the side structure. The angular deflection due to a moment applied to the beam is:

$$\theta_M = \frac{M\ell_2}{E_2I_2} \quad \text{D.30}$$

Because the total angular deflection must be zero:

$$\frac{F\ell_2^2}{2E_2I_2} + \frac{M\ell_2}{E_2I_2} = 0 \quad \text{D.31}$$

With a force F being applied to the end of this beam the moment on the beam must be:

$$M = -\frac{F\ell_2}{2} \quad \text{D.32}$$

The total lateral deflection due to this force and moment is:

$$\delta = \frac{F\ell_2^3}{3E_2I_2} - \frac{F\ell_2^3}{4E_2I_2} = \frac{F\ell_2^3}{12E_2I_2} \quad \text{D.33}$$

Therefore, the lateral stiffness of this beam is:

$$\frac{F}{\delta} = \frac{12E_2I_2}{\ell_2^3} \quad \text{D.34}$$

Because the structure as built has three beams, the total stiffness to a lateral force applied to the top of the structure is:

$$\frac{F}{\delta} = \frac{36E_2I_2}{\ell_2^3} \quad \text{D.35}$$

The structure with the canted beams has a virtual pivot point or instantaneous center at the point where lines extended from these beams intersect. Referring to Figure D.7, it can be seen that a force F at the center of compliance will cause a force at the top of the structure of

$$F_T = F \left(\frac{L_2}{L_1 + L_2} \right) \quad \text{D.36}$$

and a deflection δ at the center of compliance translates into a deflection at the top of the structure of

$$\delta_T = \delta \left(\frac{L_1 + L_2}{L_2} \right) \quad \text{D.37}$$

Therefore, the lateral stiffness of the side structure, k_{ℓ_2} , to a force applied to the center of compliance is approximately:

$$k_{\ell 2} = \left(\frac{L_1 + L_2}{L_2} \right)^2 \frac{36 E_2 I_2}{\ell_2^3} \quad \text{D.38}$$

Using equation D.8, the total lateral stiffness k_{ℓ} is:

$$k_{\ell} = \left(\frac{L_1 + L_2}{L_2} \right) \frac{36 E_2 I_2}{\ell_2^3} \quad \text{D.39}$$

This design procedure is only an approximation and will not yield an exact solution. The structure in Figure D.6 was designed to have a center of compliance 200 mm (7.9 in) from the top, a lateral stiffness of 10 N/mm (55 lb_f/in) and a rotational stiffness of 0.40 Nm/mrad (6.5 in-lb_f/mrad). The actual measured values yields a center of compliance 145 mm from the top structure, a lateral stiffness of almost exactly 12 N/mm (1320 lb_f/in) and a rotational stiffness of approximately 0.42 Nm/mrad (6.8 in lb_f/in). Part of the error in the location of the center of compliance is attributed to the compliance of the force sensor. The accuracy to which the structure can be built depends to an extent on the size of the compliant structure compared to the distance from the center of compliance to the top of the structure.

One problem with the compliant structure in the above design is that it exhibits almost no damping. Because the compliance has a low natural frequency, it is possible to excite the structure with the motion of the assembly machine when the compliance is unlocked. One proposed solution is to build a distributed compliance similar to that shown in Figure D.10. The joints are made using a elastomer similar to that used in shock mounts while the links are assumed to be rigid members. Another proposed solution is to build a compliance device using metal/elastomer laminates (Figure D.11). Because the ratio of bulk modulus to shear modulus is very high for elastomers, the deformations of the laminates are almost entirely shear deformations. It should also be possible to build a device with the desired compliance characteristics using a single elastomer element by balancing the relative shear and compression/extension deformations (Figure D.12). A major advantage of these last two designs is that they should be capable of supporting relatively large compressive loads.

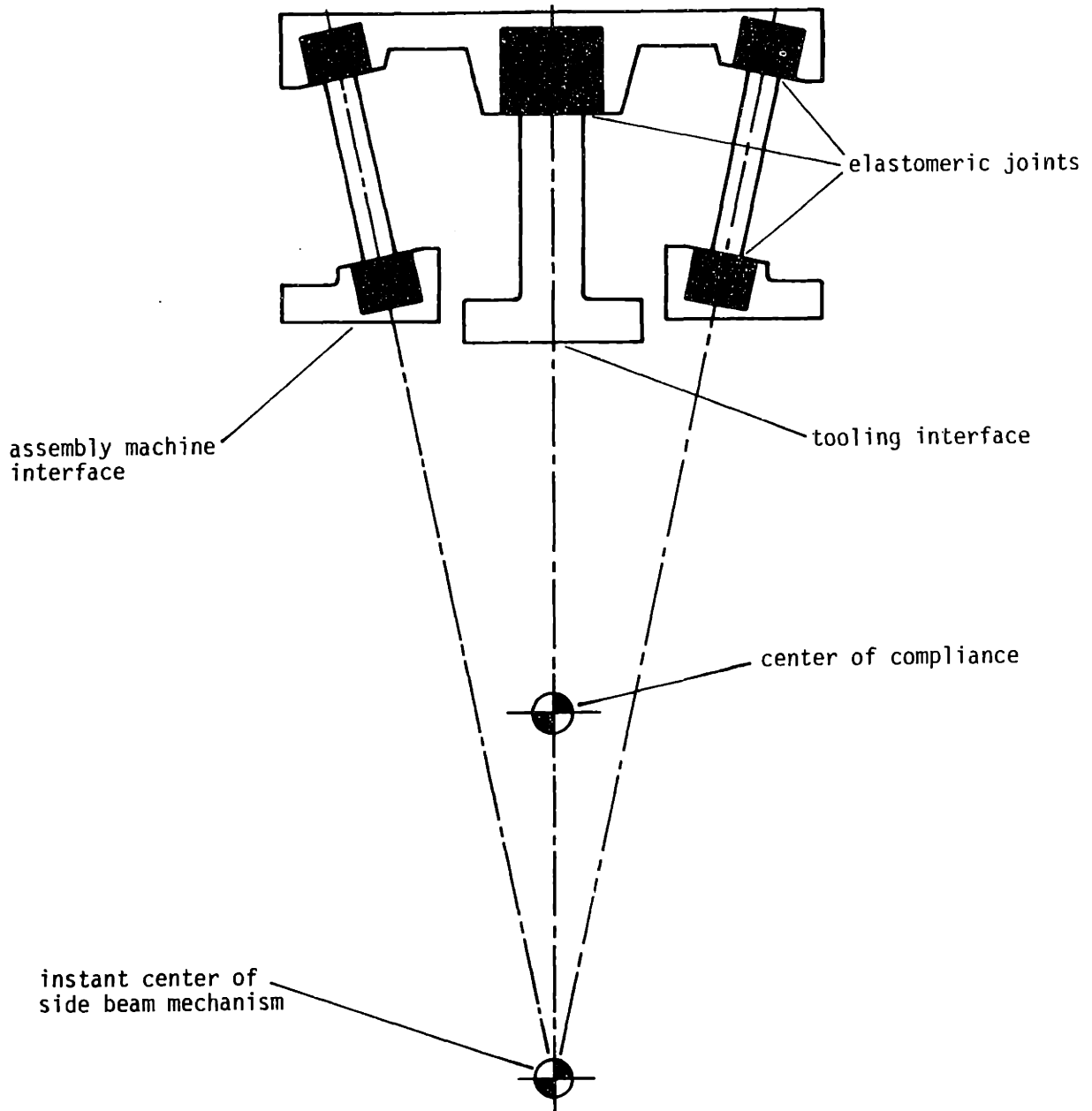


Figure D.10. Distributed compliant mechanism using elastomeric joints.

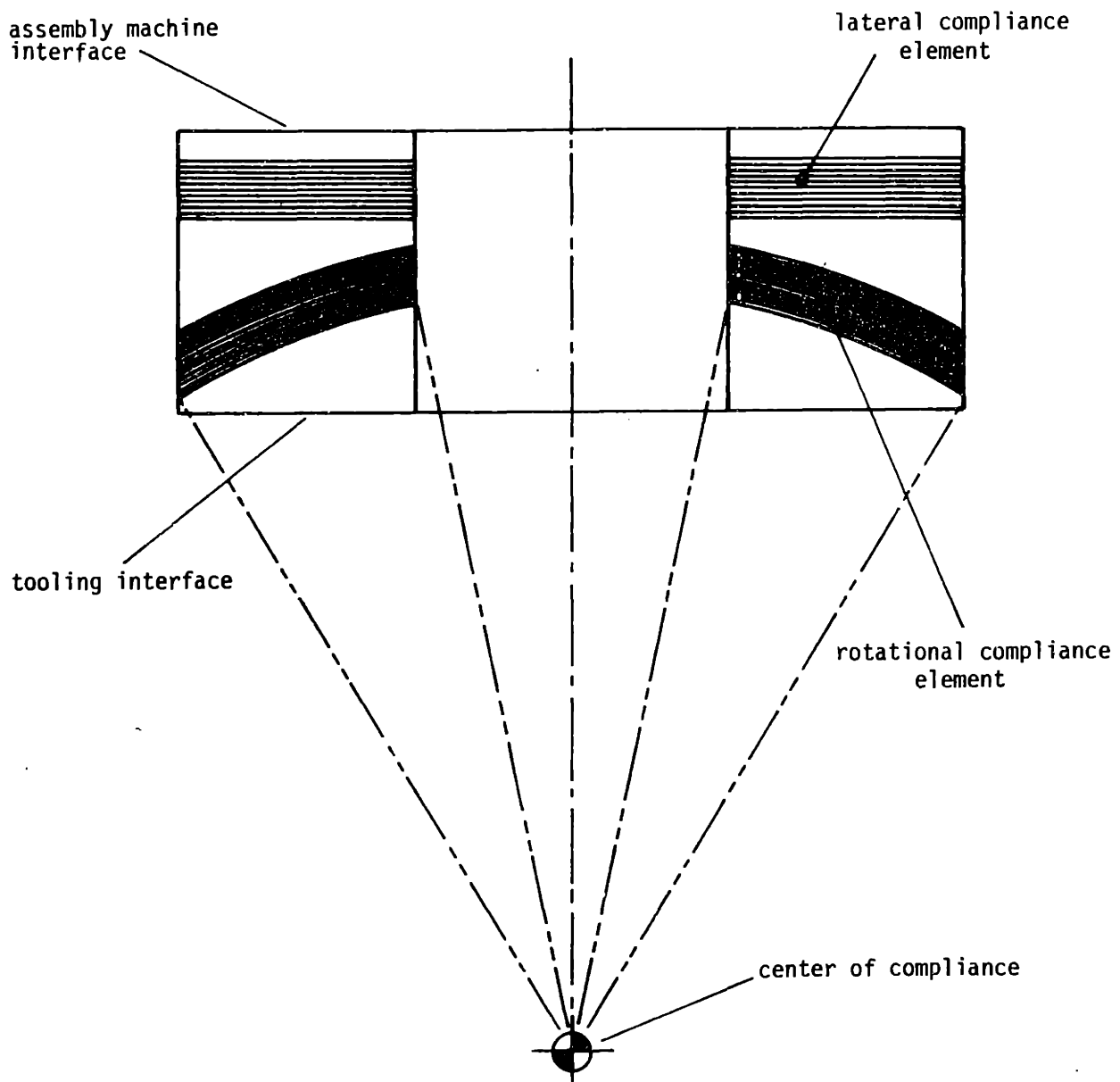


Figure D.11. Compliance device using two elastomeric elements that deform only in shear.

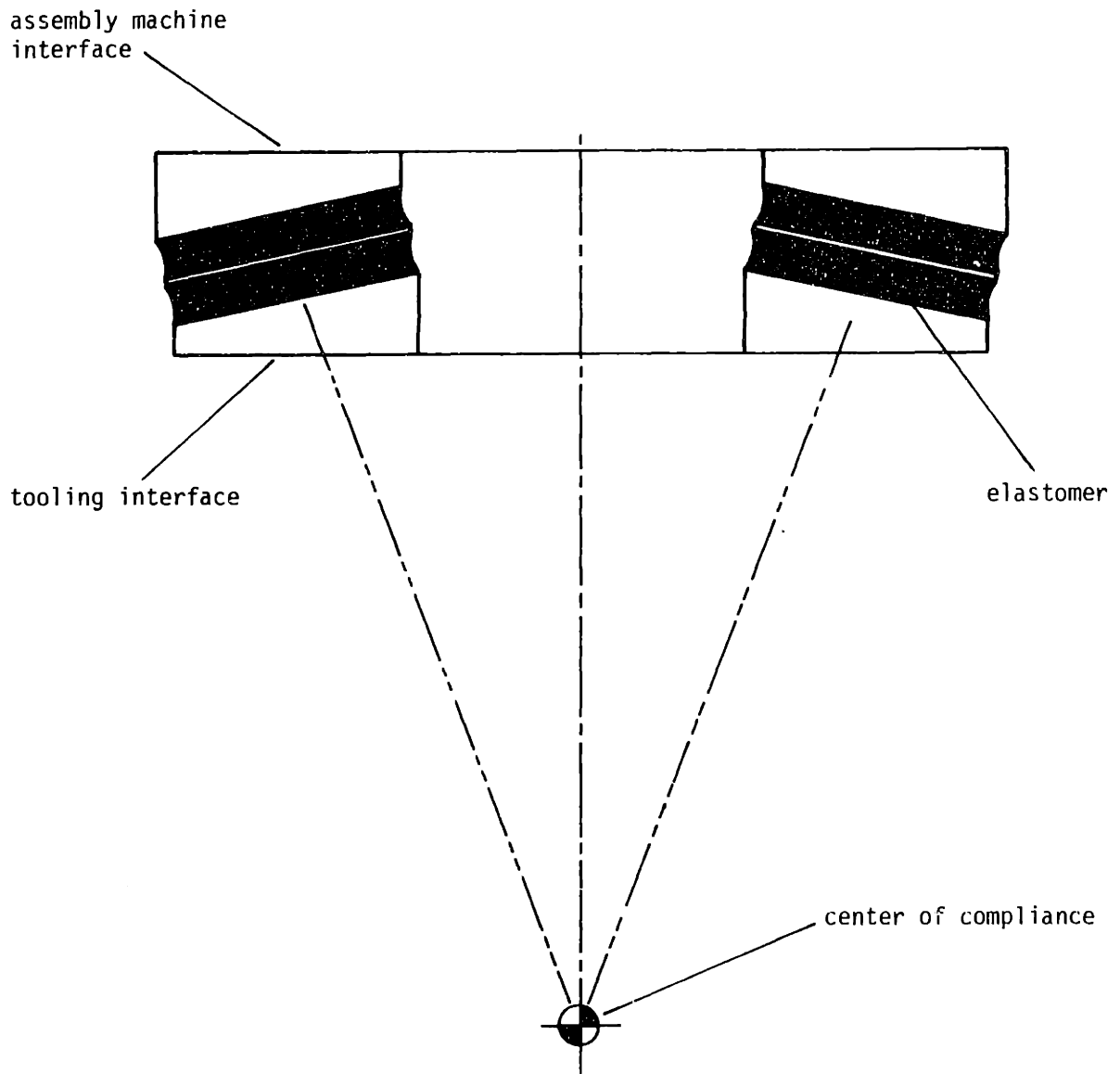


Figure D.12. Compliance device using an elastomeric element that deforms in both shear and compression/extension.

APPENDIX E: DETERMINATION OF THE COMPLIANCE MATRIX

The general 6 x 6 compliance matrix relates a six-dimensional displacement vector to a six-dimensional force vector at a point in space. This matrix can be found experimentally in a manner analogous to the determination of the force sensor calibration matrix (see Appendix G). Six known linearly independent displacements are forced, one at a time, upon the compliant device while the six components of the force vector referenced to the same point in space as the displacements, are recorded for each displacement.

This information is arranged in the form:

$$\begin{bmatrix} f_{11} & f_{12} & \dots & f_{16} \\ f_{21} & f_{22} & \dots & f_{26} \\ \cdot & & & \\ \cdot & & & \\ \cdot & & & \\ f_{61} & f_{62} & \dots & f_{66} \end{bmatrix} = \begin{bmatrix} s_{11} & s_{12} & \dots & s_{16} \\ s_{21} & s_{22} & \dots & s_{26} \\ \cdot & & & \\ \cdot & & & \\ \cdot & & & \\ s_{61} & s_{62} & \dots & s_{66} \end{bmatrix} \begin{bmatrix} d_{11} & d_{12} & \dots & d_{16} \\ d_{21} & d_{22} & \dots & d_{26} \\ \cdot & & & \\ \cdot & & & \\ \cdot & & & \\ d_{61} & d_{62} & \dots & d_{66} \end{bmatrix} \quad \text{E.1}$$

or:

$$F = SD \quad \text{E.2}$$

where $f_{11} f_{21} \dots f_{61}$ are the force vector components obtained when the compliance is subject to the first displacement vector with components $d_{11} d_{21} \dots d_{61}$; $f_{12} f_{22} \dots f_{62}$ are the force components obtained when the compliance is subject to the second displacement, etc. The stiffness matrix S is the inverse of the compliance matrix C .

The stiffness matrix found by the relationship:

$$S = FD^{-1} \quad \text{E.3}$$

and the compliance matrix is found by inverting the stiffness matrix:

$$C = S^{-1} \quad \text{E.4}$$

The compliance matrix can be determined in a single step with only one inversion using the relationship:

$$C = S^{-1} = \left[FD^{-1} \right]^{-1} \quad \text{E.5}$$

or:

$$C = DF^{-1} \quad E.6$$

It is also possible to determine the compliance matrix by turning the procedure around and measuring the displacements that result from six linearly independent force vectors being applied one at a time to the compliance. In this case the information would be arranged in the form:

$$\begin{bmatrix} d_{11} & d_{12} & \dots & d_{16} \\ d_{21} & d_{22} & \dots & d_{26} \\ \cdot & & & \\ \cdot & & & \\ \cdot & & & \\ d_{61} & d_{62} & \dots & d_{66} \end{bmatrix} = \begin{bmatrix} c_{11} & c_{12} & \dots & c_{16} \\ c_{21} & c_{22} & \dots & c_{26} \\ \cdot & & & \\ \cdot & & & \\ \cdot & & & \\ c_{61} & c_{62} & \dots & c_{66} \end{bmatrix} \begin{bmatrix} f_{11} & f_{12} & \dots & f_{16} \\ f_{21} & f_{22} & \dots & f_{26} \\ \cdot & & & \\ \cdot & & & \\ \cdot & & & \\ f_{61} & f_{62} & \dots & f_{66} \end{bmatrix} \quad E.7$$

or:

$$D = CF \quad E.8$$

where $d_{11} \ d_{21} \ \dots \ d_{61}$ are the measured components of the displacement vector obtained when the compliance is subjected to the first vector with components $f_{11} \ f_{21} \ \dots \ f_{61}$, etc. In this case, the compliance matrix can be found by the relationship:

$$C = DF^{-1} \quad E.9$$

and, if desired, the stiffness matrix can be found by the relationship:

$$S = C^{-1} = \left[DF^{-1} \right]^{-1} \quad E.10$$

or:

$$S = FD^{-1} \quad E.11$$

This technique is probably not practical for finding the full 6 x 6 compliance matrix due to the difficulty of measuring six displacement components. However, it may be a practical method for obtaining a 2 x 2 planar compliance matrix. The advantage of this technique is that it does not require a multi-axis force sensor.

The 6 x 6 compliance matrix for several of the experimental compliant structures was obtained by the first technique. The forces were measured with a six-axis force sensor and the displacements were imposed on the structure using a mil-

ling machine and a tilting rotary table (Figure E.1). The particular displacements used formed an orthogonal set but it is only necessary that they be linearly independent. The input displacement components, the output force components, and the resulting compliance matrix for one of the compliant structures is given in Table E.1. Note that:

$$\begin{bmatrix} c_{11} & c_{51} \\ c_{15} & c_{55} \end{bmatrix} \quad \text{E.12}$$

and:

$$\begin{bmatrix} c_{22} & c_{42} \\ c_{24} & c_{44} \end{bmatrix} \quad \text{E.13}$$

are the components for the 2 x 2 compliance matrices for x, θ_y and y, θ_x respectively. The measured compliance matrices should be symmetric. The extent to which they are not symmetric is an indication of measurement errors.

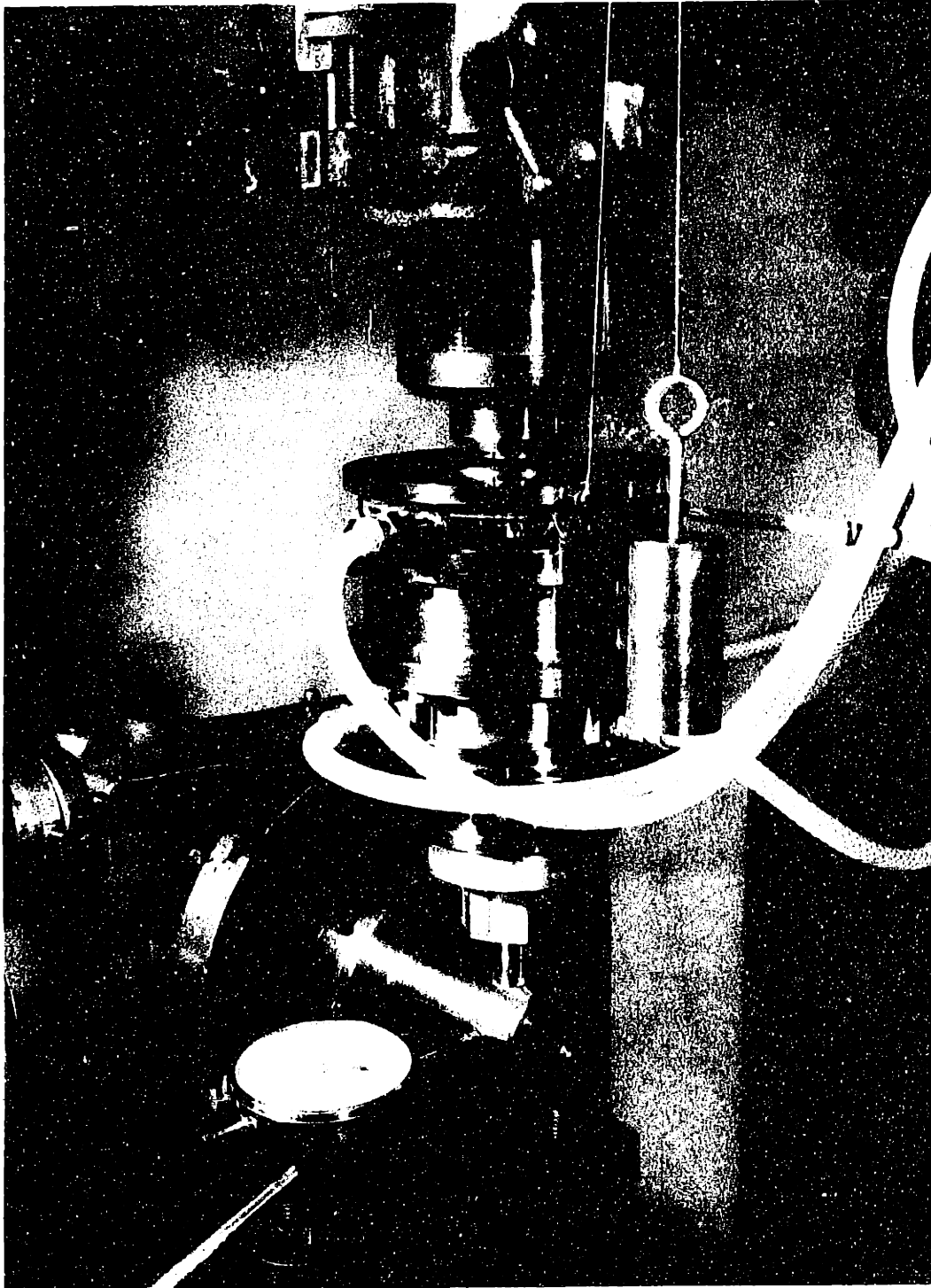


Figure E.1. Apparatus used to experimentally determine the 6 X 6 compliance matrix.

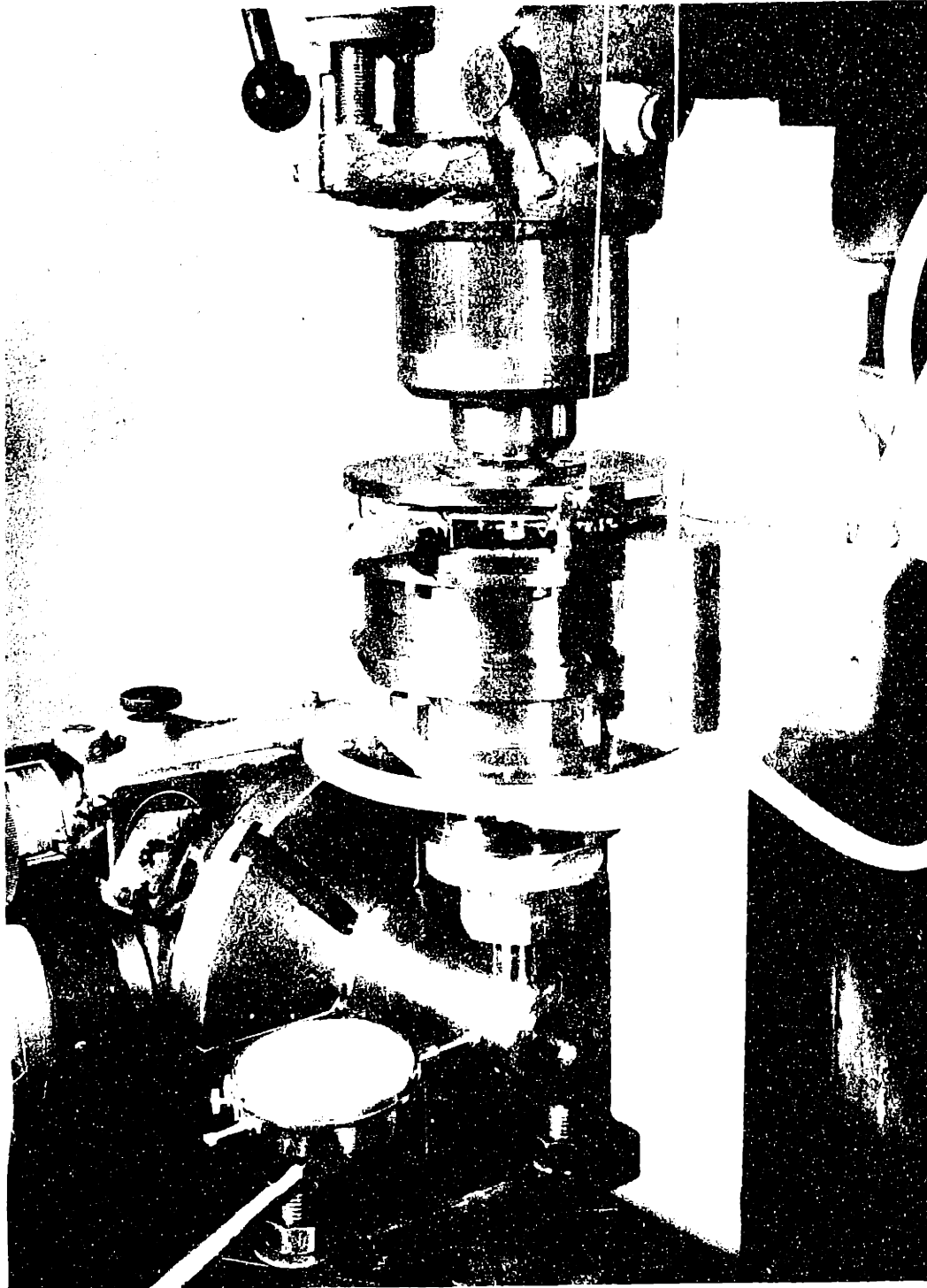


Figure E.1. Apparatus used to experimentally determine the 6 X 6 compliance matrix.

Matrix of Input Displacement Vectors					
+1.0000	+0.0000	+0.0000	+0.0000	+0.0000	+0.0000
+0.0000	+1.0000	+0.0000	+0.0000	+0.0000	+0.0000
+0.0000	+0.0000	+0.1000	+0.0000	+0.0000	+0.0000
+0.0000	+0.0000	+0.0000	+5.8180	+0.0000	+0.0000
+0.0000	+0.0000	+0.0000	+0.0000	+5.8180	+0.0000
+0.0000	+0.0000	+0.0000	+0.0000	+0.0000	+52.3600

Matrix of Measured Force Vectors					
+13.2100	-0.7180	-1.5920	+1.7190	+6.2780	+0.5280
+0.5200	+13.3130	+0.9570	-7.6610	+1.7760	-1.2750
-5.3570	+10.6960	+143.7710	-27.7980	-14.6930	-50.0930
+0.2250	-0.9590	-0.2500	+3.0940	+0.1290	+0.0110
+0.9200	+0.2380	-0.1610	-0.0250	+2.8890	-0.3740
+0.0030	+0.0120	+0.0270	+0.0210	+0.0000	+0.3880

Compliance Calibration Matrix					
+0.0898 [*]	+0.0058	+0.0007	-0.0292	-0.1937 [*]	-0.1955
-0.0034	+0.0924 [@]	-0.0004	+0.2255 [@]	-0.0614	+0.1955
-0.0001	-0.0004	+0.0007	+0.0047	+0.0036	+0.0916
-0.0374	+0.1651 [@]	+0.0023	+2.3246 [@]	-0.1127	+0.7121
-0.1655 [*]	-0.0580	+0.0007	-0.0426	+2.4148 [*]	+2.4551
-0.0122	-0.2169	-0.0260	-1.6724	+0.0816	+130.9437

^{*} these values form a 2x2 compliance matrix for x and θ_y .
[@] these values form a 2x2 compliance matrix for y and θ_x .

Table E.1. Matrices of the input displacement vectors and the measured force vectors and the resulting compliance calibration matrix for one of the deformable structure compliance devices.

APPENDIX F: FORCE SENSOR DESIGN

The experimental force and moment data in this thesis was taken using a series of six-axis force sensors based on prior work [37],[25]. The major difference between these force sensors and other multi-axis force sensors is that no attempt is made to mechanically separate the force responses along the different axes. The separation is achieved by multiplying the transducer output vector (strain gage voltages; in this case) by a predetermined calibration matrix. Techniques for obtaining this calibration matrix are discussed in the following appendix.

The major advantage of this force sensor design is that it utilizes a very simple mechanical structure. It is not necessary to precisely balance or null the gages nor is it important that the gages be located in an exact location or orientation. It is also not important that the structure be machined to tight tolerances. The major disadvantage is that it is necessary to use a processor capable of multiplying the 6×6 calibration matrix by the six-dimensional transducer output vector to obtain the force vector. However, if the force data is ultimately going to be processed using a digital computer, this is not a serious problem.

The sensors that were used in this work are essentially cylinders that were cut away to leave three equally spaced legs (Figures F.1 through F.3). On two of the sensors, an extensional strain gage and a half-shear bridge strain gage pair were bonded to each leg. On the third sensor, two of each gage type were applied to each leg to increase the sensitivity to strength ratio of the sensor. The extensional gages are intended to primarily measure the elongation and compression, not the bending of the legs. The outputs from these gages primarily contribute to the measurement of f_z , m_x , and m_y . The half-shear-bridge pairs are intended to measure shear forces applied to the legs. The outputs from these gage pairs primarily contribute to the measurement of f_x , f_y and m_z . The cross couplings that result from the fact that these are not pure measurements of extension or compression and shear are eliminated by the 6×6 calibration matrix.

The cutaway cylindrical structure is not the only design that will work. The only requirements are that the structure be stable (i.e. there are no joints that

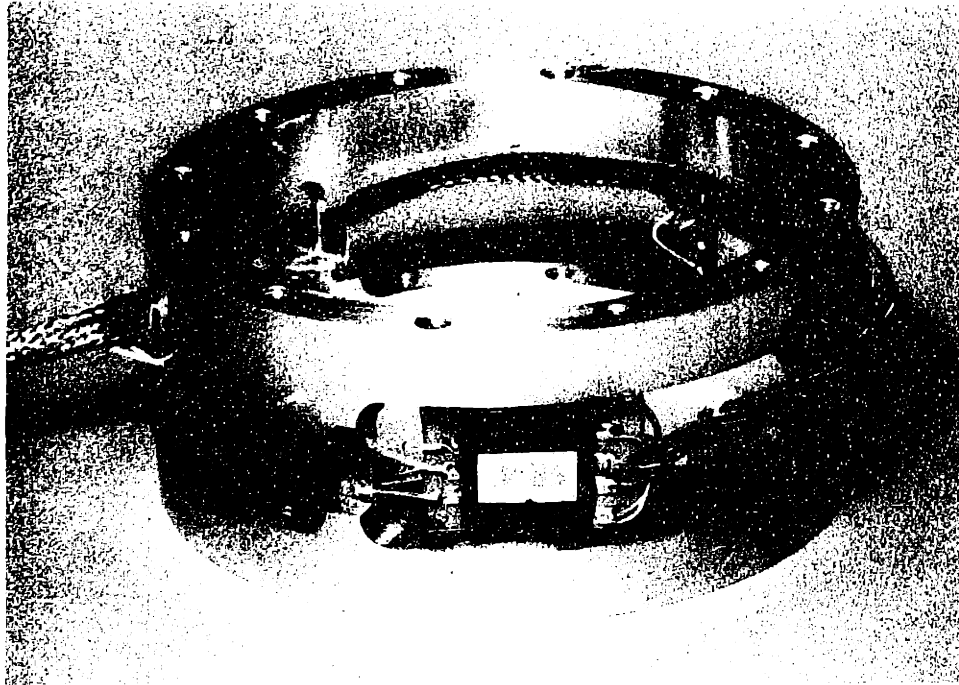


Figure F.1. Original aluminum six-axis wrist force sensor.

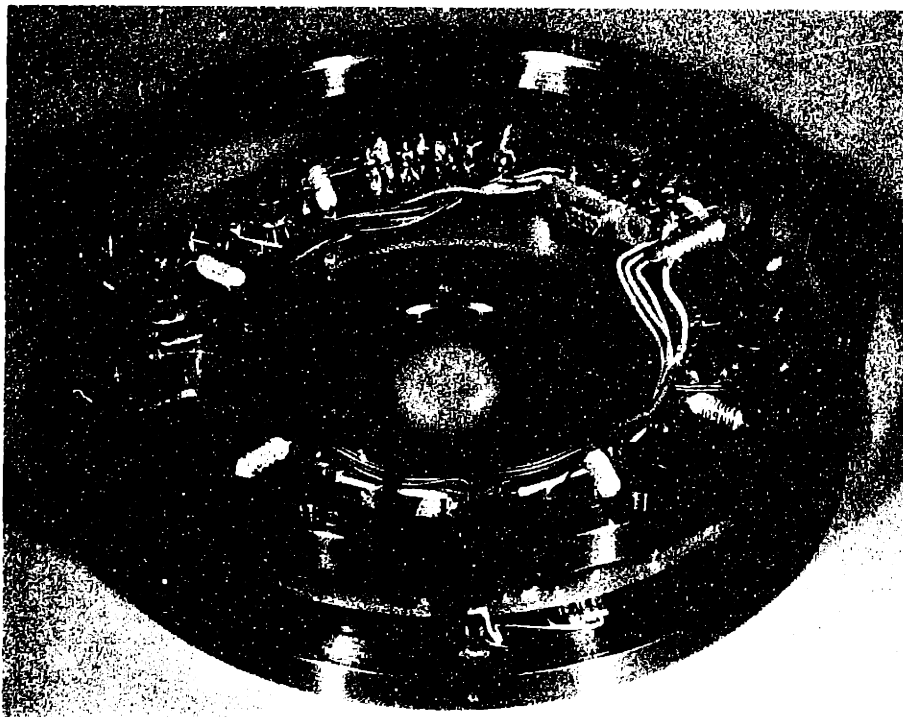


Figure F.2. Steel six-axis force sensor with integrated instrumentation amplifier package.

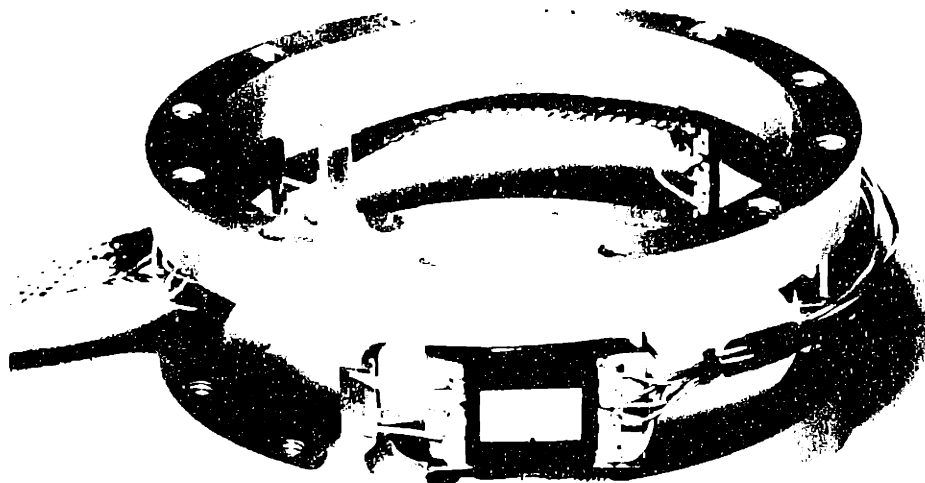


Figure F.1. Original aluminum six-axis wrist force sensor.

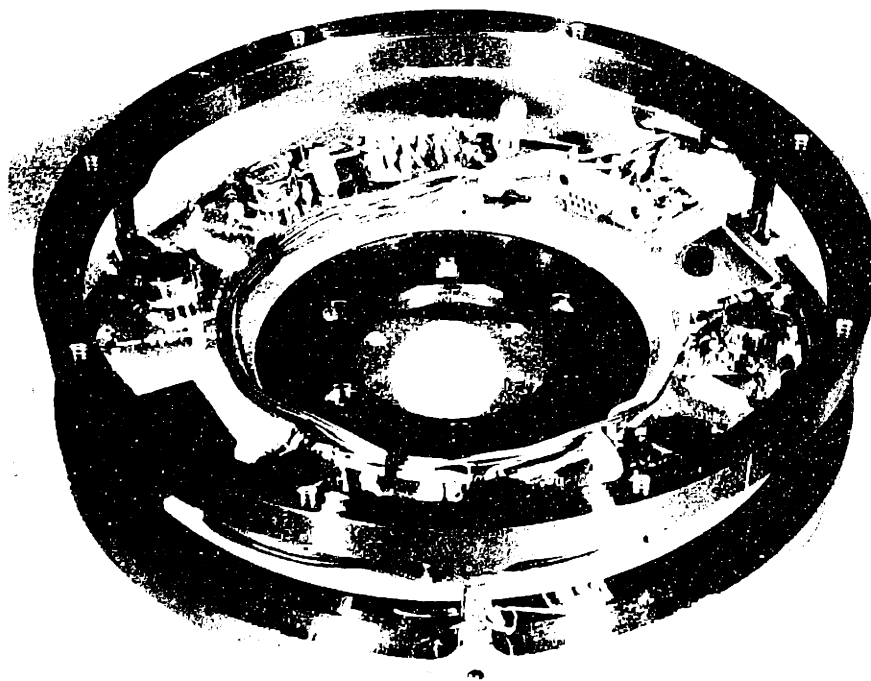


Figure F.2. Steel six-axis force sensor with integrated instrumentation amplifier package.

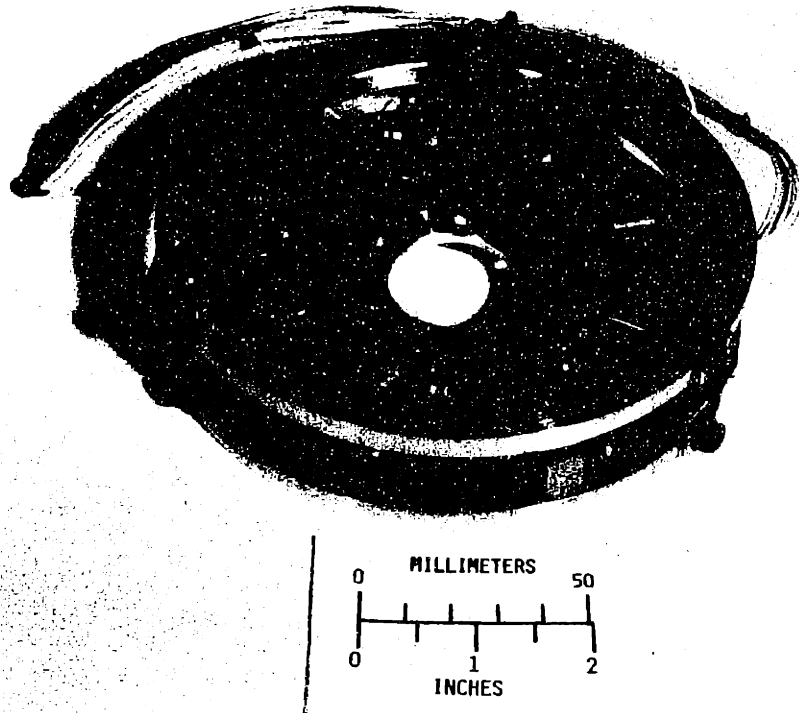


Figure F.3. High-sensitivity aluminum six-axis force sensor.

slip when the structure is loaded), the deflections that occur must be linear with respect to the forces, and that the transducers be placed so that the output vector spans the space corresponding to the input (i.e., there is no non-zero input which results in a zero output). The signal to noise ratio will be improved if the structure tend to concentrate the deflections at the transducers and tends to separate the responses. The output response of the transducers must either be linear or be linearized before multiplying by the calibration matrix.

The important parameters that affect the sensitivity of the force sensors used in this thesis are the cross-sectional area of each leg, the modulus of elasticity (Young's modulus), the shear modulus, the radius at which the legs are located, the gage factor or the strain gages used, and the gain of the instrumentation amplifiers. Metallic foil strain gages with a gage factor of approximately 2 (i.e., the ratio of the change in resistance of the gage in response to change in strain is 2) were used. Single-chip integrated circuit instrumentation amplifiers with a maximum gain of 1000 were used with all of the sensors. The amplifiers for

INTENTIONAL DUPLICATE EXPOSURE

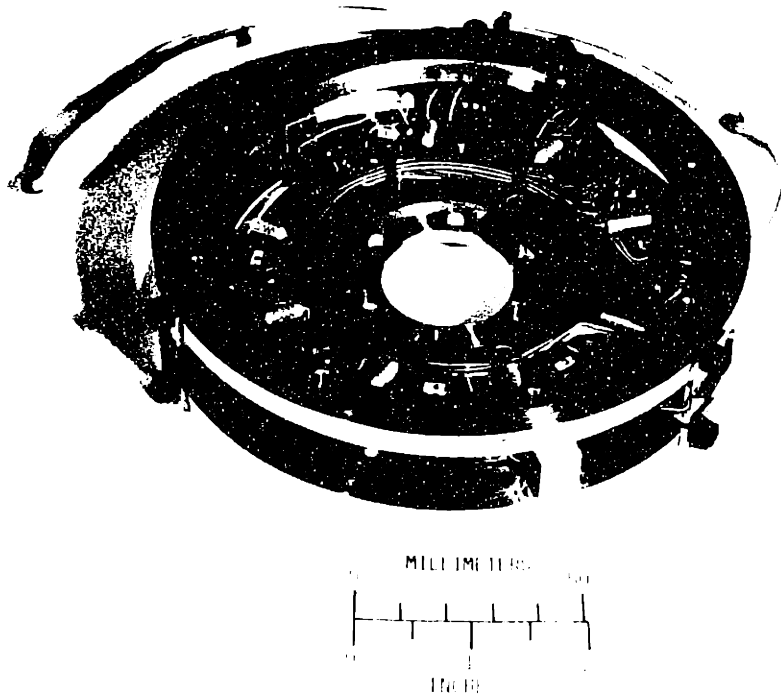


Figure F.3. High-sensitivity aluminum six-axis force sensor.

slip when the structure is loaded), the deflections that occur must be linear with respect to the forces, and that the transducers be placed so that the output vector spans the space corresponding to the input (i.e., there is no non-zero input which results in a zero output). The signal to noise ratio will be improved if the structure tend to concentrate the deflections at the transducers and tends to separate the responses. The output response of the transducers must either be linear or be linearized before multiplying by the calibration matrix.

The important parameters that affect the sensitivity of the force sensors used in this thesis are the cross-sectional area of each leg, the modulus of elasticity (Young's modulus), the shear modulus, the radius at which the legs are located, the gage factor or the strain gages used, and the gain of the instrumentation amplifiers. Metallic foil strain gages with a gage factor of approximately 2 (i.e., the ratio of the change in resistance of the gage in response to change in strain is 2) were used. Single-chip integrated circuit instrumentation amplifiers with a maximum gain of 1000 were used with all of the sensors. The amplifiers for

the first sensor were mounted separately while on the latter two sensors, the amplifiers were mounted on the sensor.

The first sensor used was made of aluminum, had legs with a cross-sectional area of $9 \times 10^{-6} \text{ m}^2$ (0.014 in^2), and had an effective diameter of 0.11 m (4.33 in). The expected sensitivity (output voltage divided by the input force) of one leg of the sensor to a force in the z direction (parallel to the axis of the cylinder) is:

$$\frac{E_o}{F_z} = \frac{E_i g_f G}{3(4EA)} \quad \text{F.1}$$

where E_i is the excitation voltage of the strain gage bridge, g_f is the gage factor of the strain gages, G is the instrumentation amplifier gain, E is Young's modulus, and A is the cross-sectional area of each leg. The factor of 4 comes from having only one active element on the strain gage bridge and the factor of 3 comes from having 3 legs sharing the load. Note that $\frac{1}{EA}$ is the strain per unit force. With a Young's modulus of $70 \times 10^9 \text{ Pa}$ ($10 \times 10^6 \text{ PSI}$), an input excitation of 15 volts, and a gain of 1000, the sensitivity becomes 0.004 volt/Newton. The measured sensitivity differed by less than a factor of two. In a like manner, the sensitivity of the sensor to x and y forces can be computed. As these forces are primarily measured by the shear bridges, the shear modulus is used instead of Young's modulus. The factor of 4 in equation F.1 becomes 2 because there are two active strain gage elements in the shear bridge. Therefore, the sensitivity is:

$$\frac{E_o}{F_x} = \frac{E_i g_f G}{3(2SA)} \quad \text{F.2}$$

where S is the shear modulus. Using the same gage factor and gain, this computed sensitivity becomes 0.025 Volt/Nt. The measured sensitivity was only 0.01 volt/Newton. However, the problem may be with the definition of the gage factor for shear bridges. The expected sensitivity to moments can also be obtained by computing the resulting forces at the radius at which the legs are located.

The strength of a sensor of this design depends on the cross-sectional area of the legs, the yield strength, the shear yield, and the effective diameter at

which the legs are located. Due to the relatively short length of the legs, the structure will fail in compression before buckling. Therefore, the yield strength of the structure to a load in tension or compression is the yield strength of the material multiplied by the total cross-sectional area of the three legs. Assuming a yield strength of $260 \times 10^6 \text{ Pa}$ ($37 \times 10^3 \text{ PSI}$) for 6061 - T6 aluminum, the yield strength along the z axis for the first sensor was approximately 7000N (1500 lbs). The shear strength of the structure along the x and y axis is found by multiplying the shear strength of the material by the total cross-sectional area of the legs. Assuming a shear yield of $150 \times 10^6 \text{ Pa}$ ($21 \times 10^3 \text{ PSI}$), the yield point of the structure in the x and y direction is approximately 4000N (900 lbs). The maximum x and y moments that can be resisted can be found by considering that these moments to be taken by two of the legs in tension and compression at the radius from the center of the sensor to the legs. For this sensor, the yield point should be at approximately 250 Nm (190 ft lbs) in m_x and m_y . The z moment is resisted by all three of the legs in shear at this radius. Therefore, the yield point for m_z should be 220 Nm (160 ft lbs).

The second sensor was designed to be used with the second compliance system. This sensor machined from 17-4 Ph stainless steel which has a yield strength of approximately $1.40 \times 10^9 \text{ Pa}$ ($200 \times 10^3 \text{ PSI}$) after heat treatment. As the Young's modulus is $190 \times 10^9 \text{ Pa}$ ($27 \times 10^6 \text{ PSI}$) compared to $70 \times 10^9 \text{ Pa}$ ($10 \times 10^6 \text{ PSI}$) for aluminum, the cross-sectional area of each leg was reduced to $3.5 \times 10^{-6} \text{ m}^2$ ($5.4 \times 10^{-3} \text{ in}^2$) to retain approximately the same sensitivity. However, the overall strength was increased by a factor of approximately 2.

A third sensor with approximately 4 times greater sensitivity is made of aluminum. Instead of being machined from one piece, this sensor has individual legs that are bolted with tapered joints and bonded with a high-strength locking compound. Two extensional gages and two half-shear-bridge gages are bonded to each leg. Thus for the same sensitivity, the legs can have twice the cross-sectional area. While this sensor has four times the sensitivity of the original aluminum sensor, the strength is decreased only by a factor of two.

APPENDIX G: FORCE SENSOR CALIBRATION

This procedure is used to obtain the 6 x 6 matrix transfer function that transforms the six-dimensional transducer output vector (strain gage voltages, in this case) into a six-dimensional force vector. The force sensor is loaded with six linearly independent force vectors applied one at a time. The six output voltages are recorded for each loading. If the outputs are non-zero when the sensor is not loaded, the bias voltages must be subtracted from these readings.

This information is arranged in the form:

$$\begin{bmatrix} v_{11}^0 & v_{12}^0 & \dots & v_{16}^0 \\ v_{21}^0 & v_{22}^0 & & v_{26}^0 \\ \cdot & & & \\ \cdot & & & \\ \cdot & & & \\ v_{61}^0 & v_{62}^0 & \dots & v_{66}^0 \end{bmatrix} = \begin{bmatrix} h_{11} & h_{12} & \dots & h_{16} \\ h_{21} & h_{22} & \dots & h_{26} \\ \cdot & & & \\ \cdot & & & \\ h_{61} & h_{62} & \dots & h_{66} \end{bmatrix} \begin{bmatrix} f_{11}^0 & f_{12}^0 & \dots & f_{16}^0 \\ f_{21}^0 & f_{22}^0 & \dots & f_{26}^0 \\ \cdot & & & \\ \cdot & & & \\ f_{61}^0 & f_{62}^0 & \dots & f_{66}^0 \end{bmatrix} \quad G.1$$

or:

$$V^0 = HF^0 \quad G.2$$

where $v_{11}^0, v_{21}^0, \dots, v_{61}^0$ are the voltages obtained when the sensor is loaded with the first force vector with components $f_{11}^0, f_{21}^0, \dots, f_{61}^0$; $v_{12}^0, v_{22}^0, \dots, v_{62}^0$ are the voltages obtained when the sensor is loaded with the second force vector, etc. H is a matrix relating the measured output voltages, V^0 , to the known input forces, F^0 . The H matrix is obtained from the relationship:

$$H = V^0 F^{0-1} \quad G.3$$

The force components of an unknown force vector applied to the force sensor obtained by multiplying the six-dimensional output voltage vector by H^{-1} . The H^{-1} matrix can be obtained with only one inversion by the relationship:

$$H^{-1} = \left[V^0 F^{0-1} \right]^{-1} = F^0 V^{0-1} \quad G.4$$

The first force sensor was calibrated by applying a set of six orthogonal forces and moments to the force sensor using a set of weights and pulleys (Figures

G.1 and G.2). By arranging the applied forces and moments in the proper order, the F^0 matrix is diagonal and obtaining the H matrix is a simple operation. The major problem with this technique is aligning the wires from the pulleys to the force sensor so that the applied force or moment does not contain small unmeasured off-axis components. This is a limiting factor in the accuracy that can be obtained.

To both simplify and improve the accuracy of the calibration procedure, a fixture was constructed to be used with a machinist's tilting rotary table. Using this fixture and a set of weights, six linearly independent but non-orthogonal force vectors are applied to the force sensor (Figures G.3 and G.4). The calibration forces and the resulting calibration matrix for the high sensitivity aluminum force sensor is shown in Table G.1. In linearity tests with this sensor, the worst case error either on-axis or off-axis was less than 0.005 of the maximum calibration load.

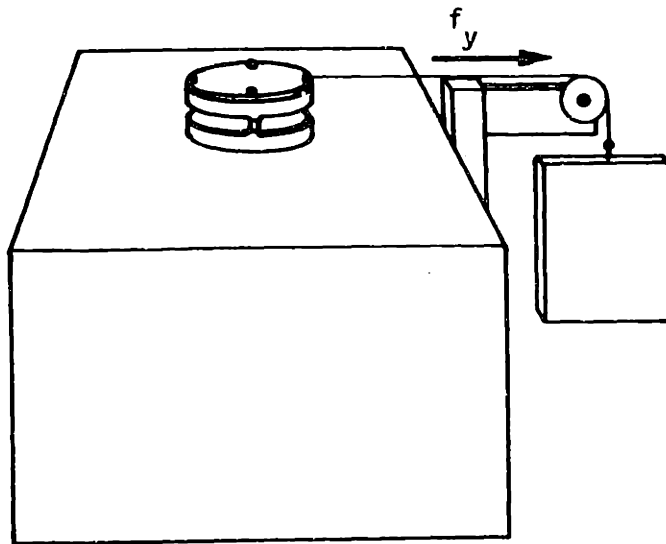


Figure G.1. Drawing of original calibration fixture illustrating f_y force loading.

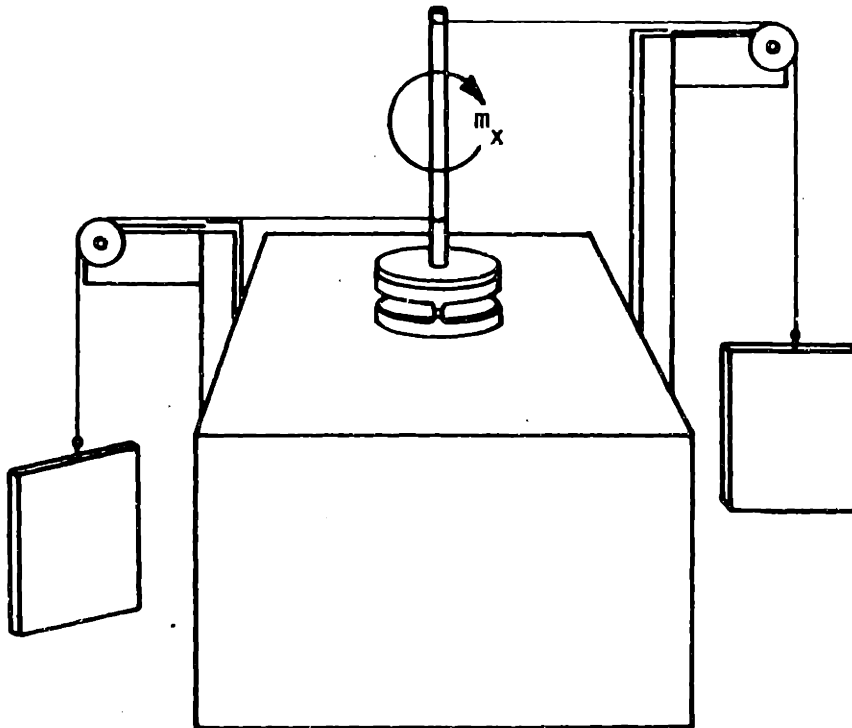


Figure G.2. Drawing of original calibration fixture illustrating m_x moment loading.

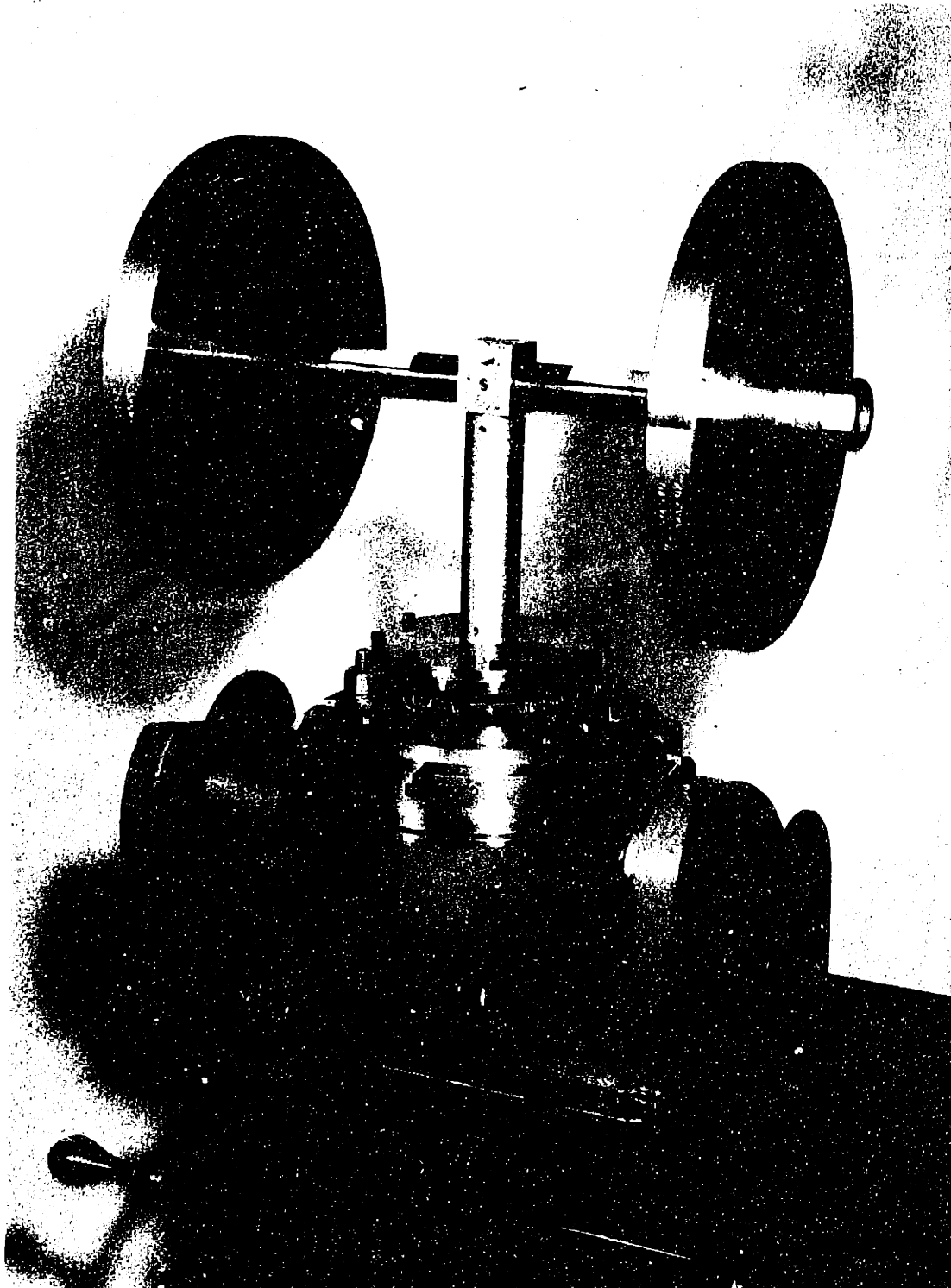


Figure G.3. Photograph of the force sensor calibration procedure with a - z-axis force being applied to the force sensor.

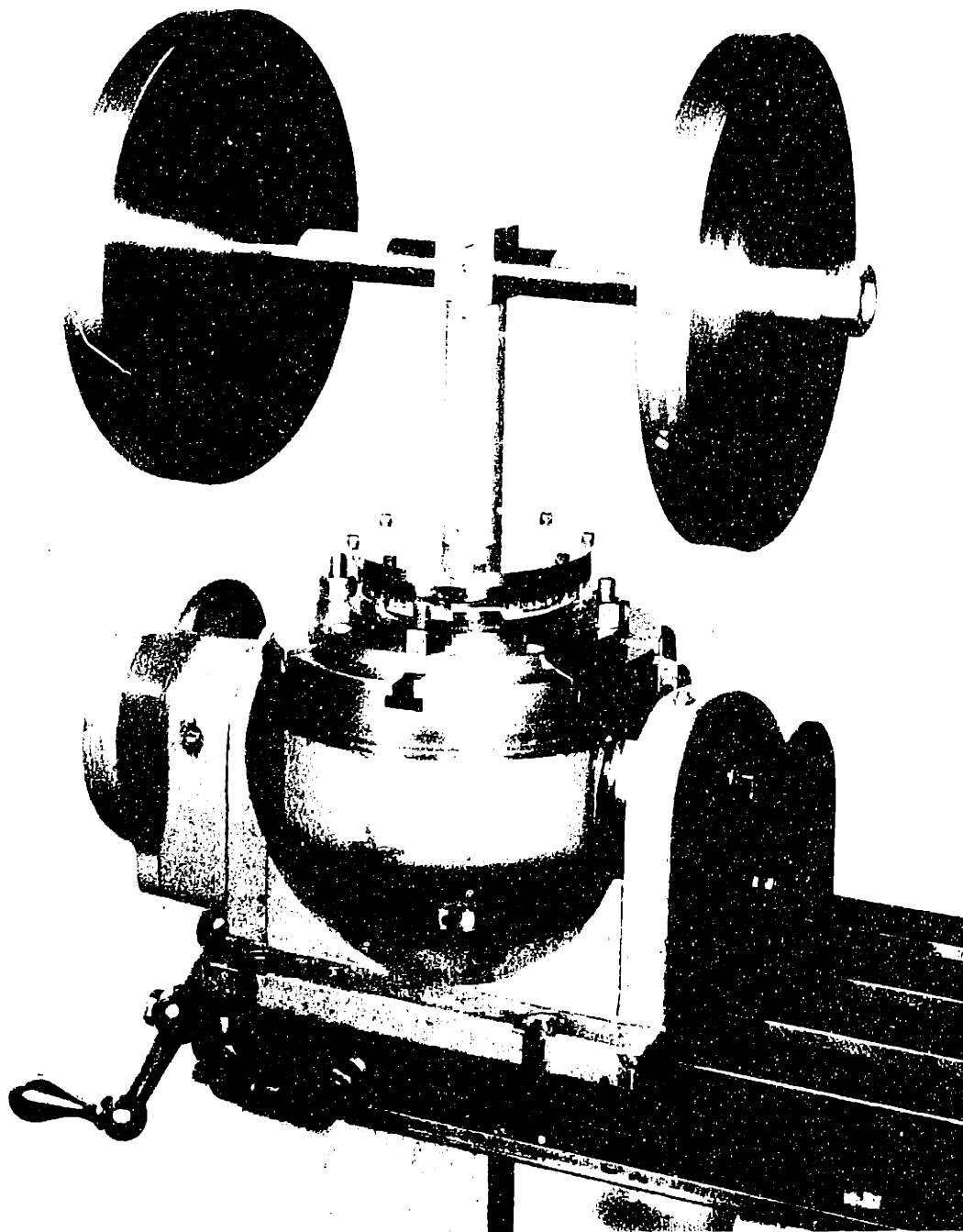


Figure G.3. Photograph of the force sensor calibration procedure with a - z-axis force being applied to the force sensor.

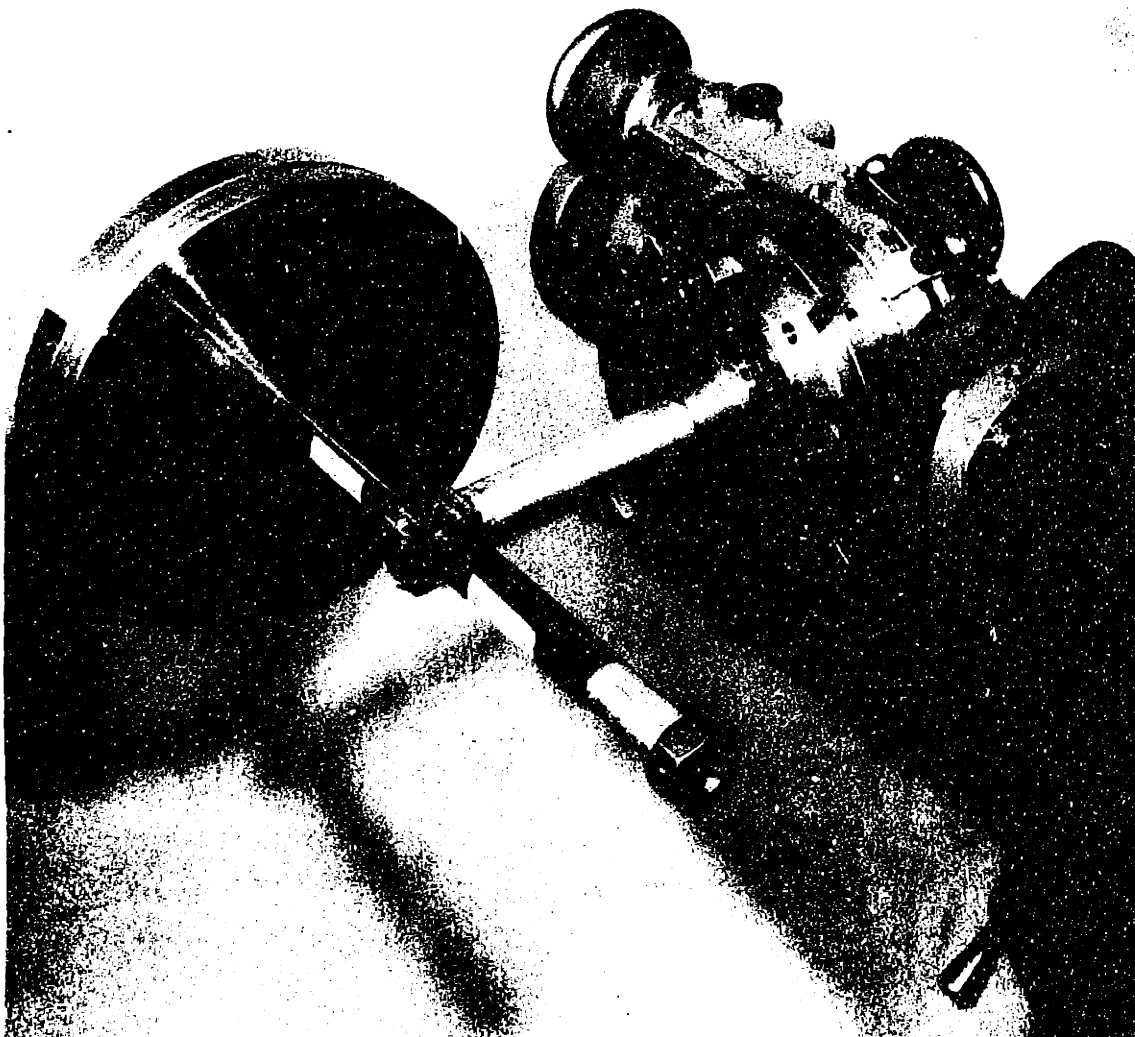


Figure G.4. Photograph of the force sensor calibration procedure with a force vector containing + x-axis force, + y-axis moment, and + z-axis moment components being applied to the force sensor.

INTENTIONAL DUPLICATE EXPOSURE

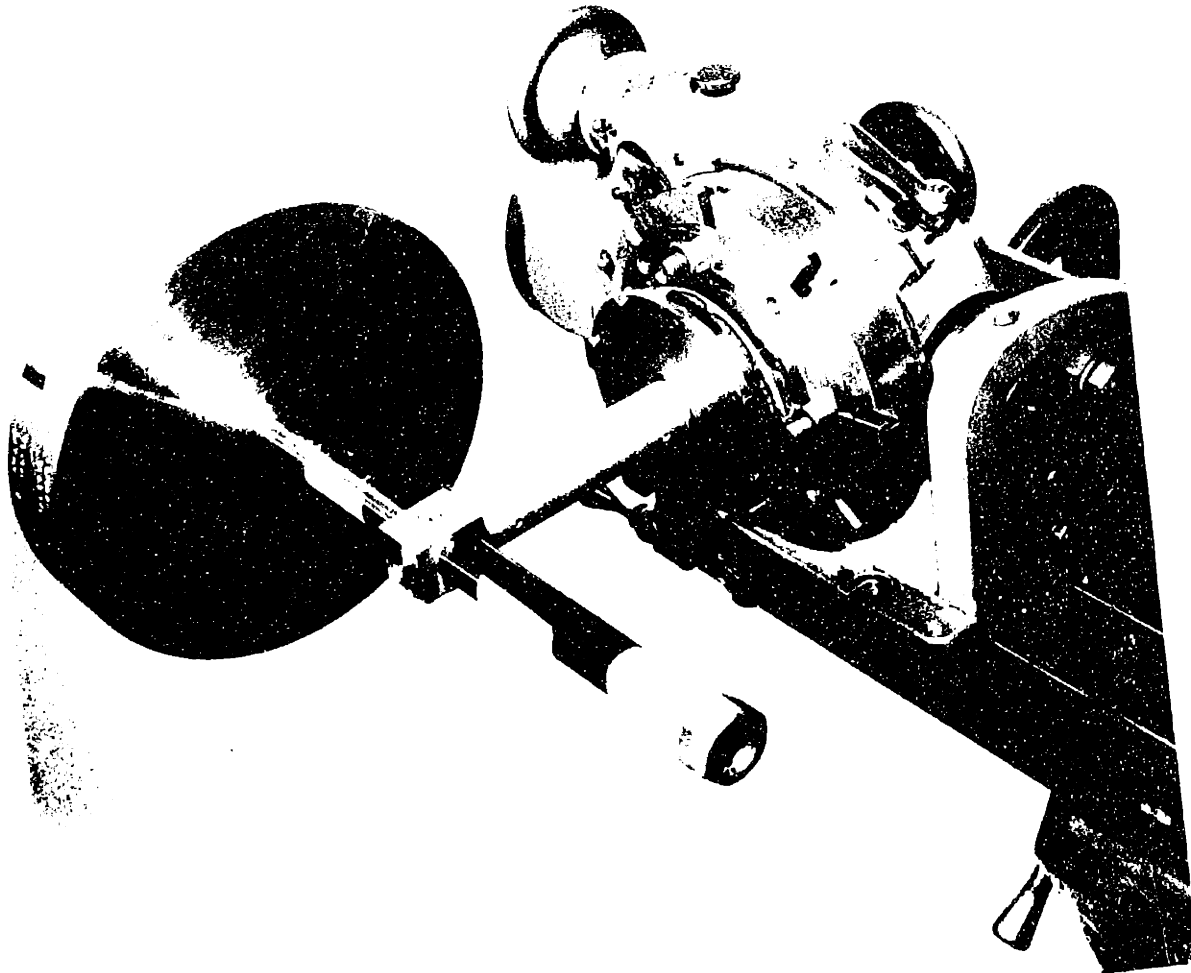


Figure G.4. Photograph of the force sensor calibration procedure with a force vector containing + x-axis force, + y-axis moment, and + z-axis moment components being applied to the force sensor.

Matrix of Input Force Vectors					
+38.2700	+0.0000	+0.0000	+0.0000	+0.0000	+0.0000
+0.0000	-38.2700	+0.0000	+0.0000	+0.0000	-19.1500
+0.0000	+0.0000	-190.9000	-60.0600	-40.9100	+0.0000
+0.0000	+6.3210	+0.0000	+9.5070	+0.0000	+3.1630
+6.3210	+0.0000	+0.0000	+0.0000	+6.1450	+0.0000
+0.0000	+0.0000	+0.0000	+0.0000	+0.0000	+2.8760
Matrix of Measured Voltage Vectors					
-3.1609	-0.8518	+0.3676	-0.7958	+0.3968	+1.6252
+1.8346	-1.8376	+0.4930	+0.7997	+0.4362	+0.6650
+5.1633	-1.8672	-4.4890	-4.3648	+3.6788	-0.8099
-0.8673	+5.9810	-5.2606	+7.4494	-1.8641	+3.0481
-4.2387	-3.2022	-4.7111	-6.2591	-5.1268	-1.6078
+1.1469	+3.4398	+0.3516	+0.5324	-0.3455	+3.8047
Force Sensor Calibration Matrix					
-7.2222	+5.2031	+0.6782	-0.7838	+0.4440	+3.1355
+0.4300	+7.8924	-0.4692	+0.0400	+0.7845	-6.3969
+0.4067	-1.0224	+14.0413	+11.9008	+13.7224	-0.7416
-0.0380	+0.0123	-0.3082	+0.6890	-0.4753	+0.0270
+0.0436	-0.0412	+0.7476	-0.0783	-0.6301	-0.0558
+0.4681	+0.5957	+0.0331	+0.0299	+0.0685	+0.4639

Table G.1. Matrices of the input force vectors and the measured voltage vectors and the resulting force sensor calibration matrix for the high sensitivity aluminum force sensor.

BIOGRAPHY

Samuel H. Drake was born May 3, 1943 in Charleston, West Virginia. He lived in Yakima, Walla Walla, and Richmond, Washington, and in Blairstown, New Jersey before entering public school in Texas City, Texas. He attended public school in Marietta, Ohio (in a white clapboard one-room school house); Madison, Ohio; Niagara Falls, New York and graduated from the Lewiston Porter Central High School in Lewiston, New York.

He entered the Massachusetts Institute of Technology in September 1961, where he majored in Physics. He was a member of the heavy-weight crew for four years and belonged to the Rocket Research Society and the Sports Car Club. In his senior year, he also worked at the M.I.T. Instrumentation Laboratory (since named the C.S. Draper Laboratory).

After graduating in 1965, he worked for Sanders Associates in Nashua, New Hampshire where he designed optics and experimental test apparatus for a laser radar system. A year-and-a-half later, he returned to the Instrumentation Lab where he designed optics and support equipment for a satellite guidance system. He also reentered M.I.T. as a special graduate student in Mechanical Engineering after deciding he was more adept at making things work than in dealing with quarks, quantum jumps, and black holes. When the satellite guidance funding was cut, he worked on the Apollo Project where he operated the Lunar Module Simulator to verify guidance programs and procedures.

In September 1969, he became a full-time graduate student at M.I.T. in the Mechanical Engineering Department. The master's thesis work was done on an oil pollution problem in the fluid mechanics lab. The thesis was titled "Dynamics of an Oil Containment Boom in a Wave Field".

After completing this work in 1970, he returned to the Instrumentation Lab and continued to work on the Apollo project. He also continued to take courses in the Mechanical Engineering Department and earned a Mechanical Engineer's degree in June 1974. Earlier that year he had successfully completed the doctoral qualifying exam.

At the end of the Apollo Project, he became involved in work on remote manipulators and, later, industrial automation. He returned to M.I.T. as a full-time student in the Mechanical Engineering Department in September 1975, to begin work on this thesis. He took several courses at the Harvard Business School to fulfill the requirement for a minor.

His outside interests include photography, bicycling, and woodworking.